SYNTHESIS AND CHARACTERIZATION OF BRONZE-TYPE MIXED OXIDES FOR THE SELECTIVE ACTIVATION OF HYDROCARBONS

PhD Thesis

Presented by:

Agustín de Arriba Mateos

Supervisor:

Prof. José Manuel López Nieto

Valencia, January 2024

Agradecimientos

Quisiera expresar en estas líneas mi más sincero agradecimiento a todas las personas que han contribuido, de muchísimas maneras, a que este trabajo vea la luz, y me han acompañado durante estos últimos cinco años en Valencia.

En primer lugar, me gustaría agradecer a mi director de tesis, el Prof. José Manuel López Nieto, por la oportunidad de llevar a cabo este trabajo dentro de su grupo de investigación. Me siento tremendamente afortunado de haber podido aprendido de él, de su esfuerzo, su motivación y de su dedicación por el mundo de la ciencia. Ha sido todo un privilegio compartir con él conversaciones sobre química, física y metafísica, fútbol, política, cultura y aprender de él como científico y como persona. Quisiera extender también este agradecimiento al Prof. Benjamín Solsona, por su ayuda y su bondad.

A la Dra. Susana Valencia y el Prof. Fernando Rey, por todo el apoyo que me han dado desde que llegué al máster, dos grandes científicos y mejores personas, y a la Prof. Carmen I. Misiego, por introducirme en el mundo de la investigación y haber estado siempre tan pendiente de mí.

A toda la gente de SpLine que me acogió, enseñó, e hizo que los tres meses en el ESRF pasasen como una semana: Juan, Ana, Germán, Jesús, Miguel Ángel, Jaime y Eugenia.

A Dani, por cuidarme, enseñarme y apoyarme siempre desde el primer día (espero que esta tesis sea leída un poquito menos que la tuya), y a Yannick que, a pesar de ser francés, sigue siendo una de las personas más buenas y

trabajadoras que he conocido en mi vida. Al resto de personas serias (Pascual, Luismi y Jaime) por las enseñanzas, los congresos, amistad y ayuda. A Xisco y Ferran, dos grandes *sutaners*. A Nuria y Silvia, por ser siempre tan increíbles conmigo.

A todas las personas con las que he compartido grupo de investigación estos últimos años: Dani (otra vez), Lidia, Yousra, Giulia, Gustavo, Anna, Jose y Bea. Para mis "hermanos menores" en el grupo: Jose, gracias por estar ahí, por nuestras conversaciones y bromas. Bea, jamás podré devolverte toda la ayuda y el buen humor que me has transmitido, todos los planes que hemos hecho y que estoy seguro de que seguiremos haciendo. Me siento muy orgulloso de compartir equipo con vosotros.

A todas las personas que me unen al ITQ más allá de las horas que pasamos allí: Adri, *Plalito*, por ser una persona increíble, siempre con una sonrisa; Aída, por su tremenda dulzura; Adri Combi, por todas las bromas; y a Isiña, por ser como eres, un auténtico trébol de cuatro hojas.

A las demás personas que conforman la república independiente de BecariesP2, espacio seguro y la mejor sala de todo el instituto: Marcos, Eva, Elena, Iván, Ferran, Lorena, Sofía, Quique y Álvaro.

A todo el personal de taller, caracterización y administración, así como a todos mis compañeros del ITQ, por nombrar unos cuantos: Dolo, Pablo del Campo, Aroa, Elena, Cris Ibáñez, Edi, Marwan, Alfonso… Especialmente a Eva Briz, por cuidarme tanto dentro como fuera del laboratorio.

A mi familia valenciana: Irene, por saber ponerme las pilas a pesar de la distancia con sólo una llamada; a Fany, por descubrirme el auténtico

significado de la palabra incombustible de fiesta; a Eva, compañera de juegos de Nintendo Switch; a Violeta, la persona más competitiva del mundo jugando al pádel; y a Juan, parte indispensable del *Dúo Estático* y compañero de todas las batallas.

A todos mis amigos de Salamanca: los maristeños (David, Álex, Fran, Fraile, Cacio, Beto, Manute, Sánchez, Andrés, Jucar y Palomero) por hacerme sentir uno más, Lydia (y ahora Vega), Isa y, en especial, a mi medio-hermana Cristina, compañera de laboratorio desde el día uno de carrera y hasta ahora.

A mis *mejores amigos siempre*: Pablo, Gómez, Barre, Manu, David y María; por estar conmigo desde que tengo uso de razón, y por haber hecho todas las bromas y rimas habidas y por haber con la palabra "sincrotrón", me siento muy afortunado de teneros.

También quiero agradecer a mis tíos, primos y mi abuelo, por el amor y la comprensión desde la distancia.

A Judith, por cuidarme y apoyarme durante estos años.

Por último, y más importante, a mis padres. Por ser las personas más buenas y dulces, y por ayudarme (y sostenerme) de manera incondicional toda mi vida, todo esto tiene sentido gracias a vosotros.

Agustín de Arriba Mateos

"Sólo el que ensaya lo absurdo es capaz de conquistar lo imposible."

Miguel de Unamuno y Jugo

Rector de la Universidad de Salamanca

Summary

The present doctoral thesis is set within the scope of the energy transition that aims to substitute non-renewable sources, especially fossil-based ones, to renewable feedstocks for the production of both fuels and chemical compounds. Therefore, this challenge is double. On one hand, prevent a cut in the never-ending global demand for energy and chemical goods supply in a context of gradual depletion of fossil sources while, on the other hand, give a response to the urge in the limitation of carbon oxides pollution that has critical impacts on human health and Earth's sustainable maintenance.

In this sense, natural gas can be considered as a bridge feedstock in this step-by-step transition between highly contaminating coal or oil, to green solutions such as hydrogen and biomass, considerably decreasing in the meantime carbon oxides emissions associated to industrial processes.

Among the chemical compounds produced worldwide, ethylene stands out as building block for the most important polymer: polyethylene. Nevertheless, current industrial synthesis of ethylene, Steam Cracking, is regretfully the most energy-demanding process in the Petrochemical industry. Conversely, a promising alternative to Steam Cracking is the oxidative dehydrogenation (ODH) of ethane, an exothermic process that requires fairly lower energy supplies. In this way, catalysts that present the best catalytic performance in the ethane ODH are the ones based on molybdenum and vanadium oxide, with crystalline structure known as M1.

Herein an exhaustive study on the synthesis, characterization and reactivity of mixed metal oxides that present the orthorhombic M1 phase has been conducted, aiming to unravel the influence of the composition on the catalytic performance of said materials.

In a first place, the hydrothermal synthesis of a bimetallic form of the M1 phase, Mo-V-O, has been explored, taking into account all the possible parameters such as temperature, atmosphere, pH of the synthesis gel, activation temperature and post-synthesis treatments. Results indicate that the combination of these parameters is capital not only for the appropriate formation of the M1 phase, but also to the catalytic performance. This is, a set of differently synthesized Mo-V-O catalysts, all of them presenting the M1 phase, may differ in the activity and selectivity to ethylene by up to 25 % depending on the chemical composition on the surface species of the catalyst.

Moreover, it was investigated the synthesis and characterization of trimetallic oxides Mo-V-Te-O presenting the M1 phase with different Te-loadings ($0 < Te/Mo < 0.17$), trying to modulate the acid properties, as well as the thermal stability and catalytic behavior in the ethane ODH. Accordingly, we observed that the introduction of tellurium into the structure of the M1 phase leads to an enhanced thermal stability, in addition to an increase on the selectivity to ethylene.

Subsequently, it was performed a comparative study between bi-, tri- and tetrametallic (Mo-V-Te-Nb-O) catalysts about the influence of composition and/or thermal activation on the catalytic behavior. Obtained results suggest that there is a correlation between surface composition, as well as the thermal activation temperature, with the selectivity of these catalysts to ethylene. Then, it was found a direct relationship between surface V^{4+} species (results from X-ray photoelectron spectroscopy, XPS) and the selectivity to ethylene. Furthermore, since all these mixed oxides can be

considered as semiconducting materials, an electrochemical parallel study was also conducted. Then, these results suggest that the oxides that showed the best selectivity to ethylene (i.e., catalyst Mo-V-O activated at 400 ºC; and Mo-V-Te-O and Mo-V-Te-Nb-O catalysts treated at 600 ºC) are also the ones that present the highest amount of V^{4+} species on the surface of the solid, in addition to the highest values of electric resistance.

Finally, a comparative study was performed between the three catalytic systems that have offered the best properties in the oxidative dehydrogenation of ethane in the literature: i) alumina supported vanadium oxide (VO_x/Al_2O_3), ii) tin promoted nickel oxide (Sn-NiO) and iii) multicomponent Mo-V-Te-Nb-O (M1) catalyst optimized in the present thesis. Thus, both the catalytic and the characterization (by means of conventional and in situ techniques) results indicate important differences in the selectivity to ethylene of these catalysts at high ethane conversion values, as a consequence of a greater or lesser degradation of the ethylene over each catalyst. In this sense, the catalyst based on mixed metal oxides, Mo-V-Te-Nb-O, shows a very low reactivity for ethylene deep oxidation (which favors a high selectivity during ethane ODH), whereas the rest of the catalytic systems display higher reactivity for deep oxidation of ethylene (which drastically reduces the selectivity to ethene during ethane ODH, specially at high ethane conversion). These results will be discussed in terms of the different adsorption properties of both ethane/ethene over the three catalytic systems.

Resumen

La presente tesis doctoral se encuentra enmarcada en un momento crucial como es el de la transición energética, en la que se pretende sustituir fuentes no renovables como son el carbón o el petróleo por alternativas renovables para la producción de energía y productos químicos de interés. Por lo tanto, el desafío es doble. Por un lado, anticiparse a la futura desaparición de fuentes fósiles en un contexto de inagotable demanda de suministro de energía, por otro, limitar de manera urgente las emisiones de gases de efecto invernadero con consecuencias nefastas tanto para la humanidad como para el planeta.

En este sentido, el uso de gas natural puede considerarse de manera estratégica como una materia prima de transición entre las demás fuentes fósiles y las fuentes renovables como el hidrógeno o la biomasa, mientras que a su vez es posible disminuir las emisiones de óxidos de carbono derivadas de los procesos industriales actuales.

De entre los compuestos químicos producidos industrialmente destaca el etileno por ser el precursor del polímero plástico más importante, el polietileno. Lamentablemente, industrialmente, el etileno se produce a través del craqueo con vapor (*Steam Cracking*) de hidrocarburos, que constituye el proceso industrial con mayor demanda de energía actualmente. En contraposición a esto, la deshidrogenación oxidativa (ODH) de etano, un proceso exotérmico que requiere de mucha menor cantidad de energía ha aparecido como una alternativa interesante al *Steam Cracking*, siendo los catalizadores basados en óxidos de molibdeno y vanadio, que presentan la fase cristalina conocida como M1, los que mejores propiedades catalíticas ofrecen.

En este trabajo se ha llevado a cabo un estudio exhaustivo sobre la síntesis, caracterización y reactividad de óxidos metálicos mixtos que presentan la fase ortorrómbica M1, con el fin de conocer la influencia de la composición en las propiedades catalíticas de dichos materiales.

En primer lugar, se ha estudiado la síntesis hidrotermal de óxidos bimetálicos, Mo-V-O que presentan la fase M1, considerando diferentes parámetros sintéticos como la temperatura de síntesis, atmósfera, pH del gel de síntesis, temperatura de activación o post tratamientos de purificación. Los resultados de caracterización indican que la combinación de estos parámetros es clave en la obtención no solo de la fase M1, si no de catalizadores óptimos en la ODH de etano, observándose diferencia de hasta 25 puntos porcentuales en la selectividad a etileno dependiendo de la composición de las especies en la superficie del catalizador.

En segundo lugar, se ha investigado la síntesis y caracterización de óxidos trimetálicos, Mo-V-Te-O, que presentan la fase M1 con diferentes proporciones de teluro en la estructura ($0 < Te/Mo < 0,17$), con el fin modular la acidez, la estabilidad térmica y el comportamiento catalítico de estos catalizadores. Se ha observado que la incorporación de teluro en la estructura de la fase M1 supone un aumento considerable de la estabilidad térmica de los catalizadores, así como de la selectividad a etileno.

Posteriormente, se ha llevado a cabo un estudio comparativo entre catalizadores bi-, tri- y tetrametálicos (Mo-V-Te-Nb-O), de la influencia de la composición y/o la activación térmica de los diferentes materiales sobre las propiedades catalíticas. Los resultados obtenidos sugieren una correlación entre la composición superficial y temperatura de activación de

los catalizadores con la selectividad a etileno. Así, se ha encontrado una relación directa entre la concentración relativa de especies V^{4+} en la superficie del catalizador (obtenida mediante de espectroscopia de fotoemisión de rayos-X, XPS) y la selectividad a etileno. Además, y dado que todos estos óxidos mixtos pueden considerarse como semiconductores, se llevó a cabo un estudio electroquímico de los catalizadores. Estos resultados sugieren que, materiales que mostraron una mayor selectividad a etileno, (el catalizador Mo-V-O activado a 400 ºC; y los catalizadores Mo-V-Te-O y Mo-V-Te-Nb-O activados a 600 ºC), presentan una mayor concentración de especies V^{4+} en la superficie y mayores valores de resistancia eléctrica.

Por último, se ha llevado a cabo un estudio comparativo entre los sistemas catalíticos que, en la literatura, presentan los mejores resultados catalíticos para ODH de etano: i) óxido de vanadio soportado sobre alúmina (VO_x/Al_2O_3); ii) óxido de níquel promovido con estaño (Sn-NiO); y iii) el catalizador Mo-V-Te-Nb-O (M1) optimizado en este trabajo. Los resultados catalíticos obtenidos, así como los resultados de caracterización (mediante técnicas de caracterización convencionales e in situ), muestran importantes diferencias en la selectividad a etileno a altas conversiones de etano, como consecuencia de la mayor o menor degradación de etileno en cada catalizador. En ese sentido, el catalizador basado en óxidos mixtos de Mo-V-Te-Nb-O presenta una muy baja reactividad a la combustión de etileno (lo que favorece una alta selectividad durante la ODH de etano), mientras que los otros dos sistemas catalíticos presentan una reactividad para la combustión de etileno mucho mayor (lo que reduce sustancialmente

la selectividad a etileno durante la ODH de etano, especialmente a altas conversiones de etano). Estos resultados se discuten en función de las propiedades de adsorción de etano y etileno en cada catalizador.

Resum

La present tesi doctoral es troba emmarcada en un moment crucial com és el de la transició energètica, en la qual es pretén substituir fonts no renovables com són el carbó o el petroli per alternatives renovables per a la producció d'energia i productes químics d'interés. Per tant, el desafiament és doble. D'una banda, anticipar-se a la futura desaparició de fonts fòssils en un context d'inesgotable demanda de subministrament d'energia, per un altre, limitar de manera urgent les emissions de gasos d'efecte hivernacle amb conseqüències nefastes tant per a la humanitat com per al planeta.

En aquest sentit, l'ús de gas natural pot considerar-se de manera estratègica com una matèria primera de transició entre les altres fonts fòssils i les fonts renovables com l'hidrogen o la biomassa, mentre que al seu torn és possible disminuir les emissions d'òxids de carboni derivats dels processos industrials actuals.

D'entre els compostos químics produïts industrialment destaca l'etilé per ser el precursor del polímer plàstic més important, el polietilé. Malauradament, a nivell industrial, l'etilé es produeix a través del craqueig amb vapor (Steam Cracking) d'hidrocarburs, que constitueix el procés industrial amb major demanda d'energia. En contraposició a això, la deshidrogenació oxidativa (ODH) d'età, un procés exotèrmic que requereix de molta menys quantitat d'energia ha aparegut com una alternativa interessant a l' Steam Cracking, sent els catalitzadors basats en òxids de molibdé i vanadi, que presenten la fase cristal·lina coneguda com M1, els que millors propietats catalítiques ofereixen.

En aquest treball s'ha dut a terme un estudi exhaustiu sobre la síntesi, caracterització i reactivitat d'òxids metàl·lics mixtes que presenten la fase

ortoròmbica M1, amb la finalitat de conéixer la influència de la composició en les propietats catalítiques d'aquests materials.

En primer lloc, s'ha estudiat la síntesi hidrotermal d'òxids bimetàl·lics, Mo-V-O que presenten la fase M1, considerant diferents paràmetres sintètics com la temperatura de síntesi, atmosfera, pH del gel de síntesi, temperatura d'activació o post tractaments de purificació. Els resultats de caracterització indiquen que la combinació d'aquestos paràmetres és clau en l'obtenció no sols de la fase M1, si no de catalitzadors òptims en la ODH d'età, observant-se diferència de fins a 25 punts percentuals en la selectivitat a etilé depenent de la composició de les espècies en la superfície del catalitzador.

En segon lloc, s'ha investigat la síntesi i caracterització d'òxids trimetàl·lics , Mo-V-Te-O, que presenten la fase M1 amb diferents proporcions de tel·luri en l'estructura ($0 < Te/Mo < 0,17$), amb la finalitat de modular l'acidesa, l'estabilitat tèrmica i el comportament catalític dels catalitzadors. S'ha observat que la incorporació de tel·luri en l'estructura de la fase M1 suposa un augment considerable de l'estabilitat tèrmica dels catalitzadors, així com de la selectivitat a etilé.

Posteriorment, s'ha dut a terme un estudi comparatiu entre catalitzadors bi-, tri- i tetrametàl·lics (Mo-V-Te-Nb-O), de la influència de la composició i/o l'activació tèrmica dels diferents materials sobre les propietats catalítiques. Els resultats obtinguts suggereixen una correlació entre la composició superficial i temperatura d'activació dels catalitzadors amb la selectivitat a etilé. Així, s'ha trobat una relació directa entre la concentració relativa d'espècies V^{4+} en la superfície del catalitzador (obtinguda mitjançant espectroscòpia de fotoemissió de raigs-X, XPS) i la selectivitat

a etilé. A més, i atés que tots aquestos òxids mixtes poden considerar-se com a semiconductors, es va dur a terme un estudi electroquímic dels catalitzadors. Estos resultats suggereixen que, materials que van mostrar una major selectivitat a etilé, (el catalitzador Mo-V-O activat a 400 °C; i els catalitzadors Mo-V-Te-O i Mo-V-Te-Nb-O activats a 600 °C), presenten una major concentració d'espècies V^{4+} en la superfície i majors valors de resistència elèctrica.

Finalment, s'ha dut a terme un estudi comparatiu entre els sistemes catalítics que, en la literatura, presenten millors resultats catalítics per a ODH d'età: i) òxid de vanadi suportat sobre alumina (VO_x/Al_2O_3); ii) òxid de níquel promogut amb estany (Sn-NiO); i iii) el catalitzador Mo-V-Te-Nb-O (M1) optimitzat en este treball. Els resultats catalítics obtinguts, així com els resultats de caracterització (mitjançant tècniques de caracterització convencionals i in situ), mostren importants diferències en la selectivitat a etilé a altes conversions d'età, a conseqüència de la major o menor degradació de l'etilé en cada catalitzador. En eixe sentit, el catalitzador basat en òxids mixtes de Mo-V-Te-Nb-O presenta una molt baixa reactivitat a la combustió d'etilé (el que afavoreix una alta selectivitat durant la ODH d'età), mentre que els altres dos sistemes catalítics presenten una reactivitat per a la combustió d'etilé molt major (el que redueix substancialment la selectivitat a etilé durant la ODH d'età, especialment a altes conversions d'età). Estos resultats es discuteixen en funció de les propietats d'adsorció d'età i etilé en cada catalitzador.

Index

Page

Chapter 1. Introduction

Chapter 2. Experimental section

Chapter 1

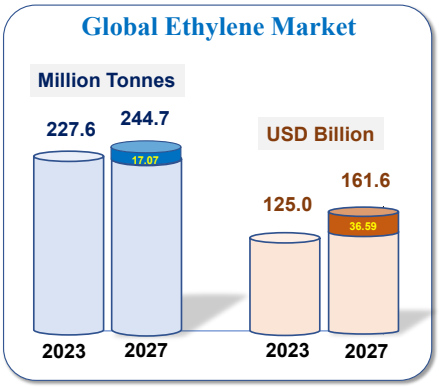

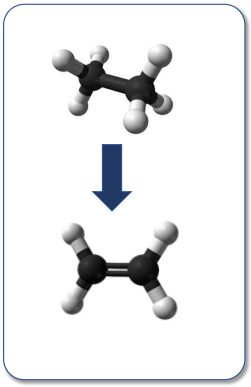

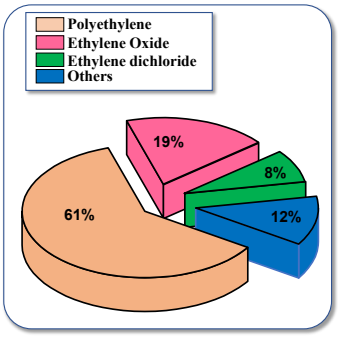

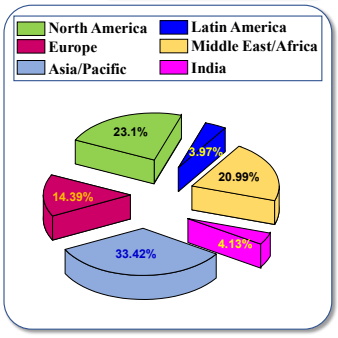

Introduction

1.1. Environmental crisis and future perspectives

According to the United Nations [1-3], global temperature has risen to 1.1-1.2 ºC above the pre-industrial era. Moreover, the last years (2015-2021) have been the warmest on record. In this time, the new proposed geological epoch known as the Anthropocene [4], social and economic changes have driven to a point in where capability of the planet for sustaining our current lifestyle has been put to a risk [5]. In fact, in reports mentioned before, by 2100, about one third of global land areas will suffer from drought [1] as a cause of the Climate Change, effects that in any case are now notorious in countries like Spain. In that sense, several organizations have analyzed and proposed some goals and boundaries that every nation must face in order to secure and guarantee a fair distribution of sources.

On one hand, United Nations has set 17 goals for a sustainable development framed into the 2030 Agenda [1, 6], **Figure 1.1**, in which: affordable and clean energy (Goal 7), industry, innovation and infrastructure (Goal 9) or climate action (Goal 13) can be encompassed into the objectives of the present thesis.

On the other hand, scientists around the world from the Global Climate Observing System (GCOS) have proposed a set of seven parameters divided in temperature and energy, atmospheric composition, ocean and water and cryosphere, presented in the conference of parties of the United Nations Framework Convention on Climate Change (UNFCCC), that have also been implemented by the European Commission in the Copernicus Climate Change Service (C3S).

Figure 1.1. United Nation 17 goals for sustainable development

The importance of these pillars lies on the fact that they comprehend key information on climate change without reducing it to only temperature (**Figure 1.2**). These seven indicators provide a more detailed picture of the changes that may occur and how the climate change affect the world in different perspectives [2, 7, 8].

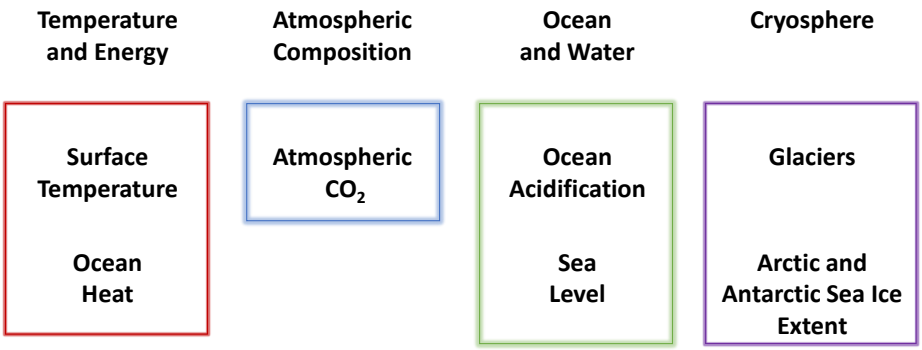

Figure 1.2. The seven headline Global Climate Indicators, adapted from [2].

Conversely, in 2009, a group of scientists identified the nine planetary boundaries (Earth system boundaries, ESBs) that must not be surpassed in order to guarantee the stability and resilience of planet Earth [9]. Recently, a new study combining modelling and literature published earlier this year by the same authors, led by Rockström *et al.* [10], updated those ESBs, representing the limits that can cause damage but also injustice in some areas of the world (**Figure 1.3**).

Then, these nine ESBs can be grouped in: climate, biosphere, fresh water, nutrients, and air pollution, all of them at global and subglobal scales. Nonetheless, one of the main outputs of this study is that they were separately defined firstly the safe (in terms of maintaining the resilience of the Earth) and secondly the just (here divided in three: **i)** interspecies, **ii)** intergenerational and **iii)** intragenerational, among countries) system boundaries that, in some cases may not present the same value.

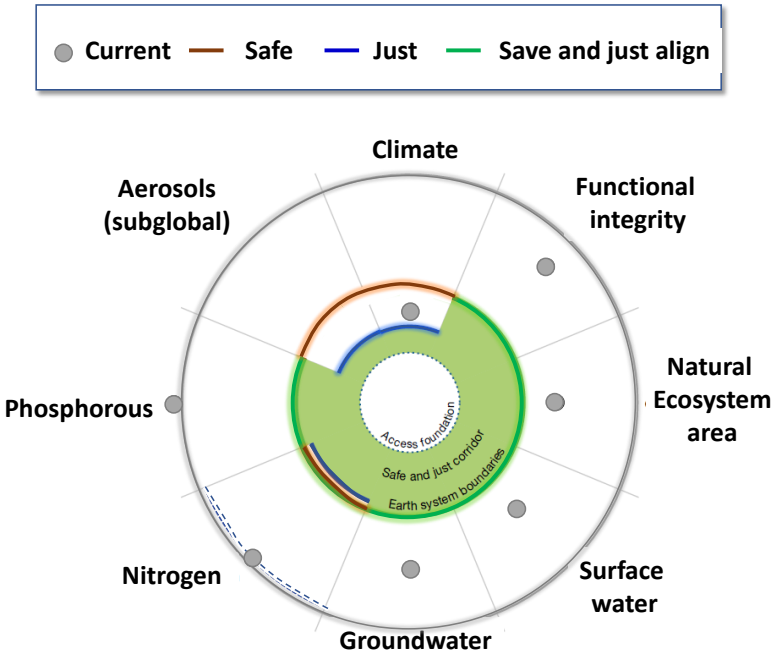

Figure 1.3. Proposed safe and just Earth System Boundaries. Reproduced from [10].

Nevertheless, when it comes to climate, these researchers concluded that 1.5 ºC global warming should avoid most of the severe impacts on all living beings on Earth, in accordance also with the recent Paris Agreement on Climate Change, signed by 193 countries and the European Union as a whole (starting in 2016, 4 November). However, this temperature rise leads and has already led to several impacts in some parts of the world, and more than 200 million people (500 million in the mid-long term) can be affected by extreme weather disasters. In fact, in the last 20 years, the number of annual natural disasters has practically doubled its value [11], with their

humanitarian and economic consequences. Therefore, apart from the safe, authors concluded that the just boundaries in this matter should be set around 1.0 ºC, a value that has already been surpassed.

In the case of the biosphere, safe boundaries (natural ecosystem area) for which many parameters depend on such as species conservation, stocks and flows of carbon or water and nutrients availability were set to 50-60 % of global natural land surface areas intact. Moreover, this number also serves to ensure carbon sequestration in the ocean and decrease the risk of marine species extinction [12]. In addition, and especially in the case of countries less favored, this number could be increased up to 60 % in order to stablish a just boundary. On top of that, another boundary that concerns biosphere is known as functional integrity, which deals with the capability of human-modified allocations (rather urban or agricultural) to provide ecological functions. This, however, can vary significantly depending on climate and topography. As a general rule, 20 to 25 % of each 1 km^2 should be under natural vegetation to prevent current and future problems related to food productivity, pollution and ecosystem capacity to deal with natural hazards [13].

In what refers to water, both surface and ground level have been considered. Then, flow alterations in rivers are of special interest due to its implications in biodiversity maintenance (land and marine) along with the production of food or drinking water availability [12], but also to the natural disasters associated with floods that have suffered more commonly some populations in last few years [14, 15]. Experimental results showed that, to avoid all this mentioned problems, variations of total flow must not exceed

20 %, and this number should be accomplished globally. Regretfully, nowadays this target is only fulfilled in 66 % of land area (which supposes less than 50 % of the planet's population), with associated problems of water scarcity and its consequences in human and biodiversity's health [16]. Groundwater follows the same path, while its safe boundary is set to not exceed the annual recharge by any means, it was shown that only 53 % of land area fits it, putting in a serious risk human needs and water quantity (and quality).

Additionally, they were also considered the anthropogenic contributions of nitrogen and phosphorus to the ground (nutrients), most likely due to agriculture and pollution, that enhance eutrophication. Thus, a set of values for both N and P were proposed. Nevertheless, as in the case of the previous boundaries, these limits are not equally set. Then, the access to fertilizers should be guaranteed to vulnerable countries in which the production of food may be limited, so just and safe boundaries must be carefully studied. On the contrary, legislations and pollution policies are to be strictly set to keep away from an excess of fertilization that, jointly to drawth lead to natural damages as the one we have face in Mar Menor (Spain), where biodiversity is being widely triggered [17].

Lastly, aerosol pollution was also studied as an ESB. In this case, it has been demonstrated that the exposure to particulate matter with a size lower than 2.5 μm ($PM_{2.5}$) cause serious damage to humans and directly affect several respiratory illnesses (related with almost 4.2 million deaths per year [18]). Then, pollution policies regulated in places like Europe (Spanish regulation R.D.1073/2002, adapted from European legislation) have

undergone reduction in some areas of the world. Nevertheless, less favored countries that clearly pollute less are more affected by this type of aerosols, without mentioning that natural disaster such as volcano eruptions (seen a couple of years ago in La Palma, Spain [19]) may appear and introduce a high amount of $PM_{2.5}$ into the system. Accordingly, these authors propose differences in safe (< 15 μg per m^3) and just (adding more strict levels of exposure) ESB for this matter.

All in all, ninth ESB is related to the amount of stratospheric ozone (Ozone Layer) which is, gratefully, the only ESB in where the human action has reverted the situation and according to a press note from the UN earlier this year [20], is on track of recovery within four decades. Implications of this new on climate change are huge, it has been estimated that this recovery can help avoid global temperature increase by ca. 0.5 ºC and, in addition, can serve as hint of hope in what humans can make in order to revert the rest of the ESBs in safe and just limits, but only if drastic measures are taken in time.

Indeed, all these ESBs (**Fig. 1.3**) recreate a more detailed outlook of the world itself and the problems the humanity face. However, it is undeniable that due to the anthropogenic action in the period after the industrial revolution, the uncontrolled emissions of greenhouse gases have led to this critical situation.

Consequently, next section of the chapter is devoted to a study of the industry (petrochemistry, concerning the present thesis) and the efforts put into carbon transition and net carbon oxide emissions to meet these ESBs.

1.2. Petrochemical industry: to the net carbon balance

In this context, in recent years the concept of carbon neutrality has appeared. This refers to net-zero carbon dioxide (CO_2) emissions attained by balancing the emission of CO_2 with its removal so as to stop its increase in the atmosphere. Logically, it is assumed to be one of the largest international achievements to date. However, information available shows that, by 2020, global average atmospheric CO_2 concentration had reached 415 ppm, which is a notable increase from its preindustrial level of 285 ppm (circa 1850). Therefore, this structural society change must be mandatory, by considering four different approaches: **i)** replacing fossil fuels with renewables, **ii)** CO_2 capture, valorization, and reutilization, **iii)** reuse of solid wastes and **iv)** reducing energy consumption (maximizing its efficiency).

In addition to this, Prof. J.M. Cheng from Toronto University defined in 2021 a chronological industrial revolution divided in five stages, associating each of them with a different amount of carbon dioxide related emissions, as it can be seen in **Figure 1.4** [21]. Starting from year 1750, a series of industrial revolutions took place: steam engines, electrical power, computers and Internet, respectively, and what this author proposes is a new revolution (the fifth) in where the transition to renewable energies occurs, limiting as a goal in 2050 an increase in the temperature to 1.5-2.0 ºC by 2100 with respect to the preindustrial level [22].

When considering the petrochemical industry, and in the purpose of the carbon neutrality, first of all an analysis of its real impact in the CO_2 emission should be carried out.

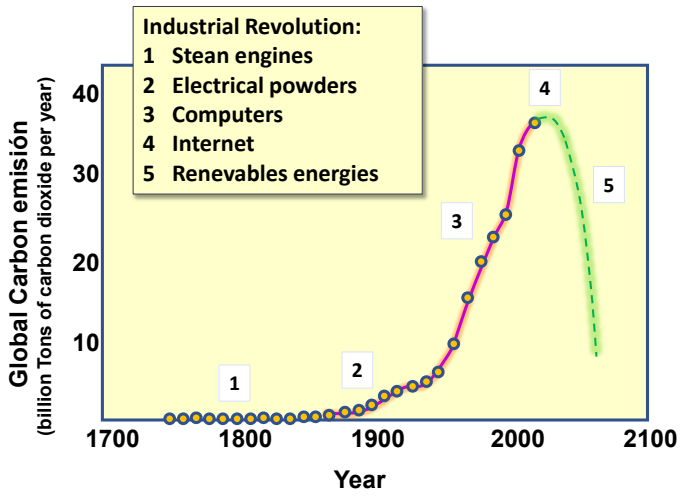

Figure 1.4. Change in the global CO_2 emissions as a function of time and industrialization of the planet. Adapted from [21].

In that sense, J. Pérez-Ramírez *et al*. proposed an absolute environmental sustainability assessment (EASA) studying the production of up to 492 chemical compounds in the lens of the planetary boundaries [23] which could be extremely useful in the green chemistry area in order to help researchers and companies to develop truly ecofriendly processes, serving this EASA as a guide and starting point to the design of holistic approaches to be able to deeply quantify the real impact of industrial production, called the absolute environmental sustainability level of these relevant chemicals.

Furthermore, these authors also performed a study regarding the petrochemical sector, analyzing the possible scenarios in the well-known term of carbon transition from fossil-based to renewable sources [24]. In said article, one of the main points is that, by shifting to renewable sources, we must also consider other aspects that may attack other ESBs. For

instance, using biomass feedstocks to produce electrolytic H_2 would imply high land-use requirements, collaterally affecting the biosphere integrity ESB. Nevertheless, continuing through this way, the current fossil-base petrochemical industry, the ecological cost would be a price too high to pay. Then, a possible solution is to select appropriate technologies that can mitigate these effects, in addition to a possible combined scenario in which CO_2- and bio-based alternatives should exist at the same time. This, needless to say, must be supported by changes and incentives in policies.

Regarding this transition from oil to renewable sources, natural gas has emerged as one interesting alternative in the production of both energy and chemical products [25]. Regrettably, due to the difficulties in extraction and transportation [26], up to 90 % of natural gas is directly employed in the generation of heat and electricity [27]. Indeed, its general low mass and energy density turns into transportation costs three times higher than oil [28], usually transported in the form of liquified natural gas (LNG) or through pipelines.

On the contrary, only 8 % is used to produce different chemical commodities such as: ammonia, methanol, light olefins, hydrogen, long-chain hydrocarbons or BTX. One of the main reasons, apart from external costs mentioned above, is that natural gas average composition is: methane (75-99 %), ethane (1-15 %), propane (1-10 %) and C_{4+} alkanes (0-5 %). These molecules are quite inert, and therefore, it is hard to activate those C-C and C-H bonds. In that sense, harsh reaction conditions, along with the use of aggressive reagents are typically required [29].

At an industrial level, two processes are now operating, namely, steam reforming and steam cracking, that can transform light alkanes into olefins [30-33].

The steam cracking process is especially interesting in the scope of the present thesis, since it is the method employed to produce ethylene at large scale. However, the high temperature and pressure conditions used in this process makes it one of the most energy-demandant in the whole industry. Then, next part of the chapter is devoted to present a general state-of-the-art revision of the ethylene industry and the different routes to produce it.

1.3. Ethylene industry: from steam cracking to alternative routes

1.3.1. Steam Cracking

Ethylene is the most used olefin in the world, in fact, by 2021 its market production capacity reached ca. 215 million tones, with an expected growth of 4 % until 2035, which makes it a forecast of 260-300 million tones by that year (**Fig. 1.5-A**) [34, 35]. The global ethylene market size amounted to $132 billion in 2022 and is expected to exceed $228 billion by 2032 [36].

A major part of its production (approximately 54 %) is dedicated to the manufacture of polyethylene, a polymer that is especially interesting in the industry due to its physicochemical properties such as flexibility, durability light-weight nature and resistance to moisture [37-39]. Polyethylene can be presented in two forms, LDPE (low density) and HDPE (high density), which comprehend up to 30 % of global thermoplastic production (**Fig. 1.5-B**) [40].

Nevertheless, ethylene is also an intermediate for a wide range of chemical products such as: ethylene oxide (used in the food industry), ethylene glycol and other linear alcohols or olefins, styrene (monomer of polystyrene), chlorination to form 1,2-dichloroethane (intermediate in the production of polyvinylchloride, PVC) or even hydroformylation with syngas to produce different aldehydes [41-44].

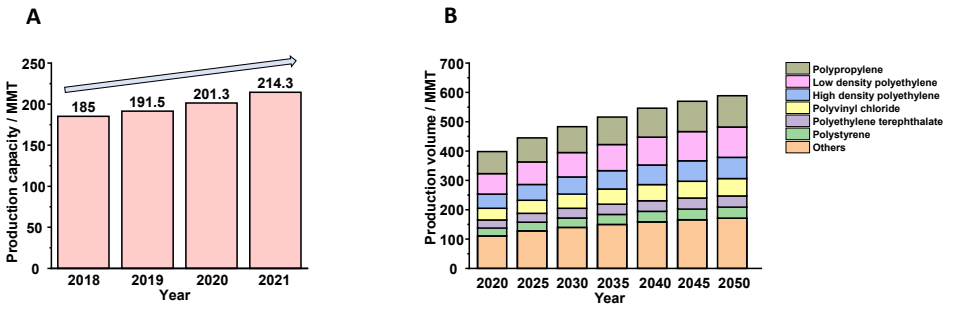

Figure 1.5. A) Production capacity of ethylene throughout the last years; and **B**) expected plastic polymer production in the coming years from ethylene raw material. Note that both graph units are expressed in million metric tons (MMT) [40].

Although at an industrial level ethylene is produced through the steam cracking process, the first ethylene plant dates back to 1921, in which Union Carbide (now part of Dow Chemical Company) developed a small plant in West Virginia (EEUU) to, at first, separate gasoline from natural gas, to subsequently produce ethylene by installing furnace units [45].

Interestingly, ethylene uses were originally thought to be as a replacement of acetylene, molecule employed as a fuel for car headlights, welding and cutting, due to the many advantages that ethylene present over acetylene in terms of synthesis and operation safety.

Originally, ethylene was produced from ethanol and sulfuric acid, nonetheless, economic and safety aspects of this process, led to the Curme´s group to develop a thermal cracking of ethane to obtain ethylene and hydrogen, a revolutionary process for the importance in the birth of petrochemistry, patented in 1922 [46]. This technology further evolved into the actual steam cracking, which is a highly productive process [47]. However, due to the apparent never-ending increasing demand of ethylene, different sources are nowadays used: naphtha, ethane, LPG by steam cracking and MTO (methanol to olefins). The evolution in the utilization of these feed sources in the last 20 years is represented in **Figure 1.6**, where we can see that, in percentage, cracking of naphtha still represents the majority, nevertheless, both the ethane steam cracking and MTO are slowly increasing throughout the years [48]. One of the main reasons for this change is that the different availability of the feedstocks along the planet plays a major role in the economic profitability of the whole process [49]. Moreover, the environmental analysis of producing ethylene from naphtha or from ethane (shale gas) showed that by using shale gas, the life cycle greenhouse gas emissions are higher [49, 50].

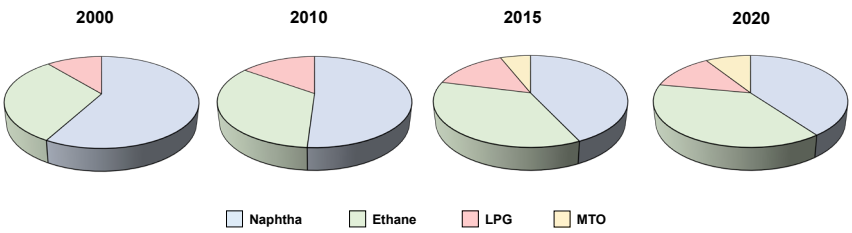

Figure 1.6 Evolution of the utilization of different feedstocks: naphtha (blue), ethane (green), LPG (red) or MTO (yellow), to produce ethylene during the years 2000, 2010, 2015 and 2020 [48]

Regretfully, in the naphtha to olefins cracking plants, although production capacity is more than 10^6 tons per year worldwide, it is estimated a conversion efficiency of ca. 67 %, with the main equipped cost associated with the cracker itself (roughly 30 %) [32], due to the enormous endothermic nature of the process (850-900 ºC temperature range) [50-56]. Then, the highly energy demanding behavior of the steam cracking turns into a heavy production of CO_2, calculated as ~1.2-2.0 metric tons per metric ton of ethylene [57, 58]. More specifically it has been proposed that the industrial ethane steam cracking process typically emits about 1.0–1.2 tons of CO_2/tons of ethylene (0.64–0.76 moles of CO_2/moles of ethylene), and naphtha steam cracking emits about 1.8–2.0 tons of CO_2/tons of ethylene (1.15–1.27 moles of CO_2/moles of ethylene) [59]. Still, the production of ethylene by steam cracking, either from naphtha or ethane, is the method mostly used to date. In Europe, where ca. 80 % of the ethylene is produced from naphtha [39, 60], there exist up to 45 crackers distributed in 18 countries, with a total production in 2021 of arguably 25000 ktones per year. In the case of Spain, three crackers in Puertollano and Tarragona from Dow and Repsol companies produce 1400 ktones of ethylene yearly [61].

Accordingly, two realities converge in this field. On one side, the year-by-year increasing demand of ethylene and other olefins and polymers and, on the other side, the urgency to limit, cut and reduce the greenhouse emissions to meet international agreements and goals of sustainable development.

Therefore, updates in the petrochemical industry, along with brand-new technological processes must be implemented in the coming years to ensure these two different tendencies. On one hand, revaluations for optimizing the steam cracking process are taking place by many researchers and industries. For instance, it has been proposed several different technological improvements, easy to be implemented, that can help to reduce by 10 % of total CO_2 emissions. This is the case of the high emissivity coatings (reducing the heat demand of the cracking process), the use of new 3D reactor designs (improving heat transfer between inner coil walls and process gas flow), added to the already mentioned carbon capture and storage [62, 63]. Not only that, optimization of the process, in terms of both economy and environment, can be also studied from the very extraction and transportation of the feedstock, apart from the processing [64, 65].

On the other hand, lots of efforts have been put in the electrification of the thermal heating in the crackers, which is one the solutions for decarbonization [47, 57, 66, 67], by employing renewable sources for green electricity (that also implies an economical benefit compared to fossil fuel-based electricity [68]). In addition, CO_2 emissions can be further reduced because of the existence of the possibility for an indirect electrification through a route based on Power-to-Gas and Oxidative Coupling of Methane (OCM-PtG), using carbon capture, although it is not very clear it can be actually implemented [69]. Even also the co-production of ethylene and hydrogen by the non-oxidative deprotonation of ethane by using a proton-conducting electrochemical deprotonation cell appeared as an emerging

technology. Authors present an estimated 65 % saving in energy and a reduction of the carbon footprint up to ca. 72 % compared to classic steam cracking [70].

In any case, Dow recently announced that they will be opening the world's first net-zero emissions and derivatives complex plant [71]. In said announce, the company stated that the plant that will be constructed in Fort Saskatchewan (Alberta, Canada) will convert cracker off-gas into hydrogen, in order to be used as a clean fuel in the whole process. Moreover, produced CO_2 will be captured onsite and subsequently transported and stored in an adjacent third-party infrastructure.

1.3.2. Alternatives to Steam Cracking

As indicated previously, steam cracking is the main route for ethylene production, but other technologies are also used in the production of other light olefins. **Figure 1.7** shows comparatively the current distribution of the main routes for the production of different olefins (**Fig. 1.7-A**) and for production of ethylene (**Fig. 1.7-B**).

It is estimated that 400 million tons of olefins are annually produced, using one billion tons as hydrocarbon feedstock, via processes such as fluid-catalytic cracking, steam cracking, and dehydrogenation (**Fig. 1.7-A**) [73], whereas ethylene is mainly produced from steam cracking.

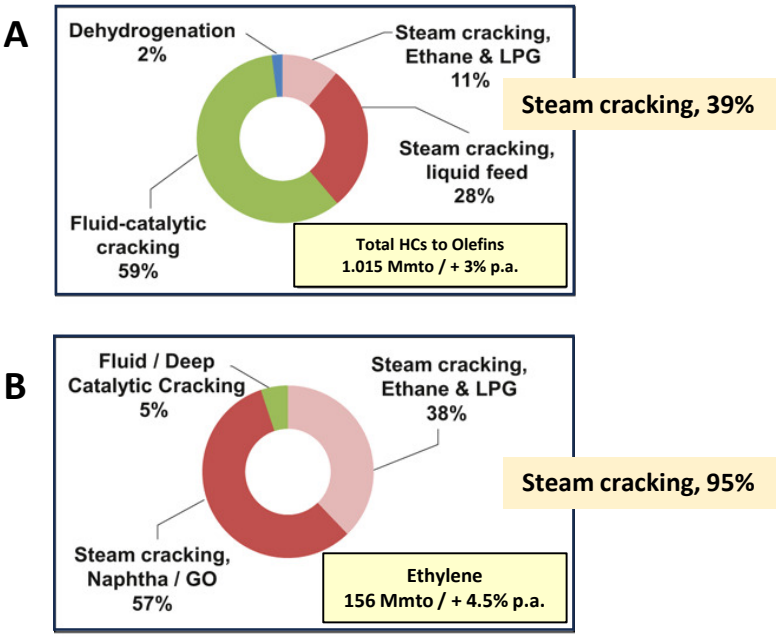

Figure 1.7. Olefin production (**A**) and ethylene production (**B**) methods using hydrocarbon feedstocks. Adapted from refs. [72] and [73].

These includes, among others, redox oxy-cracking of ethane [59, 79, 80], hydrocarbon catalytic cracking [81, 82], oxidative and non-oxidative coupling of methane [83-88], alkane dehydrogenation [75, 89-91], alcohol dehydration [72, 73, 92-97] methanol to olefins by improving the ethylene production [98-101], or biomass and waste pyrolysis when starting from oxygenates compounds [73, 102, 103], or selective transformation of CO/CO_2 by thermal catalysis or electrocatalysis [104-107], although the economical and production volume needs are not already met.

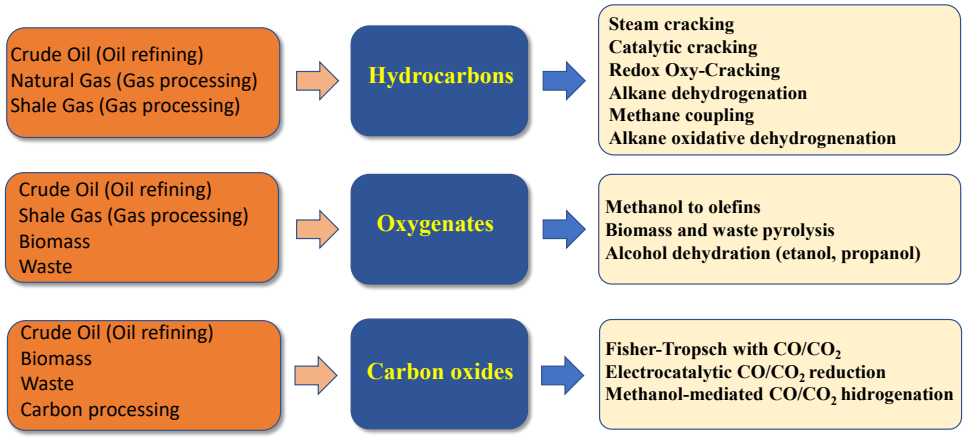

Figure 1.8. Raw materials and reaction processes for olefin production. Adapted from ref. [77].

In this way, a comparative study on manufacturing ethylene from wet shale gas (in two processing steps, with the shale gas processing to produce ethane and this by steam cracking to produce ethylene) and biomass (in two processing steps; bioethanol production via fermentation and ethylene manufacturing via bioethanol dehydration) concluded that the shale-gas-based pathway could be of more interest as a consequence of the lowest ethylene prices (0.32-1.67 \$/kg), although it presents the highest greenhouse gas emissions (ca. 1.4 kg_{CO2}-equiv/$kg_{ethylene}$). In an opposite trend, the biomass-based pathway presents higher ethylene prices (2.0-4,1 \$/kg) but lower greenhouse gas emissions (ca. 1.0 kg_{CO2}-equiv/$kg_{ethylene}$) [78].

For a better comparison, it will be summarized the main alternative routes for ethylene production.

Catalytic dehydrogenation

There are numerous studies on the non-oxidative catalytic dehydrogenation routes for the production of light olefins [75, 89-91, 108, 109]. However, although it has been implemented for C_3-C_4-olefins (several industrial plants), there are much fewer studies for the catalytic dehydrogenation of ethane [108]. If we take into account the greater chemical stability of the C-H bonds in ethane, and that the enthalpy required to dehydrogenate alkanes decreases as the chain becomes longer (ΔH_{298}^0= 117.6 kJ mol^{-1} for isobutane dehydrogenation; 124.3 kJ mol^{-1} for propane dehydrogenation, and 137 kJ mol^{-1} for ethane dehydrogenation), a considerably larger amount of energy is required to dehydrogenate ethane on a mass basis [89]. As a consequence, the direct dehydrogenation reactions will require higher reaction temperatures to obtain satisfactory performance for the production of ethylene [80, 108, 109]. Thus, in the temperature range of 500 to 700ºC, for the transformation of ethane, equilibrium conversions of between 10 and 40% are obtained, while at 600ºC the equilibrium conversion for propane is ca. 50% [108]. Furthermore, the adsorption of alkanes is much lower than that of olefins, so the efficient and selective activation of the C-H bond (with the suppression of the cleavage of C-C bonds, which decreases the selectivity of the process) is another important factor to achieve ethylene yields lower than those observed for propylene.

In fact, although industrially implemented, non-oxidative dehydrogenation presents several important drawbacks for this reaction to meet the economic and environmental challenges faced nowadays to break the hegemony of steam cracking. The most important one, also energy-related,

is the above-mentioned endothermic nature of the process, so lots of energy and CO_2 emissions are associated with this process. Moreover, for temperatures exceeding 600-650 ºC, it is generally accepted that side reactions such as catalytic cracking and the formation of coke may occur [109]. Furthermore, the second main drawback of this reaction is the thermodynamic equilibrium limitation, in which a reduction in the partial pressure of the hydrocarbon by diluting it into inert gases is needed to increase the conversion. The other possible solution is to reduce the partial pressure of hydrogen that, in any case, adds operational costs related to separation processes (separation of both unreacted paraffin, as well as hydrogen and formed olefin) that make the process economically expensive.

However, to date, five main industrial processes for the dehydrogenation of light alkanes have been patented, two of which are currently being used to produce light olefins [90]: **a)** Catofin Process (by CB&I Lummus), originally used for the dehydrogenation of isobutane to isobutene, is currently employed for the dehydrogenation of propane to propylene, consisting of 5-8 adiabatic fixed bed reactors in parallel (some in dehydrogenation, some in regeneration mode) working at ca. 575 ºC (0.2-0.5 bar of pressure); using as catalyst a 18-20 wt % alumina supported CrO_x, promoted with 1-2 wt % Na or K [100]; **b)** Oleflex Process (by UOP), that differs from the previous one in the design of the reactor, using in this case a fluidized bed consisting of three parts (reactors, product recovery and catalyst's regeneration), as well as the working conditions, pressure (1-3 bar) and temperature (525-705 ºC); using as catalyst a Pt-Sn alumina

supporter material (< 1 wt % Pt and 1-2 wt % Sn), promoted with alkali Na or K cations (<1 wt %) [101].

In addition to these, three more technologies are patented for catalytic dehydrogenation of light paraffins, although not industrially implemented, namely [89-91, 108]: **(i)** Steam Active Reforming (STAR), with working conditions of 6-9 bar and 500-600 ºC, over Pt-Sn/zinc-aluminate and calcium/magnesium-aluminate binder catalytic system in a fixed bed reactor that limits coke deposition while enabling low paraffin partial pressure; **(ii)** Fluidized Bed Dehydrogenation (FBD), working in fluidized beds at 1.1-1.5 bar, 550-600 ºC, employing alkali promoted CrO_x/Al_2O_3 catalysts that, due to deactivation, are continuously transported to a regenerator; and **(iii)** Linde-BASF PDH process, very similar to the STAR process, in which paraffins are isothermally dehydrogenated at 590 ºC over Pt-Sn/ZrO_2 catalysts.

An alternative non-oxidative pathway to produce olefins is the autothermal alkane dehydrogenation [74]. Since thermal cracking requires lots of energy (extremely high temperatures are needed to break C-C and C-H bonds), the use of a sacrificial fuel or the selective hydrogen combustion have been studied to amend the exigent energetic needs of non-oxidative dehydrogenation.

In this way, to produce ethylene, optimizing the design of a proper reactor working at high space velocity can lead to yields > 50 % [110, 111], and different materials such as Pt/Al_2O_3 or perovskite-like $BaMnAl_{11}O_{19}$ or $LaMnO_3$ can act as combustion catalysts by using ethane itself as both reactant and sacrificial fuel. Moreover, produced H_2 or co-fed can be also

used as the sacrificial fuel, obtaining similar values of selectivity to ethylene.

Thus, from another point of view, a single or multi-catalytic system strategy can be adopted. In the latter case, dehydrogenation and combustion of the sacrificial fuel usually takes place over different catalysts/active phases. Then, in a combined Pt-$LaMnO_3$ catalyst and using H_2 as sacrificial fuel, up to 65 % yield to ethylene can be achieved, taking advantage of the robustness of $LaMnO_3$ and the high selectivity to hydrogen oxidation by Pt atoms [112], displacing the equilibrium forward and using that combustion temperature to lower the energy requirement of the endothermic process. On top of that, this catalytic system also showed acceptable results in autothermal propane dehydrogenation, with a 23 % propylene selectivity at 70 % of propane conversion [112 c].

In addition to this, the catalytic set up may also play an important role in autothermal dehydrogenation. In a conventional fixed bed reactor, for instance, it is mandatory to add a solid oxygen carrier (SOC) that can be physically mixed with the dehydrogenation catalyst. Consequently, this SOC should meet some requirements such as to be inert to hydrocarbons, easily reduced by hydrogen and with a deactivation rate slower than the dehydrogenation catalyst. Regretfully, traditional SOC materials like Y/Ca-ZrO_2 work at higher temperatures than the ones used for dehydrogenation, and p-block metals active in hydrogen combustion usually present melting points lower than that temperature [113]. Therefore, a suitable material that can meet the required criteria is CeO_2, but only when doped with different

metals (i.e., Cu, Fe, W or Zn) that make it selective to hydrogen combustion [114].

Conversely, a second approach is to use a membrane or a fuel cell reactor system. The reason to use these types of reactors is associated from the inherent risk of explosion in a fixed bed reactor as the reactant mixture is composed of oxygen + hydrocarbon (alkane and/or alkene) + hydrogen at temperatures in the 550-600 ºC range. Then, in this configuration, alkane and oxygen feed are supplied on opposite sides of the membrane. Moreover, as the hydrogen combustion takes place in the same partition of the membrane, this heat can be directly offset to use it for the dehydrogenation reaction and, also very important, operation handling and costs may be diminished as in this case there are no reduction-reoxidation cycles (i.e., hydrogen combustion + regeneration) [115,116]. Typically used membranes in this process are perovskite oxides, although apatite-type silicates such as $La_{9.33}(SiO_4)_6O_2$ can potentially be suitable membranes for dehydrogenation of alkanes [117]. In the case of fuel cell reactor, although there are no appropriate configurations to date, an example is the use of Y-doped $BaCeO_3$ as solid oxide fuel cell, with deposited platinum catalyst working as an anode. Nevertheless, since reaction temperatures were set to 700 ºC for the system to work, the selectivity to propene drastically decays as side cracking reactions are much more favored under these conditions [118], observing better results in the case of ethane (90 % selectivity to ethylene at ca. 67 % of ethane conversion) using the chemical looping technology over Li_2CO_3-promoted $La_{0.8}Sr_{0.2}FeO_3$ catalysts [119].

Ethanol to ethylene

In this sense, several studies have been conducted exploring the possibilities of bioethylene production, especially from ethanol, focusing on the fact that, in addition to the lower greenhouse emissions, ethanol can be considered as a renewable source, instead of petroleum-based feedstocks. Moreover, it is estimated that worldwide biomass reserves by 2050 could lead to an energy production of 1.5 - 4.5 · 10^{11} GJ [92], so it won't suffer from shortage. Interestingly, even this process has attracted attention in the last decades as a result of the availability of bio-based ethanol [93-97], the catalytic dehydration of ethanol to obtain ethylene is actually the first industrialized chemical reaction, being an endothermic process which requires temperatures of ca. 300-500 ºC, with the selectivity to ethylene dependent of the reaction temperature: for temperatures below 300 ºC, diethyl ether is the main product, whereas increasing beyond 500 ºC shifts the equilibrium to the formation of acetaldehyde [92].

Accordingly, the dehydration of ethanol to ethylene is an acid catalyzed reaction and several types of catalysts have been proposed [93-98], including phosphoric acid on clay systems, γ-Al_2O_3 based materials, and heteropoly acids, but specially catalysts based on zeolites and zeotypes [120-123].

In this way, the use of molecular sieves as catalysts was also studied. In particular, zeolites like ZSM-5 and zeotypes like Si-Al phosphates (SAPO) were tested in this reaction. Different results were obtained varying the composition of the zeolitic catalysts introducing multiple cations (i.e., H-ZSM-5, HNa-ZSM-5, CuNa-ZSM-5, PH-ZSM-5 or even Zn, Mg and Sr)

and modifying reaction parameters such as temperature, concentration of ethanol, pressure, or space velocity [120, 121]. In the case of silicoaluminophosphates, several studies using catalyst SAPO-34 were conducted, due to the excellent results of this material in the methanol-to-olefin reaction (MTO) [122, 123]. Nevertheless, although molecular sieves present a higher catalytic activity at lower reaction temperatures, even for aqueous low concentrated ethanol solutions, their related problems with stability and deactivation do not make them suitable for industrial application at large scale at this moment.

Methanol to olefins

Furthermore, another interesting way to obtain olefins is the methanol-to-olefins reaction (MTO) developed By Mobil Corporation in 1977 [124]), which constitutes one of the most important reactions in the C_1 chemistry. Nonetheless, despite being methanol a simple molecule (nowadays obtained from natural gas or coal), its transformation into short-chain molecules (C_2-C_5) is quite triggering. MTO is believed to occur through an indirect hydrocarbon pool (HP) mechanism, in where organic species obtained from methanol can act as co-catalysts within the pores of the catalyst (typically, H-ZSM-5 and H-SAPO-34 zeolites) being methylated by another methanol (or dimethyl ether) molecule and subsequently split into light olefins [125, 126]. Several authors reported that aromatic polymethylbenzenes (PMBs), carbenium ions (MB^+) and polymethylcyclopentenyl (MCP^+) cations are the main species that conform this HP, especially in small pore zeolites [127]. However, within

this mechanism, two competitive routes appear as possible pathways, namely the side-chain and the paring routes, each of them resulting in different product composition [128]. In the side-chain route, methanol alkylates PMB intermediates following a side-chain elimination to preferent form ethylene and propylene. On the other hand, the paring route starts with a contraction of the MB^+ cations followed by the expansion of the MCP^+, forming in this case propylene and butene, mainly.

In this sense, a greater or lesser ability of a given zeolite to form and stabilize the above-mentioned organic molecules will drive the reaction pathway for one way or the other. For instance, small pore zeolites like SSZ-39 or RUB-13 tend to yield more propylene over ethylene than high-silica CHA zeolite, despite pore and cavity sizes are quite similar [129, 130]. Consequently, many studies deal with the perfect control in size and shape of ZSM-5 as well as SAPO-34 and other zeolites, from different approaches, to improve both activity, selectivity, and lifetime [131, 132].

Moreover, apart from the work related to improve and control the shape of the catalyst, a really important parameter to overcome, especially in the industrial scale-up, is the fast catalyst deactivation due to coking. With this regard, scientists from the Dalian Institute of Chemical Physics have studied this process for the last 35 years and successfully implemented the first coal to olefins plant in 2010, operating in fluidized bed reactors to optimize reaction-regeneration step [133].

1.4. Partial oxidation and oxidative dehydrogenation of short chain alkanes

Heterogeneous gas phase selective catalytic oxidation of hydrocarbons is a technology highly developed during the last 50 years of the last century and represents about 25% of the most relevant organic compounds in the production of consumer goods [134, 135]. It should be noted that through these processes, the functionalization of organic compounds is carried out for their subsequent use as monomers in polymerization reactions. However, to date, most of these derivatives are carried out through selective oxidation of olefins (ethylene oxide, acrolein, acrylic acid, acrylonitrile, methacrolein, methacrylic acid or 1,2-dichloroethane) or aromatic hydrocarbons (phthalic anhydride, benzonitrile or benzoic acid). The relatively easy production from petroleum, together with their high reactivity (moderate reaction temperatures can be employed, in the range of 300- 450 ºC) have made olefins and aromatic hydrocarbons become one of the basic raw materials (building blocks) in petrochemical industry.

However, due to the great demand and increase in prices of low molecular weight olefins (C_2-C_4), in the eighties of the last century, an intense study on the functionalization of low molecular weight paraffins began, through partial oxidation processes. These studies were aimed not only at the direct obtention of olefins (through processes of oxidative dehydrogenation of C_2-C_4 alkanes), but also at the partial (amm)oxidation processes of alkanes (for the direct formation of α,β-unsaturated aldehydes, acids, anhydrides and nitriles). In this way, the different factors that affect the selectivity in partial oxidation processes of light alkanes have been examined for years, showing

that for the most effective catalytic systems, the nature of the active and selective sites for oxidative functionalization of alkanes and/or the characteristics of the reaction may influence the choice of reactor type [134-138].

A clear example is the partial oxidation of n-butane to maleic anhydride, on catalysts based on vanadyl pyrophosphate, an industrial process that displaced processes based on benzene throughout the 1990s [139-143]. Moreover, the use of n-butane involves the use of a cheaper, less polluting raw material that generates less waste than the process based on benzene [139-143].

However, at this moment, no further industrial process has been developed from saturated hydrocarbons through partial oxidation reactions, although, as we will see later, the processes of (amm)oxidation of propane, to obtain acrylic acid and acrylonitrile, have been studied intensively in the last twenty years, especially after the first patents developed by Mitsubishi using catalysts based on multicomponent mixed oxides [144].

1.4.1. Key aspects in the oxidative functionalization of light alkanes

In general, partial oxidation processes of alkanes are carried out using transition metal oxides, with redox properties (with the reduction/reoxidation of active sites), in which vanadium appears as a key element in the activation of the alkane, through the abstraction of a first hydrogen of the alkane [134-138, 141-144]. In other words, the selective

formation of certain desired compounds by partial oxidation of hydrocarbons requires chemically and structurally sophisticated catalysts [145,146].

In fact, several aspects have been proposed to determine the catalytic properties of new catalytic systems. Thus, in addition to the nature of active sites for alkane activation, other physicochemical properties (i.e., redox, acid/base, oxygen transport, etc.) in addition to well-defined structures are required. From the reaction point of view, the adsorption/desorption of intermediates is also a key aspect to be considered.

In this way, the nature of oxygen species in the catalyst surface determines the higher/lower capability of catalysts for O-insertion (and/or deep oxidation) but also to the reoxidation of catalysts. Then, [V^{5+}- O^{2-} →V^{4+}-O^{-}] sites seem to be responsible of the first H-abstraction, which has been proposed as the rate limiting step [147] However, nucleophilic oxygen species, O^{2-}, are usually involved in the O-insertion reaction following a Mar-van Krevelen based mechanism [134-148].

It is clear that after the first hydrogen abstraction (o in parallel to the first hydrogen abstraction), an abstraction of a second hydrogen must occur with the formation of the adsorbed olefin (**Figure 1.9**) [144]. In the case of the oxidative dehydrogenation (ODH) of alkanes, the process would be completed with the final desorption of the adsorbed olefin. However, if the catalysts have active centers capable of selectively activate the olefin formed (adsorbed or desorbed), partial (amm)oxidation would continue towards the oxygen insertion step and the formation of unsaturated

aldehydes, acids or nitriles (**Figure 1.9**), depending on the characteristics of catalysts.

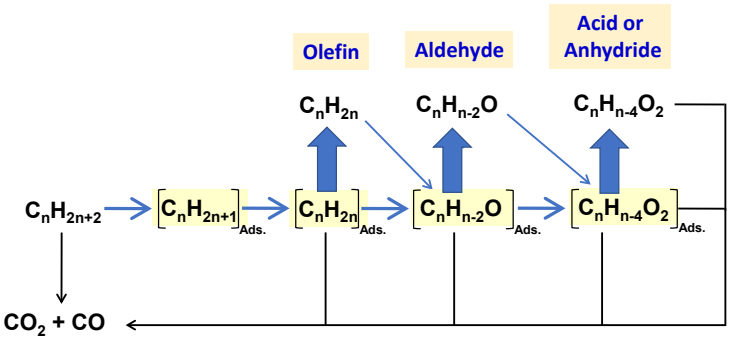

Figure 1.9. Possible reaction network in the oxidative catalytic transformation of short chain alkane. Adapted from ref. [144].

In this way, the coordination and environment of Vanadium-sites, the redox (and the oxidation average of the catalyst surface) and the acid-base properties (and the capability to adsorb/desorb intermediate molecules) of catalysts must be considered as key aspect to selectively transform alkane in olefins, as well as in O- or N-containing products [137, 141, 142]. But, in reference to the importance of the characteristics of vanadium atoms, it has been proposed that the coordination and the aggregation of V-sites can determine the selective aerobic transformation of alkanes into olefins or into O-containing products (**Figure 1.10**) [137, 144].

Thus, the lower both the coordination and the aggregation of V-sites the higher is the olefin formation; whereas the higher both the coordination and the aggregation of V-sites the higher is the formation of oxygenates.

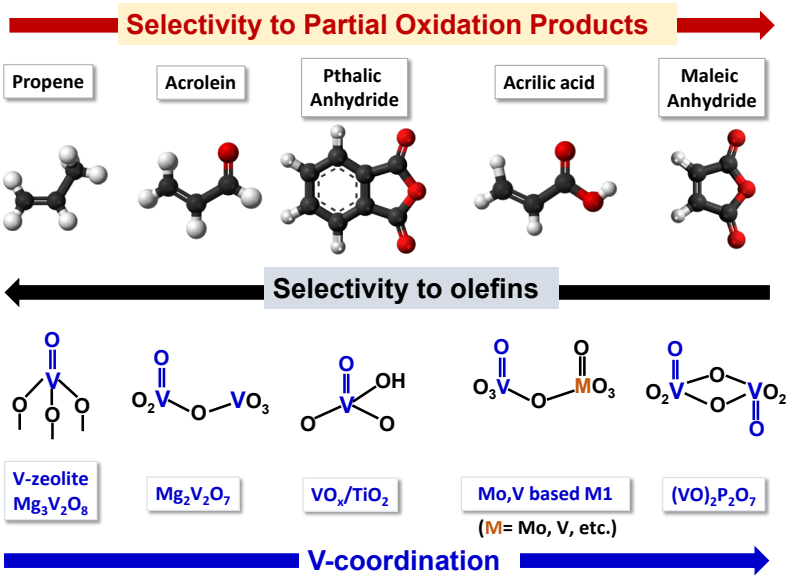

Figure 1.10. Active vanadium oxide species and catalytic properties of vanadium-based catalysts. Adapted from refs. [137, 144].

On the other hand, **Figure 1.11** shows schematically the ammoxidation of propane to acrylonitrile for a mixed catalyst: a multicomponent mixed metal $Ni_aCo_bM_cMoM_x$ for propane activation; and a multicomponent mixed metal molybdate, e.g., $Cs_aK_bNi_cMg_dMeBi_fSb_gMo_hO_x$ for olefin ammoxidation catalyst, in which propylene is desorbed and then adsorbed in the second catalysts) [134, 148].

The ammoxidation of propane to acrylonitrile requires different active centers for each reaction step: **i)** centers capable of activating propane (by abstracting two hydrogens, forming propylene); **ii)** centers capable of activating propene; **iii)** centers capable of inserting -NH groups; **iv)** rearrangements of the chemisorbed activated surface species with

additional hydrogen extraction, ending with the desorption of acrylonitrile; and, **v)** the different active centers that are reduced in each of the stages need to be regenerated, in situ, by the gaseous oxygen present in the feed mixture. Accordingly, the reoxidation step can be very important in the case of olefin partial oxidation (being is some cases the rate limiting step), but it is usually less important in the partial oxidation of alkanes, because it is not the rate limiting step [135-139].

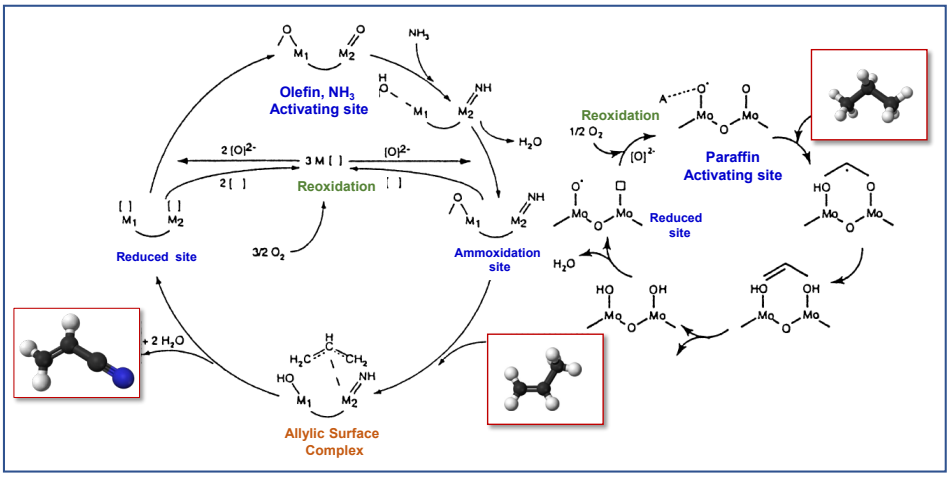

Figure 1.11. Generalized mechanistic cycle for alkane ammoxidation using two types of catalysts: a multicomponent mixed metal $Ni_aCo_bM_cMoM_x$ for propane activation; and a multicomponent mixed metal molybdate, e.g., $Cs_aK_bNi_cMg_dM_eBi_fSb_gMo_hO_x$ for olefin ammoxidation catalyst [148].

However, strong differences in the capability to desorbed olefins or intermediates, depending on the alkane fed [149-153] or the type of catalyst [138, 144], have been reported in the last years, which will have high

importance in the reaction network and the kinetic behavior of these reactions.

Thus, in the case of n-butane, the formation of maleic anhydride from n-butane on VPO catalysts is carried out through consecutive reactions of adsorbed species (butene, butadiene, furane, etc.) on the surface of the catalyst, with the final desorption of maleic anhydride [138, 155]. In this case, the different reactions of the species adsorbed on the surface of the catalyst occur on pairs of attached vanadium atoms with a square pyramid coordination. However, the partial oxidation of n-pentane over VPO can selectively produce phthalic anhydride (low temperature and low C_5/O_2 ratio) and/or maleic anhydride (higher temperature and relatively higher C_5/O_2 ratio) [149-151]. Both the catalytic results and nature of reaction products suggest the intermediate formation of either a lactone or furan. However, the presence of side methyl groups in n-pentane decreases the formation of furan intermediate with the final formation of phthalic anhydride, whereas the formation of furan intermediate could be favored at high temperature achieving higher selectivity to maleic anhydride.

However, in other cases, the olefin initially formed could be desorbed (from the active sites responsible of alkane activation) and adsorbed in other sites in order to continue the partial oxidation process. This is the case of the oxidation of propane to acrylic acid or the ammoxidation of propane to acrylonitrile over multicomponent mixed metal oxides, MoVTeNbO, in which now is generally accepted that the reaction can be described as a multi-step process [152-154]: **i**) the formation of propylene (through the oxidative dehydrogenation of propane) in V^{5+} centers, and its subsequent

desorption; **ii**) the posterior adsorption of the olefin in Mo^{6+} centers, and its activation (through the abstraction of an H-allylic in adjacent Te^{4+} centers), with the formation of the adsorbed aldehyde; and **iii**) the adsorbed aldehyde is finally oxidized into Mo^{6+}-O-Nb^{5+} pairs with the final formation of acrylic acid. The particularity of these selective catalysts, which will be discussed later, lies on the fact that all the active centers involved are found in the same defined structure (the so-called M1 phase), at atomic distances, which facilitate the multistage process. However, the fact that propylene is desorbed and subsequently adsorbed to be partially oxidized, limits the yield of acrylic acid up to 48% [155], therefore making it difficult its industrial use as a catalyst for this reaction (since it has been proposed that the yield to acrylic acid should be up to 60% to be economically feasible [156]).

In a similar way, the olefins facility to react in active sites for alkane activation can partially explain the relatively low yield to olefins during the oxidative dehydrogenation of alkanes over supported vanadium oxide catalysts [52, 53, 55, 137]. Accordingly, it could be important to modify the environment of V-sites in order to facilitate the alkane activation but decreasing the consecutive attacks to the olefins.

On the other hand, strong changes are also observed when comparing several alkanes over a specific catalyst. This is the case of VPO [149, 150], MoV-O(M1-type) [157] or MoVTeNbO(M1-type) [158], in which the reaction pathway in each case could be explained by considering the characteristics of the alkane fed, the stability and reactivity of both the

reaction intermediates and the reaction products, as well as the nature of the catalytic sites (and their environment) involved in each reaction.

R.K. Grasselli, summarizing the characteristics of processes and catalysts for hydrocarbon oxidation (partial oxidation and deep oxidation), as well as the factors that determine the selectivity towards partial oxidation products, proposed some fundamental principles, generally observed in the most selective catalysts, which he called the "seven pillars" [159, 160]: **i)** the participation of the network oxygens of the catalyst; **ii)** the strength of the metal-oxygen bond; **iii)** the crystalline structure in which the active centers are incorporated; **iv)** the redox properties; **v)** the multifunctionality of the active sites; **vi)** the isolation of the active center; and, **vii)** the possible cooperation of crystalline phases. These seven aspects are key when designing effective catalysts in partial oxidation processes.

In recent years, different reviews have appeared on the partial oxidation processes of light alkanes [55, 141, 143, 161-165].

An important factor that can determine the different characteristics required to carry out a desired reaction is the structure in which the active centers can be accommodated. In fact, in the case of partial oxidation of hydrocarbons, suitable catalysts have been developed at an industrial level based on the majority presence of a specific crystalline phase. This is the case of bismuth molybdate (for the oxidation of propylene to acrolein), iron molybdate (for the partial oxidation of methanol to formaldehyde), and, more recently, vanadyl pyrophosphate (for the oxidation of n-butane to maleic anhydride) or the VSbO rutile phase (for the ammoxidation of propane to acrylonitrile) [55, 141, 143, 146, 161-165]. Lately, the

multicomponent MoVTe(Sb)NbO mixed oxides, with an orthorhombic Mo-bronze structure (named as M1), has been proposed as active and selective catalysts in the (amm)oxidation of propane to acrylonitrile or acrylic acid [166], or the ODH of ethane to ethylene [167]. This type of catalysts will be summarized below.

In the last years, it has been proposed several approaches in order to determine catalytic properties in partial oxidation reactions. Current knowledge about the characteristics of catalysts and their behavior during partial oxidation and oxidative dehydrogenation reactions should help us to significantly improve the catalytic properties of systems based on mixed oxides, but also to consider new crystalline structures. Thus, it has been proposed reactivity and selectivity descriptors for the activation of C-H bonds in hydrocarbons and oxygenates on metal oxides [168], for oxidation and acid catalysis of methanol [170] or for dioxygen activation routes on metal oxides [169]. In that sense, the group of Prof. Trunschke has recently proposed the use of artificial intelligence to improve the catalyst design by identifying key physicochemical descriptive parameters correlated with the underlying processes triggering, favoring or hindering the catalytic performance [146]. This way, by considering 55 physicochemical parameters and the reactivity of 12 catalysts (based on vanadium or manganese redox-active elements and presenting diverse phase compositions and crystallinities) toward ethane, propane, and n-butane oxidation reactions, they can identify nonlinear property−function relationships that govern the formation of olefins and oxygenates (local transport, site isolation, surface redox activity, adsorption, and the material

dynamical restructuring under reaction conditions). Accordingly, these results suggest the most relevant characterization techniques to be used for catalyst design and how the catalytic properties could be tuned by changing the characteristics of catalysts.

Moreover, in all cases there is a main element (molybdenum or vanadium) and a second element (Fe, Bi, Te, Sb, etc.) that favors the formation of a certain crystalline phase (when the composition and oxidation states of the constituent elements are well-controlled). Below, some of the characteristics of the catalysts based on mixed oxides of MoVTe(Sb)NbO will be shown in more detail, which, given its catalytic properties for various reactions, has received great attention in recent years.

1.4.2. Bronze-type orthorhombic Mo-V-(Te)-(Nb) mixed oxides: M1 phase

In the nineties of the last century, researchers of Mitsubishi proposed a new catalytic system, MoVTe(Sb)NbO mixed metal oxides, presenting yields of acrylonitrile of 60% at reaction temperatures of 400–450 ºC during the ammoxidation of propane [166]. In addition, similar catalysts were also proposed as effective in the partial oxidation of propane to acrylic acid (yield of ca. 42%) [166c], which could be an alternative to two step industrial process from propylene.

Later, at the beginning of this century, an intense study was carried out on the synthesis and characterization of this type of materials. Initially, the possibility of two different crystalline phases has been proposed, which

were called M1 and M2 (the first responsible for the formation of the olefin from propane, and the second responsible for the oxidation of the olefin to acrylonitrile), without specifically determine what the characteristics of these crystalline phases were [166]. Only until 2002, it was not concluded that the majority of the effective catalysts for these oxidation reactions contained two crystalline phases: **i)** an orthorhombic $(Te_2O)M_{20}O_{56}$ (M = Mo, V, Nb) oxide, named as M1, in which MO_6 octahedra and MO_7 pentagonal bipyramids assemble forming 5-, 6- and 7-fold channels (**Fig. 1.12-A**), with -Te-O-Te- infinite chains along the hexagonal channels [171]; and **ii)** a pseudo-orthorhombic structure with formula $(TeO)M_3O_9$ (M = Mo, V, Nb) [172], named M2, which is isomorphous with a hexagonal tungsten bronze structure, (**Fig. 1.12-B**), and it is formed by corner-sharing MO_6 octahedra, that only form hexagonal cavities [171-173]. However, in addition to these, other crystalline phases such as $TeMo_5O_{16}$ [171, 173], (V, Nb)-containing Mo_5O_{14} [171, 173], or Te-containing crystalline phases, i.e., $M_{17}O_{47}$ the tetragonal tungsten bronze (TTB) type structure [173] can also be observed, depending on the catalyst preparation methods and the final activation procedure.

Furthermore, some of these structures are derived from Mo_5O_{14} (**Fig. 1.12-C**), which consists of pentagonal bipyramids and octahedrally coordinated metallic centers [174], in where the inclusion of vanadium atoms deforms the pentagonal structure creating these hexagonal (and heptagonal in the case of the M1 phase) channels.

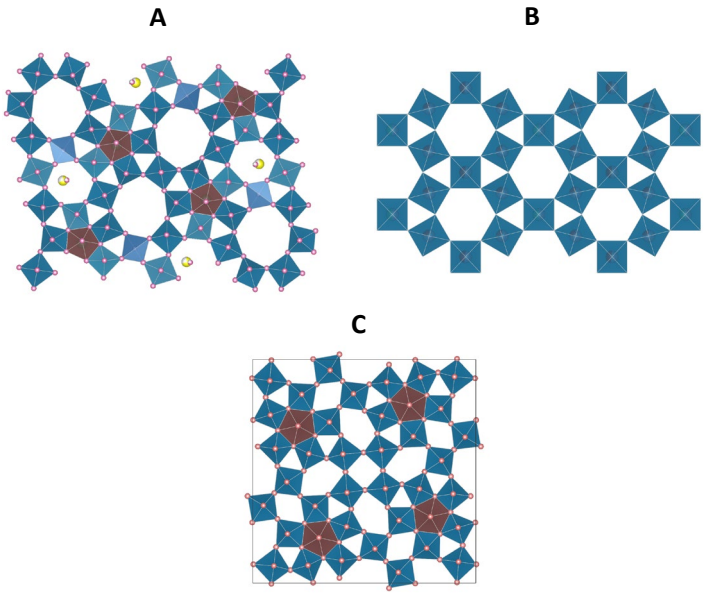

Figure 1.12. Representation of orthorhombic M1 (**A**) and hexagonal M2 (**B**) crystalline structures, derived from Mo_5O_{14} (**C**).

The first application of these types of catalysts was the selective oxidation of propane to acrylic acid, as well as the ammoxidation to acrylonitrile [166, 171, 173, 175-180]. But, in addition, the M1 crystalline structure resulted to be an excellent catalyst in the oxidative dehydrogenation of ethane to produce ethylene [167].

To date, several preparation procedures have been reported for preparing M1-based catalysts, including hydrothermal synthesis [173, 173-179], co-precipitation or "dry-up" method [171, 180, 181], spray drying [166, 182], reflux of an aqueous solution [183], by microwave-assisted techniques [184], or others [185]. A summary of aspects studied for catalyst preparation procedure has been described recently [183].

In addition, different post-treatment methods have been also proposed in order to modulate the morphology and catalytic performance of M1-containing catalysts. This is the case of H_2O_2 treatment [186], oxalic acid treatment [187], HNO_3 [188] or post-treatment water agitation [189a], as well as mechanical post-treatments [189b]. In general, these post-treatments seek to modulate the morphology of phase-pure M1 catalysts (promoting a specific increase of the catalyst surface area), in some cases by restraining the anisotropic growth of the basal (001) plane of the M1-phase in calcination and decreasing the diameter of M1 needles [187, 189].

A second alternative for improving M1-containing catalysts could be the incorporation of promoters in order to modify physicochemical characteristics (redox, acidity, etc.) or morphology. This is the case of Bi-doped [190], Ce-doped [191], or MnO_x-doped M1 catalysts [192]. Also, modification by Nd, Mn, Ga, and Ge substantially affect both physicochemical and catalytic properties of MoVNbTeO oxides in ethane ODH [193]. Finally, changes in catalytic behavior have been also observed in supported M1-based. Thus, Te-free and Te-containing Mo–V–Nb mixed oxide catalysts were diluted with several metal oxides (CeO_2, SiO_2, γ - Al_2O_3, α-Al_2O_3, Nb_2O_5, or ZrO_2) and tested in the ethane ODH and propane partial oxidation [194]. It was concluded that the higher or lower interaction between diluter and active-phase precursors, promoting or hindering an unfavorable formation of the active and selective crystalline phase (i.e., $Te_2M_{20}O_{57}$ (M = Mo, V, and Nb)), determines the catalytic performance of these materials, being α-Al_2O_3 a relatively efficient diluter. However, it has been reported that M1/CeO_2 catalyst (e.g., with 50 wt.% CeO_2) loading

remains highly active after 3 cycles of refreshment in situ, and its crystal structure and surface morphology keep stable compared to the fresh catalyst [195]. In the same way, it has been recently proposed that a composite catalyst based on the phase-pure M1 $MoVNbTeO_x$ catalyst and anatase-phase TiO_2 improves catalytic performance, increasing the space time yields (STY) of 0.38 $kg_{C2H4}/kg_{cat}/h$ (for pure M1) to 0.67 $kg_{C2H4}/kg_{cat}/h$ (for M1/TiO_2). In a similar way, it has been reported that M1 $MoVNbTeO_x$ can be coated on cordierite monolith by PVP-sol binder solution, i.e., M1@CeO_2@Cordierite structured catalyst, increasing the STY of ethylene up to ~ 0.9 $kg_{C2H4}/kg_{cat}/h$ (normalized to M1 ~ 1.05 $kg_{C2H4}/kg_{cat}/h$) [196, 249].

Recently, it has been proposed new methods of catalyst surface modification in order to improve catalytic performance. This is the case of the treatment by using oxygen plasma to change the oxidation state of active sites in M1 catalysts, in which apparently it is possible modulate $V^{5+/}V^{4+}$ ratios on the catalyst surface [197].

The orthorhombic M1 phase, initially reported as Mo-V-Te-Nb-O catalysts, was also observed in Mo-V-X-O catalyst prepared hydrothermally, in which X can be Tellurium [198-201], Antimony [199, 202-209] and others [184]. However, all of them show a different performance with the activation temperature (in both the formation/stabilization of the crystalline phases and the catalytic performance) than that observed for Mo-V-Te-Nb-O catalysts [199, 201].

In the case of Mo-V-Te-O, it has been observed the formation of the M1-phase ($(Te_2O)M_{20}O_{56}$, M = Mo, V) [198] and the pseudo-orthorhombic

structure with formula $(TeO)M_3O_9$ (M = Mo, V) [172]. On the other hand, alternative catalysts based on M1-containing Mo-based bronzes, with Sb^{3+} rather than Te^{4+} (i.e., Mo-V-Sb-O mixed oxides) have been also proposed as efficient catalysts in the oxidation of propane to acrylic acid [202-204, 206] and also in the ODH of ethane [201, 205, 207-209]. They are characterized by presenting crystalline phases similar to those observed in Te-containing catalysts. Thus, it has been proposed [202] the orthorhombic $(SbO)_2M_{20}O_{56}$ (with M = Mo, V) as the M1-like phase and the pseudohexagonal $(Sb_2O)M_6O_{19}$ (with M = Mo, V) as the M2-like phase.

The fact that the stoichiometries normally found in the literature for Te and Sb in the M1 and M2 phases are respectively different can be explained if these structures are considered as networks of octahedra forming negatively charged sheets, $[M_{10}O_{28}]^{3-}$ for the M1 phase and $[M_3O_9]^{2-}$ for the M2 phase, neutralized by tellurium or antimony cations and O^{2-} anions inside the channels of the structure [210]. Thus, in the case of Te, two Te^{4+} cations and one O^{2-} ($[2Te^{4+}\text{-}O^{2-}]^{6+}$) are needed for every two M1 phase sheets, and one Te^{4+} cation and one O^{2-} ($[Te^{4+}\text{-}O^{2-}]^{2+}$) for each M2 phase sheet. However, when neutralizing with Sb cations, one Sb^{5+} cation and one O^{2-} ($[Sb^{5+}\text{-}O^{2-}]^{3+}$) are considered per sheet $[M_{10}O_{28}]^{3-}$, whereas two Sb^{3+} cations and one O^{2-} is considered ($[2Sb^{3+}\text{-}O^{2-}]^{4+}$) for every two sheets $[M_3O_9]^{2-}$. In fact, the c-axis unit cell parameter in this type of lamellar structures is approximately 4 Å for all cases [172].

During the last year, it has been also conducted an intense study for improving the catalytic performance of these catalysts by optimizing the catalyst activation temperature [201] or incorporating alkali metals as

promoters [209]. In addition, the catalytic performance of these materials can be tuned by removing Sb species formed on the catalyst surface during post-synthesis treatment [206], by tailoring the activation procedure [207] and/or incorporating adequate promoters [214]. Nevertheless, the thermal stability of MoVSbO based catalysts seems to be slightly lower than those achieved over multicomponent Mo-V-Te-Nb-O catalysts [201].

More recently, a bimetallic Mo-V-O catalyst, presenting M1 phase (orthorhombic Mo_3VO_x), have also been prepared hydrothermally, by changing the catalyst preparation procedure (specially pH of solution) than those used in multicomponent metal oxide catalysts [157, 212-220]. In fact, depending on the catalysts preparation conditions, one of the following structures have been detected: a) orthorhombic Mo-V-O M1 type; pseudotetragonal Mo_5O_{14}-type; and c) Mo-V-O with trigonal bronze structure. This type of catalysts, prepared in the simplest form, demonstrated to be way more active and selective than non-M1 Mo-V oxides [212-220]. Recently, it has been also proposed a thermally induced transformation of Sb-containing trigonal Mo_3VO_x to orthorhombic Mo_3VO_x (and its effect on the catalytic propane ammoxidation) [213b]. It can be noted that both orthorhombic Mo_3VO_x and trigonal Mo_3VO_x are structurally analogous, both being constituted by pentagonal $\{Mo_6O_{21}\}^{6-}$ units and $\{MO_6\}$ (M = Mo, V) octahedra to form hexagonal and heptagonal channels in the crystal structure, although presenting different catalytic performance [213-220].

Nevertheless, despite being far more active than trimetallic (Mo-V-Te-O) and tetrametallic (Mo-V-Te-Nb-O) M1-based catalysts, the absence in Mo-

V-O catalysts of Me-O-Me chains (Me= Te, Sb or other) in the hexagonal channels (as occurs in Mo-V-Te-Nb-O [198] or in Mo-V-X-O [183, 173]) results in a lower thermal stability (below 500 ºC) [199, 201, 205]. In this way, it has been recently proposed that the lower thermal stability of Mo-V-O catalysts could be modified by optimizing the activation procedure [219, 220].

Furthermore, it has been proposed that V atoms are not present in the hexagonal channels when orthorhombic Mo−V−O oxide is calcined in the presence of oxygen [219], which facilitates its conversion to Mo_5O_{14} phase when heating the catalysts, in a second step, at temperatures higher than 400 ºC (**Fig. 1.13**).

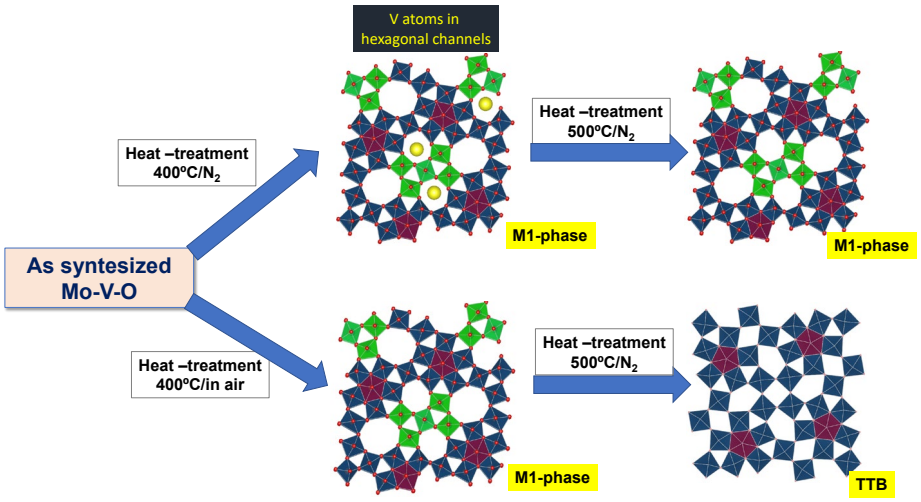

Figure 1.13. Influence of the activation procedure on the stability of M1 phase for Mo-V-O catalysts. Adapted from ref. [220].

However, the stability of catalysts could be a little higher when the activation is carried out in an inert atmosphere. In this case, V atoms seem to be incorporated in the hexagonal channels, improving the thermal stability [220]. Thus, in this case, the activation procedure enhances the formation of catalysts with M1 phase after heating, in a second step, in inert atmosphere.

Accordingly, the presence of atoms in hexagonal channels (such as Te, Sb by synthesis or V during the activation step) seems to be a key factor for improving the thermal stability of these materials during the heat-treatment (for catalyst activation), increasing in the following trend [199]: Mo-V-O > Mo-V-Sb-O > Mo-V-Te-O > Mo-V-Te-Nb-O. However, the stability of M1 phase also decreases when working in reaction conditions. Thus, a loss of tellurium atoms in Mo-V-Te-Nb-O catalysts has been observed when working in reaction conditions at temperatures about 500ºC (in both propane oxidation or ethane ODH) [221]. This suggest that both the amount of oxygen inside the reactor and the reaction temperature should be controlled, avoiding hot spots along the reactor.

The catalytic behavior of M1 phase catalysts have been related to the ab plane (**Fig. 1.14**), in which heptagonal channels are free of any metals [152, 173, 178, 200, 216]. In fact, the heptagonal channels free of elements seem to be crucial in the catalytic activity of these catalysts, since it has been observed that increasing the Te/Mo content (and incorporating Te atoms in the heptagonal channels), decrease the catalytic activity [173]. Moreover, the activity for alkane activation is probably related to the S2, S4 and S7 sites [152, 177, 178, 200, 215, 216].

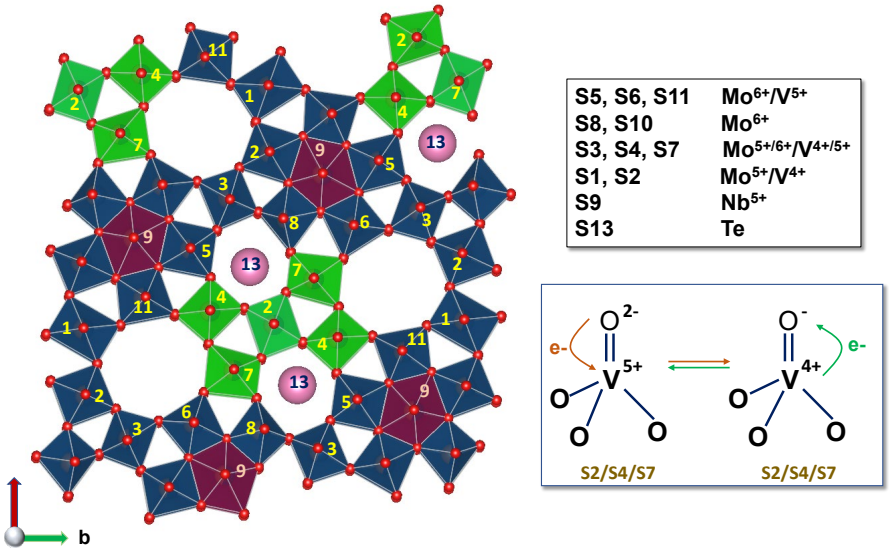

Figure 1.14. Catalytically active center of Mo-V-Te-Nb-O (M1) in [001] projection. Adapted from ref. [152, 177, 178, 200, 215, 216].

In addition, it has been proposed that the content of V in the catalyst surface in phase-pure M1 catalysts had a linear relationship with alkane (propane or ethane) conversion, whereas a synergetic interaction between Te−O and V−O sites can be related to the better selectivity in both acrylic acid (from propane, [152-154]) or ethylene (from ethane, [167, 200]) selectivity. In this way, these excellent catalytic properties for propane partial (ammoxidation) of Te- or Sb-containing M1-based has been related to the positive involvement of Te or Sb in the removal of hydrogen atoms from the propene molecule intermediately formed [152-154, 184]. Moreover, the presence of Nb^{5+} affects the cationic and valence distributions in the M1 phases [186], and the thermal stability [186, 201].

Below, some basic aspects of ethane ODH and, more specifically, ethane ODH on catalysts containing phase M1 (including a summary of the characterization of these catalysts in in situ conditions) will be described.

1.5. Oxidative dehydrogenation of ethane to produce ethylene.

One of the most promising alternatives for the production of light olefins, and especially ethylene, is the oxidative dehydrogenation (ODH) of ethane. In general, the ODH of short chain alkanes have been extensively studied from more than 30 years [51-53, 136-138, 142-144, 161-163, 222-229].

Although not industrially implemented yet, goodness of this reaction comprehends its lack of thermodynamic limitations (exothermic nature), compared to catalytic dehydrogenation (**Eq. 1.1** and **Eq. 1.2**), which results into lower reaction temperatures (350-500 ºC), considering that catalytic dehydrogenation and steam cracking work in the 500-600 ºC and 800-950 ºC range, respectively. This, in fact, results into notably lower CO_2-associated emissions. On top of that, one of the main drawbacks of both steam cracking and catalytic dehydrogenation is the formation of coke, that leads to increased operational costs due to deactivation/regeneration steps. However, in the ODH reaction, the formation of coke is avoided by the oxidant conditions, moreover, catalysts are in situ regenerated by the oxygen feed, so no further steps are needed. On the contrary, since O_2 is added to a hydrocarbon feed, additional safety measures must be taken to prevent explosions. Then, experimental conditions must be carefully

selected. Nevertheless, for the present thesis, flammability diagrams and appropriate experimental conditions will be discussed later.

$$C_2H_6 \rightleftharpoons C_2H_4 + H_2 \qquad \Delta_r H_{298} = 136\ KJ\ mol^{-1} \qquad \textbf{Eq. 1.1}$$

$$C_2H_6 + {}^1/_2\, O_2 \rightarrow C_2H_4 + H_2O \qquad \Delta_r H_{298} = -105.5\ KJ\ mol^{-1} \qquad \textbf{Eq. 1.2}$$

As indicated previously, the gas phase partial oxidation of hydrocarbons is known to be driven by a Mars-van Krevelen mechanism [52, 53, 55, 136, 137, 136-144, 161, 163, 165]. A similar mechanism has been proposed in the case of ethane ODH (**Fig. 1.15**) [222-229], which typically involves the presence of reducible metal oxides and an oxidant, O_2 mainly (but also N_2O or even CO_2, although working at higher reaction temperatures [230]).

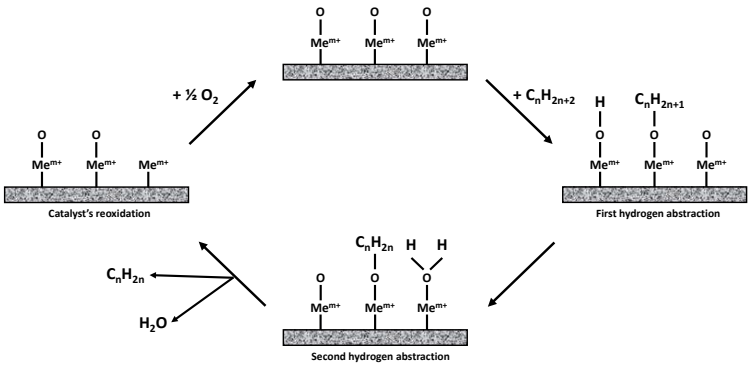

Figure 1.15. General scheme for ethane ODH by considering a Mars-van Krevelen mechanism.

In said process, two consecutive hydrogen abstractions occur to produce the ethylene, and then, the surface of the catalyst is reoxidized with the production of a molecule of water. Therefore, it is proposed that oxygen feed does not participate in the reaction itself but on the reoxidation of the catalyst.

Among the catalysts employed during that time, three different systems stand out of the rest: **i)** alumina supported vanadium oxide [231], **ii)** doped nickel oxide [232, 233] and **iii)** multicomponent bronze-type Mo-V-(Te)-(Nb)-O mixed metal oxides, with orthorhombic structure known as M1 [158, 167, 234].

Figure 1.16 shows the differences in selectivity to ethylene over these three types of catalytic systems [51, 52, 223]. It can be seen that the three catalytic systems are able to transform ethane to ethylene, with relatively high selectivity, at low ethane conversion level. However, by increasing the ethane conversion, enormous differences in ethylene selectivity are observed. According to the general discussion, the differences in catalytic behavior at high ethane conversions are strongly related to the greater or lesser reactivity of ethylene depending on the catalytic system, which gives rise to a greater or lesser capacity for combustion of ethylene and the formation of CO and CO_2. Moreover, at this moment, it is not clear why these catalysts present these strong differences during the ethylene deep oxidation.

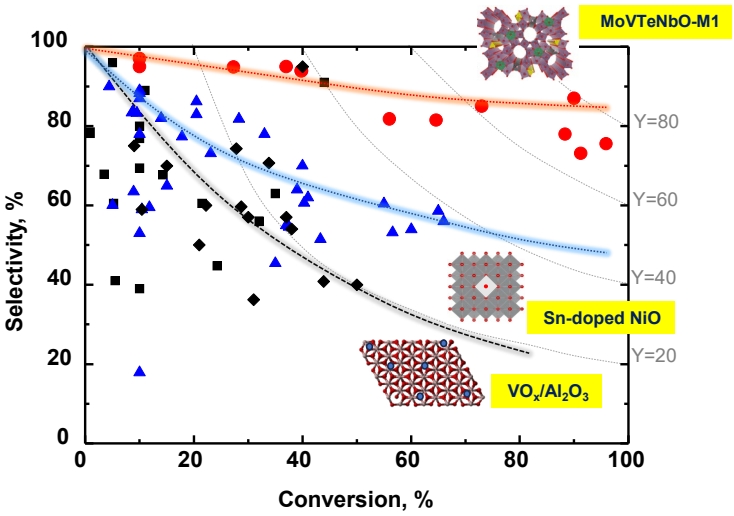

Figure 1.16. Selectivity to ethylene as a function of ethane conversion for alumina supported vanadium oxide (**VO_x/Al_2O_3**, symbols in black), tin-doped NiO (**Sn-NiO**, triangles in blue), and multicomponent **MoVTeNb-M1** oxide (circles in red).

1.5.1. Ethane ODH over Multicomponent mixed oxides with M1 phase

As indicated previously, several reviews on the ethane ODH have been reported in the last years [51-53, 142-144, 161-163, 222-229]. Although the development of supported vanadium oxide catalysts, especially alumina supported catalysts, and NiO-based catalysts represented also a quantitative advance in terms of ethylene selectivity supposing a clear advance in the knowledge of the factors involved in the alkane ODH reactions, the best catalytic results in the oxidative dehydrogenation of ethane to ethylene have been obtained over mixed metal oxides [52, 136-138, 144, 231].

Thorsteinson *et al.* [235] presented a catalyst based on mixed oxides, $Mo_{0.73}V_{0.18}Nb_{0.09}O_x$ with high activity and high selectivity in the ODH of ethane to ethylene, in the temperature range of 300 to 400 ºC The catalyst, prepared by coprecipitation and calcined in air at 450 ºC, did not show crystalline phases (it was a pseudo-amorphous material), in which, according to the authors, the active sites were the molybdenum species (while the role of the vanadium species, would be related to the reoxidation of Mo-sites) [235]. The subsequent modification of these catalysts with certain promoters (especially antimony) facilitated obtaining higher yields, reaching a yield of ca. 52% (71% ethylene selectivity for 73% ethane conversion) [236].

Subsequently, Ueda *et al.* [237], reported the synthesis of Mo-V-Me catalysts (Me= Te, Sb, Al, Ga, etc.), prepared hydrothermally and activated at 380 ºC/N_2. They reported the best catalytic results for catalysts presenting M1 phase at a reaction temperature of 340 ºC: $Mo_6V_2Sb_1Ox$ (ethane conversion of 16.8% and selectivity to ethylene of 74.7%) and $Mo_6V_2Te_1Ox$ (ethane conversion of 18.2% and selectivity to ethylene of 72.5%).

However, the preparation of very effective catalysts for ethane ODH based on multicomponent mixed oxides was reported in 2002. Thus, the most effective catalysts for ethane ODH, so far, are those based on multicomponent mixed oxides Mo-V-Te-Nb-O [167], especially those in which the orthorhombic phase M1 is the majority phase [234], with which ethylene yields of 75% can be achieved [167, 234]. The catalysts were

prepared hydrothermally, with a final activation, in an inert atmosphere, in the 500-750 ºC temperature range [167] (**Figure 1.17**).

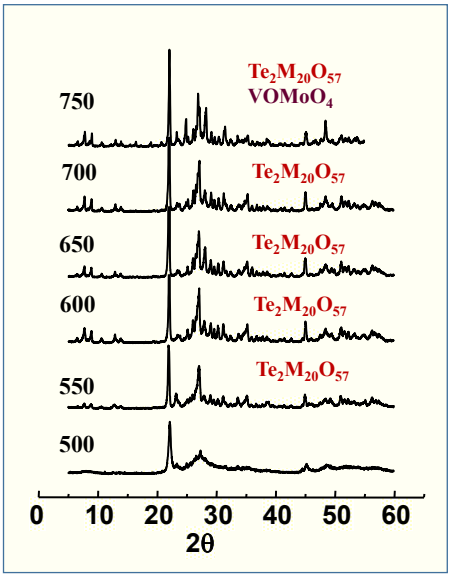

Activation temperature (ºC)	Ethane Conv. (%)	Select. Ethylene (%)
750	16.3	95.7
700	38.0	95.3
650	49.0	94.3
600	29.4	94.4
550	26.2	93.8
500	22.0	75.1

Figure 1.17. XRD patters of Mo-V-Te-Nb-O catalysts, heat-treated in the 500-750 ºC temperature interval. On the right, comparative catalytic results are shown for catalysts activated in the same temperature interval. Adapted from ref. [167b].

From these results, it was concluded that both the catalytic performance and the appearance of M1 phase strongly depend on the final activation temperature, being the catalysts activated in the 550-650 ºC range the best catalytic results. In this way, and according to the results of XRD and the catalytic properties of the materials thermally activated between 500 and 750ºC (**Figure 1.17**), it was concluded that the catalytic properties, especially the selectivity to ethylene, are directly related to the presence of the orthorhombic phase M1, $Te_2M_{20}O_{57}$ (M= Mo, V, Nb) [167, 234].

Furthermore, since from an industrial point of view, ethylene yields between 65% and 70% are required to compete with the stream cracking process [156], these catalysts seemed attractive, both from a fundamental and industrial perspective.

Subsequently, it was shown that the use of a different synthesis method such as precipitation [238], gave similar selectivity to ethylene, although the catalytic activity could vary depending on the synthesis method. In fact, as stated in **Section 1.4.2**, these M1 phase materials can be prepared through different synthetic routes (typically hydrothermally, slurry, reflux or spray drying) and with different chemical compositions methods [178, 183-189], as well as several modifications such as the addition of dopants, diluters/promoters or post treatment methods [191-199]. However, none of these have meant a significant increase in the selectivity to ethylene (**Table 1.1**).

The M1 phase, as mentioned in the previous section, is characterized by being a short of a complex structure, dealing with dissimilar compositions and partial occupation of the metallic sites. Many authors mentioned throughout the present chapter have dealt with the main attributes of the M1 phase that make it strongly suitable for the ODHE reaction, including several reviews [52, 55, 142, 161-163, 219]. However, recently a new review by Y. Cheng *et al.* [227] aimed to perform a state-of-the-art of the different parameters including synthesis, post treatments, characterization and reactor design that may contribute to the catalytic performance of $MoVTeNbO_x$ based catalysts.

Table 1.1. Catalytic properties for ethane ODH of multicomponent mixed oxides catalysts.

Catalyst	Conv. (%)	Sel. (%)	Temp. (ºC)	STY [a]	Ref.
MoVSbOx	65.0	82.0	400	0.19	**205**
MoVOx	27.5	92.4	300	0.19	**121a**
$MoVTeNbO_x$	89.0	90.0	400	0.29	**167**
M1-$MoVTeNbO_x$ **M1-$MoVTeNbO_x$ (mechanically treated)**	19.2 57.6	93.1 90.6	400 400	0.27	**189b**
MoVTeNbOx (H_2O_2-treatment) **MoVTeNbOx (oxalic acid/treatment)**	73 73	85 85	400 400	0.77 0.77	**187a** **187b**
MoVTeNbCe-0.1	56.2	95.4	425	1.11	**191b**
MoVTeNbOx/α-Al_2O_3 **MoVTeNbOx/Nb_2O_5** **MoVTeNbOx/ZrO_2**	30 19 14	95 93 94	400 400 400	0.21 0.13 0.10	**194a**
MoVTeNbOx/SiO_2	66	90	380	0.21	**194b**
MoVTeNbO/CeO_2	65	83	400	0.66	**194c**
MoVTeNbOx (M1) **MoVTeNbOx/30%CeO_2 (M1) (non-termal plasma treated)**	 44	 84.0	400 400	0.37 0.74	**197b**
MoVTeNbOx (H_2O treated for 7 days) **MoVTeNbOx (pure M1)**	53 62	92.8 90.8	400 400	0.81 0.93	**189a**
MoVTeNbOx@CeO_2@Cordierite	65	83	400	0.90	**249**
MoVTeNbOx	60	85	420	0.64[c]	**253**
MoVTeNbOx	68	88	280 [d]	029	**254**

a) As previously mentioned, for the commercialization of the ODHE process, a catalyst should exhibit high ethylene selectivity (> 90%), ethylene productivity (> 1.0 kg_{C2H4}/kg_{cat} h), and catalytic stability simultaneously, see ref. [223]. **b)** STY, Space time yield in (kg_{C2H4} kg_{cat}^{-1} h); **c)** Micro-channel reactor; **d)** Total pressure 100 atm.

Initially, it was proposed that the isolated VO_6 octahedra could be the active sites in ethane ODH [158, 234], as was originally suggested in the (amm)oxidation of propane over similar catalysts [177], while the presence of MoO_6 octahedra could favor increased catalytic activity of the $V^{5+/4+}$ sites (i.e., the formation of V^{5+}-O-Mo^{5+} pairs). However, for these authors, the role of Te atoms could not be interpreted as a promoting effect, but as a key element in the formation of the M1 phase. In this sense, the study of the possible promoting effect of Te atoms in Mo-V-Nb-O type catalysts demonstrated that, at least in those cases, the tellurium atoms would not be directly involved in the ODH of ethane in these catalysts. [239].

Recently, Sadovskaya *et al.* [240], by using isotopic oxygen exchange, determined that strongly bonded oxygen species (lattice nucleophilic O^{2-}) are responsible for the partial oxidation in the M1 phase, whereas weakly bonded electrophilic O^- species lead to the deep oxidation of ethane and/or ethylene to carbon oxides, so this is another factor that must be considered.

Although still controversial, it is generally accepted that active centers, i.e., believed to be V^{5+} species in close vicinity to Te^{4+} oxo-sites (*S2*, *S4* and *S7* positions in the structure, see **Figure 1.14** [152, 177, 178, 200]) are located in the {001} basal plane. Nevertheless, STEM analyses by Melzer *et al.* [241] showed that for M1-presenting catalysts with different morphologies, a similar amount of {001} surface area led to dissimilar catalytic activity, therefore, some other planes must be responsible for the catalytic performance. Accordingly, exposed surface area of M1 catalysts also consisted of {010}, {120} and {210} basal planes in addition to {001}.

In the case of {010} plane, facet must be composed of only pentagonal M_6O_{21} units, linked by MO_6 octahedra in a smooth zigzag pattern (positions *S5*, *S6*, *S8*, *S9*, *S10* and *S11* in **Fig. 1. 14**). Therefore, no active centers should be exposed within this plane. On the contrary, both {120} and {210} planes would show pentagonal units connected alternatively by single MO_6 octahedron, or a group of octahedra, resulting in half hexagonal or heptagonal units. Interestingly, these two latter planes do contain S2, S4 and S7 positions of the M1 structure, forming what Schlögl called half-pipe channels [242], suggesting that they are also active planes in the ODH of ethane. In the same manner, Millet *et al.* [206] used environmental transmission electron microscopy (ETEM) to perform in situ studies over trimetallic Mo-V-Te-O (M1) catalysts for the first time under reaction conditions and provide some insights into the dynamic changes that may occur during the redox reaction at atomic scale. Interestingly, since Mo-V-Te-O and Mo-V-Te-Nb-O catalysts show different shape of the crystals, the study was centered in the {001} plane, they did not find any {120} nor {210} lateral facets on trimetallic catalysts. However, they report that within the former plane, S2, S4 and S7 sites are not exposed, which also strongly suggests that these two latter planes should be active and selective in the ethane ODH. On the other hand, what they did found was an extraordinary atomic stability of the structure, even at reaction conditions (350 ºC and catalytic reaction gas mixture). Moreover, under extremely reducing conditions, part of the Te^{2+} formed can disproportionate into Te^{4+} and volatile metallic Te^0, suggesting that the importance of tellurium in the M1 phase lies on the fact that it can act as a labile oxygen reservoir in the hexagonal channels, participating in the reoxidation of the catalyst under

reaction conditions. Following with this, *in situ* XPS characterization of the M1 phase during ethane ODH by Hävecker *et al.* [243] demonstrated that surface and bulk composition on the M1 phase may significantly differ, explained by the exposure of the inner surface of hexagonal and heptagonal channels, {120} and {210} planes suggestion. Then, reaction products are associated with a decrease in the MO^{6+} and an increase in the V^{5+} relative abundance, only observing a dynamic behavior in the case of the latter, supporting the hypothesis that bulk M1 phase acts as a stable support containing the active V^{5+} species in close vicinity to Te^{4+} oxo-sites [221].

Furthermore, microporosity of the M1 phase, mostly due to the empty heptagonal channels, have also been studied. In this way, since the diameter of said heptagonal units is ca. 4 Å, which is very close to the kinetic diameter of the ethane molecule, steric/confinement effects have also been studied. Accordingly, density functional theory (DFT) calculations were carried out for ethane and cyclohexane (as a size-probe molecule) over microporous Mo-V-Te-Nb-O and non-microporous VO_x/SiO_2 materials [244, 245]. Said study concluded that most of the ethane activation occurs inside the micropores, since differences in the activation energy between C_2H_6 and C_6H_{12} are lower over the M1 catalysts than in the case of the supported vanadium oxide one, this explained by the C-H stabilization inside the micropores of the M1 structure through van der Waals interactions.

Consequently, due to the difficulties and different possibilities in the ethane ODH shown above, a simple general Mars-van Krevelen (MvK) mechanism like the one displayed in **Figure 1.15** seems uncomplete to

explain the possible reaction pathways over Mo-V-Te-Nb oxide catalysts. With the purpose of a more comprehensive study of the kinetics of the process, the group of Bollini [246] aimed to propose a global kinetic model for this type of catalysts. Then, the different kinetic models studied in the past few years, in addition to MvK have been [247, 248]: Langmuir-Hinshelwood-Hougen-Watson (LHHW), single site Eley-Rideal, two-site LHHW and hybrid MvK-LHHW. Although these models provide a somehow accuracy for the ethane ODH network, all of them are only focused on the ethylene formation kinetics that, despite showing this excellent selectivity over Mo-V-Te-Nb-O catalysts, it is not the only product formed during the reaction, so deep oxidation products must be considered.

Accordingly, four different types of MvK mechanisms were proposed, and they are represented in **Figure 1.18**. The first mechanism (**Fig. 1.18-A**) is characterized by the presence of a single type of lattice oxygen. There, ethane can be physisorbed onto said lattice oxygen followed by a hydrogen abstraction by a neighboring lattice oxygen. After the formation of an ethoxide intermediate, it can evolve through a β-hydrade elimination to form ethylene, or the O-insertion of an adjacent oxygen atom to form CO_x, nevertheless, nature of bond forming/excision is not explained.

A second mechanism (**Fig. 1.18-B**) proposes the ethane physisorption followed by its direct decomposition into ethene in single step – singe active site pathway, in where the radical intermediate formed after the hydrogen abstraction may interact with adjacent lattice oxygens to form

CO_x. In any case, there is a lack of consistency between the model and the experimental data by using only one active oxygen specie.

Therefore, the third possible mechanism (**Fig. 1.18-C**) also involves a single oxygen site model but accounting, two possible routes: **i)** outer (scission/formation of Me-O bonds) and **ii)** inner (kinetically accessible scission/formation of that Me-O bonds) sphere routes for reoxidation of isolated two-electron reduced centers (H/OH*) to lattice oxygen (O*), as a consequence of recombinative water desorption forming an oxygen vacancy (*). Then, O_2 adsorption onto a vacancy generates a peroxo intermediate that can be consumed either in the formation of C_2H_4 or CO_x, both leading to regenerate (O*) species. Outer sphere routes comprehend the regeneration of lattice oxygen directly from (H/OH*) by Me-O scission. Also, these reduced centers can also interact with O_2 to form H_2O_2 that further reacts with another (H/OH*) or (*) center to form the lattice oxygen. Regretfully, even this mechanism includes the presence of an additional oxygen intermediate (OO*), primary oxidation rate data is not accurately described.

Therefore, in **Figure 1.18-D** a dual oxygen site model is proposed. There, it is postulated the presence of a dissociatively adsorbed oxygen pool in quasi-equilibrium with gas phase oxygen (O**), different from lattice oxygens. Pathway for this mechanism comprise the adsorption of ethane over lattice oxygen (O*), irreversible abstraction of hydrogen by a neighboring O*, irreversible recombinative water desorption and dissociative oxygen adsorption to regenerate lattice oxygen sites. Then, while the hydride elimination of the ethoxide intermediate results in the

formation of ethylene, the formation of a C-O bond by this intermediate and O** species result into deep oxidation products formation.

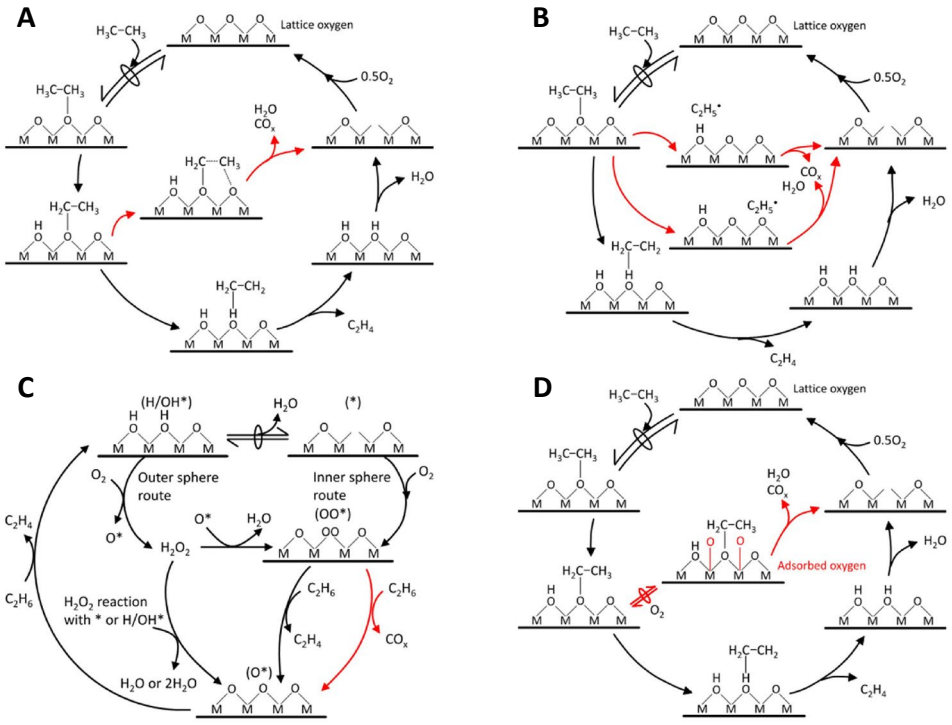

Figure 1.18. Mars-van Krevelen mechanisms for ethane ODH considering: **A)** single oxygen site model with two close lattice oxygens involved in hydrogen abstraction, **B)** single oxygen site model without hydrogen abstraction by close oxygen, **C)** single oxygen site model accounting inner and outer sphere reoxidation routes and **D)** dual oxygen site model considering irreversible dissociative adsorption steps and adsorbed oxygen species in quasi-equilibrium with gas phase O_2. Reproduced from [246].

Despite it has been clearly exposed that the ethane ODH, although presenting excellent results over Mo-V-Te-Nb-O (M1) catalysts, is influenced by a notable number of parameters kinetically and structurally related to the M1 phase itself, another importer factor is the nature of the

molecule, in this case ethylene. Thus, the stability and reactivity of the produced olefin should influence the final selectivity. In this way, by employing the same Mo-V-Te-Nb-O M1 catalyst, different results were observed depending on the paraffin. This is the case of propane and higher C-number hydrocarbons ODH where, as seen above in **Fig. 1.9**, the adsorbed corresponding olefin may continue reacting to form oxygenated products.

On the other hand, and when the catalytic properties of MoVTeNbO catalysts are compared during the selective oxidation of short chain alkanes and olefins (C_2-C_4), notable differences are observed in the reactivity, but also in the nature of the reaction products (**Figure 1.19**) [158]. Thus, the main reaction products were: ethylene (from ethane), acrylic acid (from propane, with propylene as a reaction intermediate), maleic anhydride (from n-butane, with C_4 olefins as reaction intermediates) and methacrolein (from isobutane, with isobutene as a reaction intermediate). Furthermore, notable differences in the reactivity of C_2-C_4 olefins were also observed, which would explain the nature of the partial oxidation products observed.

These results have been explained by the different reactivity of the olefins, especially ethylene (vinylic hydrogens in ethylene are more reactive than aliphatic hydrogens in ethane) compared to the rest of the C_3 and C_4 olefins (allylic hydrogens with great reactivity) [158]. In fact, it is well known that these molecules produced from C_{3+} hydrocarbons possess allylic hydrogens, which are quite more reactive than vinylic ones (370 vs 470 kJ mol^{-1}, respectively). Accordingly, all those alkanes with the possibility of producing H-allylic activation give rise to partially oxidized products when

working on catalysts presenting adequate sites for activating those allylic hydrogens. This is similar to what was obtained with V-P-O catalysts, which present a high selectivity in the oxidation of n-butane to maleic anhydride, being relatively selective in the oxidation of ethane to ethylene, without the formation of partial oxidation products [144, 149, 150].

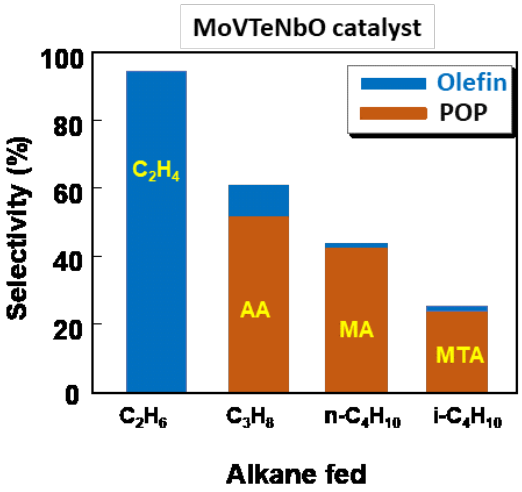

Figure 1.19. Variation of the selectivity to olefin and partially oxygenated products (POP) during C_2-C_4 oxidation over a MoVTeNbO mixed oxide. Reaction conditions of 400 ºC and 25 % of hydrocarbon conversion. Adapted from [158].

Finally, despite the interesting results displayed by these catalysts in the ethane ODH, some other considerations must be studied in order to scale from laboratory to industrial implementation.

One issue that appear when scaling the ODH of ethane, and due to the exothermic nature of the reaction, is the possible apparition of hot spots in the reactor that would negatively affect both the selectivity to ethylene as well as the stability of the reactor. In this sense, the use of cordierite as a

carrier have been studied since it is chemically inert, presents a high thermal stability and low thermal expansion coefficient [249]. On the other hand, foam SiC has been also proposed as a carrier for M1 phase catalysts, using its high thermal conductivity, this way eliminating the possible hot spots maintaining the selectivity to ethylene [250].

Moreover, reactor design must also be considered. Then, studies from Chen *et al.* [251] demonstrated that an autothermal reactor should be the most favorable configuration for the ODH process, since in steady multi-tubular reactors the control would be difficult. Accordingly, an autothermal reactor with a cold feed would allow an almost complete oxygen conversion.

Conversely, other different strategies to overcome hot spots have been also proposed, as the removal of water in a fixed-bed configuration, that can be maximized using membrane-like or micro-channel reactors [252, 253] or working at high pressure [254].

Alternatively, in the last years, the ODH of ethane by employing a chemical looping process has also focused lots of attention. Interesting results were described by Luongo *et al.* [255], where highly selective M1 phase catalyst is combined with an oxygen carrier such as $NaNO_3$-modified $Sr_{0.8}Ca_{0.2}FeO_{3-\delta}$ perovskite for a cyclic CL-ODH process that, in addition, allows optimization of the two different materials independently.

Anyway, apart from this chemical and engineering issues that affect the possible industrial implementation of the ethane ODH process, it is important to mention that competing companies may have their own vision upon new technology transition. In this sense, expert in the field Dr. Anne

Gaffney from Idaho National Laboratory, but former employee of leading petrochemical companies such as ARCO, DuPont, Rohm and Haas and Lummus, commented hew vision on this matter [55]. Thus, for membrane ODH reactor to be a reality, reticence may come from an economical point of view (new technology, risk aversion, capital already in the ground) as well as the challenge of commercialize new catalytic materials. These membrane ODH units, however, should be located near to natural gas sites. Nevertheless, in the mid-long term, the cheap and available supply of light alkanes (especially there in the US) will unequivocally lead to a restructuration of the industry in the coming years.

All in all, the oxidative dehydrogenation of ethane has been studied for almost 30 years, with promising results. In fact, a couple of years ago, Clariant jointly with Linde Engineering unveiled the very first ODHE plant based on mixed metal oxide catalysts that will count with additional CO_2 sequestration units and the potential for electrification [256], expected to be in use by 2025. With this new technology, according to company sources, carbon footprint can be lowered up to 60 % compared to traditional steam cracking [257].

1.6. Main objectives

The present doctoral thesis is set within the scope of the energy transition between non-renewable sources to sustainable renewable ones, with the parallel objective of reducing pollutant greenhouse emissions to the atmosphere. However, in the meantime, natural gas has arisen as a cheap and available source to be used during that transition to produce both fuels and chemical goods.

In that scenario, the production of light olefins (ethylene mainly) is doubly interesting because, on one hand, the demand of plastic polymers is far from decrease in the foreseeable future but, on the other hand, they are industrially manufactured by highly energy-demanding steam cracking. A promising alternative is the oxidative dehydrogenation (ODH) of ethane, allowing less reaction temperatures, with orthorhombic Mo-V-based mixed oxides (M1 phase) presenting the best catalytic properties.

Given the complexity of the M1 phase, the most important part of this thesis is devoted to an exhaustive study of its possibilities and implications in terms of synthesis and characterization, as well as the evaluation of their properties in the ODH of ethane (Chapters 3, 4 and 5, respectively). Thus, in a first approach, it will be presented a study of the synthetic parameters implied in the formation of the bimetallic Mo-V-O M1 phase in order to obtain an optimized catalyst. Subsequently, this investigation will be extended to a trimetallic Mo-V-Te-O system, contemplating the stability, morphological and catalytic changes that occur when progressively doping the M1 structure with higher tellurium contents.

Furthermore, the fifth chapter will consist of a complete comparative study of the M1 phase catalysts, hydrothermally prepared, in three different chemical compositions (i.e., Mo-V-O, Mo-V-Te-O and Mo-V-Te-Nb-O) and activation temperatures (400, 500 or 600 ºC). Within this comparison, catalytic results will be explained in terms of surface chemical composition (calculated by XPS) and electrochemical activity (characterization techniques such as Mott-Schottky plots or calculations of electrical resistance).

Finally, the last part of the thesis will deal with a comparative study between the catalysts that have reported in the literature the best catalytic performance in the ethane ODH throughout the years: M1 phase Mo-V-Te-Nb oxide, tin doped NiO and alumina supported vanadium oxide. In this case, the differences in the catalytic performance among these three catalytic systems will be pointed out by in situ IR techniques, as well as adsorption properties of ethane/ethene.

1.7. References

1) https://www.un.org/sustainabledevelopment/climate-change/ 17 goals for Sustainable Development from the United Nations.

2) https://library.wmo.int/doc_num.php?explnum_id=5789 World Meteorological Organization (WMO) Statement on the State of the Global Climate in 2018.

3) https://www.ncdc.noaa.gov/sotc/global/202013 NOAA National Centers for Environmental Information. State of the climate: global climate Report for annual 2020.

4) J. Zalasiewicz, C. N. Waters, C. P. Summerhayes, A. P. Wolfe, A. D. Barnosky, A. Cearreta, P. Crutzen, E. Ellis, I. J. Fairchild, A. Galuzska, P. Haff, The Working Group on the Anthropocene: summary of evidence and interim recommendations, Anthropocene 19 (2017) 55–60.

5) Z. Glasnovic, K. Margeta, N. Z. Logar, Humanity can still stop Climate Change by implementing a New International Climate Agreement and applying radical new technology, Energies 13 (2020) 6703.

6) https://www.mdsocialesa2030.gob.es/agenda2030/index.htm Spanish Ministry of Social Rights and 2030 Agenda.

7) https://unfccc.int/ Conference of Parties of the United Nations Framework Convention on Climate Change.

8) https://climate.copernicus.eu/ESOTC The European State of the Climate by the Copernicus Climate Change Service.

9) J. Rockström, W. Steffen, K. Noone, Å. Persson, F. Stuart Chapin III, E. F. Lambin, T. M. Lenton, M. Scheffer, C. Folke, H. J. Schellnhuber, B. Nykvist, C. A. de Wit, A safe operating space for humanity, Nature 461 (2009) 472-475.

10) J. Rockström, J. Gupta, D. Qin, S. J. Lade, J. F. Abrams, L. S. Andersen, D. I. Armstrong McKay, X. Bai, G. Bala, S. E. Bunn, D. Ciobanu, Safe and just Earth system boundaries, Nature 619 (2023) 102-111.

11) P. Wallemacq, R. House, Economic Losses, Poverty & Disasters (1998–2017). loUnited Nations Office for Disaster Risk Reduction (UNISDR) and Centre for Research on the Epidemiology of Disasters

(CRED). 2018. Available online: https://www.unisdr.org/files/61119_credeconomiclosses.pdf

12) E. Sala, J. Mayorga, D. Bradley, R. B. Cabral, T. B. Atwood, A. Auber, W. Cheung, C. Costello, F. Ferretti, A. M. Friedlander, S. D. Gaines, C. Garilao, Protecting the global ocean for biodiversity, food and climate, Nature 592 (2021) 397-402.

13) L.A. Garibaldi, F.J. Oddi, F. E. Miguez, I. Bartomeus, M.C. Orr, E. G. Jobbágy, Cl. Kremen, L.A. Schulte, A.C. Hughes, C. Bagnato, G. Abramson, P. Bridgewater, D. Gomez Carella, S. Díaz, L. V. Dicks, E.C. Ellis, M. Goldenberg, Cl.A. Huaylla, M. Kuperman, H. Locke, Z. Mehrabi, F. Santibañez, Ch. Zhu, Working landscapes need at least 20% native habitat, Conserv. Lett. 14 (2020) e12773.

14) R. Rojas, L. Feyen, P. Watkiss, Climate change and river floods in the European Union: Socio-economic consequences and the costs and benefits of adaptation, Glob. Environ. Change 23 (2013) 1737-1751.

15) Y. Hirabayashi, R. Mahendran, S. Koirala, L. Konoshima, D. Yamazaki, S. Watanabe, H. Kim, S. Kanae, Global flood risk under climate change, Nature Climate Change 3 (2013) 816-821.

16) X. Liu, W. Liu, L. Liu, Q. Tang, J. Liu, H. Yang, Environmental Flow requirements largely reshape global surface water scarcity assessment, Environ. Res. Lett. 16 (2021) 104029.

17) J. Álvarez-Rogel, G. G. Barberá, B. Maxwell, M Guerrero-Brotons, C. Díaz-García, J. J. Martínez-Sánchez, A. Sallent, J. Martínez-Ródenas, M. N. González-Alcaraz, F. J. Jiménez-Cárceles, C. Tercero, R. Gómez, The case of Mar Menor eutrophication: State of the art and description of tested Nature-based solutions, Ecol. Eng. 158 (2020) 106086.

18) A. J. Cohen, M. Brauer, R. Burnett, H. R. Anderson, J. Frostad, K. Estep, K. Balakrishnan, B. Brunekreef, L. Dandona, V. Figin, G. Freedman, B. Hubbell, A. Jobling, Estimates and 25-year trends of the global burden of disease attributable to ambient air pollution: an analysis of data from the Global Burden of Diseases Study 2015, The Lancet 389 (2017) 13-19.

19) C. Milford, C. Torres, J. Vilches, A.-K. Gossman, F. Weis, D. Suárez-Molina, O. E. García, N. Prats, A. Barreto, E. Cuevas, Impact of the

2021 La Palma volcanic eruption on air quality: Insights from a multidisciplinary approach, Sci. Total Environ. 869 (2023) 161652.

20) https://www.unep.org/news-and-stories/press-release/ozone-layer-recovery-track-helping-avoid-global-warming-05degc Press note published 9 January 2023 by the United Nations environment programme.

21) J.M. Chen, Carbon neutrality: Towards a sustainable future, Innovation 2 (2021) 100127.

22) IEA, CO_2 Emissions in 2021 Global emissions rebound sharply to highest ever level (2022); https://www.iea.org/reports/global-energy-review-co2-emissions-in-2021-2

23) V. Tulus, J. Pérez-Ramírez, G. Guillén-Gosálbez, Planetary metrics for the absolute environmental sustainability assessment of chemicals, Green Chem. 23 (2021) 9881-9893.

24) A. Galán-Martín, V. Tulus, I. Díaz, C. Pozo, J. Pérez-Ramírez, G. Guillén-Gosálbez, Sustainability footprints of a renewable carbon transition for the petrochemical sector within planetary boundaries, One Earth 4 (2021) 565–583.

25) G. Zichittella, J. Pérez-Ramírez, Status and prospects of the decentralised valorisation of natural gas into energy and energy carriers, Chem. Soc. Rev. 50 (2021) 2984-3012.

26) C. Hammond, S. Conrad and I. Hermans, Oxidative Methane Upgrading, ChemSusChem, 5 (2012) 1668–1686.

27) R. Horn and R. Schlögl, Methane Activation by Heterogeneous Catalysis, Catal. Lett. 145 (2014) 23–39.

28) S. Mokhatab, J. Y. Mak, J. V. Valappil and D. A. Wood, Handbook of Liquefied Natural Gas, Elsevier, Oxford (2014), pp. 1–591.

29) J. A. Labinger and J. E. Bercaw, Understanding and exploiting C–H bond activation, Nature 417 (2002) 507–514.

30) T. Ren, M. Patel, K. Blok, Energy use in steam cracking and alternative processes, Energy 31 (2006) 425-451.

31) E. Nduagu, H. Rahmanifard, A. Sow, K. Macarenhas, Economic Impacts and Market Challenges for the Methane to Derivatives Petrochemical Sub-Sector, 2018.

32) O. Czuprat, S. Werth, S. Schirrmeister, T. Schiestel, J. Caro, ChemCatChem, 1 (2009) 401-405.

33) D. R. Palo, R. A. Dagle, J. D. Holladay, Chem. Rev. 107 (2007) 3992-4021.

34) https://www.chemanalyst.com/industry-report/ethylene-market-638

35) https://www.statista.com/statistics/1067372/global-ethylene-production-capacity/

36) https://www.precedenceresearch.com/ethylene-market#:~:text=The%20global%20ethylene%20market%20size%20was%20accounted%20at%20USD%20132,5.7%25%20from%202023%20to%202032 (October 2023)

37) https://www.chemanalyst.com/

38) K. Weissermel, H.J. Arpe, Industrial organic chemistry, 4th edn. Wiley-VCH, Washington DC (2003).

39) K. Zimmermann, H. Walzl. Ethylene. *In*: S. Hawkins, W.E. Russey, M. Pilkart-Muller (eds.). Ullmann's Encyclopedia of industrial chemistry. Wiley-VCH, New York (2009) p. 36.

40) https://www.statista.com/statistics/1192886/thermoplastics-production-volume-by-type-globally/

41) H. Yue, Y. Zhao, X. Ma, J. Gong, Ethylene glycol: properties, synthesis, and applications, Chem. Soc. Rev. 41 (2012) 4218-4244.

42) M. G. Farpón et al., Rhodium Single-Atom Catalyst Design through Oxide Support Modulation for Selective Gas-Phase Ethylene Hydroformylation, Agew. Chem. Int. Ed., 2023, 62, e202214048.

43) H. Ma, Y. Wang, Y. Qi, K.R. Rout, D. Chen, Critical Review of Catalysis for Ethylene Oxychlorination, ACS Catal. 10 (2020) 9299–9319.

44) S. Rebstad, D. Mayer, Ethylene Oxide, *in* Ullmann's Encyclopedia of industrial chemistry. Wiley-VCH Verlag GmbH & Co., Weinheim (2012) 547-572.

45)https://www.acs.org/education/whatischemistry/landmarks/petrochemical-industry-birthplace.html

46) G.O. Curme “Process of separating ethylene and other components from gaseous mixtures containing the same”, US Patent, US1422184A (1922).

47) M.E.H. Tijani, H. Zondag, Y. Van Delft, Review of Electric Cracking of Hydrocarbons, ACS Sustainable Chem. Eng. 10 (2022) 16070−16089.

48) B. V. Vora, Development of Catalytic Processes for the Production of Olefins, Trans. Indian Acad. Eng. 8 (2023) 201-219.

49) M. Yang, F. You, Comparative Techno-Economic and Environmental Analysis of Ethylene and Propylene Manufacturing from Wet Shale Gas and Naphtha, Ind. Eng. Chem. Res., 56 (2017) 4038-4051.

50) M. Ghanta, D. Fahey, B. Subramaniam, Environmental impacts of ethylene production from diverse feedstocks and energy sources, Appl. Petrochem. Res. 4 (2014) 167–179.

51) C. A. Gärtner, A. C. van Veen, J. A. Lercher, Oxidative Dehydrogenation of Ethane: Common Principles and Mechanistic Aspects, ChemCatChem 5 (2013) 3196-3217.

52) S. Najari, S. Saeidi, P. Concepción, D. D. Dionysiou, S. K. Bhargava, A. F. Lee, K. Wilson, Chem. Soc. Rev., 2021, 50, 4564-4604.

53) Y. Gao, L. Neal, D. Ding, W. Wu, C. H. Baroi, A. M. Gaffney, F. Li, ACS Catal., 2019, 9, 8592-8621.

54) P. K. Ladwig, J. E. Asplin, G. F. Stuntz, W. A. Wachter, B. E. Henry, US Patent, 6069287, 2000.

55) F. Cavani, A. Chieregato, J.M. López Nieto, J.M.M. Millet, Gas-Phase Oxidation of Alkanes, in: A.J.L. Pombeiro, M.F. C. Guedes da Silva (Eds.), in *Alkane Functionalization*, JohnWiley & Sons, 2019, pp. 159–188.

56) T. Ren, M K. Patel, K. Blok, Steam cracking and methane to olefins: Energy use, CO_2 emissions and production costs, Energy, 33 (2008) 817-833.

57) V. P. Haribal, Y. Chen, L. Neal, F. Li, Intensification of Ethylene Production from Naphtha via a Redox Oxy-Cracking Scheme: Process Simulations and Analysis, Engineering 4 (2018) 714-721.

58) D. Fairuzov, I. Gerzeliev, A. Maximov, E. Naranov, Catalytic Dehydrogenation of Ethane: A Mini Review of Recent Advances and Perspective of Chemical Looping Technology, Catalysts 11 (2021) 833.

59) A. N. Biswas, Zh. Xie, J. G. Chen, Can CO2-assisted alkane dehydrogenation lead to negative CO2 emissions?, Joule 6 (2022) 269-273.

60) K. Weissermel, H.-J. Arpe, *Industrial organic chemistry*, 4th edn., Wiley-VCH Verlag GmbH & Co. KGaA, Washington DC (2003).

61) https://www.petrochemistry.eu/about-petrochemistry/petrochemicals-facts-and-figures/cracker-capacity/

62) O. Mynko, K. M. Van Geem et al., Reducing CO_2 emissions of existing ethylene plants: Evaluation of different revamp strategies to reduce global CO_2 emission by 100 million tonnes, J. Clean. Prod. 362 (2022) 132127.

63) I. Amghizar, K. M. Van Geem, Sustainable innovations in steam cracking: CO2 neutral olefin production, React. Chem. Eng. 5 (2020) 239-257.

64) W. Shen, Z. Tian, L. Zhao, F. Qian, Life Cycle Assessment and Multiobjective Optimization for Steam Cracking Process in Ethylene Plant, ACS Omega, 7 (2022) 15507-15517.

65) S. Gong, Multi-scale energy efficiency recognition and diagnosis scheme for ethylene production based on a hierarchical multi-indicator system, Energy 267 (2023) 126478.

66) J. Gu, H. Kim, H. Lim, Electrified steam cracking for a carbon neutral ethylene production process: Techno-economic analysis, life cycle assessment, and analytic hierarchy process, Energ. Convers. Manage., 270 (2022) 116256.

67) D. S. Mallapragada, Y. Dvorkin, M. A. Modestino, D. V. Esposito, W. A. Smith, D.-M. Hodge, M. P. Harold, V. M. Donnelly, A. Nuz, C.

Bloomquist, Decarbonization of the chemical industry through electrification: Barriers and opportunities, Joule 7 (2023) 23-41.

68) G. P. Thiel, A. K. Stark, To decarbonize industry, we must decarbonize heat, Joule 5 (2020) 531-550.

69) L. S. Layritz, I. Dolganova, M. Finkbeiner, G. Luderer, A. T. Penteado, F. Ueckerdt, J-U. Repke, The potential of direct steam cracker electrification and carbon capture & utilization via oxidative coupling of methane as decarbonization strategies for ethylene production, Appl. Energy 296 (2021) 117049.

70) D. Ding, Y. Zhang, W. Wu, D. Chen, M. Liu, T. He, A novel low-thermal-budget approach for the co-production of ethylene and hydrogen via the electrochemical non-oxidative deprotonation of ethane, Energy Environ. Sci. 11 (2018) 1710.

71) https://investors.dow.com/en/news/news-details/2021/Dow-announces-plan-to-build-worlds-first-net-zero-carbon-emissions-ethylene-and-derivatives-complex/default.aspx

72) Bender, M. An Overview of Industrial Processes for the Production of Olefins—C4 Hydrocarbons. ChemBioEng Rev. 1 (2014) 136–147.

73) V. Zacharopoulou, A. A. Lemonidou, Olefins from Biomass Intermediates: A Review, Catalysts 8 (2018) 2.

74) O. O. James, S. Mandal, N. Alele, B. Chowdhury, S. Maity, Lower alkanes dehydrogenation: Strategies and reaction routes to corresponding alkenes, Fuel Process. Technol. 149 (2016) 239-255.

75) I. Amghizar, L. A. Vandewalle, K. M. Van Geem, G. B. Marin, New Trends in Olefin Production, Engineering 3 (2017) 171-178.

76) I. Fechete, J. C. Védrine, Recent development of heterogeneous catalysis in ring-opening, biocatalysis, and selective partial oxidation reactions on metal oxides, C. R. Chimie 21 (2018) 408-418.,

77) S.A. Chernyak, M. Corda, J.-P. Dath, V. V. Ordomsky, A. Y. Khodakov, Light olefin synthesis from a diversity of renewable and fossil feedstocks: state-of the-art and outlook, Chem. Soc. Rev. 51 (2022) 7994-8044.

78) Yang, X. Tian, F. You, Manufacturing Ethylene from Wet Shale Gas and Biomass: Comparative Technoeconomic Analysis and

Environmental Life Cycle Assessment, Ind. Eng. Chem. Res. 57 (2018) 5980–5998.

79) R.B. Dudek, X. Tian, M. Blivin, L. M. Neal, H. Zhao, F. Li, Perovskite oxides for redox oxidative cracking of n-hexane under a cyclic redox scheme, Appl. Catal. B: Environm. 246 (2019) 30-40.

80) X. Tian, R B. Dudek, Y. Gao, H. Zhao, F. Li, Redox oxidative cracking of n-hexane with Fe-substituted barium hexaaluminates as redox catalysts, Catal. Sci. Technol. 9 (2019) 2211-2220.

81) S.M. Sadrameli, Thermal/catalytic cracking of liquid hydrocarbons for the production of olefins: A state-of-the-art review II: Catalytic cracking review, Fuel 173 (2016) 285-297

82) Z. Gholami, F. Gholami, Z. Tišler, M. Tomas, M. Vakili, Review on Production of Light Olefins via Fluid Catalytic Cracking, Energies 14 (2021)1089.

83) A. Galadima, O. Muraza, Revisiting the oxidative coupling of methane to ethylene in the golden period of shale gas: A review, J. Ind. Eng. Chem. 37 (2016) 1-13

84) B. L. Farrell, V. O. Igenegbai, S. Linic, A Viewpoint on Direct Methane Conversion to Ethane and Ethylene Using Oxidative Coupling on Solid Catalysts, ACS Catal. 6 (2016) 4340–4346.

85) Y. Miao, P. Kreider, I. Reddick, J. Pommerenck, R. Collin, N. AuYeung, A. von Jouanne, G. Jovanovic, A. Yokochi, Methane Coupling to Ethylene and Longer-Chain Hydrocarbons by Low-Energy Electrical Discharge in Microstructured Reactors, Ind. Eng. Chem. Res. 60 (2021) 6950–6958.

86) J. Liu, J. Yue, M. Lv, F. Wang, Y. Cui, Zh. Zhang, G. Xu, From fundamentals to chemical engineering on oxidative coupling of methane for ethylene production: A review, Carbon Resources Conv. 5 (2022) 1-14.

87) L. Ye, Zh. Shang, K. Xie, Selective Oxidative Coupling of Methane to Ethylene in a Solid Oxide Electrolyser Based on Porous Single-Crystalline CeO_2 Monoliths, Angew. Chem.Int. Ed. 61 (2022) e202207211.

88) R. S. Postma, L. Lefferts, Effect of ethane and ethylene on catalytic non oxidative coupling of methane, React. Chem. Eng. 6 (2021) 2425-2433

89) J. J. H. B. Sattler, J. Ruiz-Martinez, E. Santillan-Jimenez, B. M. Weckhuysen, Catalytic Dehydrogenation of Light Alkanes on Metals and Metal Oxides, Chem. Rev. 114 (2014) 10613-10653.

90) Z. Nawaz, Light alkane dehydrogenation to light olefin technologies: a comprehensive review, Rev. Chem. Eng. 31 (2015) 413-436.

91) C. Li, G. Wang, Dehydrogenation of light alkanes to mono-olefins, Chem. Soc. Rev. 50 (2021) 4359-4381.

92) M. Zhang, Y. Yu, Dehydration of Ethanol to Ethylene, Ind. Eng. Chem. Res. 52 (2013) 9505-9514.

93) A. Mohsenzadeh, A. Zamani, M. J. Taherzadeh, Bioethylene Production from Ethanol: A Review and Techno-economical Evaluation, ChemBioEng Rev. 4 (2017) 75-91.

94) A. Tripodi, M. Belotti, I. Rossetti, Bioethylene Production: From Reaction Kinetics to Plant Design, ACS Sustainable Chem. Eng. 7 (2019) 13333-13350.

95) M. Frosi, A. Tripodi, F. Conte, G. Ramis, N. Mahinpey, I. Rossetti, Ethylene from renewable ethanol: Process optimization and economic feasibility assessment, J. Ind. Eng. Chem. 104 (2021) 272-285.

96) I. Rossetti, M. Compagnoni, E.Finocchio, G. Ramis, A. Di Michele, Y. Millot, S. Dzwigaj, Ethylene production via catalytic dehydration of diluted bioethanol: A step towards an integrated biorefinery, Appl. Catal. B: Environ. 210 (2017) 407-420.

97) F. Jamil, M. Aslam, A.H. Al-Muhtaseb, A. Bokhari, S. Rafiq, Z. Khan, A. Inayat, A. Ahmed, Sh. Hossain, M.Sh. Khurram, M. S. Abu Bakar, Greener and sustainable production of bioethylene from bioethanol: current status, opportunities and perspectives, Rev. Chem. Eng. 38 (2022) 185-207.

98) M.R. Gogate, Methanol-to-olefins process technology: current status and future prospects, Petroleum Sci. Technol. 37 (2019) 559–565.

99) https://www.lummustechnology.com/process-technologies/petrochemicals/ethylene-production/methanol-to-olefins-mto

100) Zh. Shi, A. Bhan, Tuning the ethylene-to-propylene ratio in methanol-to-olefins catalysis on window-cage type zeolites, J. Catal. 395 (2021) 266–272.

101) K. Lu, J. Huang, L. Ren, Ch. Li, Y. Guan, B. Hu, H. Xu, J. Jiang, Y. Ma, P. Wu, High Ethylene Selectivity in Methanol-to-Olefin (MTO) Reaction over MOR-Zeolite Nanosheets, Angew. Chem. Int. Ed. 59 (2020) 6258 –6262.

102) P. S. Rezaei, H. Shafaghat, W.M.A.W. Daud, Production of green aromatics and olefins by catalytic cracking of oxygenate compounds derived from biomass pyrolysis: A review, Appl. Catal. A: Gen 469 (2014) 490-511.

103) M. Sharifzadeh, L. Wang, N. Shah, Decarbonisation of olefin processes using biomass pyrolysis oil, Appl. Energy 149 (2015) 404-414.

104) X. Liu, M. Wang, Cheng Zhou, W. Zhou, K. Cheng, J. Kang, Q. Zhang, W. Deng, Y. Wang, Selective transformation of carbon dioxide into lower olefins with a bifunctional catalyst composed of $ZnGa_2O_4$ and SAPO-34, Chem. Commun. 54 (2018) 140-143.

105) S. Wang, L. Zhang, P. Wang, X. Liu, Y. Chen, Zh. Qin, M.Dong, J. Wang, L. He, U. Olsbye, W. Fan, Highly effective conversion of CO_2 into light olefins abundant in ethene, Chem 8 (2022) 1376-1394.

106) B. Pawelec, R. Guil-López, N. Mota, J. L. Garcia Fierro, R.M. Navarro Yerga, Catalysts for the Conversion of CO_2 to Low Molecular Weight Olefins—A Review, Materials 14 (2021) 6952.

107) O. A. Ojelade, Sh. F. Zaman, A review on CO_2 hydrogenation to lower olefins: Understanding the structure-property relationships in heterogeneous catalytic systems, J. CO_2 Utilization 47 (2021) 101506.

108) Y. Dai, X. Gao, Q. Wang, X. Wan, Ch. Zhou, Y. Yang, Recent progress in heterogeneous metal and metal oxide catalysts for direct

dehydrogenation of ethane and propane, Chem. Soc. Rev. 50 (2021) 5590-5630.

109) A. Corma, E. Corresa, Y. Mathieu, L. Savanaud, S. Al.Bogami, M. S. Al-Ghrami, A. Bourane, Crude oil to chemicals: light olefins from crude oil, Catal. Sci. Tecnhnol. 7 (2017) 12-46.

110) D. A. Henning, L. D. Schmidt, Oxidative dehydrogenation of ethane at short contact times: species and temperature profiles within and after the catalyst, Chem. Eng. Sci. 57 (2002) 2615-2625.

111) H. J. Dar, H. A. Jakobsen, K. R. Rout, K. J. Jens, D. Chen, Autothermal Gas-Phase Oxidative Dehydrogenation of Ethane to Ethylene at Atmospheric Pressure, Ind. Eng. Chem. Res. 60, 18 (2021) 6784-6802.

112) **a)** F. Donsì, S. Cimino, R. Pirone, G. Russo, Autothermal Oxidative Dehydrogenation of Ethane on $LaMnO_3$- and Pt-Based Monoliths: H_2 and CO Addition, Ind. Eng. Chem. Res. 44, 2 (2005) 285-295; **b)** S. Cimino, F. Donsì, G. Russo, D. Sanfilippo, Optimization of Ethylene Production via Catalytic Partial Oxidation of Ethane on Pt–$LaMnO_3$ Catalyst, Catal. Lett. 122 (2008) 228-237; **c)** S. Cimino, F. Donsì, G. Russo, D. Sanfilippo, Olefins production by catalytic partial oxidation of ethane and propane over Pt/$LaMnO_3$ catalyst, Catal. Today 157 (2010) 310-314.

113) E. A. de Graaf, G. Zwanenburg, G. Rothenberg, A. Bliek, Two-step catalytic oxidative dehydrogenation of propane: An alternative route to propene, Org. Process. Res. Dev. 9 (2005) 397-403.

114) S. Crapanzano, I. V. Babich, L. Lefferts, Selection of mixed conducting oxides for oxidative dehydrogenation of propane with pulse experiments, Appl. Catal. A-Gen., 391 (2011) 70-77.

115) H. Jiang, H. Wang, S. Werth, T. Schiestel, J. Caro, Simultaneous Production of Hydrogen and Synthesis Gas by Combining Water Splitting with Partial Oxidation of Methane in a Hollow-Fiber Membrane Reactor, Angew. Chem. Int. Ed. 47 (2008) 9341-9344.

116) H. Jiang, H. Wang, F. Liang, S. Werth, T. Schiestel, J. Caro, Angew. Chem. Int. Ed. 48 (2009) 2983-2986.

117) X. Zhang, X. Yi, J. Zhang, Z. Xie, J. Kang, L. Zheng, Fabrication of Apatite-Type $La_{9.33}(SiO_4)_6O_2$ Hollow Nanoshells as Energy-Saving Oxidative Catalysts, Inorg. Chem. 49 (2010) 10244-10246.

118) Y. Feng, J. Luo, K. T. Chuang, Propane dehydrogenation in a proton-conducting fuel cell, J. Phys. Chem. C 112 (2008) 9943-9949.

119) L. Brody, L. Neal, J. Liu, F- Li, Autothermal chemical looping oxidative dehydrogenation of ethane: redox catalyst performance, longevity, and process analysis, Energy Fuels 36 (2022) 9736-9744.

120) W. Xia, J. Wang, L. Wang, C. Qian, C. Ma, Y. Huang, Y. Fan, M. Hou, K. Chen, Ethylene and propylene production from ethanol over Sr/ZSM-5 catalysts: A combined experimental and computational study, Appl. Catal. B: Environ. 294 (2021) 120242.

121) Z. Wang, L. A. O'Dell, X. Zeng, C. Liu, S. Zhao, W. Zhang, M. Gaborieau, Y. Jiang, J. Huang, Insight into Three-Coordinate Aluminum Species on Ethanol-to-Olefin Conversion over ZSM-5 Zeolites, Angew. Chem. Int. Ed. 58 (2019) 18061-18068.

122) J. Zhong, J. Han, Y. Wei, P. Tian, X. Guo, C. Song, Z. Liu, Recent advances of the nano-hierarchical SAPO-34 in the methanol-to-olefin (MTO) reaction and other applications, Catal. Sci. Technol. 7 (2017) 4905-4923.

123) T. Zhou, X. Shi, L.N. Wu, Q. Cui, H.Y. Wang, Y. Hu, H. Huang. Catalytic Properties of SAPO-11/HZSM-5 for ethanol dehydration to ethylene, J. Chem. Eng. Chin. Univ. 25 (2011) 453– 458.

124) C. D., Chang, A. J. Silvestri, The conversion of methanol and other O-compounds to hydrocarbons over zeolite catalysts, J. Catal., 47 (1977) 249-259.

125) U. Olsbye, S. Svelle, M. Bjørgen, P. Beato, T.V. W. Janssens, F. Joensen, S. Bordiga, K.P. Lillerud, Conversion of Methanol to Hydrocarbons: How Zeolite Cavity and Pore Size Controls Product Selectivity, Angew. Chem. Int. Ed. 24 (2012) 5810-5831.

126) S. Ilias, A. Bhan, Mechanism of the Catalytic Conversion of Methanol to Hydrocarbons, ACS Catal. 3 (2013) 18-31.

127) S. Xu et al., Direct observation of cyclic carbenium ions and their role in the catalytic cycle of the methanol-to-olefin reaction over chabazite zeolites, Angew. Chem. Int. Ed. 52 (2013) 11564-11568.

128) M. McCann, D. Lesthaegher, P. W. Kletnieks, D. R. Guenther, M. J. Hayman, V. Van Speybroeck, M. Waroquier, J. F. Haw, A Complete

Catalytic Cycle for Supramolecular Methanol-to-Olefins Conversion by Linking Theory with Experiment, Angew. Chem. Int. Ed. 47 (2008) 5179-5182.

129) N. Martin, Zh. Li, J. Martínez-Triguero, J. Yu, M. Moliner, A. Corma, Nanocrystalline SSZ-39 zeolite as an efficient catalyst for the methanol-to-olefin (MTO) process, Chem. Commun. 52 (2016) 6072-6075.

130) M. Dusselier, M. A. Deimund, J. E. Schmidt, M. E. Davies, Methanol-to-Olefins Catalysis with Hydrothermally Treated Zeolite SSZ-39, ACS Catal. 5 (2015) 6078-6085.

131) C. Li, C. París, J. Martínez-Triguero, M. Boronat, M. Moliner, A. Corma, Synthesis of reaction-adapted zeolites as methanol-to-olefins catalysts with mimics of reaction intermediates as organic structure-directing agents, Nat. Catal. 1 (2018) 547-554.

132) E. M. Gallego, M. T. Portilla, C. París, A. León-Escamilla, M. Boronat, A. Corma, "Ab initio" synthesis of zeolites for preestablished catalytic reactions, Science 355 (2017) 1051-1054.

133) P. Tian, Y. Wei, M. Ye, Z. Liu, Methanol to olefins (MTO): from fundamentals to commercialization, ACS Catal. 5 (2015) 1922-1938.

134) R. K. Grasselli, Handbook of Heterogeneous Catalysis, vol. 4.6.6, Willey-VCH, (1997) 302 (and references therein).

135) R. Grasselli, J. Burrington, Selective Oxidation and Ammoxidation of Propylene by Heterogeneous Catalysis, Adv. Catal. 30 (1981) 133-163.

136) **a)** F. Cavani, F. Trifirò, Some aspects that affect the selective oxidation of paraffins, Catal. Today 36 (1997) 431-439; **b)** F. Cavani, F. Trifirò, Selective oxidation of light alkanes: interaction between the catalyst and the gas phase on different classes of catalytic materials, Catal. Today 51 (1999) 561-580.

137) T. Blasco, J.M. López Nieto, Oxidative dehydrogenation of short chain alkanes on supported vanadium oxide catalysts, Appl. Catal. A: Gen. 157 (1997) 117-142.

138) S. Albonetti, F. Cavani, F. Trifiró, Key Aspects of Catalyst Design for the Selective Oxidation of Paraffins, Catal. Rev. Sci. Eng. 38 (1996) 413-438.

139) M. Müller, M. Kutscherauer, S. Böcklein, G.D. Wehinger, T. Turek, G. Mestl, Modeling the selective oxidation of n-butane to maleic anhydride: From active site to industrial reactor, Catal. Today, 387 (2022) 82-106.

140) M. Faizan, Y. Li, R. Zhang, X. Wang, P. Song, R. Liu, Progress of vanadium phosphorous oxide catalyst for n-butane selective oxidation, Chinese J. Chem, Eng. 43 (2022) 297-316.

141) A. Chieregato, J. M. López Nieto, F. Cavani, Mixed-oxide catalysts with vanadium as the key element for gas-phase reactions, Coord. Chem. Rev. 301–302 (2015) 3–23.

142) J.M. López Nieto, The selective oxidative activation of light alkanes. From supported vanadia to multicomponent bulk V-containing catalysts, Top. Catal. 41 (2006) 3-15.

143) F. Cavani, J. Henrique Teles, Sustainability in catalytic oxidation: an alternative approach or a structural evolution?, ChemSusChem 2 (2009) 508 – 534.

144) F. Ivars, J. M. López Nieto, Light Alkanes Oxidation: Targerts reached and current Challenges, in Advanced Methods and Processes in Oxidation Catalysis: From Laboratory to Industry, D. Duprez, F. Cavani (Eds.), Imperial College Press, London (2014), pp. 767-833.

145) P. Kube, B. Frank, R. Schlögl, A. Trunschke, Isotope Studies in Oxidation of Propane over Vanadium Oxide. ChemCatChem 2017, 9, 3446– 3455.

146) L. Foppa, F. Rüther, M. Geske, G. Koch, F. Girgsdies, P. Kube, S. J. Carey, M. Hävecker, O. Timpe, A. V. Tarasov, M. Scheffler, F. Rosowski, R. Schlögl, A. Trunschke, Data-Centric Heterogeneous Catalysis: Identifying Rules and Materials Genes of Alkane Selective Oxidation, J. Am. Chem. Soc. 2023, 145, 3427−3442.

147) J.M.M. Millet, Mechanism of first hydrogen abstraction from light alkanes on oxide catalysts, Top Catal. 38 (2006) 83-92.

148) R.K. Grasselli, Advances and future trends in selective oxidation and ammoxidation catalysis, Catal. Today 49 (1999) 141-153.

149) G. Centi, J. Lopez Nieto, D. Pinelli, F. Trifiró, Synthesis of Phthalic and Maleic Anhydrides from n-Pentane. 1. Kinetic Analysis of the Reaction Network, Ind. Eng. Chem. Res. 28 (1989) 400-406.

150) G. Centi, D. Pinelli, F. Trifiro, F. Ungarelli, J. Lopez Nieto, Synthesis of Phthalic and Maleic Anhydrides from n-Pentane: Reactivity of Possible Intermediates and co-Feeding Experiments, Stud. Surf. Sci. Catal. 55 (1990) 635-642.

151) G. Busca, G Centi, Surface Dynamics of Adsorbed Species on Heterogeneous Oxidation Catalysts: Evidence from the Oxidation of C4 and C5 Alkanes on Vanadyl Pyrophosphate, J. Am. Cehm. Soc., 11 (1989) 46 – 54.

152) R. K. Grasselli, J. D. Burrington, D. J. Buttrey, P.DeSanto Jr., C.G. Lugmair, A F. Volpe Jr., Thomas Weingand, Multifunctionality of active centers in (amm)oxidation catalysts: from Bi–Mo–Ox to Mo–V–Nb–(Te, Sb)–Ox, Top. Catal. 23 (2003) 5-22.

153) P. Botella, J. M. López Nieto,1 B. Solsona, A. Mifsud, F. Márquez, The Preparation, Characterization, and Catalytic Behavior of MoVTeNbO Catalysts Prepared by Hydrothermal Synthesis, J. Catal. 209 (2002) 445–455.

154) Ch. Sprung, G. S. Yablonsky, R. Schlögl, A. Trunschke, Constructing A Rational Kinetic Model of the Selective Propane Oxidation Over a Mixed Metal Oxide Catalyst, Catalysts 8 (2018) 330.

155) H.-G. Lintz, S. P. Müller, The partial oxidation of propane on mixed metal oxides—A short overview, Appl. Catal. A: Gen 357 (2009) 178-183.

156) G. Grubert, E. Kondratenko, S. Kolfa, M. Baerns, P. van Geem, R. Parton, Fundamental insights into the oxidative dehydrogenation of ethane to ethylene over catalytic materials discovered by an evolutionary approach, Catal. Today 81 (2003) 337–345.

157) A. M. Wernbacher, P. Kube, M. Haevecker, R. Schlögl, A. Trunschke, Electronic and dielectric properties of MoV-oxide (M1 Phase) under alkane oxidation conditions, J. Phys. Chem. C 123 (2019) 13269-13282.

158) J.M. López Nieto, B. Solsona, P. Concepcion, F. Ivars, A. Dejoz, M.I. Vazquez, Reaction products and pathways in the selective oxidation of

C_2-C_4 alkanes on MoVTeNb mixed oxide catalysts. Catal. Today 157 (2010) 291– 296.

159) R.K. Grasselli, Fundamental principles of selective heterogeneous oxidation catalysis, Top. Catal., 21 (2002) 79-88.

160) R.K. Grasselli, Site isolation and phase cooperation: Two important concepts in selective oxidation catalysis: A retrospective, Catal. Today 238 (2014) 10–27.

161) J.M. López Nieto, B. Solsona, Gas phase heterogeneous partial oxidation reactions, in Metal oxide in Heterogeneous catalysis, J. Vedrine (Ed.), Elsevier (2018), pp. 211-286.

162) J. T. Grant, J.M. Venegas, W.P. McDermott, I. Hermans, Aerobic Oxidations of Light Alkanes over Solid Metal Oxide Catalysts, Chem. Rev. 118 (2018) 2769−2815.

163) J. S. Valente, R. Quintana-Solórzano, H. Armendáriz-Herrera, J.-M. M. Millet, Decarbonizing Petrochemical Processes: Contribution and Perspectives of the Selective Oxidation of C_1−C_3 Paraffins, ACS Catal. 13 (2023) 1693−1716.

164) R. Schlögl, Selective Oxidation: From a Still Immature Technology to the Roots of Catalysis Science, Top. Catal. (2016) 1461–1476.

165) J.F. Brazdil, Selective oxidation in industry: Application of metal oxides in petrochemistry industry, in J. Vedrine (Ed.), Metal oxide in Heterogeneous catalysis, Elsevier (2018), pp. 455-502.

166) **a)** T. Ushikubo, H. Nakamura, Y. Koyasu, S. Wajiki, US Patent 5,380,933 (1995) assigned to Mitsubishi; **b)** T. Ushikubo, K. Oshima, A. Kayou, M. Hatano, Ammoxidation of propane over Mo-V-Nb-Te mixed oxide catalysts, Stud. Surf. Sci. Catal., 112 (1997) 473-480; **c)** T. Ushikubo, K. Oshima, A. Kayo, T. Umezawa, K. Kiyono, I. Sawaki, EP Patent 0,529, 853 A2 (1992), assigned to Mitsubishi.

167) **a)** J.M. López Nieto, P. Botella, M.I. Vázquez, A. Dejoz, WO Patent 0346035 (2003); assigned to UPV-CSIC; **b)** J. M. López Nieto, P. Botella, M. I. Vázquez, A. Dejoz, The selective oxidative dehydrogenation of ethane over hydrothermally synthesised MoVTeNb catalysts, Chem. Commun. (2002) 1906-1907.

168) **a)** P. Deshlahra, E. Iglesia, Reactivity and Selectivity Descriptors for the Activation of C–H Bonds in Hydrocarbons and Oxygenates on Metal Oxides, J. Phys. Chem. C 120 (2016) 16741 – 16760; **b)** S. Kwon, P. Deshlahra, E. Iglesia, Dioxygen activation routes in Mars-van Krevelen redox cycles catalyzed by metal oxides, S. Kwon, P. Deshlahra, E. Iglesia, J. Catal. 364 (2018) 228-247.

169) D. Deshlahra, R.T. Carr, S.-H. Chai, E. Iglesia, Mechanistic Details and Reactivity Descriptors in Oxidation and Acid Catalysis of Methanol, ACS Catal. 5 (2015) 666 – 682.

170) S. Kwona, P. Deshlahra, E. Iglesia, Reactivity and selectivity descriptors of dioxygen activation routes on metal oxides, J. Catal. 377 (2019) 692–710.

171) J. M. M. Millet, H. Roussel, A. Pigamo, J. L. Dubois, J. C. Jumas, Characterization of tellurium in MoVTeNbO catalysts for propane oxidation or ammoxidation, Appl. Catal. A: Gen., 232 (2002) 77-92.

172) E. García-González, J. M. López Nieto, P. Botella, J. M. González-Calbet, On the Nature and Structure of a New MoVTeO Crystalline Phase, Chem. Mater. 14 (2002) 4416-4421.

173) P. Botella, E. García-González, J.M. López Nieto, J.M. González-Calbet, MoVTeNbO multifunctional catalysts: Correlation between constituent crystalline phases and catalytic performance, Solid State Sci. 7 (2005) 507–519.

174) S. Knobl, G. A. Zenkovets, G. N. Kryukova, O. Ovsitser, D. Niemeyer, R. Schlögl, G. Mestl, The synthesis and structure of a single-phase, nanocrystalline MoVW mixed-oxide catalyst of the Mo5O14 type, J. Catal., 215 (2) (2003) 177-187.

175) P. DeSanto, D. J. Buttrey, R. K. Grasselli, C. G. Lugmair, A. F. Volpe, B. H. Toby, T. Vogt, Structural Characterization of the Orthorhombic Phase M1 in MoVNbTeO Propane Ammoxidation Catalyst, Top. Catal., 23 (2003) 23-38.

176) D. Vitry, Y. Morikawa, J. L. Dubois, W. Ueda, Mo-V-Te-(Nb)-O mixed metal oxides prepared by hydrothermal synthesis for catalytic selective oxidations of propane and propene to acrylic acid, Appl. Catal. A-Gen., 251 (2003) 411-424.

177) A. Celaya Sanfiz, T.W. Hansen, A. Sakthivel, A. Trunschke, R. Schlögl, A. Knoester, H.H. Brongersm, M.H. Looi, S.B.A. Hamid, How important is the (001) plane of M1 for selective oxidation of propane to acrylic acid?, J. Catal. 258 (2008) 35–43.

178) D. Melzer, G. Mestl, Kl. Wanninger, Y. Zhu, N.D. Browning, M. Sanchez-Sanchez, J.A. Lercher, Design and synthesis of highly active MoVTeNb-oxides for ethane oxidative dehydrogenation, Nature Commun. 10 (2019) 4012.

179) **a)** Y. Zhu, P. V. Sushko, D. Melzer, E. Jensen, L. Kovarik, C. Ophus, M. Sanchez-Sanchez, J. A. Lercher, N. D. Browning, Formation of Oxygen Radical Sites on MoVNbTeOx by Cooperative Electron Redistribution, J. Am. Chem. Soc. 2017, 139, 12342−12345; **b)** D. Melzer, G. Mestl, Kl. Wanninger, A. Jentys, M. Sanchez-Sanchez, J.A. Lercher, Top. Catal. 63 (2020) 1754–1764.

180) H. Tsuji, Y. Koyasu, Synthesis of MoVNbTe(Sb)Ox Composite Oxide Catalysts via Reduction of Polyoxometalates in an Aqueous Medium, J. Am. Chem. Soc. 124 (2002) 5608-5609.

181) J. M. Oliver, J. M. López Nieto, P. Botelal, A. Mifsud, The effect of pH on structural and catalytic properties of MoVTeNbO catalysts, Appl. Catal. A: Gen. 2004, 257, 67–76.

182) P. Beato, A. Blume, F. Girgsdies, R.E. Jentoft, R. Schlogl, O. Timpe, A. Trunschke, G. Weinberg, Q. Basher, F.A. Hamid, S.B.A. Hamid, E. Omar, L. Mohd Salim, Analysis of structural transformations during the synthesis of a MoVTeNb mixed oxide catalyst, Appl. Catal A: Gen. 307 (2006) 137–147.

183) A. Massó, A. de Arriba, F. Ivars-Barceló, A. Ykrelef, B Solsona, José M. López Nieto, Upgrading the reflux method as novel route for competitive catalysts in alkane selective oxidation Catal. Sci. Technol.13 (2023) 4802-4812.

184) **a)** T.M.N. Le, R. Checa, P. Bargiela, M. Aouine, J.M.M. Millet, New synthesis of pure orthorhombic Mo-V-A oxide phases, where A = Sb, Bi and Pb, and testing for the oxidation of light alkanes, Journal of Alloys and Compounds 910 (2022) 164745; **b)** Thi M.N. Le, M. Aouine, J.-M. M. Millet, Effect of Introducing Thallium in Microporous Vanado-molybdate with Orthorhombic or Trigonal

Structures and Catalytic Properties, J. Phys. Chem. C 16 (2022) 19647−19659.

185) **a)** Y. V. Kolen'ko, W. Zhang, R. N. d'Alnoncourt, F. Girgsdies, T. W. Hansen, T. Wolfram, R. Schlögl and A. Trunschke, Synthesis of MoVTeNb Oxide Catalysts with Tunable Particle Dimensions, ChemCatChem, 2011, 3, 1597–1606; **b)** Y. V. Kolen'ko, K. Amakawa, R. N. d'Alnoncourt, F. Girgsdies, G. Weinberg, R. Schlögl and A. Trunschke, Unusual Phase Evolution in MoVTeNb Oxide Catalysts Prepared by a Novel Acrylamide-Gelation Route, ChemCatChem, 2012, 4, 495–503.

186) **a)** B. Deniau, G. Bergeret, B. Jouguet, J.L. Dubois, J.M.M. Millet, Preparation of Single M1 Phase MoVTe(Sb)NbO Catalyst: Study of the Effect of M2 Phase Dissolution on the Structure and Catalytic Properties, Top. Catal. 50 (2008) 33–42; **b**) Th. Th. Nguyen, B. Deniau, M. Baca, J.-M. M. Millet, Influence of Nb Content on the Structure, Cationic and Valence Distribution and Catalytic Properties of MoVTe(Sb)NbO M1 Phase Used as Catalysts for the Oxidation of Light Alkanes, Top. Catal. 59 (2016) 1496–1505.

187) **a)** B. Chu, L. Truter, T.A. Nijhuis, Y. Cheng, Performance of phase-pure M1 $MoVNbTeO_x$ catalysts by hydrothermal synthesis with different post-treatments for the oxidative dehydrogenation of ethane, Appl. Catal. Gen. 498 (2015) 99–106; **b)** B. Chu, H. An, X. Chen, Y. Cheng, Phase-pure M1 MoVNbTeOx catalysts with tunable particle size for oxidative dehydrogenation of ethane, Appl. Catal. A-Gen. 524 (2016) 56–65.

188) M. Baca, M. Aouine, J. Dubois, J. Millet, Synergetic effect between phases in MoVTe (Sb) NbO catalysts used for the oxidation of propane into acrylic acid, J. Catal. 233 (2005) 234–241.

189) **a)** Y. Chen, B. Yan, Y. Cheng, Microporous exposure on catalytic performance of MoVNbTeOx mixed metal oxides in the oxidative dehydrogenation of ethane, J. Catal. 426 (2023) 308–318; **b)** Y. Chen, S. Qian, K. Feng, Z. Li, B. Yan, Y. Cheng, Determination of highly active and selective surface for ther oxidative dehydrogenation of ethane over phase-pure M1 $MoVNbTeO_x$ catalyst, J. Catal. 416 (2022) 277-288.

190) E.V. Shchenko, R.V. Gulyaev, T.Yu. Kardash, A.V. Ishchenko, E. Yu. Gerasimov, V.I. Sobolev, V.M. Bondareva, Effect of Bi on catalytic performance and stability of MoVTeNbO catalysts in oxidative dehydrogenation of ethane, Appl. Catal. Gen. 534 (2017) 58–69.

191) **a)** G.A. Zenkovets, A.A. Shutilov, V.M. Bondareva, V.I. Sobolev, A.S. Marchuk, S.V. Tsybulya, I. P. Prosvirin, A.V. Ishchenko, V.Yu. Gavrilov, New Multicomponent MoVSbNbCeOx/SiO2 Catalyst with Enhanced Catalytic Activity for Oxidative Dehydrogenation of Ethane to Ethylene, ChemCatChem 12 (2020) 4149–4159**; b)** 198) Y. S. Yun, M. Lee, J. Sung, D. Yun, T.Y. Kim, H. Park, K. R. Lee, Ch. K. Song, Y. Kim, J. Lee, Y.-J. Seo, I. K. Song, J. Yi, Promoting effect of cerium on MoVTeNb mixed oxide catalyst for oxidative dehydrogenation of ethane to ethylene, Appl. Catal. B Environ. 237 (2018) 554-562.

192) Ch. Xin, D. Dang, A. Hang, Ch. Bozhao, Ch. Yi, MnOx promoted phase-pure M1 MoVNbTe oxide for ethane oxidative dehydrogenation, J. Taiwan Inst. Chem Eng. 95 (2019) 103-111.

193) E.V. Lazareva, V.M. Bondareva, D.A. Svintsitskiy, A.V. Ishchenko, A.S. Marchuk, E.P. Kovalev, T.Yu. Kardash, Oxidative dehydrogenation of ethane over M1 MoVNbTeO catalysts modified by the addition of Nd, Mn, Ga or Ge, Catal. Today 361 (2021) 50-56.

194) **a)** B. Solsona, M.I. Vázquez, F. Ivars, A. Dejoz, P. Concepción, J.M. López Nieto, Selective oxidation of propane and ethane on diluted Mo–V–Nb–Te mixed-oxide catalysts, J. Catal. 252 (2007) 271–280; **b)** T. T. Nguyen, M. Aouine, J. M. M. Millet, Opitimizing the efficiency of MoVTeNbO catalysts for ethane oxidative dehydrogenation to ethylene, Catal. Commun. 21 (2012) 22-26; **c)** B. Chu, H. An, T. A. Nijhuis, J. C. Schouten, Y. Cheng, A self-redox pure-phase M1 MoVNbTeOx/CeO_2 nanocomposite as a highly active catalyst for oxidative dehydrogenation of ethane, J. Catal. 329 (2015) 471-478.

195) D. Dang, X. Chen, B. Yan, Y. Li, Y. Cheng, Catalytic performance of phase-pure M1 MoVNbTeOx/CeO2 composite for oxidative dehydrogenation of ethane, J. Catal. 365 (2018) 238–248.

196) **a)** Y. Chen, D. Dang, B. Yang, Y. Cheng, Mixed Metal Oxides of M1 MoVNbTeOx and TiO_2 as Composite Catalyst for Oxidative Dehydrogenation of Ethane, Catalyst 12 (2022) 71; **b)** Y. Chen, D. Dang, B. Yang, Y. Cheng, Nanocomposite catalysts of non-purified

MoVNbTeOx with CeO_2 or TiO_2 for oxidative dehydrogenation of ethane, Chem. Eng. Sci. 264 (2022) 118154.

197) **a)** X. Chen, Q. Yang, B. Chu, H. An, Y. Cheng, Valence variation of phase-pure M1 MoVNbTe oxide by plasma treatment for improved catalytic performance in oxidative dehydrogenation of ethane, RSC Adv. 5 (2015) 91295-9130; **b)** Sh. Qian, Y. Chen, B. Yan, Y. Cheng, Plasma treated M1 $MoVNbTeO_x$–CeO_2 composite catalyst for improved performance of oxidative dehydrogenation of ethane, Green Energy Environm. 8 (2023) 904-914.

198) D. Vitry, Y. Morikawa, J. L. Dubois, W. Ueda, Propane selective oxidation over monophasic Mo–V–Te–O catalysts prepared by hydrothermal synthesis, Top. Catal. 23 (2003) 47-53.

199) P. Botella, A. Dejoz, M.C. Abello, M.I. Vázquez, L. Arrua, J.M. López Nieto, Selective oxidation of ethane: developing an orthorhombic phase in Mo–V–X (X = Nb, Sb, Te) mixed oxides, Catal. Today 142 (2009) 272–277.

200) M. Aouine, Th. Epicier, J.-M.M. Millet, In Situ Environmental STEM Study of the MoVTe Oxide M1 Phase Catalysts for Ethane Oxidative Dehydrogenation, ACS Catal. 6 (2016) 4775−4781.

201) P. Concepción, S. Hernández, J.M. López Nieto, On the nature of active sites in MoVTeO and MoVTeNbO catalysts: The influence of catalyst activation temperature, Appl. Catal. A: Gene. 391 (2011) 92–101.

202) J.M.M. Millet, M. Baca, A. Pigamo, D. Vitry, W. Ueda, J.L. Dubois, Study of the valence state and coordination of antimony in MoVSbO catalysts determined by XANES and EXAFS, Appl. Catal. A 244 (2003) 359.

203) T. Blasco, P. Botella, P. Concepción, J.M. López Nieto, A. Martínez-Arias, C. Prieto, Selective oxidation of propane to acrylic acid on K-doped MoVSbO catalysts: catalyst characterization and catalytic performance, J. Catal. 228 (2004) 362.

204) F. Ivars, B Solsona, E Rodríguez-Castellón, J. M. López Nieto, Selective propane oxidation over MoVSbO catalysts. On the preparation, characterization and catalytic behavior of M1 phase, J. Catal. 262 (2009) 35-43.

205) P. Botella, A. Dejoz, J.M. López Nieto, P. Concepción, M.I. Vázquez, Selective oxidative dehydrogenation of ethane over MoVSbO mixed oxide catalysts, Appl. Catal. A 298 (2006) 16–23.

206) F. Ivars, B Solsona, E Rodríguez-Castellón, J. M. López Nieto, Selective propane oxidation over MoVSbO catalysts. On the preparation, characterization and catalytic behavior of M1 phase, J. Catal. 262 (2009) 35-43.

207) M. Sadakane et al., Synthesis of Orthorhombic Mo-V-Sb Oxide Species by Assembly of Pentagonal Mo_6O_{21} Polyoxometalate Building Blocks, Angew. Che. Int. Ed. 48 (2009) 48, 1 – 5.

208) J. S. Valente, H. Armedariz-Herrera, R. Quintana-Solorzano, C Angeles-Chavez, A. Rodríguez-Hernandez, M L. Guzman-Castillo, J.M. López Nieto, T.M.N. Le, J.-M. M. Millet, Pathway to defective highly active and stable MoVSbOx catalysts for ethane oxidative dehydrogenation through a dislodging process involving controlled combustion of amino-organic compounds, J. Catal. 427 (2023) 115106.

209) J.S. Valente, J.M. López Nieto, H. Armendariz Herrera, A. Massó Ramírez, F. Ivars Barceló, M.L.A. Guzman Castillo, R. Quintana Solorzano, A. Rodríguez Hernandez, V. Paz del Angel, M. Flores Etel, Oxidative dehydrogenation of ethane to ethylene and preparation of multimetallic mixed oxide catalyst for such process, US Pat. 9409156 B2 (2016); assigned to PEMEX-IMP-UPV.

210) F. Ivars-Barceló, B. Solsona, E. Asedegbega-Nieto, J.M. López Nieto, Enhancement of ethylene production by alkali metal doping of MoVSb mixed oxide catalyst for ethane oxidative dehydrogenation, Appl. Catal. A, Gen 660 (2023) 119200.

211) F. Ivars, PhD Thesis, Universidad Politécnica de Valencia (2010).

212) **a)** T. Katou, D. Vitry, W. Ueda, Structure dependency of Mo-V-O-based complex oxide catalysts in the oxidations of hydrocarbons, Catal. Today 91-92 (2004) 237-240; **b)** W. Ueda, D. Vitry, T. Katou, Structural organization of catalytic functions in Mo-based oxides for propane selective oxidation, Catal. Today, 96 (2004) 235-240.

213) **a)** T. Konya, T. Katou, T. Murayama, S. Ishikawa, M. Sadakane, D. Buttrey, W. Ueda, An orthorhombic Mo_3VOx catalyst most active for

oxidative dehydrogenation of ethane among related complex metal oxides, Catal. Sci. Technol. 3 (2013) 380-387; **b)** Sh. Inukai, S. Ishikawa, T. Tanabe, Y. Jing, T. Toyao, K.-I. Shimizu, W, Ueda, Thermally Induced Transformation of Sb-Containing Trigonal Mo3VOx to Orthorhombic Mo3VOx and Its Effect on the Catalytic Ammoxidation of Propane, Chem. Mater. 32 (2020) 1506–1516.

214) **a)** S. Ishikawa, Zh. Zhang, W.Ueda, Unit Synthesis Approach for Creating High Dimensionally Structured Complex Metal Oxides as Catalysts for Selective Oxidations, ACS Catal. 8 (2018) 2935−2943; **b)** M. Sadakane et al., Molybdenum–Vanadium-Based Molecular Sieves with Microchannels of Seven-Membered Rings of Corner-Sharing Metal Oxide Octahedra, Angew. Chem. Int. Ed. 47 (2008) 2493 –2496.

215) **a)** S. Ishikawa, X. Yi, T. Murayama, W. Ueda, Heptagonal channel micropore of orthorhombic Mo_3VO_x as catalysis field for the selective oxidation of ethane, Appl. Catal. A-Gen. 474 (2014) 10-17; **b)** T. Konya, T. Katou, T. Murayama, S. Ishikawa, M. Sadakane, D. Buttrey, W. Ueda, An orthorhombic Mo_3VO_x catalyst most active for oxidative dehydrogenation of ethane among related complex metal oxides, Catal. Sci. Technol. 3 (2013) 380-387.

216) A. Trunschke, J. Noack, S. Trojanov, F. Girgsdies, Th. Lunkenbein, V. Pfeifer, M.l Hävecker, P. Kube, Ch. Sprung, F. Rosowski, R. Schlögl, The Impact of the Bulk Structure on Surface Dynamics of Complex Mo−V-based Oxide Catalysts, ACS Catal. 7 (2017) 3061−3071.

217) **a)** A. Kubas, J. Noak, A. Trunschke, R. Schlögl, F. Neese, D. Maganas, A combined experimental and theoretical spectroscopic protocol for determination of the structure of heterogeneous catalysts: developing the information content of the resonance Raman spectra of M1 MoVOx, Chem. Sci. 8 (2017) 6338-6353; **b)** Th. Lunkenbein, L. Masliuk, M. Plodinec, G. Algara-Siller, S. Jung, M. Jastak, P. Kube, A. Trunschke, R. Schlögl, Site specific and localized structural displacements in open structured multimetallic oxides, Nanoscale 12 (2020) 6759-6766.

218) **a)** L. Masliuk, M. Heggen, J. Noack, F. Girgsdies, A. Trunschke, K. E. Hermann, M. G. Willinger, R. Schlögl, Th. Lunkenbein, Structural Complexity in Heterogeneous Catalysis: Cataloging Local

Nanostructures, J. Phys. Chem. C 121 (2017) 24093−24103; **b)** Th. Lunkenbein, F. Girgsdies, A. Wernbacher, J. Noack, Gudrun Auffermann, A. Yasuhara, A. Klein-Hoffmann, W. Ueda, M. Eichelbaum, A. Trunschke, R.Schlögl, M.G. Willinge, Direct Imaging of Octahedral Distortion in a Complex Molybdenum Vanadium Mixed Oxide, Angew. Chem. Int. Ed. 54 (2015) 6828 –6831.

219) S. Ishikawa, D. Kobayashi, T. Konya, S. Ohmura, T. Murayama, N. Yasuda, M. Sadakane, W. Ueda, Redox treatment of orthorhombic $Mo_{29}V_{11}O_{112}$ and relationships between crystal structure, microporosity and catalytic performance for selective oxidation of ethane. J. Phys. Chem. C 119 (2015) 7195−7206.

220) M.Sadakane, K. Kodato, N.Yasuda, S. Ishikawa, W. Ueda, Thermal Behavior, Crystal Structure, and Solid-State Transformation of Orthorhombic Mo−V Oxide under Nitrogen Flow or in Air, ACS Omega 4 (2019) 13165−13171.

221) J. S. Valente, H. Armendáriz-Herrera, R. Quintana-Solórzano, P. Del Ángel, N. Nava, A. Massó, J. M. López Nieto, Chemical, Structural, and Morphological Changes of a MoVTeNb Catalyst during Oxidative Dehydrogenation of Ethane, ACS Catal. 4 (2014) 1292-1301.

222) M.M. Bashin, Is true ethane oxydehydrogenation feasible?, Top. Catal. 23 (2003) 145-149.

223) F. Cavani, N. Ballarini, S. Luciani, Oxidative dehydrogenation of ethane and propane: How far from commercial implementation?, Catal. Today 127 (2007) 113.

224) Z.-J. Zhao, Ch.-ch. Chiu, J. Gong, Molecular understandings on the activation of light hydrocarbons over heterogeneous catalysts, Chem. Sci., 6 (2015) 4403-4425.

225) Y. Wang, P. Hu, J. Yang, Y.-A. Zhu, D. Chen, C–H bond activation in light alkanes: a theoretical perspective, Chem. Soc. Rev. 50 (2021) 4299-4358.

226) A. Alamdari, R. Karimzadeh, S. Abbasizadeh, Present state of the art of and outlook on oxidative dehydrogenation of ethane: catalysts and mechanisms, Rev. Chem. Eng., 37 (2019) 1-52.

227) Y.Chen , B. Yan, Y. Cheng, State-of-the-Art Review of Oxidative Dehydrogenation of Ethane to Ethylene over MoVNbTeOx Catalysts, Catalysts 13 (2023) 204.

228) A.M. Gaffney, J.W. Sims, V.J. Martin, N.V. Duprez, K.J. Louthan, K.L. Roberts, Evaluation and analysis of ethylene production using oxidative dehydrogenation, Catal. Today 369 (2021) 203–209.

229) G.J. Maffia, A.M. Gaffney, O.M. Mason, Techno-economic analysis of oxidative dehydrogenation options, Top. Catal. 59 (2016) 1573–1579.

230) **a)** J. Dou, J. Funderburg, F. Li et al., $Ce_xZr_{1-x}O_2$-supported CrO_x catalyts for CO_2-assisted oxidative dehydrogenation of propane-probing the active sites and strategies for enhanced stability, ACS Catal. 13 (2023) 213-223; **b)** Y. Zhou, J. Lin, S. Lin, X. Wang, Sulfate-modified NiAl mixed oxides as effective C-H bond-breaking agents for the sole production of ethylene from ethane, ACS Catal. 10 (2020) 7619-7629; **c)** X. Wang, Y. Wang, B. Robinson, Q. Wang, J. Hu, Ethane oxidative dehydrogenation by CO_2 over stable $CsRu/CeO_2$, J. Catal. 413 (2022) 138-149.

231) **a)** T. Blasco, A. Galli, J. M. López Nieto, F. Trifiró, Oxidative Dehydrogenation of Ethane and n-Butane on VOx/Al_2O_3 Catalysts, J. Catal. 169 (1997) 203-211; **b)** J. M. Lopez Nieto, J. Soler, P. Concepción, J. Herguido, M. Menendez, J. Santamaría, Oxidative Dehydrogenation of Alkanes over V-based Catalysts: Influence of Redox Properties on Catalytic Performance, J. Catal. 185 (1999) 324-332.

232) E. Heracleous, A. F. Lee, K. Wilson, A. Lemonidou, Investigation of Ni-based alumina-supported catalysts for the oxidative dehydrogenation of ethane to ethylene-effect of promoting metal Me, J. Catal. 270 (2010) 67-75.

233) B. Solsona, P. Concepción, B. Demicol, S. Hernández, J. J. Delgado, J. J. Calvino, J. M. López Nieto, Selective oxidative dehydrogenation of ethane over SnO_2-promoted NiO catalysts, J. Catal. 295 (2012) 104-114.

234) P. Botella, E. García-González, A. Dejoz, J.M. López Nieto, M.I. Vázquez, J. González-Calbet, Selective oxidative dehydrogenation of

ethane on MoVTeNbO mixed metal oxide catalysts, J. Catal. 225 (2004) 428-438.

235) **a)** E. M. Thorsteinson, T. O. Wilson, F. G. Young, P. H. Kasai, The oxidative dehydrogenation of ethane over catalysts containing mixed oxides of molybdenum and vanadium, J. Catal. 52 (1978) 116-132; **b)** E. M. Thorsteinson, T. O. Wilson, F. G. Young, P. H. Kasai, US Patent 4,250,236 (1981) assigned to Union Carbide.

236) J. H. McCain, W. V. Charleston, Process for oxydehydrogenation of ethane to ethylene, U. S. Patent No. 4524236 (1985).

237) W. Ueda, K. Oshihara, Selective oxidation of light alkanes over hydrothermally synthesized Mo-V-M-O (M=Al, Ga, Bi, Sb, and Te) oxide catalysts, Appl. Catal. A: Gen 200 (2000) 135-143.

238) H. Zhisan, Y. Xiaodong, X. Qi, L. Rongchun, L. Hong, H. Yiming, C. Luqian, W. Weizheng, W. Huilin, Oxidative dehydrogenation of ethane over MoVTeNbO catalyst prepared by a slurry method, Chinese J. Catal. 26 (2005) 441 – 442.

239) J.M. López Nieto, P. Botella, P. Concepción, A. Dejoz, M.I. Vázquez, Catal. Today 91–92 (2004) 241–245.

240) E. Sadovskaya, V. Goncharov, G. Popova, E. Ishchenko, D. Frolov, A. Fedorova, T. Andrushkevich, Mo-V-Te-Nb oxide catalysts: reactivity of different oxygen species in partial and deep oxidation, J. Mol. Catal. A. Chem. 392 (2014) 61-66.

241) D. Melzer, P. Xu, D. Hartmann, Y. Zhu, N. D. Browning, M. Sánchez-Sánchez, J. A. Lercher, Atomic-scale determination of active facets on the MoVTeNb oxide M1 phase and their intrinsic catalytic activity for ethane oxidative dehydrogenation, Angew. Chem. Int. Ed. 55 (2016) 8873-8877.

242) R. Schlögl, Active sites for propane oxidation: some generic considerations, Top. Catal. 54 (2011) 627-638.

243) M. Hävecker, S. Wrabetz, J. Kröhnert, L.-L. Csepei, P. Naumann d'Alnoncourt, Y. V. Kolen'ko, F. Girgsdies, R. Schlögl, A. Trunschke, Surface chemistry of phase-pure M1 MoVTeNb oxide during operation in selective oxidation of propane to acrylic acid, J. Catal. 285 (2012) 48-60.

244) L. Annamalai, Y. Liu, S. Ezenwa, Y. Dang, S. L. Suib, P. Deshlahra, Influence of tight confinement on selective oxidative dehydrogenation of ethane on MoVTeNb mixed oxides, ACS Catal. 8 (2018) 7051-7067.

245) **a)** L. Annamalai, S. Ezenwa, Y. Dang, H. Tan, S. L. Suib, P. Deshlahra, Comparison of structural and catalytic properties of monometallic Mo and V oxides and M1 phase mixed oxides for oxidative dehydrogenation, Catalysis Today 368 (2021) 28–45; **b)** Y. Liu, L. Annamalai, P. Deshlahra, Effects of Lattice O Atom Coordination and Pore Confinement on Selectivity Limitations for Ethane Oxidative Dehydrogenation Catalyzed by Vanadium-Oxo Species, J. Phys. Chem. C 123 (2019) 28168−28191.

246) J. Chen, Z. Sun, V. Balakotaiah, P. Bollini, A global kinetic model for the oxidative dehydrogenation of ethane over mixed metal oxide catalysts at supra-ambient pressures, Chem. Eng. J. 445 (2022) 136605.

247) J. S. Valente, R. Quintana-Solórzano, H. Armendáriz-Herrera, G. Barragán-Rodríguez, J. M. López Nieto, Kinetic Study of Oxidative Dehydrogenation of Ethane over MoVTeNb Mixed-Oxide Catalyst, Ind. Eng. Chem. Res. 2014, 53, 1775−1786.

248) **a)** R. Quintana-Solórzano, G. Barragán-Rodríguez, H. Armendáriz-Herrera, J. M. López Nieto, J. S. Valente, Understanding the kinetic behavior of a Mo-V-Te-Nb mixed oxide in the oxydehydrogenation of ethane, Fuel 138 (2014) 15-26; **b)** G. Che-Galicia, R. Quintana-Solórzano, R. S. Ruíz-Martínez, J. S. Valente, C. O. Castillo-Araiza, Kinetic modeling of the oxidative dehydrogenation of ethane to ethylene over a MoVTeNb catalytic system, Chem. Eng. J. 252 (2014) 75-88.

249) Y. Chen, S. Qian, K. Feng, Y. Wang, B. Yan, Y. Cheng, $MoVTeNb_x$ M1@CeO_2@Cordierite structured catalysts for ODHE process, Chem. Eng. Sci. 253 (2022) 117597.

250) P. Yan, Y. Chen, Y. Cheng, Industrially potential MoVTeNbx@FoamSiC structured catalyst for oxidative dehydrogenation of ethane, Chem. Eng. J. 427 (2022) 131813.

251) J. Chen, P. Bollini, V. Balakotaiah, Oxidative dehydrogenation of ethane over mixed metal oxide catalysts: autothermal or cooled tubular reactor design?, AlChE J. 67 (2021) e17168.

252) A. Fazlinezhad, A. Naeimi, E. Yasari, Theoretical investigation of ethane oxidative dehydrogenation over MoVTeNbO catalyst in fixed-bed reactors with intermediate water removal, Chem. Eng. Res. Des. 146 (2019) 427-435.

253) B. Chu, L. Truter, T. A. Nijhuis, Y. Cheng, Oxidative dehydrogenation of ethane to ethylene over phase-pure M1 $MoVNbTeO_x$ catalysts in a micro-channel reactor, Catal. Sci. Technol. 5 (2015) 2807-2813.

254) I. I. Mishanin, V. I. Bogdan, Advantages of ethane oxidative dehydrogenation on the MoVNbTeOx catalyst under elevated pressure, Mendeleev Commun.29 (2019) 455–457.

255) G. Luongo, F. Donat, A. H. Bork, E. Willinger, A. Landuyt, C. R. Müller, Highly selective oxidative dehydrogenation of ethane to ethylene via chemical looping with oxygen uncoupling through structural engineering of the oxygen carrier, Adv. Energy Mater. 12 (2022) 2200405.

256) https://www.clariant.com/en/Corporate/News/2021/10/Clariant-unveils- groundbreaking-catalysts-developed-jointly-with-Linde-Engineering-for-novel-ethylen

257)https://www.icis.com/explore/resources/news/2021/10/05/10691746/clariant-odh-catalysts-enabling-low-carbon-ethylene-production-expected-to-be-in-use-by-2024-2025-execs/

Chapter 2

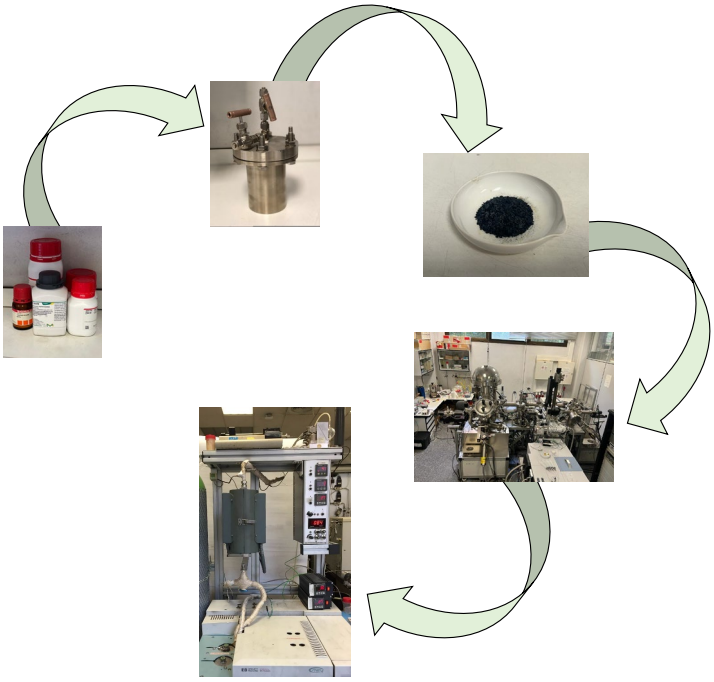

Experimental section

2.1. Preparation of catalysts

The synthesis of the catalysts prepared throughout the present thesis has been carried out by three different synthetic routes: hydrothermal (multicomponent MoV-based mixed oxides), evaporation (tin-doped nickel oxide) and wet impregnation (supported vanadium oxide).

Accordingly, MoV-based mixed oxides have been prepared employing the hydrothermal method, from aqueous solutions of the metallic precursors. On the contrary, tin-doped nickel oxide catalyst was synthesized by evaporation of nickel and tin salts. Finally, a supported vanadium oxide catalyst was prepared by wet impregnation of the vanadium precursor onto a proper support. A deep explanation of the synthetic methods is explained in the following sections:

2.1.1. Materials

For M1-presenting MoV-based mixed oxide catalysts, the chemical precursors used in the synthesis are: **ammonium heptamolybdate hydrate** ($(NH_4)_6Mo_7O_{24}\cdot 4H_2O$, Merck, 99%), **vanadyl sulfate hydrate** ($VOSO_4\cdot xH_2O$, Sigma-Aldrich, 97%), **tellurium dioxide** (TeO_2, Sigma-Aldrich, 99%), **telluric acid** (H_6TeO_6, Sigma-Aldrich, 98%), **ammonium niobate(V) oxalate hydrate** ($C_4H_4NNbO_9\cdot xH_2O$, Sigma-Aldrich, 99.99% trace metal basis), **aqueous ammonium hydroxide** (NH_4OH, Panreac, 25%) and **nitric acid** (HNO_3, Panreac, 69%).

Conversely, in the case of tin-doped nickel oxide, the precursors used in the synthesis were **nickel(II) nitrate hexahydrate** ($Ni(NO_3)_2\cdot 6H_2O$, Sigma-

Aldrich, 99.99% trace metal basis), **tin(II) oxalate** (SnC_2O_4, Sigma-Aldrich, 98%) and **oxalic acid** (HO_2CCO_2H, Sigma-Aldrich, 98%).

Finally, regarding the synthesis of alumina-supported vanadium oxide, the compounds used were **ammonium metavanadate** (NH_4VO_3, Sigma-Aldrich, 99.5%) and **alumina** (γ-Al_2O_3, ABCR, 97%).

2.1.2. Hydrothermal synthesis of M1-presenting Mo-V-(Te)-(Nb)-O catalysts

The synthesis of MoV-derived mixed metal oxides presenting the orthorhombic structure known as M1 has been carried out by using the hydrothermal method [1-11]. This method, widely used in a great amount of both inorganic and material science situations, consist of the production of heterogenous chemical reactions in an aqueous media derived from relatively high temperatures and partial pressures. Then, the employment of the hydrothermal method allows to synthesize powder materials with a high degree of chemical purity since different ions or pH adjusting agents are commonly removed from the reaction media together with the crystallization solution. Furthermore, the synergy existing between the high temperature and pressure leads to a one-step process that disables post-treatment issues.

Consequently, M1 presenting mixed oxides in the form of bi-, tri- and tetrametallic oxides were synthesized via this method. Our synthesis consisted of an aqueous solution of the desired metallic precursors. Then, these aqueous solutions are transferred into a Teflon vessel, that is

subsequently put into a stainless-steel autoclave (**Fig. 2.1-A**), which is modified with a set of valves that enable the control of the atmosphere within the autoclave. Once the autoclave is properly sealed, it was maintained in a static furnace at 175 ºC for 72 hours. After that time, the autoclave is suddenly cooled to room temperature and the resulting solid was filtrated under vacuum conditions (**Fig. 2.1-B**), subsequently washed with a proper amount of distilled water, and dried for 16 h in a 100ºC furnace. Obtained solids have been purified either with an aqueous oxalic acid solution or with diluted hydrogen peroxide. Lastly, the materials were thermally activated at 400, 500 or 600 ºC for 2 h under N_2 flow (ca. 15 mL min^{-1} g_{cat}^{-1}).

Figure 2.1. Stainless-steel autoclave employed for variable atmosphere hydrothermal synthesis (**A**) and synthesis mixture after hydrothermal treatment under vacuum filtration (**B**).

Then, in the case of bimetallic M1-MoVO oxides (chemical composition of $Mo_1V_{0.37}O_x$), a certain amount of ammonium heptamolybdate hydrate and vanadyl sulfate were separately dissolved in milliQ water. The resulting

solution mixture was transferred to the Teflon coated by a stainless-steel autoclave where it was purged with an N_2 flux for 10 minutes and sealed (inner N_2 pressure of 1 bar). After that, filtrated and dried solids were thermally activated. Accordingly, synthesis time and different parameters such atmosphere, pH, purification method and activation temperature were varied in order to optimize the presence of the orthorhombic M1 phase, detailed results are explained throughout **Chapter 3**.

Additionally, trimetallic catalysts studied in **Chapter 4** ($Mo_1V_{0.37}Te_yO_x$, where y = 0.01-0.17), were also prepared adapting this method. In this case, an aqueous solution of ammonium heptamolydate hydrate was heated at 80 ºC, then, the specific amount of tellurium dioxide required for each composition was added to that solution. After 10 minutes of stirring, the solution of vanadyl sulfate was poured into the former, and 10 minutes later the synthesis gel was cooled down to room temperature under stirring. Likewise, the final mixture was transferred to a Teflon vessel, and this one into the stainless-steel autoclave. Synthesis time and temperature were set to 72 h and 175 ºC, respectively. Filtered solids were purified before thermal activation (N_2 flux of 15 mL min^{-1} g_{cat}^{-1}, at 400 or 600 ºC for 2 h) with a hydrogen peroxide solution (15 wt%, with a relationship of 15 $mL_{H2O2}/1\ g_{cat}$) for 2 h, drying overnight after filtering and washing with distilled water (2 x 500 mL).

Finally, quaternary $Mo_1V_{0.25}Te_{0.17}Nb_{0.17}O_x$ M1 phase catalysts were prepared from aqueous solutions of the metallic precursors above mentioned, including ammonium niobate(V) oxalate hydrate as niobium source, mixed upon stirring in a silica bath at 80 ºC. Cooled synthesis gel

was autoclaved under inert atmosphere (N_2) at 175 ºC for 48 h and thermally activated (N_2 flux of 15 mL min^{-1} g_{cat}^{-1}) afterwards at 400 ºC (see **Chapter 5**) or 600 ºC (see **Chapters 5** and **6**).

2.1.3. Synthesis of metal promoted nickel oxide

Tin-promoted nickel oxide catalyst was prepared by evaporation of an ethanolic solution of the metallic precursors [12-15]. In this sense, a proper amount nickel nitrate was dissolved into ethanol. To that solution, oxalic acid (in an oxalic acid / nickel molar ratio of 1.3) and tin oxalate, with a Ni/(Ni+Sn) molar ratio of 0.08 were added (**Fig. 2.2**), and the gel was evaporated upon stirring at 60 ºC into a silica bath. The solid was dried overnight at 120 ºC in a furnace, subsequently calcined at 500 ºC for 2 h in static air.

Figure 2.2. Evaporation solution of nickel nitrate, oxalic acid and tin oxalate into a silica bath at 60 ºC.

2.1.4. Synthesis of supported vanadium oxide catalyst

A supported vanadium oxide catalyst was prepared by wet impregnation [16-20]. Initially, an aqueous solution of the vanadium precursor (vanadium metavanadate) was adjusted to pH= 7 with diluted nitric acid. To that solution, γ-Al_2O_3 (S_{BET}= 188 $m^2 g^{-1}$) was added and then the mixture was rotary evaporated to dryness. Dried solid was calcined later in static air for 6 h at 550ºC. In our case, the final catalyst presented a metal content of ca. 5 wt% of V atoms.

2.2. Physicochemical characterization of catalysts

All the catalysts synthesized within the present thesis have been further characterized by several physicochemical techniques. Therefore, in the following sections, the main physical principles of each technique are briefly summarized and explained.

2.2.1. Powder X-Ray diffraction

Powder X-Ray diffractogram (XRD) has been a key non-destructive technique in the identification of the crystalline phases present in the materials prepared. These XRD analyses were performed in a PANalytical CUBIX X'pert PRO diffractometer, equipped with a graphite monochromator, with measures taking place in Bragg-Bretano geometry. Additionally, the radiation employed was CuKα (λ= 0.1542 mm) working at 45 kV and 4 mA.

An X-Ray diffractogram is based on the elastic scattering of of X-ray photons by atoms periodically arranged in a lattice [21], then, a constructive interference occur between the incident beam and the scattered one that satisfy the Bragg's Law (**Equation 2.1**)

$$n\,\lambda = 2\,d_{hkl}\,sin\,\theta \qquad \textbf{Eq. 2.1.}$$

in a way represented in **Fig. 2.3**.

In this case, n in an integer of the wavelength (λ) of the radiation, while d_{hkl} is the interplanar distance of the planes with h, k and l Miller indices (set of numbers that univocally describe a crystallographic plane), and θ is the diffraction angle.

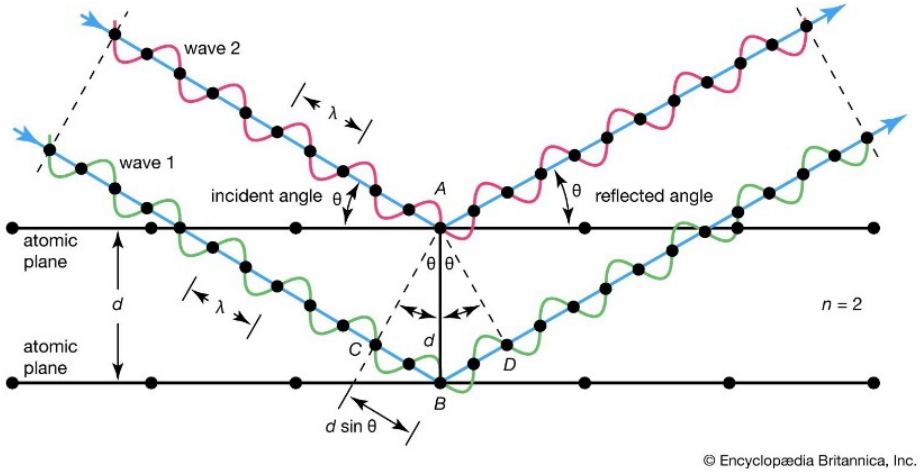

Figure 2.3. Graphical scheme of the diffraction phenomena (extracted from [22]).

Therefore, each crystallographic structure will present its unique diffractogram pattern that will be used throughout the present thesis to elucidate the success on the synthesis of the different catalysts. Moreover, this technique can be also used to determine the average particle size of the catalysts by employing the Scherrer's equation (**Eq. 2.2**),

$$D = \frac{\lambda}{\beta cos\theta} \qquad \textbf{Eq. 2.2}$$

in which the mean particle size (D) is calculated by the relationship of the wavelength of the radiation (λ) and the line broadening at half maximum intensity (β), considering the instrumental broadening particular of each apparatus, of a specific diffraction angle (θ).

2.2.2. Raman spectroscopy

Further characterization of the catalysts was performed by Raman spectroscopy, in which metal-oxygen bonds were studied. In this case, Raman spectra were recorded in an 'in via' Renishaw spectrometer equipped with an Olympus microscope. Typically, samples are excited with a 514.5 nm line Ar^+ laser (Spectra Physics Model 171, laser power of 2.5 mW), however, when comparing catalysts that contain nickel atoms (see **Chapter 6**), the use of the 325 nm wavelength (using a Renishaw HPNIR devise, laser power of 15 mW) is also considered.

The fundamentals of Raman spectroscopy lie on the inelastic scattering of a liquid/solid irradiated by light. Then, when a sample is irradiated by a

monochromatic source (514.5 or 325 nm), most of the photons will undergo elastic scattering, this is, molecules will be vibrationally excited with a subsequent fall to the ground state with no change in the wavelength (effect known as Rayleigh scattering). Nevertheless, when photons do not decay to the ground state, they present an effective exchange in energy leaving the sample with lower energy (decay from an excited state to the also excited first vibrational level, Stokes band) or higher energy (interaction of the photon with a vibrationally excited molecule that is further excited to an unstable energy level, anti-Stokes band). However, Raman spectroscopy only detects vibrational modes in which a change in the polarizability occur (change in shape) [23, 24]. In contrast, due to the lower intensity of inelastic scattering compared to the elastic one and also the possible fluorescence phenomena, Raman spectroscopy can be considered as a complementary technique to FTIR.

2.2.3. Fourier-transform infrared spectroscopy (FTIR)

FTIR spectra were collected using a Nicolet 205xB spectrophotometer, with measures taking place at room temperature in the 400-4000 cm^{-1} region, a spectral resolution of 1 cm^{-1} and 128 accumulations per scan. Samples have been mixed, milled, and pressed into pellets with KBr (spectroscopic grade) prior to the analysis.

Unlike Raman spectroscopy, FTIR spectroscopy is based on the absorption of photons, derived from the transitions in vibrational/rotational levels that produce a change in the dipolar moment, being the intensity of the FTIR related to the magnitude of the change in the dipolar moment.

In the present thesis, despite 4000-3000 cm^{-1} and 1700-1300 cm^{-1} regions are associated to the presence of O/N-H stretching (the former) and bending (the latter) vibrations, most of the analyses have been focalized in the 1100-500 cm^{-1} region, in which metal-oxygen or metal-oxygen-metal vibrations ca be observed [25, 26].

2.2.4. N_2/CO_2 physisorption

Textural properties of the solids synthesized have been studied by N_2/CO_2 adsorption isotherms. Experimental analyses for both molecule isotherms were performed in a Micromeritics ASAP 2000 apparatus. Samples (250 mg) were degassed before adsorption under vacuum conditions.

In the case of N_2 adsorption isotherms, the experiment took place in the 0-1 relative pressure range (p/p_0) at 77 K, and surface areas of the catalysts were calculated first by using the Brunauer-Emmet-Teller method (BET), in its linear form of the equation (**Eq. 2.3**) to know the monolayer capacity:

$$\frac{1}{n[\left(\frac{p}{p_0}\right)-1]} = \frac{1}{n_m C} + \frac{p}{p_0}\frac{C-1}{n_m C} \qquad \textbf{Eq. 2.3}$$

There, n is the amount of absorbate while n_m is the monolayer capacity (note that BET model only applies for monolayer calculations), p/p_0 stands for the relative pressure and C is a constant that deals with absorbate-absorbent interactions. Once the value of the monolayer capacity is calculated, the surface area value is estimated by **Equation 2.4**, in which

N_A is the Avogadro constant and σ is the cross-sectional area of the Nitrogen molecule (ca. 0.162 nm^2):

$$S_{BET} = n_m N_A \sigma \qquad \textbf{Eq.2.4}$$

Moreover, micropore volume calculations were extracted from BET data by using the t-Plot statistical thickness method, with points between 5-8 Å used for the linear fit [27].

Conversely, for CO_2 adsorption isotherms (seen in **Chapter 4**), measures took place at 25 ºC and surface area estimations were calculated by the Dubinin-Astakhov method. This is so because of the fact that in highly microporous materials such as small pore zeolites or this type of mixed oxides, the physical concept of surface area may be distorted since adsorbent uptake is due to pore volume filling and not to monolayer adsorption [28]. Then, for microporous materials with heterogeneous distributions it is proposed the following equation (**Eq. 2.5**), Dubinin-Astakhov method:

$$W = W_0 \exp\left[-\left(\frac{-RT\ln\left(\frac{P}{P_0}\right)}{E}\right)^n\right] \qquad \textbf{Eq. 2.5}.$$

Where W is the weight adsorbed at a given P/P_0 and temperature, W_0 is the total adsorbed weight, E is the characteristic energy and n is a non-integer value (usually between 1 and 3). Besides, n and E values are calculated iteratively by non-linear fitting of the isotherm in the low relative pressure region.

2.2.5. Pulse chemisorption and temperature programmed desorption of ammonia (TPD-NH_3)

In order to study the acid properties of the catalysts synthesized along the present thesis, pulse chemisorption and successive TPD of ammonia tests were carried out.

Experimental set up consisted of a Micromeritics TPD/290 devise in where samples (ca. 100 mg) were pretreated at 300 ºC, under Ar flow, for one hour. Afterwards, samples were cooled down to 100 ºC and saturated with NH_3, being subsequently kept under Argon flow (at 100 ºC/15 min) to desorb the possible ammonia physically absorbed. Then, TPD-NH_3 analyses were performed in the 100-500 ºC temperature range, with a heating ramp of 10 ºC/min. Ammonia desorbed was online analyzed by both mass spectrometer and a thermal conductivity detector (TCD).

In this case, the TPD-NH_3 allow us to study the strength of the acid sites of a catalyst by measuring the amount of chemisorbed ammonia at a given temperature (expressed in $mmol_{NH3}$ desorbed per gram of catalyst), thus, the higher the temperature of desorption the higher the strength of the acid site.

Nevertheless, NH_3 is a hard base that can interact with both Lewis (electron pairs in the nitrogen atom) and Brönsted (accepting a proton from the surface) acid sites, therefore the distinction between these two types of acid sites cannot be ascertained employing this technique, and so, the use of infrared spectroscopy with different probe molecules is mandatory.

2.2.6. Fourier-transform infrared spectroscopy (FTIR) of adsorbed CO or NH_3 molecules

FTIR spectroscopy of adsorbed molecules was employed to characterize the different Lewis/Brönsted acid sites (see **Chapter 6**).

In the case of IR spectra of adsorbed NH_3, experiments were recorded with a Thermo "is50" spectrometer equipped with a DTGS detector, resolution of 4 cm^{-1}. The IR cell in where in situ treatments of both controlled atmosphere and temperature was homemade manufactured and connected to a vacuum system that allows gas dosing. Catalysts were pretreated at 250 ºC in an oxygen flow (10 mL min^{-1}) for 1.5 hours, followed by evacuation at 10^{-4} mbar for another hour (same temperature). Next, samples were cooled down to room temperature under vacuum conditions, and once the temperature is reached, NH_3 was dosed at increasing pressure (0.4-25 mbar) until saturation (followed by evacuation at 25 ºC). Then, temperature was raised up to 100 ºC under vacuum conditions and IR measurements were collected after each dosage and evacuation temperature.

Regarding IR spectra of adsorbed CO, experimental data was recorded at low temperature (-165 ºC) with a Bruker Vertex 70 spectrometer using the same detector (i.e., DTGS, resolution of 4 cm^{-1}) and IR cell as for IR-NH_3 experiments. Samples, that have been pressed into self-supported wafers, were pretreated (250 ºC, O_2 flow, 1.5 h) and evacuated (10^{-4} mbar, 1 h) before cooling at -165 ºC under dynamic vacuum. After that, CO was dosed at increasing pressure (0.4-8.5 mbar), with IR spectra recorded after each dosage.

In contrast to ammonia, CO is a soft base, highly polarizable, that interacts poorly with the surface of the sample, therefore the use of notably low temperatures is required. Moreover, the CO molecule is very sensitive to protic and aprotic acid sites, so Lewis acid sites in addition to its strength can be discriminated.

2.2.7. In situ Fourier-transform infrared spectroscopy (FTIR) of adsorbed C_2H_4 and coadsorbed O_2+C_2H_4

Further in situ IR experiments were also conducted, adsorbing in one case only ethylene and in the other case coadsorption of ethylene and oxygen. In both cases, the activation of the samples was identical to the ones used in the previous section. Afterwards, 43 mbar of ethylene (and 84 mbar of oxygen) were adsorbed at room temperature (25 ºC). Once the reactive/reactives was/were adsorbed, the IR cell was closed and temperatures increased to 100, 150, 200 and 250 ºC (maintaining the sample at each temperature for 30 minutes) at constant pressure. In this case, spectra were collected at each temperature on the pellet before and after cooling down.

2.2.8. Temperature-programmed reduction (TPR)

Since all the catalysts prepared are involved in partial oxidation reactions, studying their reducibility (redox behavior) is very interesting in order to understand the performance of the different materials.

Then, temperature programmed reduction with hydrogen (H_2-TPR) experiments were performed in a Micromeritics Autochem 2910 devised, attached to a TCD detector. For these experiments, ca. 50 mg of sample were exposed to a 10 % H_2 in Ar stream (50 mL min^{-1}) at increasing temperatures, up to 600 ºC, with a heating ramp of 10 ºC min^{-1}.

In these analyses, the different hydrogen uptake, along with the temperature at which it is consumed, can provide valuable information about the reducibility of V^{4+}/V^{5+} and Ni^{2+} species in the materials studied.

2.2.9. Thermogravimetric analysis (TG-DTA)

Thermogravimetric experiments were used to study the possible changes in the samples' weight when increasing the temperature under a given atmosphere (air, in our case). Analyses of both as-made and used catalysts were conducted to study the changes in the material during the thermal activation, in the case of as-made materials, since ammonia cations are usually filling the micropores of the structure, or the deposition of carbonous species, considering used catalysts.

Experimental set up for TG-DTA analyses consisted of a Mettler-Toledo thermobalance "TGA/SDTA 851" in where 10 mg of sample were heat-treated up to 700 ºC under synthetic air (50 mL min^{-1}), with a heating ramp of 10 ºC min^{-1}.

2.2.10. Scanning electron microscopy (SEM)

Crystal morphology was studied by SEM. Micrographs were taken in a field-emission ZEISS Ultra-55 electron microscope, at a working voltage of 2 kV, equipped with an Oxford LIK ISIS X-Ray detector to perform energy-dispersive X-Ray spectroscopy analyses (XEDS), devices from the Microscopy Service of the Polytechnical University of Valencia (UPV).

Figure 2.4. FESEM Microscope with attached focalized ion beam (FIB) located at the UPV.

Principles of this technique lie on the interaction of an electron beam with the solid sample, analyzing rather secondary (SE) or backscattered (BSE) electrons, however, a wide range of signals can be studied (**Fig. 2.5**) from the primary electron beam. SEM analyses detect SE or BSE, being the former the ones that result in a clearer imaging since secondary electrons are mainly emitted from the surface of the catalyst, in contrast to backscattered ones, that come from deeper layers of the sample. Nevertheless, BSE detector is sensitive to changes in the atomic number, then different compositional phases can be observed with this detector.

Image construction is based on contrast, consequently, orientation of the crystals plays a key role in the brightness of the image, i.e., zones pointing directly to the detector will appear brighter than zones that do not [29].

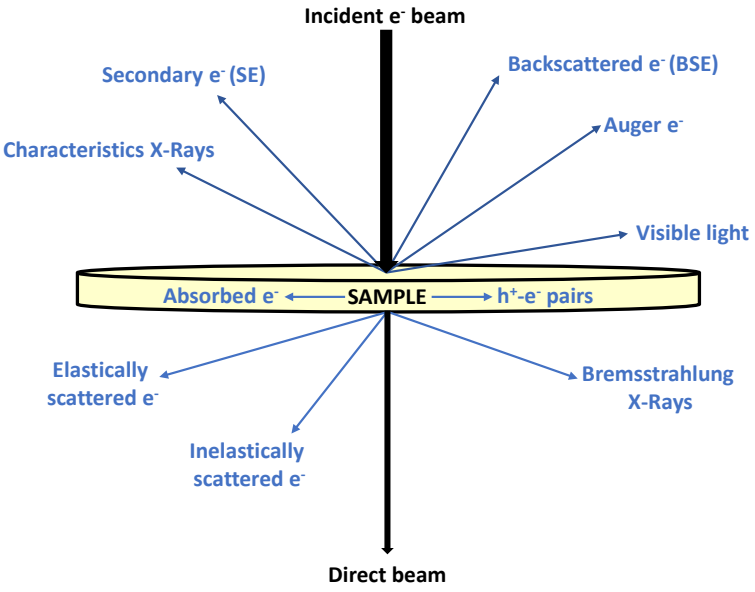

Figure 2.5. Types of signals generated from the electron beam to sample interaction.

2.2.11. Transmission electron microscopy (TEM)

Microstructural characterization was obtained by High Resolution Transmission Electron Microscopy (HRTEM) on a JEOL JEM300F electron microscope working at 300 kV, with a point resolution of 0.17nm, from the Complutense University of Madrid (UCM).

Preparation of samples for TEM micrographs consisted in supporting the solid into carbon coated copper grids that have been previously ultrasonically dispersed in n-butanol.

This technique is based on the detection of transmitted and dispersed electrons after the sample is hit by an electron beam (previously focalized whether in charge-couple device (CCD) or in a fluorescent film), as it can be seen above in **Fig 2.5**, to form the image. Nevertheless, the use of magnetic lenses to focalize the electrons lead to the appearance of aberrations in the micrographs, therefore an atomic resolution (< 1 Å) is only achieved by using aberration-corrected electron microscopes: based of Titan models (working up to 300 keV) with a Wien-filter type monochromator and aberration correctors in both illumination and condenser lens [30].

Moreover, it was also performed TEM analyses in the scanning-transmission mode (STEM) that, by rostering an electron beam along the sample, a compositional mapping along with high angle annular dark field mode (HAADF) can be obtained. In this mode, electrons scattered at angles higher than Bragg's diffraction form an image whose contrast is directly related to the number of electrons of the elements in the sample.

Lastly, analyses of selected area electron diffraction (SAED) were also performed. In this case, the interaction of the electrons (considered also as waves) with the sample can produce a diffraction pattern in the reciprocal space that, by analyzing the distribution and the distances of the pattern in the reciprocal space, it can provide information about space groups, defects of the crystallographic structure and its lattice parameters.

2.2.12. Energy-dispersive X-Ray spectroscopy (XEDS)

All the microscopes used in the present thesis are equipped with X-Ray detectors that have allow us to perform XEDS analyses. Spectra obtained by this technique were used to determine either the average chemical composition of catalysts studied in **Chapters 4**, **5** and **6** (acquiring spectra at low magnifications). Furthermore, a detailed crystal-by-crystal chemical analysis of materials presented in **Chapter 4** was performed by XEDS in the same microscope in where the TEM micrographs were acquired by attaching an Oxford ISIS 300 system with a LINK "Pentafet" detector (resolution of 135 eV).

Physical principles of XEDS are based on the inelastic interaction of an electron beam with the sample. Then, when the electron beam hits the sample, electrons of the core level are excited to an unoccupied electron state above the Fermi level (last occupied orbital) leaving a hole. Next, an electron of the outer shell may decay to fill the hole formed by the previously excited electron, thus emitting X-rays or Auger electrons (see **Fig. 2.5**) that, in any case, are element specific, therefore a quantification of the metal species can be obtained.

2.2.13. X-Ray photoelectron spectroscopy (XPS)

The X-Ray photoelectron spectroscopy (XPS) is a very specific technique that is based on the detection of photoelectrons emitted by a sample when it is irradiated with X-Rays (the well-known photoelectric effect [31]). The importance of XPS is that information about the oxidation state of the

atoms of the top few layers can be observed, so it has attracted a lot of attention in the Catalysis field.

Typically, in samples irradiated by an X-Ray source (Al K_α: 1486.6 eV or Mg K_α: 1253.6 eV are the most commonly used) a core-level electron is promoted to an electronic state over the Fermi level (E_F). Interestingly, the energy needed to promote one core electron of a given electronic state to the Fermi level is characteristic of each element, and this energy is called binding energy (E_b). Then, this binding energy can be calculated through the following equation (**Eq. 2.6**) by using the kinetic energy of the photoelectrons emitted. In this sense, the use of ultra-high vacuum conditions (10^{-9} mbar) is mandatory in order to not disturb the energy of the photoelectrons detected.

$$E_b = h\nu - E_k - \phi \qquad \textbf{Eq. 2.6}$$

In which E_b is the binding energy of the emitted electrons, $h\nu$ is the energy of the incident X-Rays, E_k is the kinetic energy of the emitted photoelectrons and ø is the work function of the XPS devise.

Figure 2.6 shows the instrument used for the XPS analyses. It consists of a SPECS spectrometer equipped with a Phoibos 150 MCD-9 detector, with measures taking place with a monochromatic Al (K_α: 1486.6 eV) X-Ray source, recording spectra at a pass energy of 30 eV (X-Ray power of 100 W). For data treatment we used the CasaXPS software, with binding energies referenced to C *1s* at 284.5 eV. The use of a monochromatic X-

Ray source in our experiments is due to the overlap of Vanadium satellites in the spectra with the O *1s* signal at ca. 530 eV of binding energy (BE).

In every XPS experiment, nomenclature of the ejected photoelectrons depends on the original orbital, this is, a given electron presenting a specific angular momentum (l = 0, 1, 2, 3… for *s*, *p*, *d*, *f*… orbitals) and a spin angular momentum (s) will show a total momentum of j = l + s [32]. Moreover, for orbitals different from *s*, in where the XPS signals appears as a singlet (i.e., l > 0), there exists a multiplicity of states (s values of $\pm\frac{1}{2}$) leading to the appearance of doublet signals in the XPS spectra of *p, d* and *f* core-levels.

For the catalysts studied in the present thesis, the only element that presents a singlet signal is O *1s*, conversely, the rest of the elements analyzed showed doublet signals: V *2p*, Mo *3d*, Nb *3d*, Te *3d* and Ni *2p*. However, each of the elements that present a doublet XPS signal have their own characteristic binding energies, areas and doublet separations, reported in several databases such as the National Institute of Standards and Technology (NIST) [33].

Moreover, although a doublet for a given element must present the same full half width at half maximum (FWHM), areas between the two signals differ as a consequence of the degeneracy of final states. Thus, for the analysis of V *2p* core level, the ratio of areas between the V $2p_{3/2}$ and V $2p_{1/2}$ levels will be: 2j + 1; $(A_{p1/2}/A_{p3/2}) = 0.5$. Conversely, when analyzing *d* core levels (such as Mo *3d*, Te *3d* or Nb *3d*), the area ratio expected between the $3d_{5/2}$ and the $3d_{3/2}$ core levels is $(A_{d3/2}/A_{d5/2}) = 0.66$.

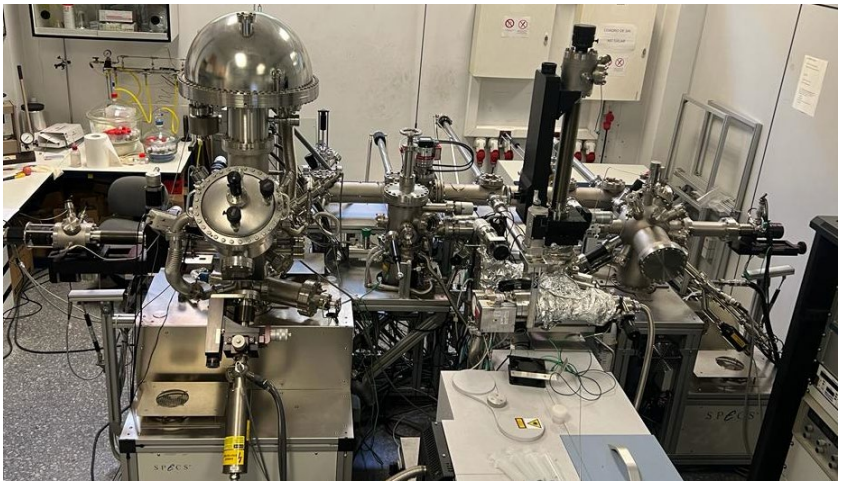

Figure 2.6. XPS spectrometer set up at the Institute of Chemical Technology (ITQ-UPV-CSIC)

Additionally, split separation between signals in a doublet are fundamental in the data treatment. In this sense, high spin-orbit separations in V *2p* and Te *3d* core levels (ca. 7.4 eV and 10.4 eV, respectively [33, 34]) allow a simpler analysis of these elements since V $2p_{3/2}$ and Te $3d_{5/2}$ are only considered for the deconvolution. Nevertheless, low separations as in the case of Mo *3d* and Nb *3d* components (3.2 eV and 2.8 eV, respectively [35, 36]) make it mandatory to analyze both signals jointly.

The interpretation of an XPS spectrum depends on the variation of the binding energies of the elements studied. These variations in BE can be due to the presence of atoms with different oxidation states within the sample or different chemical environments (chemical species in different environments will give rise to different shifts in BE).

Typically, elements in a highly oxidized chemical state will present higher BE values since those electrons are more strongly attracted to the nucleus (for instance, in this thesis it will be shown that V^{5+} species appear at binding energies of ca. 517 eV, while V^{4+} species appear at ca. 516 eV). Moreover, there also exist different phenomena that also may occur during an XPS experiment and they are directly related to the intrinsic physics of the analysis such relaxation or shake-up/off processes.

Furthermore, in semiconducting materials as the ones studied in here, problems of differential charging may also happen (see **Chapter 5**), therefore the use of a low energy electron flood-gun might be necessary to neutralize the charge, however the power of the flood-gun is experimentally adjusted, so it may lead to spectra misinterpretation in some cases.

2.2.14. Electrochemical studies

Electrochemical characterization of the materials prepared in the present thesis is shown in **Chapter 5**. Then, Electrochemical Impedance Spectroscopy (EIS), Mott-Schottky plots and cyclic voltammetries were carried out. For the three types of analyses, set up consisted of a three-electrode electrochemical cell in where samples were used as the working electrodes (previously deposited on FTO), exposing a total area of 0.5 cm^2 of catalyst to the electrolyte, connected to a potentiostat. Additionally, a platinum tip was employed as the counter electrode and Ag/AgCl (3 M KCl) as the reference electrode.

In the case of EIS, it is a technique that allows to study the electrochemical properties at the interface of a given material (the catalysts working as the electrodes) and an electrolyte. All the measures were conducted by applying a 0.5 $V_{Ag/AgCl}$ potential (0.01 V amplitude) and scanning frequencies from 100 kHz to 0.01 Hz in a Na_2SO_4 electrolyte (0.1 M). Prior to EIS analyses, samples were kept in the solution for 30 minutes.

For the Mott-Schottky plots, that deal with the semiconducting behavior of the catalysts, tests were performed at 5000 Hz frequency in the same electrolyte as in the EIS experiments, with scanning potential in the 0.5 to -1 $V_{Ag/AgCl}$ range at 0.05 V/s (0.01 V amplitude).

Accordingly, cyclic voltammetry studies took place in the potential range of -0.1 to 0.6 V $_{Ag/AgCl}$ at 0.01 V/s, using in this case a solution of 10 mM of $Fe(CN)_6K_4$ with 0.1 M Na_2SO_4.

2.2.15. Microcalorimetry

Microcalorimetry experiments were conducted in order to study the different adsorption enthalpy of both ethane and ethylene (results shown in **Chapter 6**). To that purpose, independent experiments were carried out in a Sensys evo TG-DSC instrument, from Setaram, attached to a 3D thermal flow sensor. In the experimental conditions, about 60-100 mg of catalysts were pretreated in a He flow (50 mL min^{-1}) at 5 ºC min^{-1} up to 300 ºC, maintaining this temperature for 30 minutes, and subsequently cooled to 35 ºC under He flow. Then, adsorption of ethane or ethylene occurred at 35 ºC

with a 10 mL min^{-1} flow of Hydrocarbon/He mixture (10% v/v) until no variations in mass or heat flow were detected.

Calculations of the hydrocarbons total enthalpies of adsorption were performed by integrating the exothermic peaks due to adsorption. Also, mean adsorption energy for both ethane and ethylene were calculated considering the total amount of hydrocarbon adsorbed.

2.3. Catalytic tests: oxidative dehydrogenation of ethane (ODHE)

Catalytic tests for the oxidative dehydrogenation of ethane to ethylene were conducted in a tubular isothermal flow reactor (i.d. 20 mm, length of 400 mm), at temperatures ranging from 300 to 450 ºC (for temperature profiling, a thermocouple attached to the quartz tubular reactor was employed). In all cases, both the catalyst loading and the flow rate were varied to achieve a wider ethane conversion range (0.2-2.0 g of catalyst and 25-100 mL min^{-1} flow rate, respectively). Moreover, catalysts with a particle size of 0.3-0.5 mm were diluted in silicon carbide (> 0.8 mm) in order to maintain a constant catalytic bed volume.

The feed consisted of a C_2H_6/O_2/He mixture with molar ratios of 5/5/90, selecting these compositions to be out of the explosivity boundaries (shown in **Fig. 2.7-A**). Further studies from Gaffney *et al.* [37] showed a proposed composition of reactants compared to existing ones, representing in yellow (**Fig. 2.7-B**) the safe zone operation, taking into account many simulations to maximize profitability and safety, minimizing operation costs. In any case, these simulations are applied to a potential industrial scale-up.

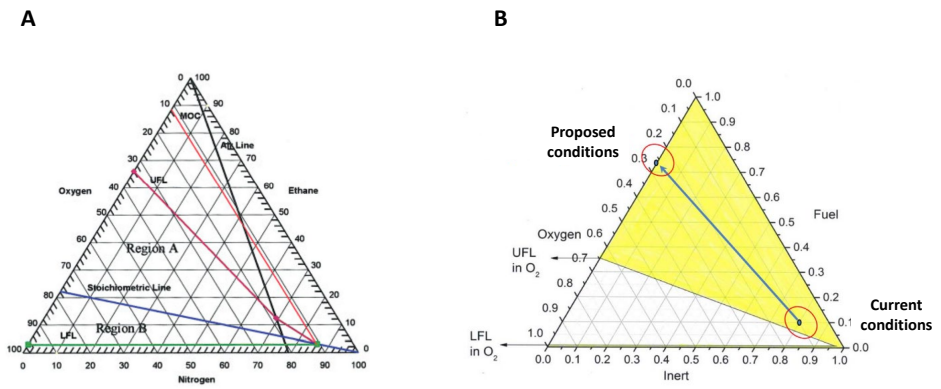

Figure 2.7. Ternary diagram of ethane/oxygen/nitrogen mixture [38] (**A**), and flammability diagram for ethane at 360 ºC (**B**), reproduced from [37].

Reactants and reaction products were analyzed by online gas chromatography, VARIAN CP-3800 model, equipped with a TCD detector, using two types of columns:

i) **"Carbosieve-S"** (2.5 m × 1/8 in.) for the separation of CO, O_2 and N_2.

ii) **"Porapak QS"** (2.0 m × 1/8 in.) for the separation of CO_2, alkanes, alkenes and oxygenated compounds.

Moreover, experiments of ethylene and CO oxidation also took place in the same device (see results in **Chapter 6**), feeding a C_2H_4/O_2/He and CO/Air molar ratios of 5/5/90 and 0.5/99.5, respectively.

Experimental set up displayed in **Figure 2.8** consists of several gas flowmeters (1) in where ethane, oxygen and helium are fed at controlled temperature (2) and flux (3) through a pre-heating pipe (4) that ends in the

reactor chamber (5) in where the catalyst mixed with SiC is disposed. Then, both the reaction products and reactants are directed through a post-heating pipe (6) to the gas chromatograph (7) for the separation and analysis. Additionally, a pump for the injection of water as a reactant is also considered in some of the experiments (8).

Then, for the calculation of the conversion, selectivity and yield of each of the products, **Equations 2.7**, **2.8** and **2.9**, respectively, were considered. Then, the ethane conversion can be expressed as:

$$X_j = \frac{\sum_{products}(\frac{A_i}{F_{ij}} \times \frac{\omega_i}{\omega_j})}{A_i + \sum_{products}(\frac{A_i}{F_{ij}} \times \frac{\omega_i}{\omega_j})} \qquad \textbf{Eq. 2.7}$$

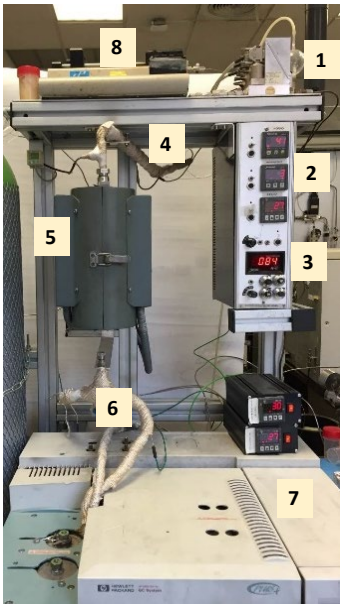

1) **Flowmeter**
2) **Temperature controller**
3) **Flow controller**
4) **Pre-heater**
5) **Reactor chamber**
6) **Post-heater**
7) **Gas chromatograph**
8) **Liquid pump**

Figure 2.8. Experimental set up for the oxidative dehydrogenation of ethane reactions.

Where: A_i is the area of the chromatographic peak corresponding to product i (ethylene, CO or CO_2 in our case, although in some cases acetic acid has been also observed as traces), F_{ij} is the experimentally calculated response factor of product i with respect to reactive j (i.e., ethane), ω_i or ω_j are the number of carbon atoms in the molecular formula of the products (i) and reactive (j). Likewise, the selectivity to the different products (S_{ij}) was calculated as:

$$S_{ij} = \frac{\frac{A_i}{F_{ij}} \times \frac{\omega_i}{\omega_j}}{\sum_{products}(\frac{A_i}{F_{ij}} \times \frac{\omega_i}{\omega_j})} \qquad \textbf{Eq. 2.8}$$

On the other hand, the yield to a given product (R_{ij}), especially ethylene, which is also the main reaction product, was expressed as:

$$R_{ij} = X_j \times S_{ij} \qquad \textbf{Eq. 2.9}$$

Another important concept is the contact time (W/F, in g_{cat} h mol_{C2}^{-1}), which gives an idea of the time it takes for the reactant to cross the catalytic bed. In this study, the contact time has been defined as the ratio between the mass of the catalyst (in grams) and the molar flow rate of the hydrocarbon (usually ethane but, in some cases, ethylene) in the reactant mixture (in mol_{C2} h^{-1}). Under normal working conditions, the reagent conversion will increase as the contact time increases.

2.4. References

1) P. Botella, J. M. López Nieto, B. Solsona, Preparation, characterization, and catalytic behaviour of a new TeVMoO crystalline phase, Catal. Lett. 78 (2002) 383-387.
2) P. Botella, J. M. López Nieto, B. Solsona, A. Mifsud, F. Márquez, The preparation, characterization, and catalytic behavior of MoVTeNbO catalysts prepared by hydrothermal synthesis, J. Catal. 209 (2002) 445-455.
3) T. Katou, D. Vitry, W. Ueda, Hydrothermal synthesis of a new Mo-V-O complex metal oxide and its catalytic activity for the oxidation of propane, Chem. Letters 32 (2003) 1028-1029.
4) D. Vitry, Y. Morikawa, J. L. Dubois, W. Ueda, Mo-V-Te-(Nb)-O mixed metal oxides prepared by hydrothermal synthesis for catalytic selective oxidations of propane and propene to acrylic acid, Appl. Catal. A-Gen. 251 (2003) 411-424.
5) F. Ivars, P. Botella, A. Dejoz, J. M. López Nieto, P. Concepción, M. I. Vázquez, Selective oxidation of short-chain alkanes over hydrothermally prepared MoVTeNbO catalysts, Top. Catal. 38 (2006) 59-67.
6) A. Celaya Sanfiz, T. W. Hansen, F. Girgsdies, O. Timpe, E. Rödel, T. Ressler, A. Trunschke, R. Schlögl, Preparation of phase-pure M1 MoVTeNb oxide catalysts by hydrothermal synthesis – influence of reaction parameters on structure and morphology, Top. Catal. 50 (2008) 19-32.
7) A. Celaya Sanfiz, T.W. Hansen, A. Sakthivel, A. Trunschke, R. Schlögl, A. Knoester, H.H. Brongersma, M.H. Looi, S.B.A. Hamid, How important is the (001) plane of M1 for selective oxidation of propane to acrylic acid?, J. Catal. 258 (2008) 35-43.
8) M. Aouine, T. Epicier, J.-M. M. Millet, In situ environmental STEM study of the MoVTe oxide M1 phase catalysts for ethane oxidative dehydrogenation, ACS Catal. 6 (2016) 4775-4781.

9) A. Trunschke, J. Noack, S. Trojanov, F. Girgsdies, T. Lunkenbein, V. Pfeifer, M. Hävecker, P. Kube, C. Sprung, F. Rosowski, R. Schlögl, The impact of the bulk structure on surface dynamics of complex Mo-V-based oxide catalysts, ACS Catal. 7 (2017) 3061-3071.
10) D. Melzer, G. Mestl, K. Wanninger, Y. Zhu, N. D. Browning, M. Sánchez-Sánchez, J. A. Lercher, Design and synthesis of highly active MoVTeNb-oxides for ethane oxidative dehydrogenation, Nat. Commun. 10 (2019) 4012-4020.
11) L. Annamalai, S. Ezenwa, Y. Dang, H. Tan, S. L. Suib, P. Deshlahra, Comparison of structural and catalytic properties of monometallic Mo and V oxides and M1 phase mixed oxides for oxidative dehydrogenation, Catal. Today 368 (2021) 28-45.
12) E. Heracleous, A. A. Lemonidou, Ni-Nb-O mixed oxides as highly active and selective catalysts for ethene production via ethane oxidative dehydrogenation. Part I: characterization and catalytic performance, J. Catal. 237 (2006) 162-174.
13) D. Delgado, B. Solsona, R. Sanchís, E. Rodríguez-Castellón, J. M. López Nieto, Oxidative dehydrogenation of ethane on diluted or promoted nickel oxide catalysts: influence of the promoter/diluter, Catal. Today, 363 (2021) 27-35.
14) B. Solsona, P. Concepción, B. Demicol, S. Hernández, J. J. Delgado, J. J. Calvino, J. M. López Nieto, Selective oxidative dehydrogenation of ethane over SnO_2-promoted NiO catalysts, J. Catal. 295 (2012) 104-114.
15) J. M. López Nieto, B. Solsona, R. K. Grasselli, P. Concepción, Promoted NiO catalysts for the oxidative dehydrogenation of ethane, Top. Catal. 57 (2014) 1248-1255.

16) H. Eckert, I. E. Wachs, Solid-state vanadium-51 NMR structural studies on supported vanadium (V) oxide catalysts: vanadium oxide surface layers on alumina and titania supports, J. Phys. Chem. 93 (1989) 6796-6805.
17) J. G. Eon, J. C. Volta, Oxidative dehydrogenation of propane on γ-Al_2O_3 supported vanadium oxides, J. Catal. 145 (1994) 318-326.
18) G. García Cortez, M. A. Bañares, A Raman spectroscopy study of alumina-supported vanadium oxide catalyst during propane oxidative dehydrogenation with online activity measurement, J. Catal. 209 (2002) 197-201.
19) M. V. Martínez-Huerta, X. Gao, H. Tian, I. E. Wachs, J. L. G. Fierro, M. A. Bañares, Oxidative dehydrogenation of ethane to ethylene over alumina-supported vanadium oxide catalysts: relationship between molecular structures and chemical reactivity, Catal. Today 118 (2006) 279-287.
20) B. M. Weckhuysen, D. E. Keller, Chemistry, spectroscopy and the role of supported vanadium oxides in heterogeneous catalysts, Catal. Today 78 (2003) 25-46.
21) Y. Waseda, E. Matsubara, K. Shinoda, X-Ray Diffraction Cystallography: Introduction, examples and solved problems, Springer, Berlin Heidelberg (2011).
22) https://www.britannica.com/science/X-ray-diffraction
23) https://wiki.anton-paar.com/us-en/basics-of-raman-spectroscopy/#:~:text=Raman%20spectroscopy%20is%20based%20on,chemical%20fingerprint%E2%80%9D%20of%20the%20substance.
24) M. A. Bañares, G. Mestl, Structural characterization of operating catalysts by Raman spectroscopy, Adv. Catal. 52 (2009) 43-128.
25) I. E. Wachs, Infrared spectroscopy of supported metal oxide catalysts, Colloids Surf. A Physicochem. Eng. Asp. 105 (1995) 143-149.
26) B. Imelik, J. C. Vedrine, Catalyst Characterization: Physical Techniques for Solid Materials, Springer, New York (1994).

27) P. Voogd, J. J. F. Scholten, H. van Bekkum, Use of the t-Plot-De Boer method in pore volume determinations of ZSM-5 type zeolites, Colloids Surf. 55 (1991) 163-171.
28) E. Pérez-Botella, R. Martínez-Franco, N. González-Camuñas, A. Cantín, M. Palomino, M. Moliner, S. Valencia, F. Rey, Unusually low heat of adsorption of CO_2 on AlPO and SAPO molecular sieves, Front. Chem. 8 (2020) 588712.
29) D. B. Williams, C. B. Carter, Transmission Electron Microscopy: A Textbook for Materials Science, Springer (1996).
30) K. Tsuno, D. Ioanoviciu, G. Martínez, Third-order aberration theory of Wien filters for monochromators and aberration correctors, J. Microsc. 217 (2005) 205-215.
31) https://www.britannica.com/science/photoelectric-effect
32) T. Robert, G. Offergeld, Selection rules and shake-up satellites in X-ray photoelectron spectra of transition metal compounds, Chem. Phys. Lett. 29 (1974) 606-608.
33) National Institute of Standards and Technology, https://www.nist.gov/
34) G. Silversmit, D. Depla, H. Poelman, G. B. Marin, R. De Gryse, Determination of the V2p XPS binding energies for different vanadium oxidation states (V^{5+} to V^{0+}), J. Electron. Spectros. Relat. Phenomena 135 (2004) 167-175.
35) J. F. Moulder, W. F. Stickle, P. E. Sobol, K. D. Bomben, Handbook of X-ray Photoelectron Spectroscopy, Perkin-Elmer Corp., Eden Prairie, MN, (1992).
36) J.-G. Choi, L. T. Thompson, XPS study of as-prepared and reduced molybdenum oxides, Appl. Surf. Sci. 93 (1996) 143-149.
37) C. Baroi, A. M. Gaffney, R. Fushimi, Process economics and safety considerations for the oxidative dehydrogenation of ethane using the M1 catalyst, Catal. Today 298 (2017) 138-144.

38) M. Palucis, T. Glowienka, V. Van Brunt, R. Ervin, W. Chastain, R. Kline, P. Lodal, Prediction of flammability speciation for the lower alkanes, carboxylic acids, and esters, Process Saf. Prog. 26 (2006) 4-9.

Chapter 3

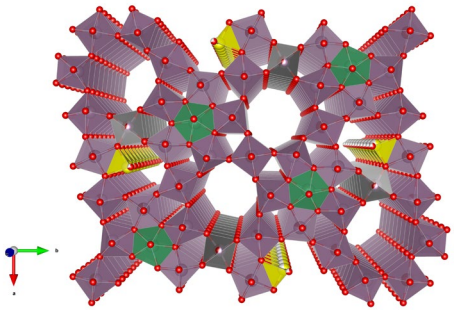

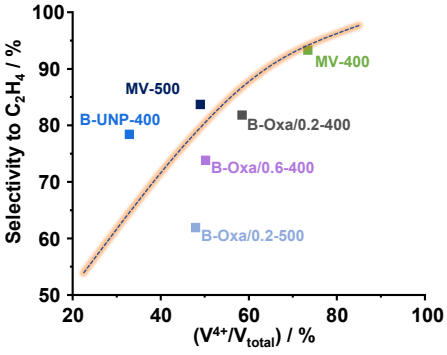

Bimetallic MoVOx mixed metal oxides: optimization of the synthesis parameters and catalytic performance

3.1. General considerations

The hydrothermal synthesis of Mo-V-M-O (M= Te or Sb) [1, 2], and then the hydrothermal synthesis of MoVTeNbO [3, 4], presenting both the M1 phase (orthorhombic bronze) were proposed at the beginning of this century. Nevertheless, a hydrothermal synthesis of the simplest system, i.e., Mo-V-O mixed metal oxides presenting M1 phase [5-8], was proposed latter. This is so because the simplest system is less stable and, therefore, requires much more specific synthesis and activation conditions.

The Mo-V-O is characterized by a composition of $Mo_{1.00}V_{0.34}Ox$, showing the characteristic XRD peaks at 2θ= 6.68º, 7.98º, 9.08º, 22º and 27º of the orthorhombic structure [7].

Since the synthesis of M1-phase MoV oxide was accomplished, comparative studies of Mo-V-O with respect to Mo-V-Te-O and Mo-V-Te-Nb-O for partial oxidation [7] and ammoxidation [8] of propane have been carried out. More recently, it has been also proposed the use of MoVO catalysts for ethane ODH [9, 10], the aerobic oxidation of alcohols [11] or the partial oxidation of acrolein to acrylic acid [12].

However, depending on the synthesis conditions, Mo-V-O presenting trigonal symmetry [13-15] can be also synthesized. On the other hand, this orthorhombic Mo_3VO_x solid, synthesized hydrothermally, appears as a result of self-organization between VO^{2+} cations pentagonal units (negatively charged), as illustrated in **Figure 3.1-A** [15].

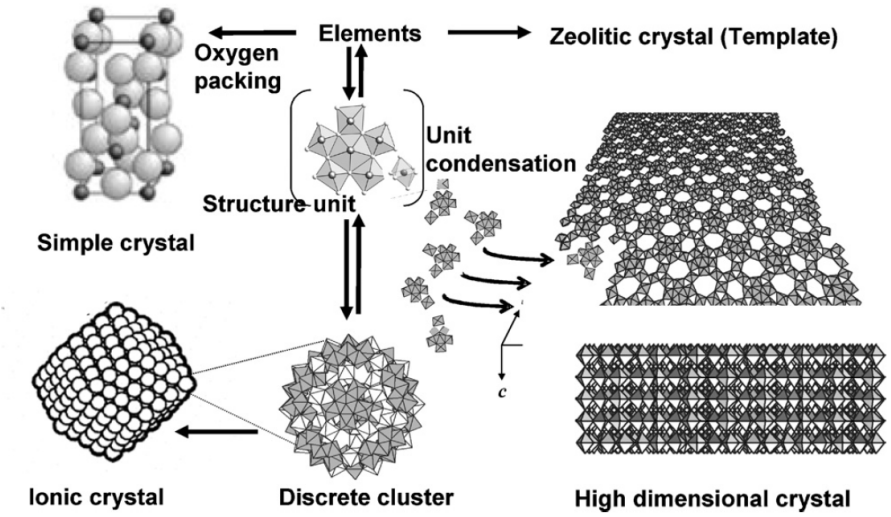

Figure 3.1-A. On the synthesis of various metal oxides. Adapted from [15]

Moreover, the intermediate in the synthesis of these materials is ball-shaped polyoxometalate $[Mo_{72}V_{30}O_{282}(H_2O)_{56}(SO_4)_{12}]^{36-}$ ($\{Mo_{72}V_{30}\}$) with 12 pentagonal $[Mo_6O_{21}]^{6-}$ polyoxomolybdate units connected to 30 $[V{=}O]^{2+}$ units, as proposed from the characterization results (UV/Vis, Raman and IR spectroscopy) [16], being this ($\{Mo_{72}V_{30}\}$) intermediate only possible to achieve at pH values higher than 1.7.

However, in some cases, intergrowth phases (i.e., orthorhombic M1-type phase intergrown with the trigonal phase) have been observed for various Mo-V-O materials using aberration-corrected high-angle annular dark-field (HAADF) imaging within a scanning transmission electron microscope (STEM) [17].

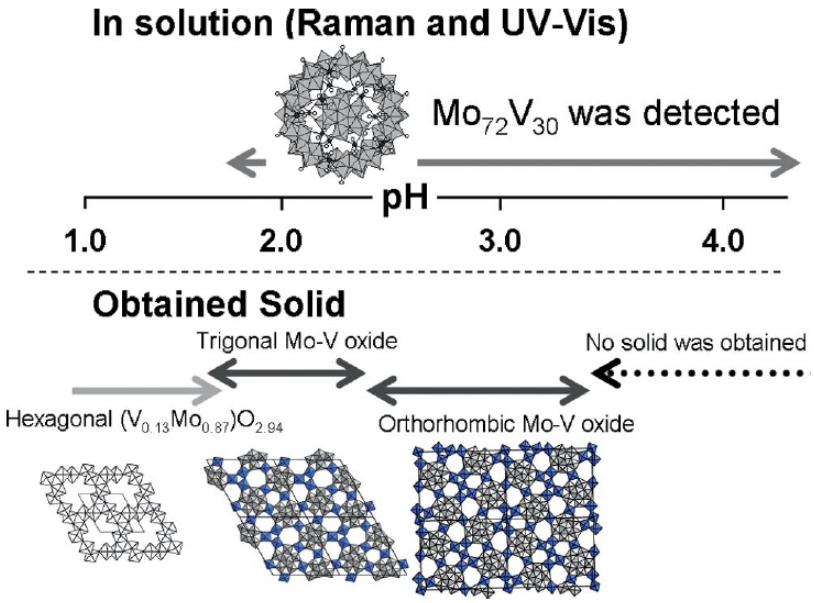

Figure 3.1-B. Relationship between the formation of MoV oxides and the presence of $\{Mo_{72}V_{30}\}$. Adapted from ref. [16].

Ueda *et al.* [18] have studied the sorption behavior (with different molecules such as CO_2, CH_4, C_2H_6, C_2H_4, n-C_4H_{10}, n-C_6H_{12}) of Mo-V (M1) oxide, proposing the nature of octahedral molecular sieve in these materials composed of seven-membered rings of corner-sharing $\{MO_6\}$ octahedra (with 0.4 nm diameter micropores) thus forming ordered microchannels [14]. Additionally, it was found too that the microporous volume of these materials decreases on partial reduction and increases on partial reoxidation [18]. In this way, a subsequent study on the influence of redox treatments on the orthorhombic $Mo_{29}V_{11}O_{112}$ catalyst suggested that in MoVO two kinds of lattice oxygen (named as α- and β-oxygen) evolve [19]. Then, at the beginning of the reduction, α-oxygen species are removed from the structure, favoring a certain expansion of the micropore channel, however,

with a greater reduction, part of the atoms of the pentagonal unit $[Mo_6O_{21}]^{6-}$ are directed towards the micropore channel, favoring a decrease in the micropore size. Parallel studies of the catalytic properties for ethane ODH indicated that during the increase in micropore size the catalytic activity for ethane ODH increased drastically. On the contrary, catalytic activity decreased in the period in which a reduction in micropore size was observed. Consequently, strong relationships were found between crystal structure, microporosity, and catalytic activity for the selective oxidation of ethane.

3.2. Previous considerations

Considering the above mentioned, the objective of this chapter is to study the synthesis of bimetallic MoV oxides, presenting the M1 phase, and to optimize their catalytic behavior in the ethane ODH to ethylene by changing both their synthesis (atmosphere, pH, time) and post-synthesis (purification, activation temperature) parameters.

3.3. Influence of the synthesis method

A brief summary of the different synthesis routes to obtain the desired M1-presenting catalysts is shown in **Table 3.1**, however, throughout the present chapter a more detailed study will be presented.

3.3.1 Differences in materials synthesized at modified pH values

In the materials and methods section shown in **Chapter 2** (see page 100) it has been explained, in agreement to other authors [15, 16], that the pH of the synthesis gel is a critical factor in order to obtain the desired crystalline phase, in our case the M1 phase. Therefore, the first part of this chapter is devoted to exploring the optimal pH in which the formation of the M1 phase is favored, maintaining the rest of the synthesis parameters unchanged, namely: synthesis time (72 hours) and atmosphere (inert gas, N_2). These series have been named as **A-x**, where "x" refers to the pH of the synthesis gel.

Table 3.1. Summary of the different synthesis strategies employed for bimetallic MoVO catalyst.

Sample	pH in synthesis gel	Synthesis time (days)	Heat-treatment Atmosphere	Main crystalline phase
A-2.0	2.0	3	N_2	Pseudocrystalline
A-2.5	2.5	3	N_2	α-MoO_3
A-3.0	3.0	3	N_2	M1
A-3.5	3.5	3	N_2	Mo-Keggin
B-N2-t2	3.0	2	N_2	M1
B-N2-t3	3.0	3	N_2	M1
B-N2-t4	3.0	4	N_2	M1
B-N2-t7	3.0	7	N_2	M1
B-Air-t2	3.0	2	Air	α-MoO_3 + Mo-Keggin
B-Air-t3	3.0	3	Air	MoO_3
B-Air-t6	3.0	6	Air	MoO_3

Regarding that, in the case of trimetallic (MoVTe) and tetrametallic (MoVTeNb) oxides, acid pH is required to obtain said crystalline phase [21-27], in **Figure 3.2** it is presented the synthesis of bimetallic MoV catalysts at different pH values ranging from 2 to ca. 3.5.

As it can be seen, only in one synthetic condition we can reach to the M1 phase (i.e., **A-3.0**) in a pure form (diffraction peaks at 6.7º, 7.9º, 9.0º, 10.8º, 23.0º and 27.3º). Nevertheless, in the case of the catalysts prepare at the immediate lower and higher pH value (**A-2.5** and **A-3.5**, respectively), we can observe the subtle formation of the M1 phase, especially in **A-3.5**, but with a preferential formation of MoO_3 (diffraction peaks at 9.7º, 19.4º, 25.8º and 29.4º), for the former, and a molybdenum based Keggin-like heteropolyacid, probably partially substituted with vanadium atoms (most representative diffraction peak at 9.4º), for the latter [28]. Moreover, in the case of the **A-2.0** sample, it can only be observed the formation of a pseudo-crystalline phase, although MoO_3 is also suggested.

Consequently, from this point, the synthesis conditions are set to a pH value of ca. 3.0. Nonetheless, the synthesis time was previously set to 72 hours (3 days) since this is the synthesis time used traditionally for tri- and tetrametallic catalysts. Therefore, the next section of the chapter is dedicated to exploring different synthesis times, as well as atmosphere (inert or oxidant), and their effect in both the crystalline structure and, if they present the M1 phase, the possible implications in their catalytic performance in the ODH of ethane.

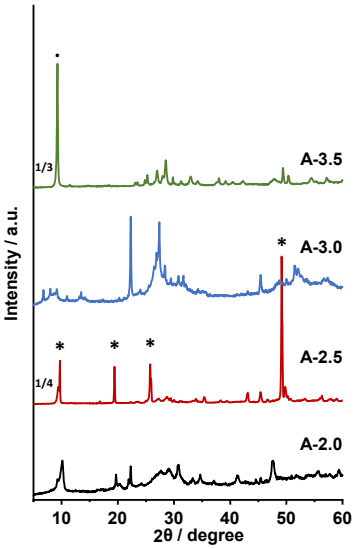

Figure 3.2. XRD patterns of bimetallic MoV oxide catalysts synthesized at pH values of: 2.0 (**A-2.0**, black), 2.5 (**A-2.5**, red), 3.0 (**A-3.0**, blue) and 3.5 (**A-3.5**, green). Main diffraction peaks of non-M1 crystalline faces are highlighted: (*) for α-MoO3 and (·) for Mo-V Keggin-like heteropolyacid.

3.3.2. Influence of the atmosphere and the synthesis time

Once the pH of the synthesis is set to ca. 3.0, next step is devoted to find out the optimal synthesis time, in terms of crystallinity, in addition to the suitable atmosphere within the autoclave, provided that mixed oxides are susceptible to drastic changes depending on the oxidative environment.

Therefore, in this section of the chapter a comparative parallel study of materials synthesized at different times (from one to seven days) and inert/oxidant atmospheres (nitrogen/air) is carried out. Materials in this section have been named as **B-x-ty**, where "**x**" stands for atmosphere (N_2

for nitrogen, Air for ambient) and "**ty**" refers to synthesis time. For instance, a solid synthesized under inert atmosphere for seven days will be named as "**B-N2-t7**".

Thus, **Figure 3.3-A** shows the XRD patterns of bimetallic MoV oxides synthesized under inert atmosphere (N_2) at four different times (2, 3, 4 and 7 days). In that figure, it can be seen that all of them present the M1 phase as majority, however, **B-N2-t2**, **-t4** and **-t7** catalysts also present an intense diffraction peak at 9.4º, associated to the presence of a molybdenum Keggin type heteropolyacid, being the **B-N2-t3** catalyst the only one that does not present that peak, suggesting a higher proportion of M1 phase for the material synthesized in 3 days' time.

Conversely, **Fig. 3.3-B** presents the XRD patterns of solids synthesized under ambient atmosphere (air), in this case at three different times (2, 3 and 6 days). As it can be seen, in none of the materials synthesized it is appreciated the formation of the M1 phase, in fact, by increasing the synthesis time the formation of hexagonal α-MoO_3 oxide (most characteristic diffraction peaks at 10º, 26º and 49.5º) is rather favored. Interestingly, those samples (i.e., **B-Air-t3** and **B-Air-t6**) present an XRD pattern fairly similar to solid **A-2.5** (oxide synthesized under N_2 atmosphere, for 3 days at pH of 2.5), although the latter showing diffraction peaks clearly less intense. However, the oxide synthesized at the shortest time (i.e., **B-Air-t2**) displays a XRD pattern that suggests a mix of heteropolyacid Mo-Keggin material in majority with α-MoO_3 in somehow minority presence. Then, these similarities between samples suggest that is not only one condition that leads to the formation of the M1 phase in the

bimetallic MoV-oxide form, but the joint use of specific synthetic conditions.

Then, after the changes introduced in the synthesis parameters, conditions have been set to 175 ºC, 3 days' time and under inert atmosphere. Nevertheless, it is also well-known that post-synthesis treatments, which comprehend purification and thermal activation steps, are also crucial in order to transform the solids into optimal performing catalysts in the oxidative dehydrogenation of ethane to ethylene. Consequently, next section of the chapter will deal with the different routes and strategies to purify these as-synthesized solids.

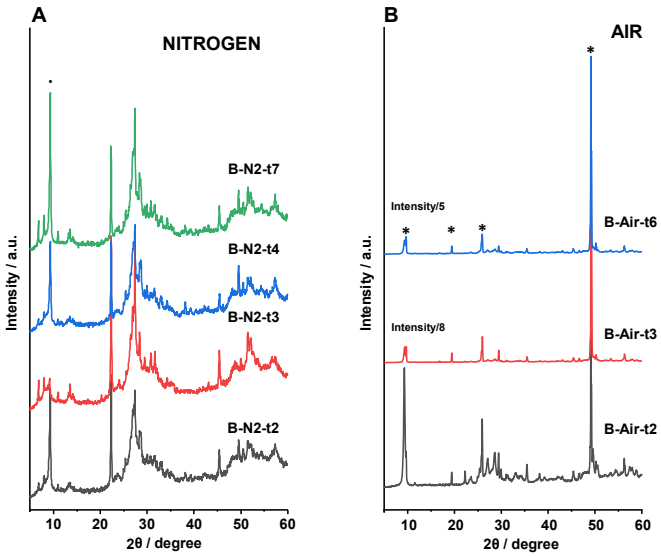

Figure 3.3. XRD patterns of solid synthesized: **A)** under N_2 atmosphere with 2 (**B-N2-t2**, black), 3 (**B-N2-t3**, red), 4 (**B-N2-t4**, blue) and 7 (**B-N2-t7**, green) days of synthesis time; and **B)** under air atmosphere with 2 (**B-Air-t2**, black), 3 (**B-Air-t3**, red) and 6 (**B-Air-t6**, blue) days of synthesis time). Main diffraction peaks of non-M1 crystalline faces are highlighted: (*) for α-MoO_3 and (·) for Mo-V Keggin-like heteropolyacid.

3.4. Influence of the post-synthesis treatments

3.4.1. Influence of the purification step

Due to the complexity of the M1 phase, and the specific conditions for its synthesis in the bimetallic form, post-synthesis treatments are usually employed to eliminate the minority subphases that can be also formed during the hydrothermal synthesis.

Therefore, this part of the chapter is dedicated to the study of different types of purification methods and strategies: washing with either hydrogen peroxide or oxalic acid solutions, different concentrations of washing solutions (in the case of the solids purified with oxalic acid) and to check the implications of doing it before or after the thermal activation. Note that experimental conditions are explained in **Chapter 2** (page 100).

Figure 3.4 shows the XRD patterns of bimetallic MoV-oxides washed with H_2O_2 or oxalic acid. As it can be seen, for oxalic acid treated solids, there is a direct relationship between the concentration of the oxalic acid solution and the crystallinity of the oxide, then, the solid with the highest crystallinity is the one treated with the most diluted oxalic acid solution (i.e., **B-Oxa/0.2**).

On the contrary, the level of crystallinity in the sample treated with diluted hydrogen peroxide (**B-H_2O_2**) appears to be similar than **B-Oxa-0.2**. Therefore, these two different purification approaches seem to be suitable for obtaining pure M1 phase MoV-oxides.

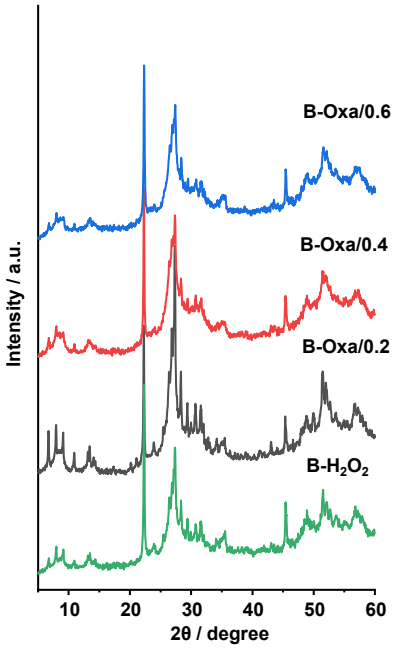

Figure 3.4. XRD patterns of oxides purified with 15%wt H_2O_2 (**B-H_2O_2**, green), or with oxalic acid solution of 0.2M (**B-Oxa/0.2**, black), 0.4M (**B-Oxa/0.4**, red) and 0.6M (**B-Oxa/0.6**, blue).

Once the solids are rather purified (whether with hydrogen peroxide or oxalic acid solutions), these samples were thermally activated at 400 ºC under N_2 stream. Moreover, an unpurified sample (i.e., **B-UNP-400**) was also activated at 400 ºC under inert atmosphere. Different results are plotted in **Figure 3.5**.

Then, catalysts purified with hydrogen peroxide and the lowest concentration of oxalic acid, samples **B-H_2O_2-400** and **B-Oxa/0.2-400**, respectively, are the ones that maintain the highest level of crystallinity upon heat treatment at 400 ºC. On the contrary, unpurified solid (**B-UNP-**

400) as well as materials treated with higher concentration of oxalic acid solutions (**B-Oxa/0.2-400, B-Oxa/0.4-400** and **B-Oxa/0.6-400**) display a clearly lower degree of crystallinity. This fact suggests that in the first case, a previous purification step is required to obtain solids presenting a pure M1 phase, however, by exceeding a certain concentration in the purification solution, it can also turn into a partial decomposition both before and after the thermal treatment.

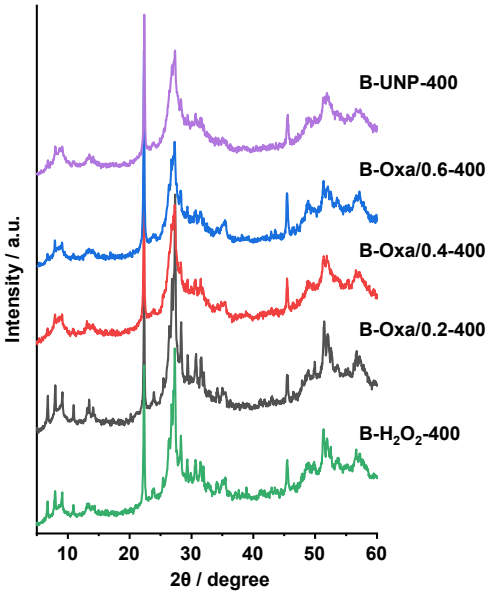

Figure 3.5. XRD pattern of 400 ºC heat-treated solids with 15%wt H_2O_2 (**B-H_2O_2-400**, green), or with oxalic acid solutions of: 0.2M (**B-Oxa/0.2-400**, black), 0.4M (**B-Oxa/0.4-400**, red) and 0.6M (**B-Oxa/0.6-400**, blue). Note that an unpurified sample, **B-UNP-400** (purple), is also displayed in the figure.

Additionally, further experiments were undertaken in order to increase the crystallinity of the solids. In that sense, two separate purifications took

place. In one hand, provided that hydrogen peroxide proved to be a softer purifying agent (seen in **Figs. 3.3** and **3.4**), an unpurified heat-treated sample (**B-UNP-400**) was subsequently washed with hydrogen peroxide, giving as a result the sample **MV-400** (**Fig. 3.6-A**). Conversely, a highly crystalline oxide as the **B-Oxa/0.2-400** material was further rewashed after thermal treatment with a more concentrated oxalic acid solution (0.4M), obtaining the solid named **MV-Oxa-400-Oxa** (**Fig. 3.6-B**).

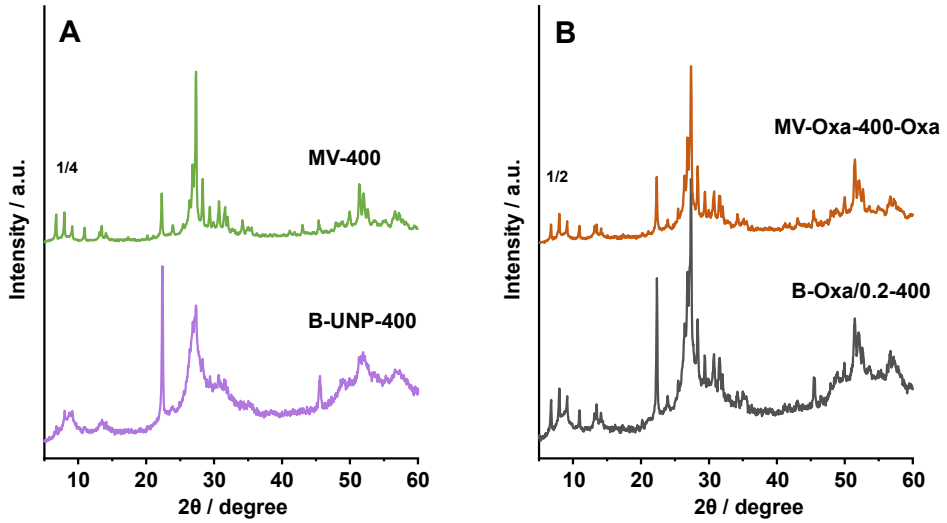

Figure 3.6. XRD pattern of: **A)** an unpurified MoV oxide solid (**B-UNP-400**, purple) washed after the heat treatment (**MV-400**, green); and **B)** MoV oxide purified with a 0.2M oxalic acid solution (**B-Oxa/0.2-400**, black) or washed with 0.4M oxalic acid solution after the heat-treatment (**MV-Oxa-400-Oxa**, orange).

As seen in **Figure 3.6**, both purification steps after the thermal treatment at 400 ºC lead to a notable increase in the crystallinity of the sample. Especially notorious is the case of the unpurified MoV oxide, in which the

H_2O_2 purification leads to the most crystalline oxide obtained throughout the present chapter, namely sample **MV-400** (note that in **Fig. 3.6-A** its relative intensity is normalized by a factor of 4, whereas two-times purified sample, **MV-Oxa-400-Oxa**, in **Fig. 3.6-B** is normalized by a factor of 2). Moreover, in neither of the two cases it is appreciated a somehow decomposition of the M1 phase, even by using a more concentrated oxalic acid solution (0.4M) in the second washing step (oxide named **MV-Oxa-400-Oxa**), suggesting that the thermal activation leads to a certain structural stability.

Consequently, the different synthesis procedures, purifications and activations have led to a branch of M1-presenting MoV oxides with higher or lower degree of crystallinity and purity. Among them, oxides washed with: **i)** oxalic acid (0.2M) before the thermal activation; or with **ii)** hydrogen peroxide 15% wt. after the calcination are the ones that showed the highest levels of crystallinity. Therefore, the next section is devoted to a deeper study of the role of the activation temperature in these two synthetic routes.

3.4.2. Influence of the activation temperature

Accordingly, it has been proposed before [24-27, 29] that bimetallic MoV oxides presenting the M1 structure have been thermally activated at 400 ºC in the presence of an inert atmosphere. Nevertheless, the absence in this kind of oxides of Te atoms in the form of …-Te-O-Te-… infinite chains [8] along the hexagonal channels of the M1 phase should notably decrease the

thermal stability of bimetallic MoVO. Thus, the solids that presented the highest levels of crystallinity along the chapter have been further investigated by treating them at 400, 500 and 600 ºC. XRD results of these treatments are displayed in **Figure 3.7**.

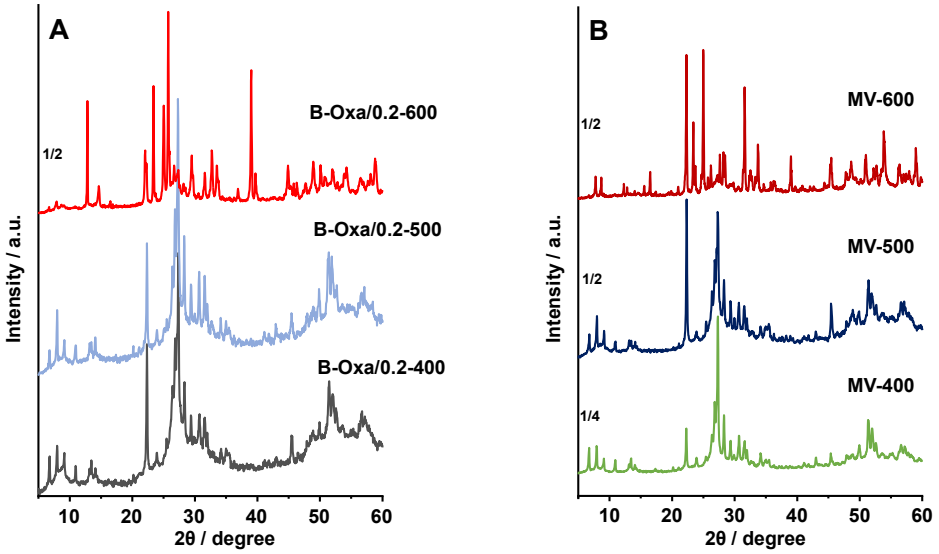

Figure 3.7. XRD of MoV-M1 oxides: (**A**) Samples washed with 0.2M oxalic acid solutions before heat-treatment at 400 (**B-Oxa/0.2-400**, black), 500 (**B-Oxa/0.2-500**, light blue) and 600 ºC (**B-Oxa/0.2-600**, red); or (**B**) Samples washed with 15% wt. hydrogen peroxide solution, after heat-treatment at 400 (**MV-400**, green), 500 (**MV-500**, dark blue) or 600ºC (**MV-600**, garnet) under N_2 stream.

XRD results indicate that there are some differences regarding the activation temperature depending on the purifying method employed. Thus, when using oxalic acid (**Fig. 3.7-A**), it can be observed that by increasing the activation temperature up to 500 ºC a better crystallization can be achieved. However, further increasing to 600 ºC leads to an apparent

collapse of the M1 structure into MoO_3 with diffraction peaks at: 12.8, 23.3, 25.8 and 39.0º [30].

On the contrary, purifying with a hydrogen peroxide solution after the calcination (**Fig. 3.7-B**) resulted into a different trend. In this case, the oxide that presents the highest degree of crystallinity is the one treated at the lowest temperature (i.e., **MV-400**), with catalysts thermally activated at 500 and 600 ºC (**MV-500** and **MV-600**, respectively) showing a clearly poorer crystallinity. In fact, the **MV-600** sample partially collapses as well into $(Mo_{0.93}V_{0.07})_5O_{14}$ crystalline phase [4, 31-34] as main diffraction peaks appear at 2θ= 22.3, 25.0, 31.6 and 33.7º. Nevertheless, it is interesting that oxides heat-treated at 600 ºC, but differently purified, collapse into two different structures: MoO_3 as main phase in **B-Oxa/0.2-600**, or $(Mo_{0.93}V_{0.07})_5O_{14}$ as majority in **MV-600**. Accordingly, there are changes at high activation temperatures that cannot only be determined through XRD analysis.

Then, Raman spectroscopic studies for these two families of catalysts (B-Oxa-series and MV-series) are displayed in **Figure 3.8**. Raman spectra for catalysts washed with oxalic acid (0.2M) before the thermal activation at 400, 500 and 600ºC are shown in **Fig. 3.8-A**. There, a principal signal at ca. 868 cm^{-1} can be observed for the three samples, this one associated with the orthorhombic M1 phase [35-37], although it is slightly shifted to lower wavenumber (ca. 862 cm^{-1}) for the oxide heat-treated at 600 ºC (**B-Oxa-0.2-600**) which, in any case presents a notably amount of MoO_3 due to its low thermal stability.

In that sense, additional Raman signals at 844 and 903 cm^{-1} are ascribed to distorted monoclinic MoO_3, stretching vibrations of Mo-O-Mo in corner-sharing octahedra (structure similar to ReO_3) [38].

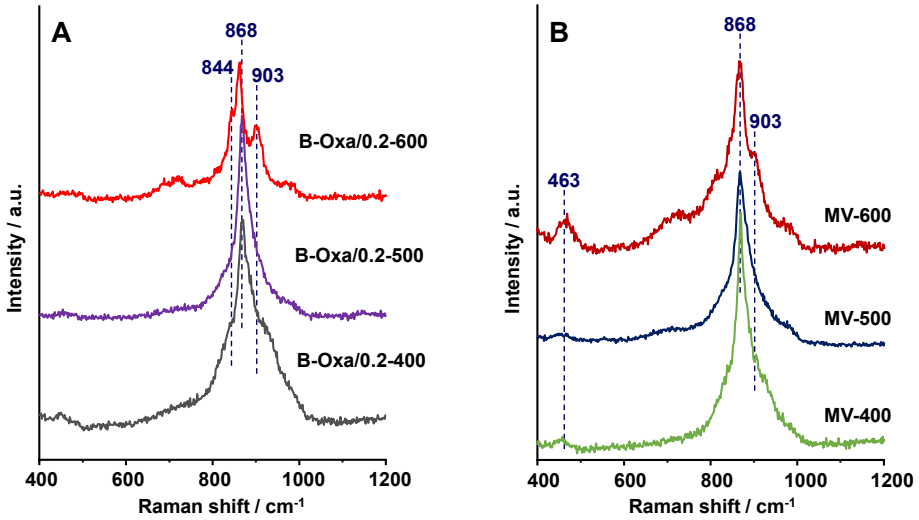

Figure 3.8. Raman spectra of MoVO-M1 oxides: (**A**) Samples washed with 0.2M oxalic acid solutions before a heat-treatment at 400 (**B-Oxa/0.2-400**, black), 500 (**B-Oxa/0.2-500**, light blue) and 600 ºC (**B-Oxa/0.2-600**, red); or (**B**) Samples washed with 15% wt. hydrogen peroxide solution after a heat-treatment at 400 (**MV-400**, green), 500 (**MV-500**, dark blue) or 600 ºC (**MV-600**, garnet) under N_2 stream.

On the other hand, Raman spectra for the oxides purified with a H_2O_2 solution after the thermal activation at 400, 500 and 600 ºC are displayed in **Fig. 3.8-B**. As seen in **Fig. 3.8-A,** spectra of M1-presenting oxides, this is the ones heat-treated at 400 and 500ºC (i.e., samples **MV-400** and **MV-500**) only show an intense sharp signal at 868 cm^{-1}, again associated with

the majority presence of the M1 phase [35-37]. Furthermore, additional bands at ca. 463 cm^{-1}, but also some wide bands at lower wavenumber than 868 cm^{-1} could confirm the presence of $(Mo_{0.93}V_{0.07})_5O_{14}$, as reported above in the diffraction analysis (**Fig. 3.7-B**).

Thus, by using activation temperatures higher than 500 ºC, a great depletion in the M1 phase structure is observed regardless of the intermediate and/or post-activation steps. However, these steps lead to differences in the degree of crystallinity depending on the nature of the purification/treatment. Therefore, all of these M1-presenting Mo-V-O oxides studied throughout the present chapter have been tested in the oxidative dehydrogenation of ethane and the results are presented in the following point.

3.5. Catalytic behavior in ethane oxidative dehydrogenation

Accordingly, a set of bimetallic Mo-V-O catalysts, all of them presenting the M1 phase in a greater or lesser extent have been tested in the oxidative dehydrogenation of ethane, with experimental conditions described in **Chapter 2**. Some catalytic results are displayed in **Table 3.2**.

Figure 3.9 shows the variation of the selectivity to ethylene as a function of the ethane conversion for binary Mo-V-O M1-presenting catalysts activated at 400 ºC and with different post-synthesis treatments. In this sense, it can be observed that most of the catalysts present similar values of selectivity to ethylene regardless of the purification method.

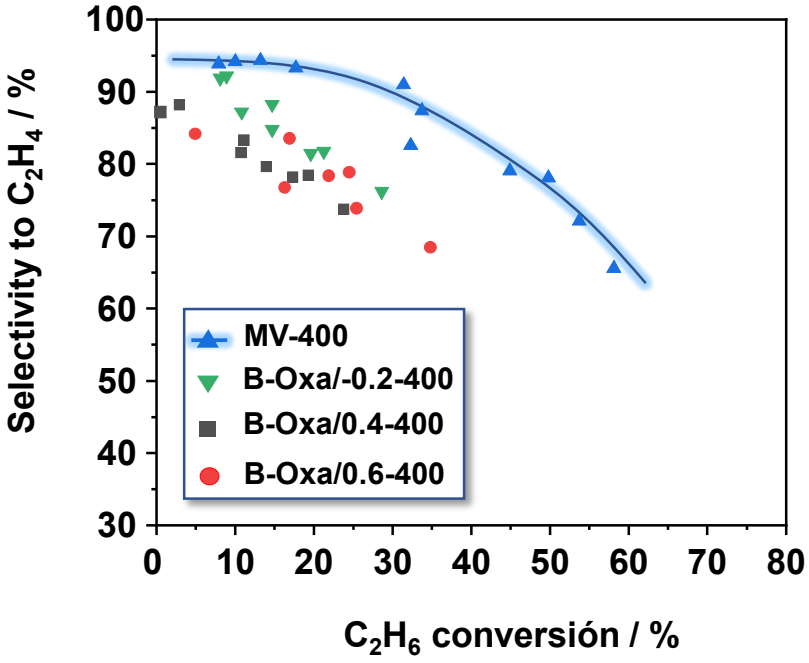

Figure 3.9. Variation of the ethylene selectivity as a function of the ethane conversion for selected M1-MoVO catalysts.

Unpurified **B-UNP-400** sample shows similar catalytic properties than those purified with oxalic acid (**B-Oxa/0.2-400** and **B-Oxa/0.6-400**) catalysts, although the catalyst treated with the less concentrated oxalic acid solution showing slightly higher selectivity to ethylene. Although, in general, a higher or lower degree of crystallinity may be associated with differences in the catalytic activity.

Therefore, it is interesting to mention that the sample **MV-400** (i.e., catalysts purified with H_2O_2 15% wt. solution after the thermal activation), in addition to presenting the highest degree of crystallinity, and

consequently being the most active catalyst, is also the one that shows the best values of selectivity to ethylene. **Figure 3.9** shows that this catalyst outperforms the rest of the binary M1-MoV oxides by ca. 10-15% points, especially at ethane conversions lower than 20%.

Furthermore, for catalysts that presented the best catalytic properties in terms of both activity and selectivity to ethylene (i.e., **MV-400** and **B-Oxa/0.2-400**), it was also studied the influence of the heat-treatment in the performance on the ODHE reaction.

Then, **Figure 3.10** shows the variation of the selectivity to ethylene as a function of the ethane conversion for catalysts purified with 0.2M solution of oxalic acid before thermal activation (**Fig. 3.10-A**) or purified with (15% wt.) H_2O_2 solution after the thermal activation (**Fig. 3.10-B**) for solids heat-treated at 400, 500 and 600 ºC.

In general, it can be seen that both series follow the same trend, the higher the thermal activation the lower the selectivity to ethylene. Nevertheless, by comparing one to the other in the same activation temperature range, huge differences are observed. In this sense, added to the marked increase in activity and selectivity for the sample **MV-400** compared to **B-Oxa/0.2-400**, catalysts calcined at 500 and 600 ºC show even larger differences.

Then, considering the catalysts treated at 500 ºC, it is displayed that the **MV-500** sample outperforms the **B-Oxa/0.2-500** oxide by 20% points of selectivity (at 20% of ethane conversion, 85% of ethylene selectivity for **MV-500** whilst 65% in the case of the **B-Oxa/0.2-500** catalyst). Additionally, for 600 ºC-treated catalysts, both **MV-600** and **B-Oxa/0.2-**

600 samples display almost no activity in the ODHE, since in any case ethane conversions beyond 5% were observed. These last results are clearly related to the low presence of M1 phase in these catalysts, although the catalyst purified with H_2O_2 after the thermal activation (**MV-600**) exhibits a notable higher initial selectivity to ethylene than that observed over the corresponding sample purified with oxalic acid (**B-Oxa/0.2-600**).

Indeed, as previously reported [4, 39, 40, 41], the active centers of this type of catalysts are the vanadium sites, and in the case of the **B-Oxa/0.2-600**, XRD and Raman results suggest the majority presence of MoO_3, while **MV-600** is mainly formed by vanadium doped Mo_5O_{14}-like crystalline phase $(Mo_{0.93}V_{0.07})_5O_{14}$, so the differences in selectivity, even at the lowest ethane conversion, could be explained on this basis.

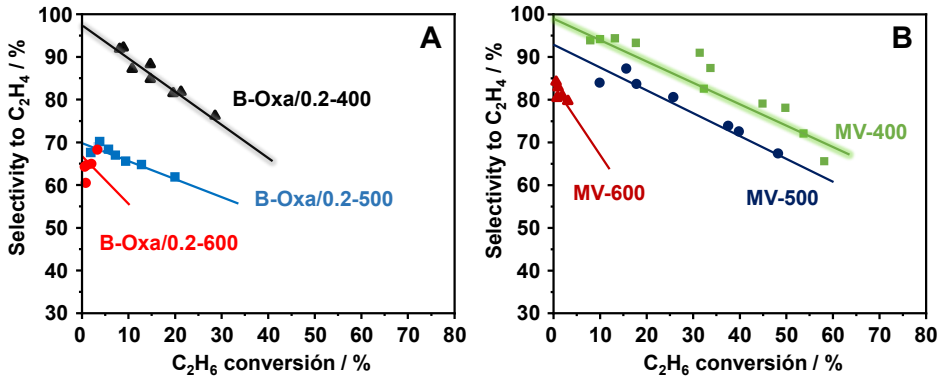

Figure 3.10. Variation of the selectivity to ethylene as a function of ethane conversion of MoV-M1 oxides: (**A**) Samples washed with 0.2M oxalic acid solutions and then activated at 400 (**B-Oxa/0.2-400**, black), 500 (**B-Oxa/0.2-500**, light blue) and 600 ºC (**B-Oxa/0.2-600**, red). (**B**) Samples washed with 15% wt. hydrogen peroxide solution and then activated at 400 (**MV-400**, green), 500 (**MV-500**, dark blue) or 600 ºC (**MV-600**, garnet) under N_2 stream.

Moreover, it has also been reported that for M1 phase presenting catalysts, the environment of the vanadium species is essential to enhance the catalytic activity. Thus, V^{5+} species are required to activate the ethane (more precisely V^{5+}=O [42-45]), however, an excess of them can also lead to the overoxidation of the olefin (ethylene) and the subsequent formation of carbon oxides (CO mainly, but also CO_2). Therefore, a control of the V^{4+}/V^{5+} relationship on the surface of the catalysts seems to be of special interest in the aim of optimize the catalytic properties of the oxides. So, an XPS study was conducted over a representative selection of the catalysts tested through the present chapter and results are plotted in **Figure 3.11** and **Table 3.2**.

Accordingly, it has been observed that the catalysts that offer the best performance in the ODHE reaction (i.e., **MV-400** and **B-0.2/Oxa-400** samples) are characterized by the majority presence of V^{4+} species, in detriment of V^{5+}. On the contrary, oxides that lead to a more enhanced combustion of the ethylene (or **B-UNP-400** or **B-Oxa/0.6-400**) show an increase in the V^{5+} species, as evidenced in **Figs. 3.11-B** and **3.11-C**, respectively.

It is also interesting to mention that, for catalysts with the same post-synthesis treatment but different activation temperatures (i.e., **MV-400** and **MV-500**, or **B-Oxa/0.2-400** and **B-Oxa/0.2-500**), elevating the heat-treatment temperature implies an increase in the relative amount of V^{5+} species, and consequently, a decrease in the selectivity to ethylene regardless of the purification method.

Table 3.2. Physicochemical properties of differently purified and heat-treated bimetallic M1-MoVO catalysts.

Catalyst	Surface composition (Mo/V)[a]	V^{4+}/V^{5+} ratio[a]	Selectivity to ethylene (%)[b]	Ethane conversion (%)[d]
MV-400	1.0/0.19	73.4/26.6	93.3	49.8
MV-500	1.0/0.16	49.0/51.0	83.7	25.7
MV-600	1.0/0.12	33.8/66.2	79.7[c]	1.0
B-Oxa/0.2-400	1.0/0.18	58.5/41.5	81.5	28.6
B-Oxa/0.2-500	1.0/0.20	47.9/52.1	61.9	9.4
B-UNP-400	1.0/0.20	50.2/49.8	78.5	23.8
B-Oxa/0.4-400	1.0/0.19	38.2/61.8	n.d.	n.d.
B-Oxa/0.6-400	1.0/0.19	32.9/67.1	78.4	34.8
B-Oxa-400-Oxa	1.0/0.18	25.5/74.5	n.d.	n.d.

a) Data extracted from XPS deconvolution by using the CasaXPS software; **b)** Selectivity to ethylene taken at 20% of ethane conversion. **c)** Selectivity to ethylene taken at 3% of ethane conversion due to the collapse of the M1 structure. **d)** Ethane conversion at 390ºC and a contact time, W/F of 16 g_{cat} h mol_{C2}^{-1}.

Moreover, although it is not the main reason, by further increasing the activation temperature to 600 ºC (sample **MV-600** in **Fig. 3.10-A**) a more enhanced proportion of V^{5+} is observed, suggesting these species are clearly favored in severe heat treatment atmospheres.

Nonetheless, it has been reported that, in the case of bimetallic Mo-V-O M1 oxides, the non-presence of Te^{4+} cations in the hexagonal channels may

facilitate the segregation of V^{5+} species from the bulk oxide to its surface [46, 47].

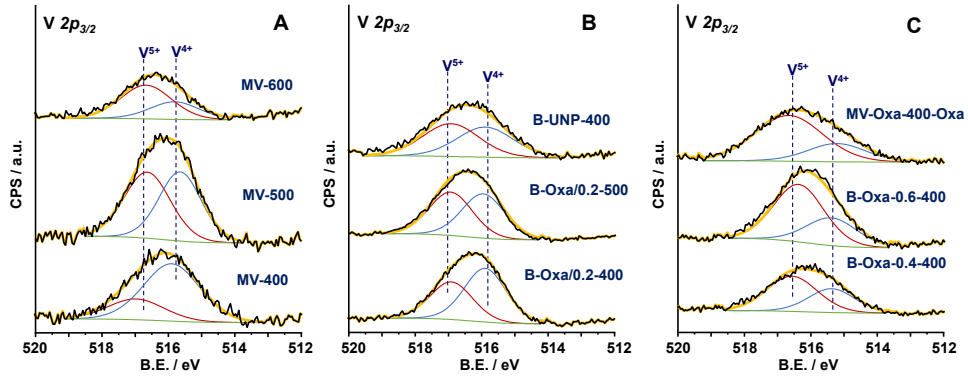

Figure 3.11. XPS spectra of V *2p3/2* core level of: A) **MV-400**, **MV-500** and **MV-600**; B) **B-Oxa/0.2-400**, **B-Oxa/0.2-500** and **B-UNP-400**; and C) **B-Oxa/0.4-400, B-Oxa/0.6-400** and **MV-Oxa-400-Oxa**, catalysts.

3.6. Conclusions

In the present chapter, different approaches in the synthesis of bimetallic Mo-V-O oxides have been studied in the aim of obtaining the orthorhombic so-called M1 phase. For this purpose, by employing the hydrothermal method, it was investigated the influence of the synthesis time, atmosphere and the pH of the synthesis gel concluding that the best results were obtained when the synthesis gel is set to a value of ca. 3.0, in an inert atmosphere (N_2) and an optimized time of 72 hours.

Furthermore, once the experimental parameters were set, post-synthesis modifications were also considered in order to obtain the bimetallic M1-

MoVO oxides with the highest degree of crystallinity. Then, two different purification agents (i.e., oxalic acid and hydrogen peroxide solutions) were tested before and after the thermal activation (set to 400 ºC), in addition to an unpurified sample that was used as a reference.

Accordingly, samples that showed the highest level of crystallinity were the one purified with a 0.2M oxalic acid solution before the thermal activation and the one that was purified with a 15% wt. hydrogen peroxide solution after the thermal activation: **B-Oxa/0.2-400** and **MV-400**, respectively.

Moreover, considering these two strategies, the influence of the activation temperature was studied. In this sense, dissimilar results were obtained. For instance, in the case of the purification with the oxalic acid solution, the crystallinity of the catalysts increased with the activation temperature (from 400 to 500 ºC) whereas it notoriously decreased when purifying with hydrogen peroxide. What is more, the activation at 600 ºC led in both cases to a collapse of the M1 structure, however, the catalyst purified with oxalic acid (**B-Oxa/0.2-600**) collapsed into the MoO_3 structure (as seen in **Fig. 3.7-A** and **Fig. 3.8-A**), while the oxide purified with hydrogen peroxide (**MV-600**) collapsed into the $(Mo_{0.93}V_{0.07})_5O_{14}$ structure (**Fig. 3.7-B** and **Fig. 3.8-B**).

Interestingly, a different degree of crystallinity did have effects on the activity of the catalysts, in other words, the purest the M1 phase the higher the activity (**Fig. 3.9**), being samples **B-Oxa/0.2-400** and **MV-400** the catalysts with the highest activity. Nevertheless, that effect on the activity did not seem to be so evident in terms of selectivity to ethylene. Then, the only catalyst that showed a remarkable increase in the selectivity to

ethylene, in addition to an increase in the activity, was sample **MV-400** (catalyst purified with hydrogen peroxide 15% wt. solution after the thermal activation). Furthermore, over these two samples that presented the best catalytic results (**B-Oxa/0.2-400** and **MV-400**) it was also studied the effect of the activation temperature, considering for the two of them heat-treatments of 500 and 600 ºC. Results in **Fig. 3.10** showed that, in both cases, an increase in the activation temperature to 500 ºC leads to a notable decrease in the selectivity to ethylene, and especially in those samples calcined at 600ºC, in which selectivity but also activity values drop dramatically. The drastic drop in the catalytic performance of oxides treated at 600 ºC, however, was associated with the majority collapse of the M1 structure at said temperature into non-catalytic crystalline phases.

These catalytic results were explained in terms of the surface composition on the differently synthesized catalysts. So, it was previously reported that a partially reduced surface (higher presence of V^{4+} species) should be beneficial to promote partial oxidation reactions, avoiding the deep oxidation of the formed olefin into carbon oxides. In this sense, in **Fig. 3.11** it was observed that, along with a higher degree of crystallinity, catalysts that presented the highest selectivity to ethylene were the ones that also displayed a higher V^{4+}/V^{5+} ratio. Not only that, but also it was observed that increasing the activation temperature led to both a decrease in the selectivity to ethylene concomitantly with a reduction in the V^{4+} relative amount. This representation can be seen in **Figure 3.12**, where a clear relationship is stablished between the selectivity to ethylene and the relative amount of V^{4+} species on the surface of the catalyst.

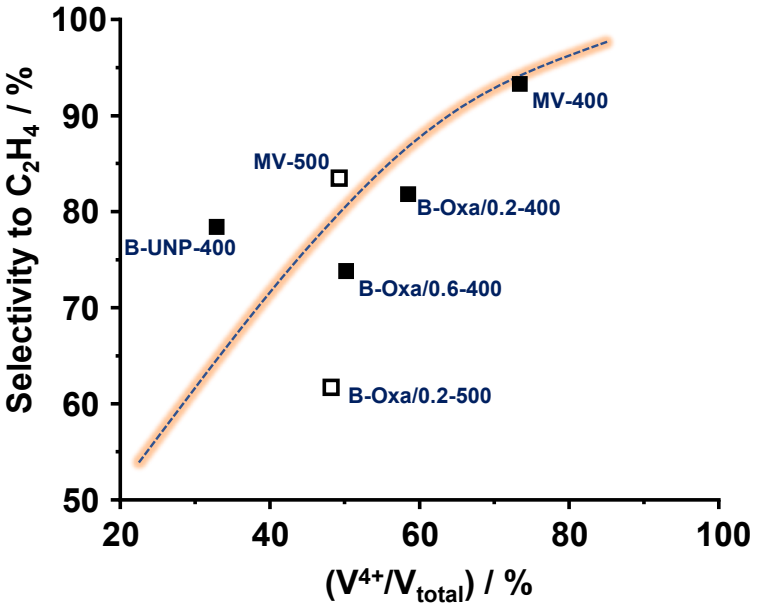

Figure 3.12. Selectivity to ethylene as a function of the V^{4+}/V_{total} ration on the surface of selected catalysts subjected to different post-synthesis treatments. Characteristics of catalysts in **Table 3.2**.

Accordingly, the best formulation of bimetallic MoVO catalysts, presenting all together the M1 phase in its maximum degree of crystallinity and the best catalytic performance in the ODH of ethane is the one that is synthesized from an aqueous gel at pH of ca. 3.0, for three days in an autoclave under inert atmosphere (N_2), subsequently activated at 400 ºC/2 hours/N_2 stream with further purification with a hydrogen peroxide solution 15% wt. This catalyst, named **MV-400** in this chapter, can perform competitive results in the ethane oxidative dehydrogenation.

3.7. References

1) W. Ueda, K. Oshihara, Selective oxidation of light alkanes over hydrothermally synthesized Mo-V-M-O (M=Al, Ga, Bi, Sb, and Te) oxide catalysts, Appl. Catal. A- Gen. 200 (2000) 135–143.

2) W. Ueda, K. Oshihara, D. Vitry, T. Hisano, Y. Kayashima, Hydrothermal synthesis of Mo-based oxide catalysts and selective oxidation of alkanes, Catal. Surv. Jap. 6 (2002) 33-44.

3) P. Botella, B. Solsona, A. Martinez-Arias, J.M. López Nieto, Selective oxidation of propane to acrylic acid on MoVNbTe mixed oxides catalysts prepared by hydrothermal synthesis, Catal. Lett. 74 (2001) 149-154.

4) P. Botella, J.M. López Nieto, B. Solsona, A. Mifsud, F. Márquez, The preparation, characterization, and catalytic behavior of MoVTeNbO catalysts prepared by hydrothermal synthesis, J. Catal. 209 (2002) 445–455.

5) W. Ueda, D Vitry, T. Katou, Structural organization of catalytic functions in Mo-based oxides for propane selective oxidation, Catal. Today 96 (2004) 235–240.

6) T. Katou, D. Vitry, W. Ueda, Structure dependency of Mo-V-O-based complex oxide catalysts in the oxidations of hydrocarbons, Catal. Today 91–92 (2004) 237–240.

7) W. Ueda, D. Vitry, T. Katou, Crystalline Mo–V–O based complex oxides as selective oxidation catalysts of propane, Catal. Today 99 (2005) 43–49.

8) N. Watanabe, W. Ueda, Comparative Study on the Catalytic Performance of Single-Phase Mo-V-O-Based Metal Oxide Catalysts in Propane Ammoxidation to Acrylonitrile, Ind. Eng. Chem. Res. 45 (2006) 607-614.

9) T. Konya, T. Katou, T. Murayama, S Ishikawa, M. Sadakane, D Buttrey, W. Ueda, An orthorhombic Mo_3VOx catalyst most active for oxidative dehydrogenation of ethane among related complex metal oxides, Catal. Sci. Technol. 3 (2013) 380-387.

10) S. Ishikawa, X. Yi, T. Murayama, W. Ueda, Heptagonal channel micropore of orthorhombic Mo_3VO_x as catalysis field for the selective oxidation of ethane, Appl. Catal. A- Gen. 474 (2014) 10–17.

11) F. Wanga, W. Ueda, Aerobic oxidation of alcohols over novel crystalline Mo–V–O oxide, Applied Catalysis A: General 346 (2008) 155–163.

12) C. Chen, N. Kosuke, T. Murayama, W. Ueda, Single-Crystalline-Phase Mo_3VOx: An Efficient Catalyst for the Partial Oxidation of Acrolein to Acrylic Acid, ChemCatChem 5 (2013) 2869 – 2873.

13) M. Sadakane, N. Watanabe, T. Katou, Y. Nodasaka, W. Ueda, Crystalline Mo_3VO_x Mixed-Metal-Oxide Catalyst with Trigonal Symmetry, Angew. Chem. Int. Ed. 46 (2007) 1493 –1496.

14) M. Sadakane, K. Kodato, T. Kuranishi, Y. Nodasaka, K. Sugawara, N. Sakaguchi, T. Nagai, Y. Matsui, W. Ueda, Molybdenum–Vanadium-Based Molecular Sieves with Microchannels of Seven-Membered Rings of Corner-Sharing Metal Oxide Octahedra, Angew. Chem. Int. Ed. 47 (2008) 2493 – 2496.

15) W. Ueda, M. Sadakane, H. Ogihara, Nano-structuring of complex metal oxides for catalytic oxidation, Catal. Today 132 (2008) 2–8.

16) M. Sadakane, K. Endo, K. Kodato, S. Ishikawa, T. Murayama, W. Ueda, Assembly of a Pentagonal Polyoxomolybdate Building Block, $[Mo_6O_{21}]^{6-}$, into Crystalline MoV Oxides, Eur. J. Inorg. Chem. 2013, 1731–1736.

17) W. D. Pyrz, D. A. Blom, Masahiro Sadakane, K. Kodato, W. Ueda, Th. Vogt, D. J. Buttrey, Atomic-level imaging of Mo-V-O complex oxide phase intergrowth, grain boundaries, and defects using HAADF-STEM, PNAS 107 (2010) 6152-6157.

18) M. Sadakane, Sh. Ohmura, K Kodato, T. Fujisawa, K. Kato, K.-i. Shimidzu, T. Murayama, W. Ueda, Redox tunable reversible molecular sieves: orthorhombic molybdenum vanadium oxide, Chem. Commun. 47 (2011) 10812–10814

19) S. Ishikawa, D. Kobayashi, T. Konya, S. Ohmura, T. Murayama, N. Yasuda, M. Sadakane, W. Ueda, Redox Treatment of Orthorhombic $Mo_{29}V_{11}O_{112}$ and Relationships between Crystal Structure, Microporosity and Catalytic Performance for Selective Oxidation of Ethane, J. Phys. Chem. C 119 (2015) 7195−7206.

20) J.M. Oliver, J.M. López Nieto, P. Botella, A. Mifsud, The effect of pH on structural and catalytic properties of MoVTeNbO catalysts, Appl. Catal. A-Gen. 257 (2004) 67–76.

21) A. Celaya Sanfiz, T. W. Hansen, F. Girgsdies, O. Timpe, E. Rödel, T. Ressler, A. Trunschke, R. Schlögl, Preparation of Phase-Pure M1 MoVTeNb Oxide Catalysts by Hydrothermal Synthesis-Influence of Reaction Parameters on Structure and Morphology, Top. Catal. 50 (2008) 19-32.

22) E. V. Ischenko, T. V. Andrushkevich, G. Ya. Popova, V. M. Bondareva, Y. A. Chesalov, T. Yu. Kardash, L. M. Plyasova, L. S. Dovlitova, A. V. Ischenko, Formation of active component of MoVTeNb oxide catalyst for selective oxidation and ammoxidation of propane and ethane, Stud. Surf. Sci. Catal. 175 (2010) 479-482.

23) T. M. N. Le, R. Checa, P. Bargiela, M. Aouine, J. M. M. Millet, New synthesis of pure orthorhombic Mo-V-A oxide phases, where A= Sb, Bi and Pb, and testing for the oxidation of light alkanes, J. Alloys Compd. 910 (2022) 164745.

24) Y. Chen, B. Yan, Y. Cheng, State-of-the-Art Review of Oxidative Dehydrogenation of Ethane to Ethylene over MoVNbTeOx Catalysts, Catalysts 13 (2023) 204.

25) G. Ya. Popova, T. V. Andrushkevich, L. S. Dovlitova, G. A. Aleshina, Yu. A. Chesalov, A. V. Ishenko, E. V. Ishenko, L. M. Plyasova, V. V. Malakhov, M. I. Khramov, The investigation of chemical and phase composition of solid precursor of MoVTeNb oxide catalyst and its transformation during the thermal treatment, Appl. Catal. A: Gen 353(2) (2009) 249-257.

26) S. Ishikawa, W. Ueda, Microporus crystalline Mo-V mixed oxides for selective oxidations, Catal. Sci. Technol. 6 (2016) 617.

27) S. Ishikawa, Y. Yamada, N. Kashio, N. Noda, K. Shimoda, M. Hayashi, T. Murayama, W. Ueda, True Catalytically Active Structure in Mo-V-Based Mixed Oxide Catalysts for Selective Oxidation of Acrolein, ACS Catal. 11 (2021) 10294-10307.

28) S. Yu, X. Zhao, G. Su, Y. Wang, Z. Wang, K. Han, H. Zhu, Synthesis and electrocatalytic performance of a P-Mo-V Keggin heteropolyacid modified Ag@Pt/MWCNTs catalyst for oxygen reduction in proton exchange membrane fuel cell, Ionics 25 (2019) 5141-5152.

29) S. Ishikawa, N. Noda, M. Wada, S. Tsurumi, W. Ueda, Selective Oxidation of Methacrolein over Crystalline Mo_3VO_x Catalysts and Comparison of Their Catalytic Properties with Heteropoly Acid Catalysts, ACS Catal. 10 (2020) 10535-10545.

30) V. Kumar, X. Wang, P. See Lee, Formation of hexagonal-molybdenum trioxide (*h*-MoO3) nanostructures and their pseudocapacitive behavior, Nanoscale 7 (2015) 11777-11786.

31) G. A. Zenkovets, A. A. Shutilov, V. M. Bondareva, V. I. Sobolev, A. S. Marchuk, S. V. Tsybulya, I. P. Prosvirin, A. V. Ishchenko, V. Yu Gavrilov, New multicomponent MoVSbNbCeOx/SiO_2 catalyst with enhanced catalytic activity for oxidative dehydrogenation of ethane to ethylene, ChemCatChem 12 (2020) 4149-4159.

32) P. Botella, E. García-González, J.M. López Nieto, J.M. González-Calbet, MoVTeNbO multifunctional catalysts: correlation between constituent crystalline phases and catalytic performance, Solid State Sci. 7 (2005) 507–519.

33) J.S. Valente, H. Armendáriz-Herrera, R. Quintana-Solórzano, P. Del Ángel, A. Massó, J.M. López Nieto, Chemical, structural, and morphological changes of a MoVTeNb catalyst during oxidative dehydrogenation of ethane, ACS Catal. 4 (2014) 1292–1301.

34) M. Baca, A. Pigamo, J.L. Dubois, J.M.M. Millet, Propane oxidation on MoVTeNbO mixed oxide catalysts: study of the phase composition of active and selective catalysts, Top. Catal. 23 (2003) 39–46.

35) I.E. Wachs, J.-M. Jehng, W. Ueda, Determination of the chemical nature of active surface sites present on bulk mixed metal oxide, J. Phys. Chem. B 109 (2005) 2275–2284.

36) G. Mestl, In situ Raman spectroscopy for the characterization of MoVW mixed oxide catalysts, J. Raman Spectrosc. 33 (2002) 333–347.

37) B. Solsona, M.I. Vázquez, F. Ivars, A. Dejoz, P. Concepción, J.M. López Nieto, Selective oxidation of propane and ethane on diluted Mo–V–Nb–Te mixed-oxide catalysts, J. Catal. 252 (2007) 271–280.

38) L. Seguin, M. Figlarz, R. Cavagnat, J.-C. Lassègues, Infrared and Raman spectra of MoO_3 molybdenum trioxide hydrates, Spectrochim. Acta A 51 (1995) 1323-1344.

39) P. Kube, B. Frank, S. Wrabetz, J. Kröhnert, M. Hävecker, J. Velasco-Vélez, J. Noack, R. Schlögl, A. Trunschke, Functional Analysis of Catalysts for Lower Alkane Oxidation, ChemCatChem 9 (2017) 573-585.

40) D. Vitry, Y. Morikawa, J. L. Dubois, W. Ueda, Propane Selective Oxidation Over Monophasic Mo-V-Te-O Catalysts Prepared by Hydrothermal Synthesis, Top. Catal. 23 (2003) 47-53.

41) P. Botella, E. García-González, A. Dejoz, J. M. López Nieto, M. I. Vázquez, J. González-Calbet, Selective oxidative dehydrogenation of ethane on MoVTeNbO mixed metal oxide catalysts, J. Catal. 225(2) (2004) 428-438.

42) J. M. López Nieto, B. Solsona, P. Concepción, F. Ivars, A. Dejoz, M. I. Vázquez, Reaction products and pathways in the selective oxidation of C_2-C_4 alkanes on MoVTeNb mixed oxide catalysts, Catal. Today 157 (2010) 291-296.

43) T. T. Nguyen, B. Deniau, P. Delichere, J. M. M. Millet, Influence of the content and distribution of vanadium in the M1 phase of the MoVTe(Sb)NbO catalysts on their catalytic properties in light alkanes oxidation, Top. Catal. 57 (2014) 1152–1162.

44) J. M. M. Millet, Mechanism of first hydrogen abstraction from light alkanes on oxide catalysts, Top. Catal. 38 (2006) 83–92.

45) P. DeSanto Jr., D. J. Buttrey, R. K. Grasselli, C. G. Lugmair, A. F. Volpe, B. H. Toby, Th. Vogt, Structural characterization of the orthorhombic phase M1 in MoVNbTeO propane ammoxidation catalyst, Top. Catal. 23 (2003) 23–38.

46) M. Sadakane, K. Kodato, N. Yasuda, S. Ishikawa, W. Ueda, Thermal behavior, crystal structure, and solid-state transformation of orthorhombic Mo-V oxide under nitrogen flow or in air, ACS Omega 4 (2019) 13165-13171.

47) A. M. Wernbacher, P. Kube, M. Hävecker, R. Schlögl, A. Trunschke, Electronic and dielectric properties of MoV-Oxide (M1 Phase) under alkane oxidation conditions, J. Phys. Chem. C. 123 (2019) 13269-13282.

Chapter 4

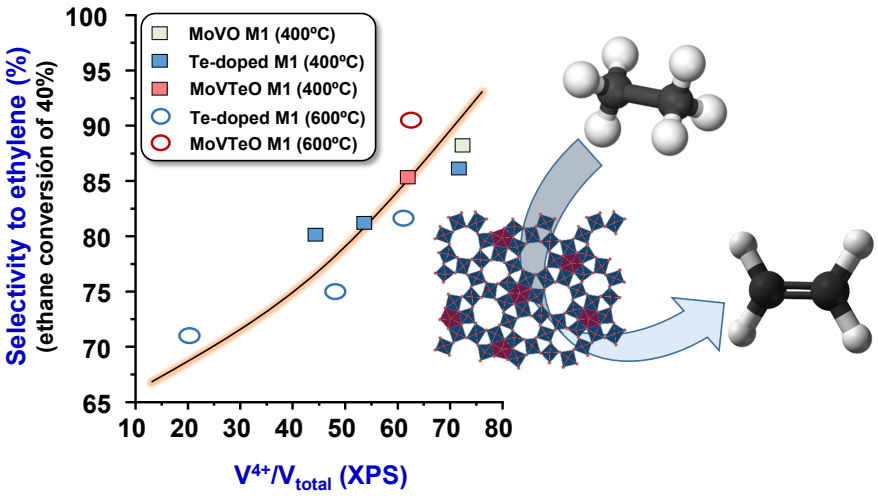

Te-doped M1-MoVOx catalysts: the role of tellurium on textural properties, thermal stability and catalytic behavior

4.1. Previous considerations

In the previous chapter, a wide range of synthesis routes and/or post-synthesis modifications in order to obtain the best catalytic performing bimetallic $MoVO_x$ catalyst were discussed. However, the following chapter is devoted to trimetallic M1-presenting Mo-V-Te-O catalysts and the study of the influence of the chemical composition (Te-content) and the final thermal activation (at 400 or 600 ºC in N_2) of catalysts on both the textural properties and the catalytic behavior in the oxidative dehydrogenation of ethane (ODHE).

It has been previously reported that M1-containing $MoVTeNbO_x$ [1-7] and $MoVTeO_x$ [8-11] materials are highly selective catalysts in propane (amm)oxidation to form acrylic acid/acrylonitrile, $MoVTeO_x$ presenting intermediate catalytic properties for propane amm(oxidation) between $MoVO_x$ (which are less selective but more active [12,13]) and $MoVTeNbO_x$ (which are more selective but less active) catalysts. The explanation for this catalytic behavior is given by the ability of the tellurium atoms of the M1 structure to selectively activate the allylic hydrogens of propylene to form acrolein (which is a reaction intermediate) [1-11], whereas Mo and V atoms are known to abstract the hydrogens of the propane to transform it into propylene.

Nevertheless, while deeper studies have been published concerting the (amm)oxidation of propane over this type of materials, scarce literature can be found for the ODH of ethane [14-17]. Moreover, it is well-known that the higher the activation temperature (600ºC usually [16]) the higher the

selectivity to the olefin is. However, the effect of the use of a lower thermal activation temperature (400 ºC) in not available anywhere.

Therefore, in this chapter, it is presented a comparative study on the physicochemical properties and catalytic performance of Te-doped $MoVO_x$ catalysts, synthesized from Te/Mo atomic ratios in the synthesis gel from 0.01 to 0.17, in order to ascertain the role of the tellurium atoms on the textural properties, thermal stability and surface chemical composition on catalysts activated at 400 ºC and 600 ºC, respectively. Furthermore, a correlation between these physicochemical properties and their catalytic performance in the oxidative dehydrogenation of ethane to ethylene will be stablish as a function of the Te-loading.

4.2. Physicochemical characterization of Te-doped $MoVO_x$ catalysts

Some of the main physicochemical properties of the synthesized $MoVTe_xO_y$ materials (i.e., **MVT-x-t**) heat-treated at 400ºC or 600ºC are displayed in **Table 4.1**, whereas results from typical characterization techniques are shown in **Figure 4.1**. In this sense, XRD patterns of samples heat-treated at 400 ºC and 600 ºC are displayed in **Figures 4.1-A** and **4.1-B**, respectively. As it can be seen, the M1 phase is the main constituent crystalline phase in every sample (2θ= 6.7º, 7.9º, 9.0º, 10.8º, 23.0º and 27.3º) [10-22], regardless of the composition and thermal activation temperature, even from the lowest tellurium promotion (samples **MVT-1-400/600**). In the case of the samples heat-treated at 400 ºC, no other crystalline phase rather than the M1 is observed.

Table 4.1. Characteristics of Te-doped MoV-Oxides catalysts.

Catalyst	Te/Mo ratio [a]	N_2-adsorption		CO_2-adsorption	H_2-TPR	TPD-NH_3
		Surface area ($m^2\ g^{-1}$) [b]	t-Plot Micropore volume ($10^3 \cdot cm^3\ g^{-1}$) [b]	Surface area ($m^2\ g^{-1}$) [c]	TMR (^oC) [d]	NH_3 desorption ($\mu mol_{NH3}\ g_{cat}^{-1}$) [e]
MV-400	0.00	35.2	10.9	68.9	465	551.8
MVT-1-400	0.01	60.0	16.9	n.d.[f]	450	n.d.
MVT-5-400	0.05	44.4	15.4	73.7	412	649.1
MVT-10-400	0.10	45.0	4.7	62.0	408	640.2
MVT-17-400	0.17	20.3	2.5	45.8	400	167.0
MV-600	0.00	7.2	1.7	n.d.	n.d.	123.2
MVT-1-600	0.01	17.9	2.8	n.d.	470	n.d.
MVT-5-600	0.05	12.9	3.5	35.6	479	186.4
MVT-10-600	0.10	13.5	3.0	27.8	517	121.8
MVT-17-600	0.17	7.9	1.9	28.3	502	160.8

[a] Te/Mo ratio in the synthesis gel; [b] Surface area and Micropore volume were calculated by BET and t-Plot methods, respectively, after N_2 adsorption isotherm; [c] Surface area calculated by Dubinin-Astakhov method. [d] TPR experiment. [e] Amount of ammonia chemisorbed at 100 ^oC during the NH_3-TPD experiment, per gram of catalyst (measured in standard temperature and pressure).[f] "n.d." stands for "non determined".

However, for solids calcined at 600 ºC, it is also observed, as traces, the minor presence of different crystalline phases such as $(Mo_{0.93}V_{0.07})_5O_{14}$ and $(V_{0.95}Mo_{0.97})O_5$ in catalyst with the lowest tellurium content, which suggests that the insertion of Te^{4+} species in the form of …Te-O-Te-… infinite chains along the hexagonal channels of the M1 structure enhances significantly the thermal stability of the catalysts [5, 17, 23-25]. In fact, M1 decomposition is mainly observed in Te-free sample during the heat-treatment at 600 ºC (see **Chapter 3**, **Figure 3.7-B**, sample **MV-600**).

Likewise, IR spectra in the low frequency region (1100 to 500 cm^{-1}) of the catalysts are shown in **Figure 4.1-C** and **Figure 4.1-D**. The majority presence of bands at 603, 653, 714, 866 and 919 cm^{-1} for all catalysts (at both activation temperatures) confirm the presence of the M1 phase, as reported by several authors [3, 10, 26]. More precisely, signals at 603, 653, 714 and 866 cm^{-1} correspond to antisymmetric Mo-O-X vibrations, where "X" can be either Mo or Te atoms, while the signal at 919 cm^{-1} is attributed to terminal (Mo, V)=O bonds.

Nevertheless, in the case of the catalysts heat-treated at 600 ºC (**MVT-x-600** series), it can also be observed the absence of any additional weak band at 896 cm^{-1} that corresponds to the pseudo hexagonal $TeMo_5O_{16}$ crystalline phase [3]. In addition to this, signals at 820 and 990 cm^{-1}, associated to MoO_3 [3], appear in samples with the highest tellurium content at both heat-treatment temperatures (**MVT-17-400** and **MVT-17-600**).

Lastly, **Figures 4.1-E** and **4.1-F** show Raman spectra for catalysts heat-treated at 400 and 600 ºC, respectively. As previously observed [27-29], a

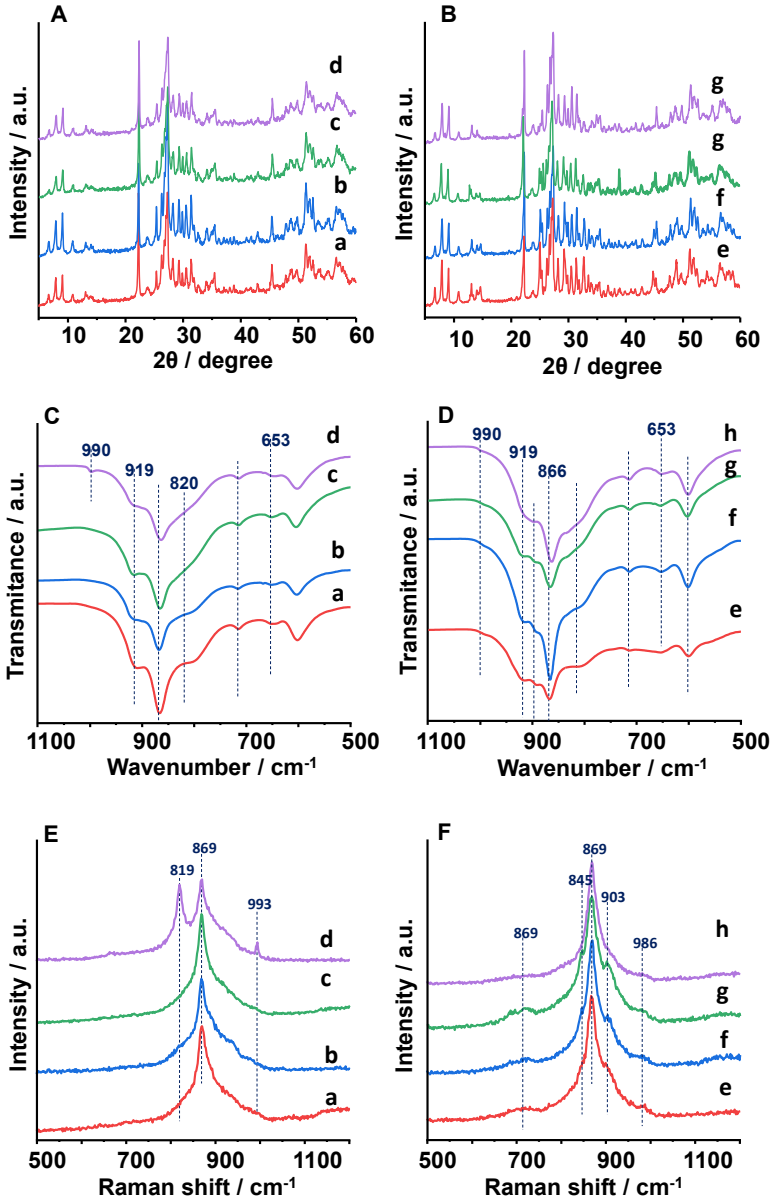

Figure 4.1. Physicochemical characterization of $MoVTe_x$ catalysts: XRD patterns (**A**, **B**), FTIR spectra (**C**, **D**) and Raman spectra (**E**, **F**) of samples heat-treated at 400 ºC (**A, C, E**) and 600 ºC (**B, D, F**): a) **MVT-1-400**; b) **MVT-5-400**; c) **MVT-10-400**; d) **MVT-17-400**; e) **MVT-1-600** ; f) **MVT-5-600**; g) **MVT-10-600**; h) **MVT-17-600**.

main band at ca. 869 cm^{-1} with a shoulder at higher frequencies (centered at ca. 903 cm^{-1}) can be seen, which have been widely attributed to the M1 phase. Moreover, and in agreement with XRD and IR results, consistent bands at 819 and 993 cm^{-1}, related to the presence of MoO_3 [30, 31], are observed for the **MVT-17-400** sample, while a weak small band centered at 986 cm^{-1}, associated in this case with the $TeMo_5O_{16}$ structure [3], is observed in **MVT-1-600**, **MVT-5-600** and **MVT-10-600** samples.

Therefore, **Figure 4.2-A to 4.2-D** presents a combined study of high-resolution transmission (HRTEM) and field emission scanning (FESEM) electronic microscopy of samples with different tellurium contents, and heat-treated at 400 ºC. In general, a clear tendency in observed among the catalysts. Thus, when looking at the FESEM analysis of the catalysts, a similar needle-like structure is obtained for all catalysts, with small differences in the width of the needles. As a general rule, the higher the tellurium content the narrower the needle.

However, by looking at the HRTEM micrographs, a completely opposite trend could be proposed. In this case, transmission microscopy results showed that in the case of the catalysts with lower tellurium contents (i.e., **MVT-1-400**, **MVT-5-400** and **MVT-10-400)** (**Figure 4.2-**(**A to C**) crystals are actually formed by a coalescence of rod-like crystallites that progressively grow to form a single crystal rod for the catalyst with the highest tellurium content (i.e., **MVT-17-400**, **Figure 4.2-D**).

In conclusion, the incorporation of Te cations into the M1 structure significantly modifies both crystallinity and crystal growth mode, even from the lowest Te-doping catalysts.

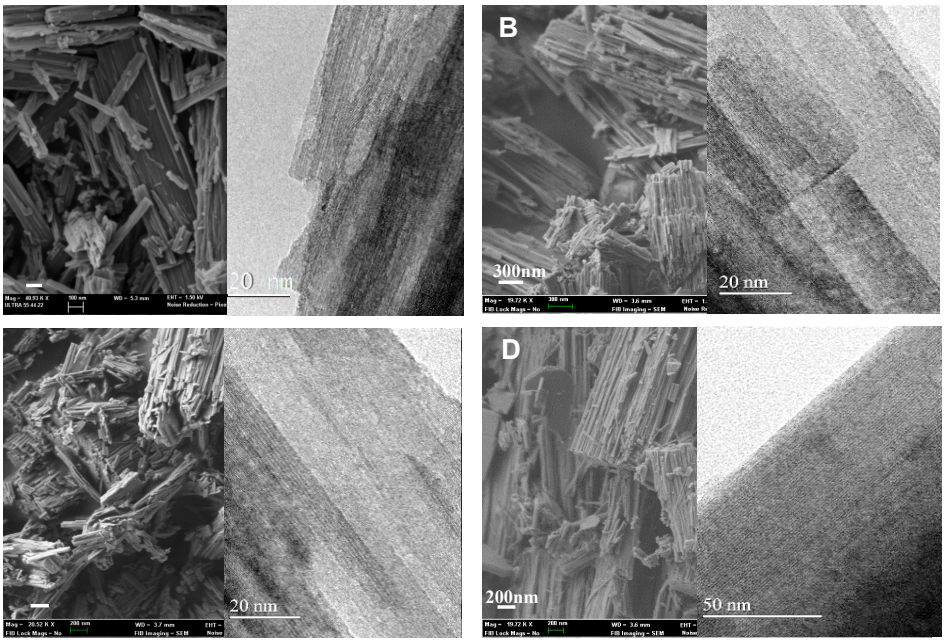

Figure 4.2. FESEM (left) and HRTEM (right) micrographs of **MVT-1-400** (**A**), **MVT-5-400** (**B**), **MVT-10-400** (**C**) and **MVT-17-400** (**D**) catalysts.

Furthermore, low magnification FESEM analysis (**Figure 4.3**) of selected as-synthesized samples (**MVT-5-as** and **MVT-17-as**) and those heat–treated at 600 ºC (**MVT-5-600** and **MVT-17-600**) were carried out with no significant differences with the ones presented in **Figure 4.2**. Accordingly, crystal growth habit depends exclusively on the chemical composition of the crystal.

Thus, in the light of the different morphology showed by the catalysts regarding their chemical composition (i.e., Te-loading), it is suggested that Te-content could have some implications in their textural properties.

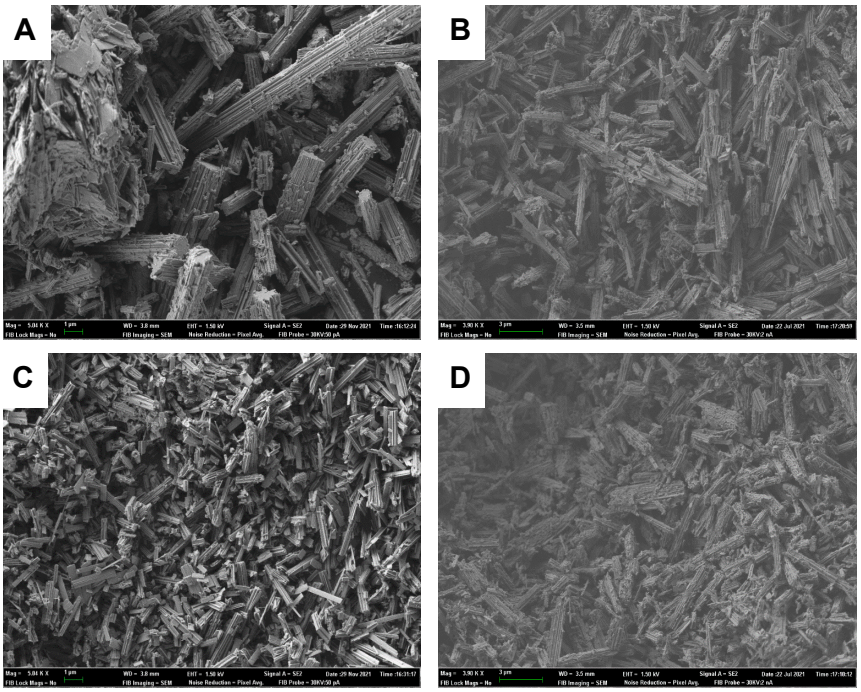

Figure 4.3. Low magnification (5K and 3.9K, respectively) of selected catalysts: **MVT-5-as** (**A**), **MVT-5-600** (**B**), **MVT-17-as** (**C**) and **MVT-17-600** (**D**).

In this sense, specific surface area and micropore volume values of Te-doped MoV-M1 oxides were estimated by N_2 adsorption isotherms, and results are shown in **Table 4.1**, while experimental plots can be seen in **Figure 4.4-(A to D)**. In this case, for comparison, **MV-400** and **MV-600** samples from **Chapter 3** (i.e., MoVO oxide heat-treated at 400 ºC and 600 ºC, respectively) have been also considered in **Table 4.1**. In order to do those estimations, BET and t-Plot methods were employed to calculate the specific surface area and the micropore volume values, respectively [18, 21, 32, 33, 34].

Regarding specific surface area, huge differences are observed considering both the activation temperature and the chemical composition of catalysts. Thus, for the catalysts heat-treated at 400 ºC (**MVT-x-400** series), an initial increase is seen for the catalyst with the lowest tellurium content, **MVT-1-400** (from 35.2 m^2 g^{-1} in the case of the **MV-400** sample to 60.0 m^2 g^{-1} for **MVT-1-400**), while a slight decrease for **MVT-5-400** and **MVT-10-400** with respect to the former is also observed. Finally, a deeper decrease is calculated for the catalyst with the highest tellurium content (**MVT-17-400**), whose specific surface area (20.3 m^2 g^{-1}) is even lower, 1.7 times, than the reference **MV-400** catalyst ($MoVO_x$ heat-treated at 400ºC).

Interestingly, similar trends are observed when it comes to the micropore volume values. In this way, low Te-contents favor an increase in the micropore volume, with maximum values of 16.9 $\cdot 10^3$ cm^3 g^{-1} and 15.4 $\cdot 10^3$ cm^3 g^{-1} for **MVT-1-400** and **MVT-5-400**, respectively. However, the most interesting results are observed when comparing samples **MVT-5-400** and **MVT-10-400**, which present similar specific surface areas (44.4 m^2 g^{-1} for the former vs 45.0 m^2 g^{-1} for the latter), but different micropore volume values when calculated from the t-Plot method. In fact, those values were up to ca. 3.3 times higher in the case of the sample with the lower tellurium content ($15.4 \cdot 10^3$ vs. $4.7 \cdot 10^3$ cm^3 g^{-1}). Indeed, these values suggest that high tellurium contents in M1-presenting catalysts may partially block the heptagonal channel of the structure [25], as well as the hexagonal ones, consequently decreasing the specific surface area but also the micropore volume of the synthesized oxides heat-treated at 400 ºC.

On the other hand, larger differences are observed in the catalysts heat-treated at 600 ºC (**MVT-x-600** series). A drastic decrease in both specific surface area and micropore volume values, compared to those observed for samples heat-treated at 400 ºC, are observed. In fact, for these catalysts, no proper micropore volume values were reported ($3.5 \cdot 10^3$ cm^3 g^{-1} in the best case, i.e., **MVT-5-600**) in addition to extremely low surface area values (the highest reported is 17.9 m^2 g^{-1} for **MVT-1-600**), regardless of the composition (see **Table 4.1**).

As a conclusion, M1-presenting undoped and Te-doped $MoVO_x$ catalysts with relatively high surface area and micropore volume values can be obtained hydrothermally by controlling the chemical composition and the thermal activation procedure [10, 19-22, 34].

Furthermore, it is known that analysis from N_2 adsorption isotherms underestimate specific surface area values when applying the BET method in the case of microporous materials, especially for small-pore zeolites like chabazite and LTA (eight membered rings) [35-38]. Moreover, it has been reported that empty heptagonal channels in the M1 phase are of a similar size than those of the small pore zeolites (ca. 4.2 Å) [19, 20]. So, in order to overcome these difficulties, CO_2 adsorption isotherms were carried out for the most representative catalysts. Results from these isotherms are presented in **Table 4.1**, while experimental data are shown in **Figures 4.4-E** and **4.4-F**. Moreover, it must be said that specific surface area values in this case were calculated by the Dubinin-Astakhov equation [39, 40]. For comparison, molybdenum trioxide (α-MoO_3) has been used as a reference

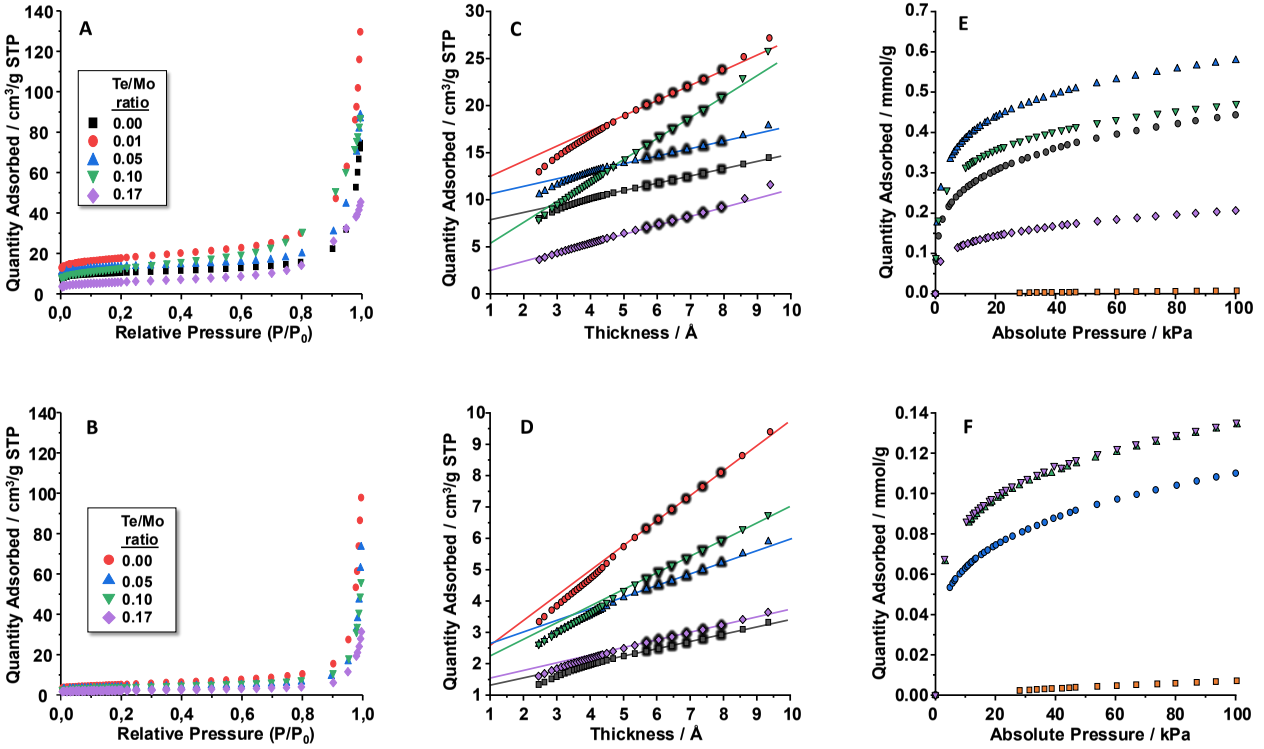

Figure 4.4. N_2-adsorption isotherms (**A**, **B**); t-Plot in N_2 adsorption, highlighting the points used for the linear fit (**C, D**) and CO_2-adsorption isotherms (**E**, **F**) of Te-doped $MoVO_x$ catalysts heat-treated at 400 ºC (**A**, **C, E**) or 600 ºC (**B**, **D**, **F**).

material with a similar structure that does not present any adsorption properties.

Therefore, and as suggested from the N_2 isotherms, the results of **Figures 4.4-E** and **4.4-F** suggest that the adsorption properties depend strongly on the heat-treatment temperature. For instance, by looking at samples **MVT-10-400** and **MVT-10-600** (i.e., same Te/Mo ratio but different thermal treatment), the adsorption capacity is ca. 3.5 times bigger in the case of the catalyst activated in N_2 at 400 ºC.

In our case, the highest CO_2 adsorption is observed for catalyst **MVT-5-400**, and the adsorption capacity decreases as the tellurium content increases, reaching the minor values for the catalysts with the highest tellurium into the structure (i.e., **MVT-10-400** and **MVT-17-400**). In any case, as shown in **Table 4.1**, the estimated specific surface values employing CO_2 as probe molecule are fairly higher than the ones obtained from N_2. Thus, in the case of **MVT-5-400**, a value of 44.4 $m^2\ g^{-1}$ is calculated from N_2 isotherm, whereas 73.7 $m^2\ g^{-1}$ is calculated from CO_2 isotherm (which supposes a 66% increase). Nevertheless, these results agree with previously reported in literature that outline that chemical composition and preparation method drastically affect the textural properties of M1-presenting MoV(Te,Nb) oxides [19-22, 34].

Besides that, the reducibility and acid properties of the Te-doped $MoVO_x$ catalysts were also studied by H_2-TPR and NH_3-TPD, respectively. **Figure 4.5-A** shows the H_2-TPR profiles of samples heat-treated at 400 ºC, while those of the ones activated at 600 ºC can be seen in **Figure 4.5-B**.

In the case of the **MVT-x-400** series (**Fig. 4.5-A**), it was observed that the temperature of the first reduction maxima decreased as the tellurium loading increased, shifting the first reduction maxima from ca. 450 ºC in **MVT-1-400** to 400 ºC for the **MVT-17-400** sample. Far smaller differences, however, were obtained for the **MVT-x-600** series (**Fig. 4.5-B**), where all the first reduction maxima appeared in a 30 ºC range, so that no clear conclusions can be drawn in this case. Nevertheless, two different clear trends were ascertained regarding the calcination temperature. Thus, for samples heat-treated at 400ºC (**MVT-x-400** series), the onset of the reduction maxima decreases as the tellurium content increases, whereas in the case of the **MVT-x-600** series, an opposite trend for the onset of the reduction maxima can be proposed. In addition, it must be said that samples heat-treated at 400 ºC seem to be more reducible than the ones activated at 600 ºC (the reduction profiles start at 300 ºC for the **MVT-x-400** series vs ca. 400 ºC for the **MVT-x-600** series).

Regarding the acid properties of some of the most representative catalysts studied in this chapter, results from NH_3-TPD are presented in **Figures 4.5-C** and **4.5-D** (normalized by BET surface area) and **Figures 4.5-E** and **4.5-F** (normalized by weight of catalyst), while the amount of ammonia desorbed during TPD-experiments can be seen in **Table 4.1**.

For samples heat-treated at 400 ºC (**Figs. 4.5-C** and **E**), **MVT-5-400** catalyst was the one that presented the highest value of NH_3 desorbed and the highest number of acid sites (see **Table 4.1**), either when normalized by surface area (**Fig. 4.5-C**) or by catalysts' mass (**Fig. 4.5-E**).

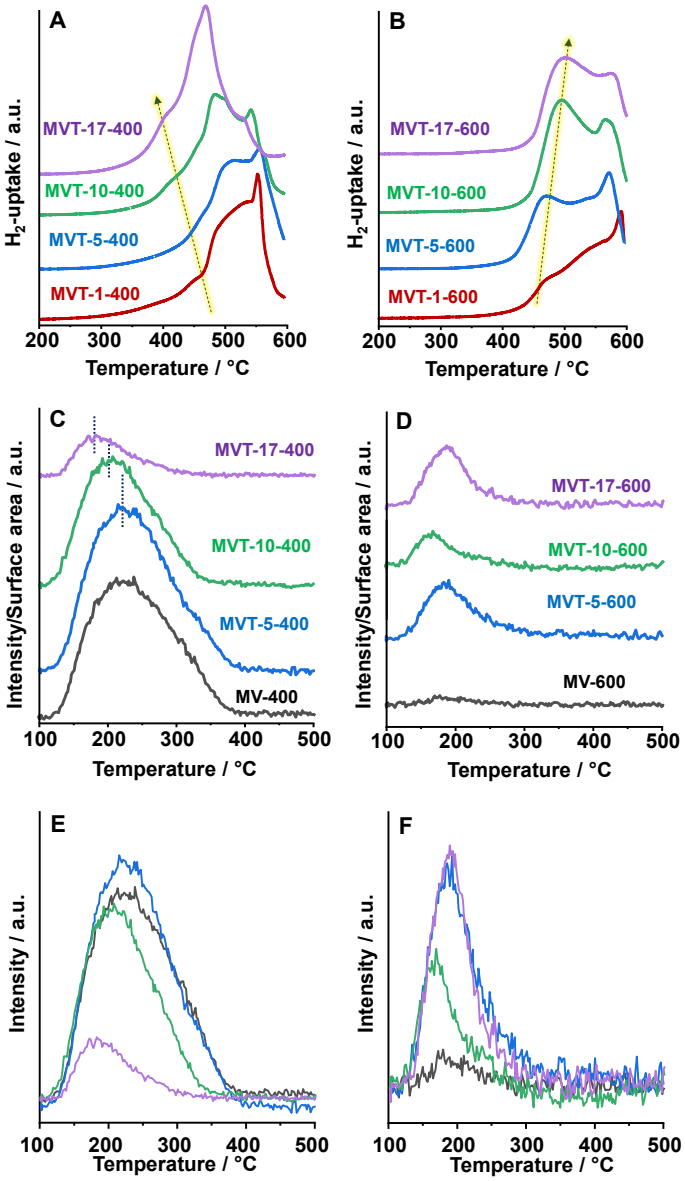

Figure 4.5. H_2-TPR profiles of **MVT** catalysts calcined at 400 ºC (**A**) and 600 ºC (**B**); NH_3-TPD profiles of representative **MVT** samples: normalized by BET surface area calcined at 400 ºC (**C**) and 600 ºC (**D**); or normalized by mass of catalyst and calcined at 400 ºC (**E**) and 600 ºC (**F**).

Nevertheless, for this series, a shift in the desorption maxima to lower temperatures is observed when increasing the tellurium content, which indicates that the different amount of tellurium into the M1 structure decreases the strength of the corresponding acid sites.

A similar trend is also observed by the catalysts activated at 600 ºC (**Figs. 4.5-D** and **F**), although it is especially interesting the case of the **MVT-17-600** sample. This catalyst is the one that reported the highest amount of NH_3 desorbed (clearly seen in **Fig. 4.5-F**), although as a result of the normalization by surface area may look different in **Fig. 4.5-D**. In fact, the quantity of ammonia desorbed in **MVT-17-600** is more than twice the one of its 400 ºC treated counterpart (i.e. **MVT-17-400**).

Furthermore, if a comparison is stablished between the catalysts calcined at 400 ºC and 600 ºC, it can be seen that the desorption maxima is shifted to lower temperatures in the case of the **MVT-x-600** series, which suggest that higher activation temperatures provoke a decrease in the strength of the acid sites of Te-doped M1-$MoVO_x$ catalysts, in agreement to previous results [41, 42].

4.3. Catalytic performance of Te-doped $MoVO_x$ catalysts in ethane ODH

Te-containing $MoVO_x$ catalysts were tested in the oxidative dehydrogenation of ethane (ODHE) and, for comparison, the best performing catalysts from **Chapter 3** heat-treated at 400 ºC and 600 ºC (**MV-400** and **MV-600**, respectively) were used as reference. Reaction

conditions in this case were set to: 350-400 ºC temperature range (to prevent possible transformations in the solids heat-treated at 400 ºC) and a contact time, W/F, of 16.0 g_{cat} h $(mol_{C2H6})^{-1}$ for the **MVT-x-400 series** or 65.0 g_{cat} h $(mol_{C2H6})^{-1}$ for the **MVT-x-600** series.

Table 4.2 shows the catalytic results (in terms of ethane conversion and selectivity to the main reaction products) for both series of catalysts, i.e., samples heat-treated at 400 or 600 ºC. In addition, it has been also included the specific activity and the rate formation of ethylene per unit mass of catalyst (STY_{C2H4}). It can be seen that the samples of the **MVT-x-400** series presented notably higher values of catalytic activity than those achieved for the **MVT-x-600** series, which can be partially explained by the higher surface area of the first series of catalysts.

Figures 4.6-A and **4.6-B** show the selectivity to ethylene as a function of the ethane conversion, at isothermal conditions, for the catalysts activated at 400 ºC (**Fig. 4.6-A**) or activated at 600 ºC (**Fig. 4.6-B**). It can be observed that, depending on the thermal treatment, completely different trends were obtained regarding the composition of the catalysts. In this sense, for **MVT-x-400** series, the higher the tellurium content the lower the ethylene selectivity. On the other hand, in the **MVT-x-600** series, the selectivity to ethylene was directly related to the tellurium content, this is, the selectivity to ethylene increased with the tellurium content, being the **MVT-17-600** catalyst the one that presents the best values in terms of selectivity, within the series and overall. Nonetheless, it must be noted that these differences in selectivity to ethylene among the series should be referred to the initial

values, since all the samples presented the same drop in selectivity at higher ethane conversions.

Table 4.2. Catalytic results during the ethane ODH over Te-free and Te-containing catalysts.[a]

Cat.	W/F[b]	Conv.	Selectivity (%)			Specific	STY_{C2H4}[d]
		(%)	C_2H_4	CO	CO_2	Activity[c]	
MV-400	16	33.7	87.4	4.0	8.6	23.0	644
MVT-1-400	16	52.5	77.1	5.3	17.6	21.0	1058
MVT-5-400	16	58.8	80.2	5.2	14.6	32.8	1225
MVT-10-400	16	26.4	84.5	3.6	11.9	10.7	381
MVT-17-400	16	5.7	88.0	3.0	9.0	5.1	85.7
MV-600	65	1.9	80.9	5.9	13.2	1.21	6.57
MVT-1-600	65	5.4	84.5	4.5	11.0	1.38	19.5
MVT-5-600	65	9.3	83.0	3.5	13.4	3.30	33.0
MVT-10-600	65	11.2	91.4	2.1	6.4	4.47	50.8
MVT-17-600	65	19.3	93.4	1.7	4.9	13.7	96.2

a) Reaction conditions: T = 390 ºC, C_2H_6/O_2/He molar ratio = 5/5/90.

b) Contact time, W/F, in g_{cat} h mol_{C2}^{-1}.

c) Catalytic activity normalized per surface area (determined by N_2-adsorption) in 10^{-3} g_{C2H4} m^{-2} h^{-1}. Determined at ethane conversions lower than 10 %.

d) Rate formation of ethylene per unit mass of catalyst, STY_{C2H4} (space time yield), in g_{C2H4} kg_{cat}^{-1} h^{-1}. Determined at ethane conversions lower than 10 %.

Furthermore, the variation of the activity of catalysts from both series was also studied. Thus, the specific activity (activity normalized per BET surface area) as a function of the Te/Mo atomic ratio (synthesis gel values) are presented in **Fig. 4.6-C** (**MVT-x-400** series) and **Fig. 4.6-D** (**MVT-x-600** series). As a general trend, it can be observed that in the case of the

catalysts with the lowest tellurium content (**MVT-1-t** and **MVT-5-t**), activity values were around one order of magnitude higher when calcined at 400 ºC, reaching a maximum for the **MVT-5-400** sample (ca. 10 times higher than that for **MVT-5-600**).

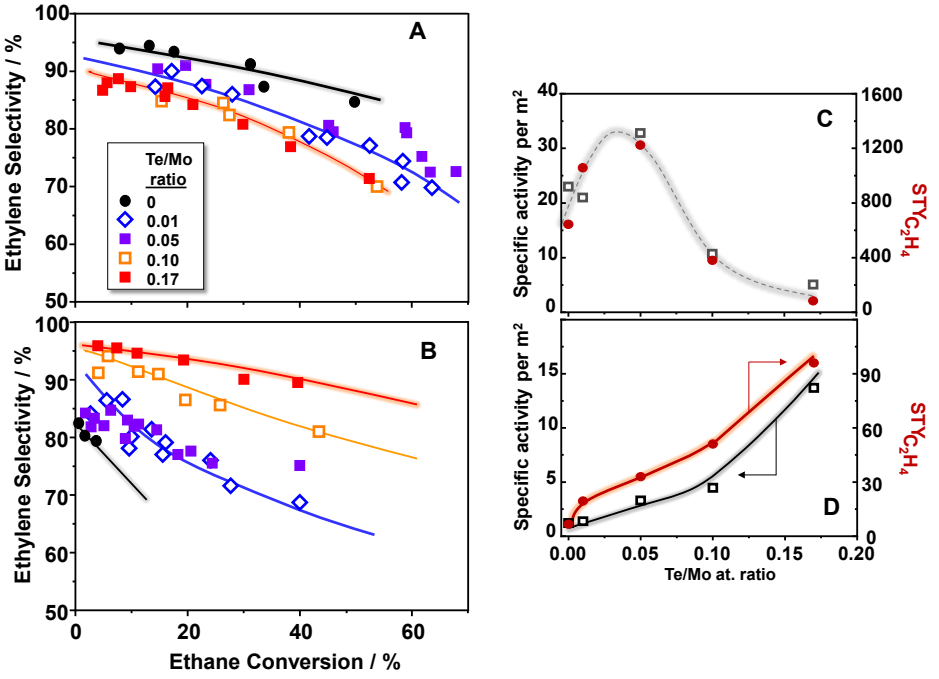

Figure 4.6. Variation of the selectivity to ethylene as a function of the ethane conversion of Te-doped $MoVO_x$ catalysts activated at 400 ºC, MVT-x-400 series (**A**) or 600 ºC, MVT-x-600 series (**B**). Experimental conditions described in page 123. Variation of the specific activity and the rate of ethylene formation (STY_{C2H4}) with the Te/Mo ratio in the synthesis gel for preparation of Te-doped MoVOx catalysts heat-treated at 400 ºC (**C**) and 600 ºC (**D**). In all cases, **MV-400** or **MV-600** catalysts (from **Chapter 3**) have been used as references.

Interestingly, depending on the activation temperature, two different performances were observed. In that sense, for the **MVT-x-400** series (**Fig 4.6-C**), the catalytic activity increased initially with the tellurium content up to **MVT-5-400**, with a dramatic loss in activity for **MVT-10-400** and **MVT-17-400** samples. For the **MVT-x-600** series (**Fig. 4.6-D**) the catalytic activity increased concomitantly with the tellurium content, observing the maximum of the series in the **MVT-17-600** sample. Unexpectedly, in the case of the catalyst with highest tellurium content (Te/Mo=0.17), the specific activity showed greater values when calcined at 600 ºC rather than the sample treated at 400 ºC.

Noteworthy, it has been also compared the values of the specific activity of the catalysts calcined at 400 ºC as a function of their micropore volume (see **Table 4.1**), these values perfectly correlate one to each other, suggesting that, in the case of the **MVT-x-400** series, the activity of the samples is governed by the micropore volume of the catalyst.

Nevertheless, regarding the **MVT-x-600** series, as almost negligible values of micropore volume were obtained, it is supposed that the driving force in terms of both activity and selectivity to ethylene must be related to the chemical composition of the sample.

4.4. Surface characterization of Te-doped $MoVO_x$ catalysts

In the light of the catalytic results showed in the last section of the chapter, since no clear relation was observed between the physicochemical properties of the catalysts and their catalytic performance in terms of

selectivity to ethylene, we decided to undertake a detailed study of the surface of the Te-doped $MoVO_x$ materials.

Therefore, the near surface region of the samples was studied by XPS analysis, and results are shown in **Figure 4.7** and **Table 4.3**.

Figures 4.7-A and **4.7-B** show the V *2p*$_{3/2}$ core level spectra of the catalysts activated in N_2 at 400 ºC and 600 ºC, respectively. In both figures, the experimental signal can be deconvoluted in two signals that can be assigned the simultaneous presence of V^{4+} (B.E. of 515.9 eV) and V^{5+} (B.E. of 517.0 eV) species [3, 6, 12, 41-46]. Nevertheless, even presenting these two types of signals, clear differences are observed within the series. Once again, Te-free samples from **Chapter 3** (**MV-400** and **MV-600**) were used as references for the two calcination temperatures.

A comparison of catalysts heat-treated at 400 ºC (**MVT-x-400** series, **Figure 4.7-A**) suggests that the relative intensity of the signal corresponding to V^{5+} species (i.e., the one centered at 517.0 eV) increased with the tellurium content, to a point that it is the main signal for the catalyst **MVT-17-400**. In contrast, Te-free catalyst (**MV-400**) and the samples doped with the lowest tellurium amount (**MVT-1-400** and **MVT-5-400**) were the ones that presented V^{4+} species as majority. In the case of the **MVT-x-600** series (**Fig. 4.7-B**), an opposite trend is observed, being the catalyst **MVT-17-600** the one that showed the highest proportion of the signal associated with V^{4+} species with a 62.6% of relative abundance (see **Table 4.3**).

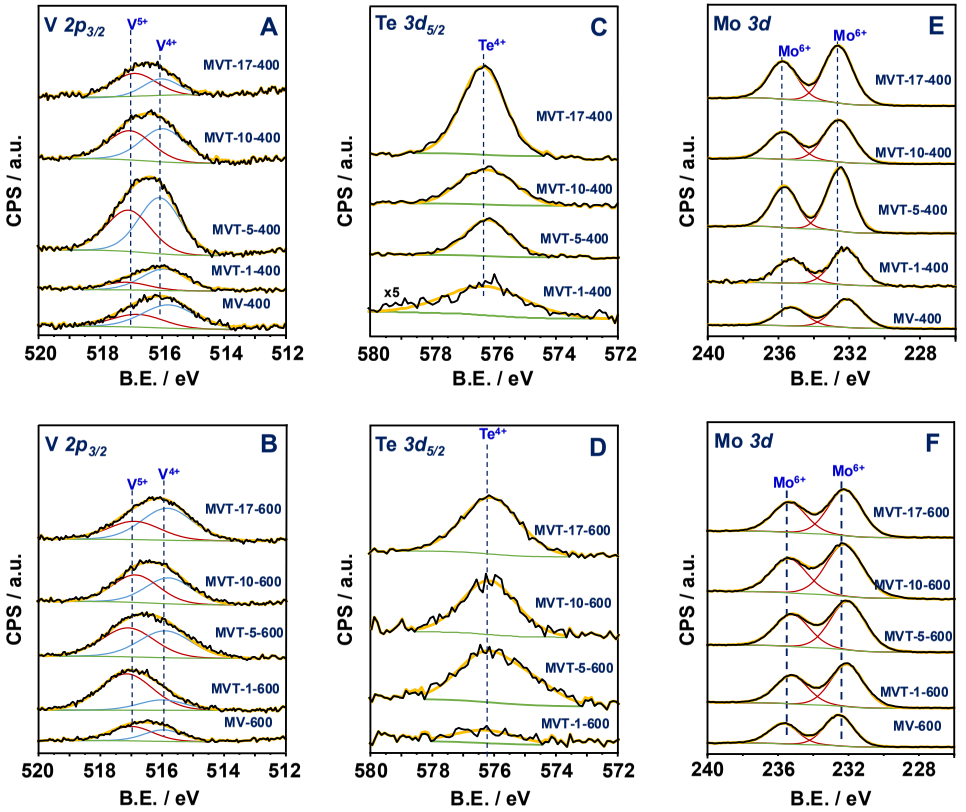

Figure 4.7. XPS spectra of V $2p_{3/2}$ (**A, B**), Te $3d_{5/2}$ (**C, D**) and Mo *3d* (**E, F**) core level of catalysts heat-treated at 400 ºC (**A, C, E**) or 600ºC (**B, D, F**).

Thus, it can be suggested that, in this case, the incorporation of Te-O-Te chains along the hexagonal channels may block the segregation of V^{5+} species during the activation step, as previously proposed by other authors [22, 46].

On the other hand, **Figures 4.7-C** and **4.7-D** shows the spectra for Te $3d_{5/2}$ core level for **MVT-x-400** and **MVT-x-600** catalysts, respectively. In both figures, a unique signal centered at 576.3 eV was ascertained, suggesting the only presence of Te^{4+} species within the samples along the series [3, 47].

Finally, Mo *3d* core level spectra for samples heat-treated at 400 ºC and 600 ºC (**Figures 4.7-E** and **4.7-F**, respectively). In general, a single signal in the form of a doublet, at 235.6 eV (Mo $3d_{5/2}$) and at 232.5 eV (Mo $3d_{3/2}$), was observed for both series confirming the single presence of Mo^{6+} species [3, 41, 42, 46-49].

Furthermore, data obtained from XPS deconvolution were compared to EDX analyses and formal synthesis composition in order to obtain a relationship between the bulk oxides and their surface, as well as the tellurium incorporation during the hydrothermal synthesis, depending on the tellurium content and the calcination temperature.

Table 4.3. XPS of Te-free and Te-containing Mo-V-O catalysts.

Catalyst	Mo/V/Te atomic ratio		XPS results			
	EDX	XPS	Mo^{6+}/Mo_{tot} (%)	Te^{4+}/Te_{tot} (%)	V^{4+}/V_{tot} (%)	Me/O ratio
MV-400	0.73/0.27/0.00	0.86/0.14/0.00	100	0	73.4	22.0/78.0
MVT-1-400	0.73/0.26/0.02	0.86/0.13/0.02	100	100	64.3	27.3/72.8
MVT-5-400	0.70/0.26/0.04	0.80/0.16/0.03	100	100	59.0	31.6/68.4
MVT-10-400	0.70/0.25/0.05	0.80/0.15/0.05	100	100	52.7	32.3/67.7
MVT-17-400	0.73/0.19/0.08	0.85/0.07/0.08	100	100	43.7	32.5/67.5
MV-600	n.d.	0.89/0.11/0.00	100	0	34.4	31.2/68.8
MVT-1-600	0.71/0.28/0.01	0.85/0.14/0.01	100	100	20.3	28.7/71.3
MVT-5-600	0.70/0.27/0.03	0.82/0.15/0.03	100	100	19.5	31.0/69.0
MVT-10-600	0.71/0.25/0.05	0.81/0.14/0.05	100	100	61.9	31.9/68.1
MVT-17-600	0.73/0.21/0.06	0.82/0.14/0.04	100	100	62.6	31.9/68.1

Therefore, in **Figure 4.8** it is presented the variation in the Te/Mo and V/Mo ratio as a function of the Te/Mo nominal value in the synthesis gel determined by EDX (**Figs. 4.8-A** and **4.8-C**) and XPS (**Figs. 4.8-B** and **4.8-D**).

In the case of the catalysts calcined at 400 ºC (**MVT-x-400** series, **Fig. 4.8-A**), as expected, the Te/Mo increased continuously as the Te-loading increased in the synthesis gel. Nonetheless, when it comes to the V/Mo proportion, it did not suffer any change until the maximum Te-loading (sample **MVT-17-400**), suggesting that, as supposed in references [22, 41], the incorporation of Te^{4+} species into the hexagonal channels of the M1 structure blocks the incorporation of vanadium species in those positions. Moreover, for the **MVT-x-600** series (**Fig. 4.8-B**), a similar trend is followed in both Te/Mo and V/Mo relationships, however, the continuous depletion in the vanadium content as the tellurium loading increases is clearly seen for this series.

In addition, in **Figures 4.8-C** and **4.8-D** is plotted the Te/Mo and V/Mo ratios with the Te/Mo proportion calculated from EDX analyses for catalysts calcined at 400 ºC and 600 ºC, respectively. Thus, in **Fig. 4.8-C** it is observed a similar trend as in **Fig. 4.8-A**, but, in the sample **MVT-17-400** the tendency is specially marked, being in fact lower the vanadium proportion in the surface of the catalyst than the tellurium content. On the contrary, in the case of the **MVT-x-600** series, **Fig. 4.8-D** shows the opposite trend in the V/Mo ratio when compared to the V/Mo proportion calculated by EDX (**Fig. 4.8-B**). This fact suggests that, as discussed in the XPS part, the joint use of higher activation temperatures and non to low

tellurium contents favor the segregation of V atoms (V^{5+} species, mainly) from the bulk to the surface [22, 46] in the catalysts from the **MVT-x-600** series. What is more important, this enrichment in the V^{5+} relative amount on the surface of the catalysts is suggested to have large influences on the selectivity to ethylene, since this kind of species have been previously related to perform total oxidation reactions, therefore favoring the transformation of ethylene into CO_x [44, 50, 51].

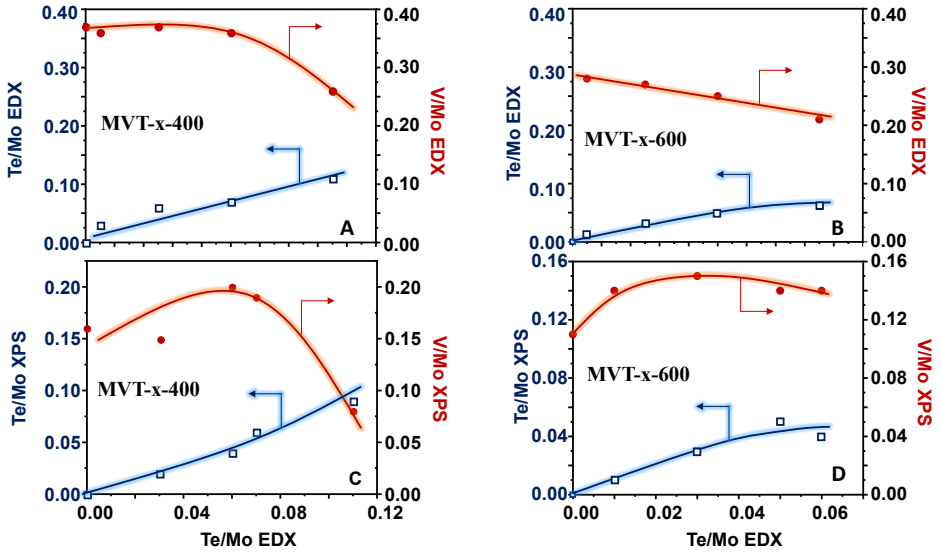

Figure 4.8. Variation of the Te/Mo and V/Mo atomic ratios, determined by EDX, with the Te/Mo ratio in the synthesis gel for catalysts heat-treated at 400 ºC (**A**) or 600 ºC (**B**). Variation of the Te/Mo and V/Mo atomic ratios, determined by XPS, with the Te/Mo atomic ratio determined by EDX for catalysts calcined at 400 ºC (**C**) and 600 ºC (**D**).

4.5. Conclusions

As evidenced in this chapter, Te-doped $MoVO_x$ catalysts can be synthesized hydrothermally with different tellurium contents and, after a thermal activation at 400 ºC or 600 ºC in a N_2 atmosphere, all of them present the M1 phase as majority.

Nevertheless, although all the catalysts studied were active and selective in the oxidative dehydrogenation of ethane to ethylene, clear differences were observed depending on the thermal activation and the tellurium content of catalysts.

In this sense, characterization results from XRD, IR and Raman shown in **Fig. 4.1** proved that, first of all, the incorporation of tellurium into the M1 structure resulted in a strong enhancement in the thermal stability of the materials, maintaining said structure at activation temperatures up to 600 ºC, even for the lowest Te-contents (i.e., sample **MVT-1-600**).

In addition, the tellurium content of catalysts has a notable effect in both the morphology (**Figures 4.2** and **4.3**) and the textural properties (**Figure 4.4**, **Table 4.1**) of the catalysts. Thus, for catalysts heat-treated at 400 ºC, the experimental results showed that little tellurium contents led to a clear increase in the specific surface area and the micropore volume (especially in **MVT-1-400** and **MVT-5-400** samples), probably due to the different morphology exhibited by these catalysts (**Figure 4.2**), going from an aggregation of microneedles (**MVT-1-400**) to finally a single needle-like crystal (**MVT-17-400**). However, for catalysts heat-treated at 600 ºC, despite showing similar morphologies (**Figure 4.3**), the higher thermal

activation led to a partial sintering of the microneedles, therefore decreasing dramatically the values obtained for specific surface area and micropore volume (**Table 4.1**).

With respect to the catalytic performance for ODHE, **Figures 4.6-A** and **4.6-B** showed that the selectivity to ethylene strongly depended on the chemical composition of the catalysts. However, the thermal activation also played an important role in the catalytic activity of said materials. Thus, for catalysts of the **MVT-x-400** series (**Figure 4.6-C**), the catalytic activity can be directly related to the micropore volume of the catalyst, reaching a maximum for the **MVT-5-400** sample (which is the one that presented the largest value of micropore volume). Moreover, the drastic drop in activity seen in **MVT-10-400** and **MVT-17-400** coincided exactly with the lower micropore volume (which were determined from t-Plot analyses for these samples). On the contrary, textural properties did not explain the different catalytic performance in catalysts calcined at 600 ºC (**Figure 4.6-D**).

Figure 4.9-A shows the variation of the selectivity to ethylene as a function of the Te/Mo relationship, at a fixed catalytic condition of 40% of ethane conversion, for the catalysts calcined at 400 ºC and 600 ºC. Interestingly, both series seemed to follow a completely different trend. On one hand, for the **MVT-x-400** series, the higher the Te content, the lower the selectivity to ethylene. These results for **MVT-x-400** series could agree with previous studies by Annamalai *et al.* [34] which reported that the micropores of the M1 phase are the place where the ethane molecule is more selectively activated. This fact was explained by the tight confinement of ethane/ethylene molecules in the micropores [18, 34], stabilized by Van der

Walls forces, preventing the O-insertion and, consequently, the formation of CO and CO_2.

However, for the **MVT-x-600** series, in which a negligible microporosity was observed, the selectivity to ethylene increased with the tellurium proportion into the sample. In fact, **MVT-17-600** was the catalyst that presented the highest selectivity value regardless of the composition and the thermal activation, with a 90% ethylene selectivity at 40% of ethane conversion. Nevertheless, paradoxically, its compositional counterpart calcined at 400ºC (**MVT-17-400**) was the catalyst that showed the lower selectivity to ethylene of its series (75% of ethylene selectivity at 40% of ethane conversion).

Nonetheless, and what bears the most attention, the selectivity to ethylene can be perfectly explained in terms of the surface composition of the catalysts and, more precisely, the relative presence of V^{4+} species. In this regard, when comparing the selectivity to ethylene as a function of the V^{4+}/V_{total} relationship obtained by XPS data treatment (**Figure 4.9-B**), it can be observed that, regardless of the chemical composition of the catalyst (i.e., Te/Mo ratio) and its thermal activation (400 or 600 ºC), the higher the amount of V^{4+} species the higher the selectivity to ethylene is.

Hence, selectivity to ethylene for the catalysts activated at 400 ºC or 600 ºC should be explained by the surface composition of the samples, especially with the concentration of V^{4+} species on the catalyst surface.

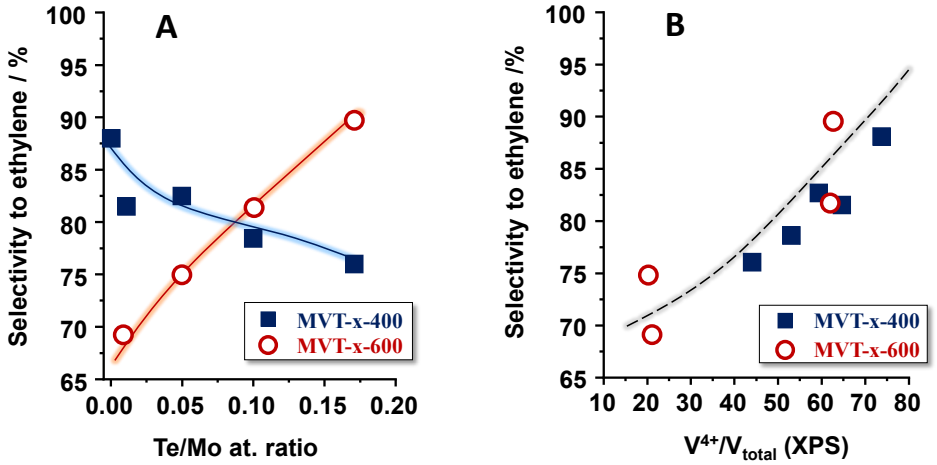

Figure 4.9. Variation of the selectivity to ethylene as a function of Te/Mo ratio in the synthesis gel (**A**) or as a function of the V^{4+}/V_{total} relationship (calculated by XPS) on the surface of the catalysts (**B**), for catalysts heat-treated at 400 ºC (**MVT-x-400** series) or 600 ºC (**MVT-x-600**, series). Data obtained for an ethane conversion of 40% and 390 ºC of reaction temperature (**Table 4.2**). V^{4+}/V_{total} ratio of catalysts, calculated by XPS (see **Table 4.3**).

Still, these results allow us to conclude that the incorporation of Te^{4+} species into the structure of the M1 phase in the form of infinite chains {-Te-O-Te-} [17, 52-54] has a determining effect in the crystallization mode and crystallinity of Te-doped $MoVO_x$ catalyst, therefore modifying their catalytic properties. However, in addition to this, the presence of Te^{4+} species could also have a strong influence on the stabilization of V^{4+} species in catalysts activated at 600 ºC.

4.6. References

1) H. Tsuji, Y. Koyasu, Synthesis of MoVNbTe(Sb)Ox composite oxide catalysts via reduction of polyoxometalates in an aqueous medium, J. Am. Chem. Soc. 124 (2002) 5608-5609.

2) J. M. M. Millet, H. Roussel, A. Pigamo, J. L. Dubois, J.C. Jumas, Characterization of tellurium in MoVTeNbO catalysts for propane oxidation or ammoxidation, Appl. Catal. A- Gen. 232 (2002) 77-92.

3) P. Botella, J. M. López Nieto, B. Solsona, A. Mifsud, F. Márquez, The preparation, characterization, and catalytic behavior of MoVTeNbO catalysts prepared by hydrothermal synthesis, J. Catal. 209 (2002) 445-455.

4) D. Vitry, Y. Morikawa, J.L. Dubois, W. Ueda, Mo-V-Te-(Nb)-O mixed metal oxides prepared by hydrothermal synthesis for catalytic selective oxidations of propane and propene to acrylic acid, Appl. Catal. A-Gen. 251 (2003) 411–424.

5) P. DeSanto, D.J. Buttrey, R.K. Grasselli, C.G. Lugmair, A.F. Volpe, B.H. Toby, T. Vogt, Structural characterization of the orthorhombic phase M1 in MoVNbTeO propane ammoxidation catalyst, Top. Catal. 23 (2003) 23–38.

6) A. Celaya Sanfiz, T.W. Hansen, F. Girgsdies, O. Timpe, E. Rodel, T. Ressler, A. Trunschke, R. Schlögl, Preparation of phase-pure M1 MoVTeNb oxide catalysts by hydrothermal synthesis-influence of reaction parameters on structure and morphology, Top. Catal. 50 (2008) 19–32.

7) J.M. Oliver, J.M. López Nieto, P. Botella, Selective oxidation and ammoxidation of propane on a Mo–V–Te–Nb–O mixed metal oxide catalyst: a comparative study, Catal. Today 96 (2004) 241–249.

8) D. Vitry, Y. Morikawa, J.L. Dubois, W. Ueda, Propane selective oxidation over monophasic Mo–V–Te–O catalysts prepared by hydrothermal synthesis, Top. Catal. 23 (2003) 47–53.

9) V.V. Guliants, R. Bhandari, J.N. Al-Saeedi, V.K. Vasudevan, R.S. Soman, O. Guerrero-Pérez, M.A. Bañares, Bulk mixed Mo–V–Te–O catalysts for propane oxidation to acrylic acid, Appl. Catal. A- Gen. 274 (2004) 123–132.

10) P. Concepción, S. Hernández, J.M. López Nieto, On the nature of active sites in MoVTeO and MoVTeNbO catalysts: The influence of catalyst activation temperature, Appl. Catal. A.: Gen. 391 (2011) 92–101.

11) P. Botella, P. Concepción, J.M. López Nieto, Y. Moreno, The influence of Te-precursor in Mo-V-Te-O and Mo-V-Te-Nb-O catalysts on their catalytic behaviour in the selective propane oxidation, Catal. Today 99 (2005) 51–57.

12) W. Ueda, D. Vitry, T. Katou, Structural organization of catalytic functions in Mo-based oxides for propane selective oxidation, Catal. Today 96 (2005) 235–240.

13) W. Ueda, D. Vitry, T. Katou, Crystalline MoVO based complex oxides as selective oxidation catalysts of propane, Catal. Today 99 (2005) 43–49.

14) W. Ueda, K. Oshihara, Selective oxidation of light alkanes over hydrothermally synthesized Mo-V-M-O (M=Al, Ga, Bi, Sb, and Te) oxide catalysts, Appl. Catal. A-Gen. 200 (2000) 135–143.

15) W. Ueda, K. Oshihara, D. Vitry, T. Hisano, Y. Kayashima, Hydrothermal synthesis of Mo-based oxide catalysts and selective oxidation of alkanes, Catal. Surv. Jpn 6 (2002) 33–43.

16) P. Botella, A. Dejoz, M.C. Abelló, M.I. Vázquez, L. Arrúa, J.M. López Nieto, Selective oxidation of ethane: developing an orthorhombic phase in Mo–V–X (X= Nb, Sb, Te) mixed oxides, Catal. Today 142 (2009) 272–277.

17) M. Aouine, T. Epicier, J. M. M. Millet, In situ environmental STEM study of the MoVTe oxide M1 phase catalysts for ethane oxidative dehydrogenation, ACS Catal. 6 (2016) 4775–4781.

18) L. Annamalai, Y. Liu, S. Ezenwa, Y. Dang, S.L. Suib, P. Deshlahra, Influence of tight confinement on selective oxidative dehydrogenation of ethane on MoVTeNb mixed oxides, ACS Catal. 8 (2018) 7051–7067.

19) T. Konya, T. Katou, T. Murayama, S. Ishikawa, M. Sadakane, D. Buttrey, W. Ueda, An orthorhombic Mo_3VOx catalyst most active for oxidative dehydrogenation of ethane among related complex metal oxides, Catal. Sci. Technol. 3 (2013) 380–387.

20) M. Sadakame, W. Ueda, Redox treatment of orthorhombic $Mo_{29}V_{11}O_{112}$ and relationships between crystal structure, microporosity and catalytic performance for selective oxidation of ethane, J. Phys. Chem. C. 119 (2015) 7195–7206.

21) S. Ishikawa, X. Yi, T. Murayama, W. Ueda, Heptagonal channel micropore of orthorhombic Mo_3VOx as catalysis field for the selective oxidation of ethane, Appl. Catal. A-Gen. 474 (2014) 10–17.

22) Sadakane, K. Kodato, N. Yasuda, S. Ishikawa, W. Ueda, Thermal behavior, crystal structure, and solid-state transformation of orthorhombic Mo–V oxide under nitrogen flow or in air, ACS Omega 4 (2019) 13165–13171.

23) N. Watanabe, W. Ueda, Comparative study on the catalytic performance of single-phase Mo-V-O-based metal oxide catalysts in propane ammoxidation to acrylonitrile, Ind. Eng. Chem. Res. 45 (2006) 607–614.

24) J.S. Valente, H. Armendáriz-Herrera, R. Quintana-Solórzano, P. Del Ángel, A. Massó, J.M. López Nieto, Chemical, structural, and morphological changes of a MoVTeNb catalyst during oxidative dehydrogenation of ethane, ACS Catal. 4 (2014) 1292–1301.

25) P. Botella, E. García-González, J.M. López Nieto, J.M. González-Calbet, MoVTeNbO multifunctional catalysts: correlation between constituent crystalline phases and catalytic performance, Solid State Sci. 7 (2005) 507–519.

26) J.M. López Nieto, P. Botella, B. Solsona, J. M. Oliver, The selective oxidation of propane on Mo-V-Te-Nb-O catalysts: The influence of Te-precursor, Catal. Today 81 (2003) 87–94.

27) I. E. Wachs, J.-M. Jehng, W. Ueda, Determination of the chemical nature of active surface sites present on bulk mixed metal oxide, Catal., J. Phys. Chem. B 109 (2005) 2275–2284.

28) G. Mestl, In situ Raman spectroscopy for the characterization of MoVW mixed oxide catalysts, J. Raman Spectrosc. 33 (2002) 333–347.

29) B. Solsona, M.I. Vázquez, F. Ivars, A. Dejoz, P. Concepción, J.M. López Nieto, Selective oxidation of propane and ethane on diluted Mo–V–Nb–Te mixed-oxide catalysts, J. Catal. 252 (2007) 271–280.

30) J.C.J. Bart, F. Cariati, A. Sgamellotti, Mixed-valence effects in tellurium-molybdenum oxides, Inorg. Chim. Acta 36 (1979) 105–112.

31) F. Ivars, B. Solsona, E. Rodríguez-Castellón, J.M. López Nieto, Selective propane oxidation over MoVSbO catalysts. On the preparation, characterization and catalytic behavior of M1 phase, J. Catal. 262 (2009) 35–43.

32) B. Chu, L. Truter, T.A. Nijhuis, Y. Cheng, Performance of phase-pure M1 MoVNbTeOx catalysts by hydrothermal synthesis with different post-treatments for the oxidative dehydrogenation of ethane, Appl. Catal. A Gen. 498 (2015) 99–106.

33) M. Thommes, K. Kaneko, A.V. Neimark, J.P. Olivier, F. Rodríguez-Reinoso, J. Rouquerol, K.S.W. Sing, Physisorption of gases, with special reference to the evaluation of surface area and pore size distribution, Pure Appl. Chem. 87 (2015) 1051–1069.

34) L. Annamalai, S. Ezenwa, Y. Dang, H. Tan, S.L. Suib, P. Deshlahra, Comparison of structural and catalytic properties of monometallic Mo and V oxides and M1 phase mixed oxides for oxidative dehydrogenation, Catal. Today 368 (2021) 28–45.

35) K. Ch Kim, T.-U. Yoon, Y.-S. Bae, Applicability of using CO_2 adsorption isotherms to determine BET surface areas of microporous materials, Microp. Mesop. Mater 223 (2016) 294–301.

36) D. Melzer, G. Mestl, K. Wanninger, A. Jentys, M. Sanchez-Sanchez, J.A. Lercher, On the promoting effects of Te and Nb in the activity and selectivity of M1 MoV-oxides for ethane oxidative dehydrogenation, Top. Catal. 63 (2020) 1754–1764.

37) G. Ya. Popova, T. V. Andrushkevich, Yu. A. Chesalov, L. M. Plyasova, L. S. Dovlitova, E. V. Ischenko, G. I. Aleshina, M. I. Khramov, Formation of active

phases in MoVTeNb oxide catalysts for ammoxidation of propane, Catal. Today 144 (2009) 312-317.

38) E. Pérez-Botella, M. Palomino, S. Valencia, F. Rey, Zeolites and other adsorbents, in: K. Kaneko, F. Rodríguez-Reinoso (Eds.), Nanoporous Materials for Gas Storage. Green Energy and Technology, Springer, Singapore, 2019, https://doi.org/ 10.1007/978-981-13-3504-4_7.

39) E. Pérez-Botella, R. Martínez-Franco, N. González-Camuñas, A. Cantín, M. Palomino, M. Moliner, S. Valencia, F. Rey, Unusually low heat of adsorption of CO_2 on AlPO and SAPO molecular sieves, Front. Chem. 8 (2020) 588712.

40) M. M. Dubinin, Physical adsorption of gases and vapors in microporesm in *Progress in Surface and Membrane Science,* eds D. A. Cadenhead, J. F. Danielli and M. D. Rosenberg (New York, NY: Elsevier), 1-70 (1975).

41) M. Baca, A. Pigamo, J. L. Dubois, J. M. M. Millet, Fourier transform infrared spectroscopic study of surface acidity by pyridine adsorption on the M1 active phase of the MoVTe(Sb)NbO catalysts used in propane oxidation, Catal. Commun. 6 (2005) 215–220.

42) F. Ivars-Barceló, J. M. M. Millet, T. Blasco, P. Concepción, J.S. Valente, J.M. López Nieto, Understanding effects of activation-treatments in K-free and K-MoVSbO bronze catalysts for propane partial oxidation, Catal. Today 238 (2014) 41–48.

43) T.Y. Kardash, E.V. Lazareva, D.A. Svintsitskiy, A.V. Ishchenko, V.M. Bondareva, R. B. Neder, The evolution of the M1 local structure during preparation of VMoNbTeO catalysts for ethane oxidative dehydrogenation to ethylene, RSC Adv. 8 (2018) 35903–35916.

44) B. Chu, H. An, X. Chen, Y. Cheng, Phase-pure M1 MoVNbTeOx catalysts with tunable particle size for oxidative dehydrogenation of ethane, Appl. Catal. A- Gen. 524 (2016) 56–65.

45) E.I. Ishchenko, R.V. Gulyaev, T. Yu. Kardash, E. Yu. Kardash, A.V. Ishchenko, E. Yu. Gerasimov, V.I. Sobolev, V.M. Dondareva, Effect of Bi on catalytic performance and stability of MoVTeNbO catalysts in oxidative dehydrogenation of ethane, Appl. Catal. A- Gen. 534 (2017) 58–69.

46) A.M. Wernbacher, P. Kube, M. Hävecker, R. Schlögl, A. Trunschke, Electronic and dielectric properties of MoV-Oxide (M1 Phase) under alkane oxidation conditions, J. Phys. Chem. C. 123 (2019) 13269–13282.

47) D.A. Svintsitskiy, T.Y. Kardash, E.V. Lazareva, A.A. Saraev, E.A. Derevyannikova, M. Vorokhta, B. Šmídc, V.M. Bondareva, NAP-XPS and in situ XRD study of the stability of Bi-modified MoVNbTeO catalysts for oxidative dehydrogenation of ethane, Appl. Catal. A, Gen. 579 (2019) 141–150.

48) T.Y. Kardash, E.V. Lazareva, D.A. Svintsitskiy, A.V. Ishchenko, V.M. Bondareva, R. B. Neder, The evolution of the M1 local structure during preparation of VMoNbTeO catalysts for ethane oxidative dehydrogenation to ethylene, RSC Adv. 8 (2018) 35903–35916.

49) A. Trunschke, J. Noack, S. Trojanov, F. Girgsdies, T. Lunkenbein, V. Pfeifer, M. Hävecker, P. Kube, C. Sprung, F. Rosowski, R. Schlögl, The impact of the bulk structure on surface dynamics of complex Mo–V-based oxide catalysts, ACS Catal. 7 (2017) 3061–3071.

50) J. M. M. Millet, Mechanism of first hydrogen abstraction from light alkanes on oxide catalysts, Top. Catal. 38 (2006) 83–92.

51) S. Benomar, A. Chieregato, A. Massó, M. D. Soriano, J. A. Vidal-Moya, T. Blasco, R. Issaadi, J.M. López Nieto, Al_2O_3-supported W–V–O bronze catalysts for oxidative dehydrogenation of ethane, Catal. Sci. Technol. 10 (2020) 8064–8075.

52) M.-J. Cheng, W. A. Goddard III, The mechanism of alkane selective oxidation by the M1 phase of Mo–V–Nb–Te mixed metal oxides: suggestions for improved catalysts, Top. Catal. 59 (2016) 1506–1517.

53) M.-J. Cheng, W. A. Goddard III, In silico design of highly selective Mo-V-Te-Nb-O mixed metal oxide catalysts for ammoxidation and oxidative dehydrogenation of propane and ethane, J. Am. Chem. Soc. 137 (2015) 13224–13227.

54) J. M. Arce-Ramos, A. Genest, N. Rösch, How TeO defects in MoVTeNbO catalysts material affect the V^{4+} distribution: a computational Study, J. Phys. Chem. C 124 (2020) 18628–18638.

Chapter 5

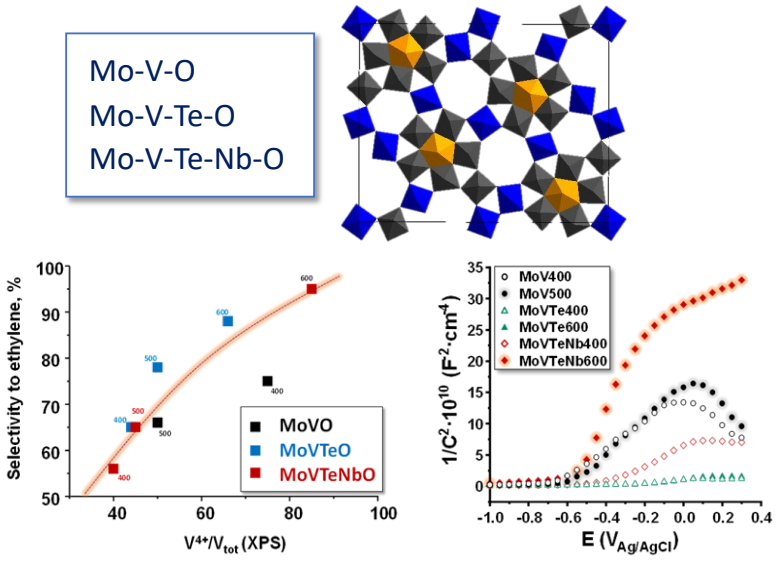

Influence of composition and thermal treatment on M1-containing catalysts: catalytic and electrochemical approach

5.1. Previous considerations

Until now, previous chapters within the thesis have been dedicated to find the best formulations for bi- and trimetallic M1-presenting catalysts. However, this chapter is dedicated to establishing a comparison between them and the tetrametallic Mo-V-Te-Nb-O catalysts that, up to date, are the materials that present the best catalytic properties in the oxidative dehydrogenation of ethane to ethylene [1-10].

In this sense, an improved selectivity to ethylene is a key step to be optimized [1-5, 11, 12] in order to develop a sufficiently competitive alternative to steam cracking for the production of light olefins (ethylene yields should be around 65-70%). Interestingly, multicomponent Mo-V-Te-Nb mixed oxide can give rise to ethylene yields up to 75% at reaction temperatures of 400 ºC, for catalysts heat-treated at 550-650 ºC.

Nevertheless, both activity and selectivity to ethylene decrease drastically when tetra-metallic catalysts are activated at temperatures between 350-500 ºC [1], temperatures at which the orthorhombic M1 phase ($Te_2M_{20}O_{58}$, M= Mo, V, Nb) is not formed. Consequently, the selectivity to ethylene is suggested to be directly related to the majority presence of the M1 phase, although its complex structure and composition supposes a great challenge.

Therefore, in the last few years, many research groups have been trying to optimize the synthesis of M1-type mixed oxides with the objective of understand the physicochemical and structural features [7-9, 13-25]. This way, bimetallic Mo-V-O [26-29] and trimetallic Mo-V-Te-O [30-32], studied in **Chapters 3** and **4**, respectively, were proposed to be active and

selective catalysts in ethane ODH, but presenting dissimilar properties than tetrametallic Mo-V-Te-Nb oxides, since selectivity to ethylene and structural stability are highly dependent on thermal activation temperatures, favoring consecutive reactions and the formation of carbon oxides [20, 30, 32].

Moreover, this type of mixed metal oxides can be considered as semiconductors, so the surface oxidation/reduction processes that take place (driven by the Mars-Van Krevelen mechanism) can be interpreted as a function of the different electrochemical properties of the solids. In this sense, the Microwave Cavity Perturbation Technique (MCPT) has been used by Wernbacher *et al.* [33] to determine the electrical conductivity of MoVTeNb oxides during the oxidation of light alkanes (i.e., ethane, propane and n-butane), and also by Heine *et al.* [34] to study the effect of steam on the electronic structure of these oxides during propane ODH. Additionally, changes in the electrical conductivity of pseudo-he xagonal M2-MoVTeNb oxide were evaluated in the oxidation of propylene to acrylic acid by the Differential Step Technique (DST) [35].

Even several electrochemical techniques have been applied to these materials, as described above, powerful non-destructive Electrochemical Impedance Spectroscopy (EIS) technique, from which catalysts' resistances can be calculated, has never been applied to study them. Furthermore, by performing Mott-Schottky plots (analysis of the capacitance) semiconductor behavior, as well as the type of semiconductivity, can be ascertained.

Consequently, the aim of the present chapter is to perform a comparative study between M1-presenting catalysts (i.e., Mo-V-O, Mo-V-Te-O and Mo-V-Te-Nb-O) and their different properties in ethane ODH. Then, this catalytic behavior will be explained in terms of their different activation temperature (400 ºC, 500 ºC or 600 ºC in N_2), main crystalline phases (studied by XRD and electronic microscopy) and surface species (determined by XPS). On top of that, detailed electrochemical characterization in order to correlate the catalytic data will be performed by using EIS, Mott-Schottky analysis and cyclic voltammetries.

5.2. Physicochemical characterization of catalysts

Most representative physicochemical features of bi-, tri- and tetrametallic M1-presenting catalysts heat-treated at 400, 500 or 600 ºC are presented in **Table 5.1**. Note that in the case of bimetallic and trimetallic catalysts, results are obtained from best performing catalysts in **Chapter 3** (**MV-400**, **MV-500** and **MV-600** samples) and **Chapter 4** (**MVT-17-400** and **MVT-17-600** catalysts), respectively.

In this sense, **Figure 5.1** (**A**, **B** and **C**) shows, separately, the XRD pattern of both as made and differently heat-treated catalysts. Interestingly, strong differences can be observed for each series of composition regarding activation temperature. In one hand, Mo-V-O and Mo-V-Te-O catalysts present a well-defined M1 phase from the as made material (i.e., diffraction peaks at 2θ= 6.7º, 7.9º, 9.0º, 10.8º, 23.0º and 27.3º) reported in previous chapters.

Table 5.1. Some physicochemical properties of the MoV(Te,Nb)O catalysts.

Catalyst	Mo/V/Te/Nb at. composition [1]	Mo/V/Te/Nb at. XPS composition	V^{+4}/V^{+5} ratio (XPS)	Surface area ($m^2\ g^{-1}$)
MV-400	1/0.37/0/0	1/0.18/0/0	75/25	35.2
MV-500	1/0.37/0/0	1/0.16/0/0	50/50	21.4
MV-600	1/0.34/0/0	1/0.13/0/0	34/66	7.2
MVT-17-400	1/0.37/0.13/0	1/0.08/0.10/0	44/56	20.3
MVT-17-500	1/0.38/0.10/0	1/0.22/0.03/0	62/38	17.6
MVT-17-600	1/0.46/0.08/0	1/0.17/0.05/0	66/34	7.9
MVTN-400	1/0.23/0.21/0.22	1/0.14/0.28/0.27	40/60	55.1
MVTN-500	1/0.23/0.21/0.22	n.d.	n.d.	35.0
MVTN-600	1/0.22/0.26/0.23	1/0.14/0.40/0.28	85/15	17.0

[1)] Catalyst composition after activation done by EDX.

Nevertheless, the lack of tellurium atoms in bimetallic catalysts lead to a notable decrease in the thermal stability when activation temperature rise above 500 ºC (depicted in the **MV-600** sample, **Fig. 5.1-A**), situation not observed in trimetallic Mo-V-Te-O catalysts, where the M1 phase is the majority in as made and heat-treated materials regardless of the thermal treatment (**Fig. 5.1-B**). On the other hand, XRD patterns for tetrametallic Mo-V-Te-Nb-O catalysts (**Fig. 5.1-C**) show a different trend. Thus, a pseudocrystalline structure, represented by wide diffraction bands (especially at $2\theta < 10.0^{o}$ and 25º-30º range) was observed in as made and heat-treated materials under 550 ºC, as previously reported [36].

However, in the case of sample heat treated at 600 ºC, the **MVTN-600** catalyst, sharp and narrow well-defined diffraction peaks are shown. In addition, clear differences in the intensity relationship of most representative 23.0º/27.3º diffraction peaks suggest that differently synthesized M1 phase crystallites should present a rather distinct shape depending on the chemical composition of the sample.

Furthermore, these catalysts activated at 400, 500 or 600 ºC were investigated by FT-IR and Raman spectroscopies. Thus, FT-IR results in the low frequency region (1200-500 cm^{-1}) for the different catalysts prepared in this chapter are shown in **Fig. 5.1 (**pictures **D**, **E** and **F)**. In the case of MoV- and MoVTe-based catalysts (**Fig. 5.1-D** and **Fig. 5.1-E**, respectively), the appearance of bands at 909, 866, 816, 714, 653 and 598 cm^{-1} demonstrate the majority formation of the M1 phase [36, 37, 38].

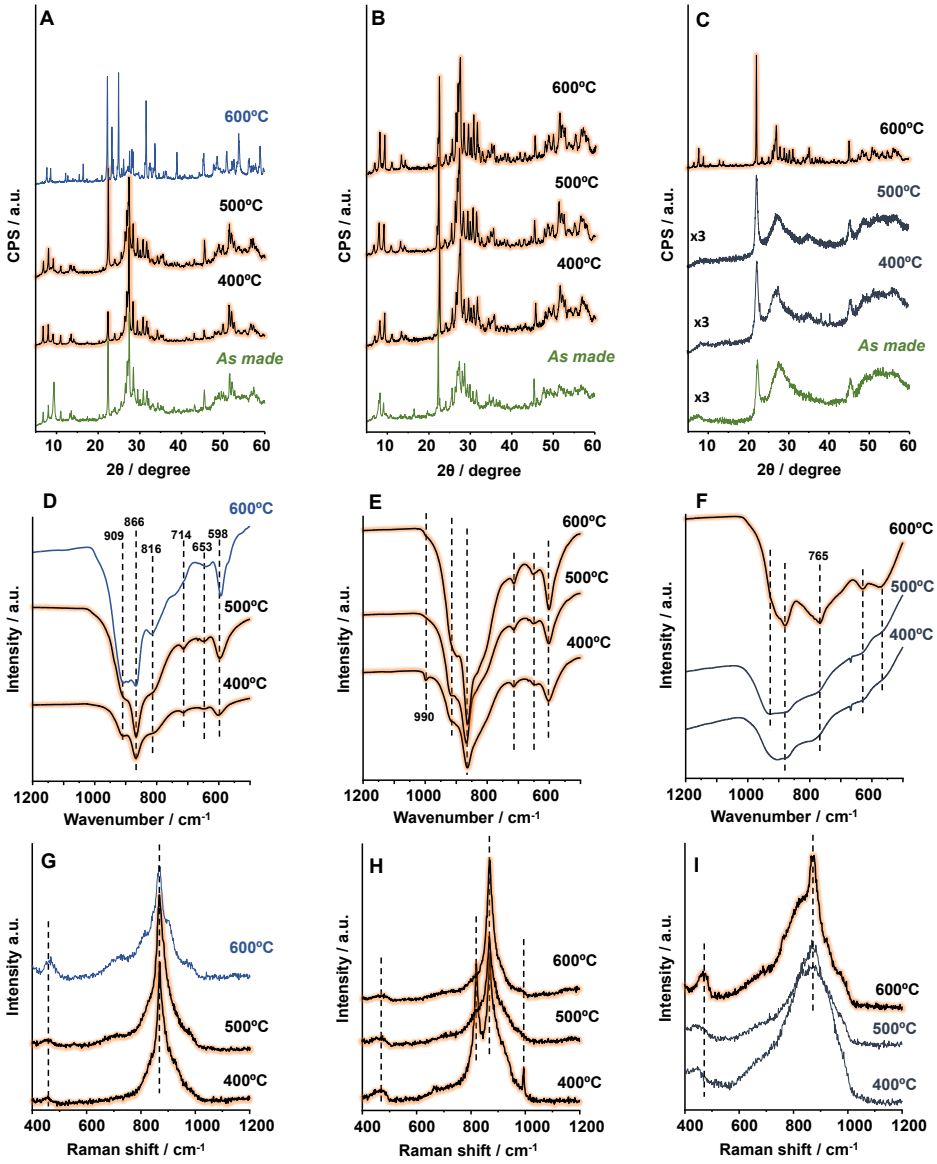

Figure 5.1. XRD patterns (**A**, **B** and **C**), FT-IR (**D**, **E** and **F**) and Raman (**G**, **H** and **I**) spectra of Mo-V-O (**A**, **D** and **G**), Mo-V-Te-O (**B**, **E** and **H**) and Mo-V-Te-Nb-O (**C**, **F** and **I**) mixed oxides heat-treated at 400, 500 or 600 ºC. Note that XRD patterns of as-synthesized materials are also shown.

In detail, signals at 598, 653, 714 and 866 cm^{-1} are assigned to antisymmetric Mo-O-X vibrations (with X= Mo, Te), but the signal at 909 cm^{-1} correspond to (Mo,V) bonded to a terminal oxygen. Nevertheless, weak signals at 820, 896 and 990 cm^{-1} allow to discriminate the minority presence of $TeMo_5O_{16}$ (signal at 896 cm^{-1}, [32]) and MoO_3 (820 and 990 cm^{-1}, [32]) crystalline phases, especially in **MV-17-400**.

Additional bands at 891 and 740 cm^{-1} in **MV-600** sample (i.e., MoVO catalyst heat-treated at 600 ºC) agree with the decomposition of the M1 phase observed in the XRD analysis. For the Nb-containing catalysts (**Fig. 5.1-F**), different spectra were obtained depending on the crystallinity of the sample. In this way, **MVTN-400** and **MVTN-500** catalysts, the ones that do not present a fully crystallised M1 phase, present an identical IR spectrum consisting of weak bands at 909 (only **MVTN-500**), 895, 860, 765, 620 and 554 cm^{-1}, whereas the **MVTN-600** sample shows intense bands at 909, 880, 765, 630 and 580 cm^{-1}, corresponding to the formation of the M1 phase [36]. In addition to this, the presence of pseudohexagonal Mo-V-Te-Nb oxide known as M2, with bands at 924, 750, 560 and 455 cm^{-1} [32] cannot be completely discarded due to the proximity of these bands to those of the M1 phase, so if the M2 phase is present it must be in a minimal proportion.

Likewise, Raman spectra for Mo-V-O, Mo-V-Te-O and Mo-V-Te-Nb-O catalysts heat-treated at 400, 500 or 600 ºC are presented in **Figures 5.1-G**, **5.1-H** and **5.1-I**, respectively. For Nb-free catalysts (i.e., Mo-V-O and Mo-V-Te-O samples), a sharp signal centred at 874 cm^{-1} is observed in all cases, which has been attributed to the M1 phase [39-41], with broad shoulders at

lower (770-840 cm^{-1}) and higher frequencies (970 cm^{-1}), in addition to a band at 470 cm^{-1}. Bands a higher frequencies are indexed to stretching vibrations of terminal (Mo,V)=O bonds [42], while those of the lower frequencies and the one at 470 cm^{-1} are ascribed to asymmetric and symmetric Me-O-Me bridge stretching modes, separately.

Nonetheless, as reported in **Chapter 3** and **4**, the appearance of additional bands in **MV-600** and **MVT-17-400** samples is surely assigned to different crystalline phases as impurities.

Differences are observed, however, regarding the **MVTN-400**, **500** and **600** samples. In this way, catalysts heat-treated at 400 and 500 ºC present a broad band centred at ca. 874 cm^{-1}, but with a fairly lower intensity compared to the **MVTN-600** sample, but also to the rest of the catalysts of the **MV-** and **MVT-** series. In addition, broad bands at ca. 817 and 650 cm^{-1} are assigned to Nb-O-Nb bonds, while NbO_6 octahedra bands appear weakly at ca. 907 cm^{-1} [43]. Rest of the bands are due to Me-O-Me and Me=O bridge stretching modes.

As a consequence of the different relationship of intensities in the diffraction peaks exhibited above in **Fig. 5.1** and shown previously in **Chapters 3** and **4** for bi- and trimetallic M1 oxides, a comparative FESEM study of catalysts heat-treated at both 400 and 600 ºC was carried out and it is shown in **Figure 5.2**.

Interestingly, contrary to what was shown in **Chapters 3** and **4**, tetra-metallic Mo-V-Te-Nb-O catalysts present a rather different shape than needle-like **MV-t** (**Fig. 5.2-A** and **B**) and **MVT-17-t** (**Fig. 5.2-C** and **D**)

samples of roughly 0.5 µm. In this case, micrographs for both **MVTN-400** (**Fig. 5.2-D**) and **MVTN-600** (**Fig. 5.2-E**) catalysts show some kind of similarity between these two samples, with a nanorod-like shape. However, by taking a closer look, augmented micrographs of **MVTN-400** and **MVTN-600** shown in **Figs. 5.2-F** and **G**, respectively, display some differences. In the case of the catalyst heat-treated at 400 ºC, an irregular shape probably due to the lack of crystallization of this sample is observed. Nevertheless, a regular polyhedral shape is well seen in the **MVTN-600** catalyst, suggested by its high degree of crystallization.

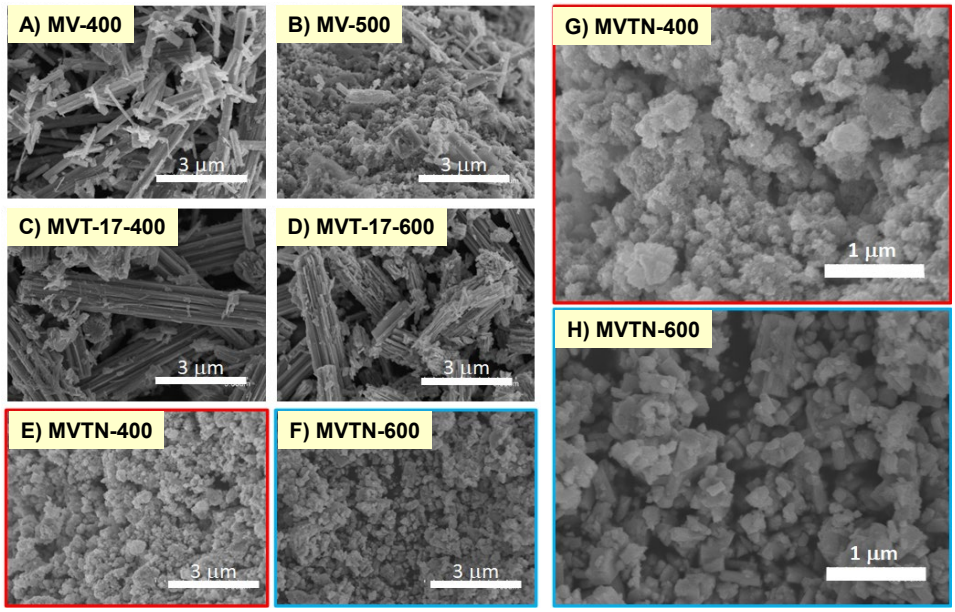

Figure 5.2. FESEM micrographs of **MV-400** (**A**), **MV-500** (**B**), **MVT-17-400** (**C**), **MVT-17-600** (**D**), **MVTN-400** (**E** and **G**) and **MVTN-600** (**F** and **H**). Note that **G** and **H** micrographs are magnifications of **E** and **F**, respectively.

Moreover, as predicted in previous chapters, chemical composition and activation temperature play a crucial role in the textural properties of the M1-type materials so, contemplating the structural changes that occur in the case of the tetrametallic Mo-V-Te-Nb catalysts, huge differences are expected.

Therefore, results of surface area and micropore volume values extracted from N_2 adsorption isotherms are displayed in **Figure 5.3** and **Table 5.1**. Regarding the catalysts heat-treated at 400 ºC, it can be seen that the **MVTN-400** sample is the one that presents the higher surface area values (ca. 55 $m^2\ g^{-1}$), followed by **MV-400** and **MVT-17-400** with values of 35.2 and 20.5 $m^2\ g^{-1}$, respectively.

Nevertheless, what it is especially interesting is that when it comes to the micropore volume values, this catalyst (**MVTN-400**) is the one that presents the lowest value along with **MVT-17-400** (ca. 0.003 $cm^3\ g^{-1}$), whereas **MV-400** shows a value more than 3 times higher, probably related to the lack of Te atoms in the hexagonal (and partially heptagonal) channels. Anyhow, the shape of the t-Plot curve in the case of the **MVTN-400** catalyst shown in **Figure 5.3-C** is considerably different than the ones displayed for the rest of the catalysts.

Conversely, a notable different trend is observed for the catalysts heat-treated at 600 ºC. For this series, the highest surface area value corresponds to the **MVTN-600** catalyst (ca. 8.8 $m^2\ g^{-1}$), while **MVT-17-600** and **MV-600** report values of 7.9 and 7.2 $m^2\ g^{-1}$, being the latter associated to the collapse of the M1 structure.

Micropore volume values, however, are quite similar among the samples, in any case these values are extremely low (no microporosity is assumed for M1 catalysts heat-treated at 600 ºC).

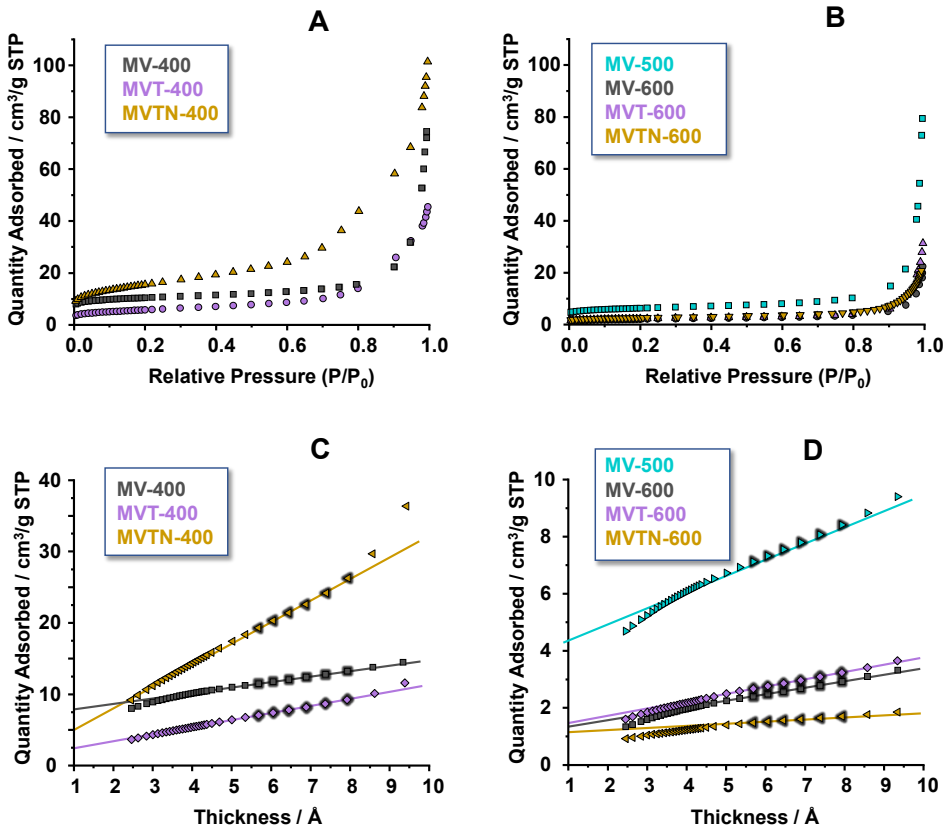

Figure 5.3. N_2 adsorption isotherms for catalysts heat-treated at 400 ºC (**A**) and 600 ºC (**B**), and t-Plot calculations derived from adsorption isotherms for catalysts heat-treated at 400 ºC (**C**) and 600 ºC (**D**), highlighting the points used for the linear fit. Note that data from bimetallic Mo-V-O catalyst (**MV-500** sample) is also shown together with the results from catalysts heat-treated at 600 ºC.

Moreover, in **Figures 5.3-B** and **D** it is also shown data from **MV-500** catalyst (i.e., Mo-V-O heat-treated at 500 ºC), as a representative bimetallic catalyst heat-treated at higher temperatures that still presents the M1 phase, showing intermediate textural properties between **MV-400** and **MV-600** (catalysts heat-treated at 400 and 600 ºC, respectively).

Furthermore, as a general trend, the higher the activation temperature the lower both the surface area and the micropore volume values for every series (**Table 5.1**).

5.3. Catalytic properties of bi-, tri- and tetrametallic M1 catalysts in the oxidative dehydrogenation of ethane

These series of catalysts with different chemical compositions and activation temperatures were tested in the oxidative dehydrogenation of ethane at 390 ºC with the feed used in previous chapter within the thesis, and comparative results are shown in **Table 5.2**.

As indicated previously, both the chemical composition and the activation temperature play a crucial role in the catalytic properties of these oxides. Accordingly, as shown in **Chapters 3** (related to bi-metallic, Mo-V-O samples) and **4** (related to tri-metallic, Mo-V-Te- O samples), completely different trends are observed when increasing the activation temperature.

In a first comparison, **Figure 5.4** presents the variation of the selectivity to the main reaction products (ethylene, CO and CO_2) with the ethane conversion for Mo-V-Te-Nb-O catalysts activated at 400 or 600 ºC.

Table 5.2. Catalytic parameters of MoV-containing catalysts in the oxidative dehydrogenation of ethane to ethylene.[a]

Catalyst	Reaction rate[b]	Areal rate[c]	Rate per active site[d]	Rate per active site and area[e]	Selectivity to ethylene (%)[f]
MV-400	15.1	0.43	143.4	4.07	75
MV-500	7.8	0.37	73.6	3.44	66
MV-600	0.34	0.05	3.2	0.45	n.d.
MVT-17-400	2.8	0.15	29,5	1.45	65
MVT-17-500	3.3	0.19	33.2	1.89	78
MVT-17-600	3.4	0.27	29.3	3.71	88
MVTN-400	2.4	0.04	37.5	0.68	56
MVTN-500	2.1	0.06	40.4	1.15	65
MVTN-600	5.2	0.31	109.5	6.44	95

[a] Conditions in the Experimental section, at 390 ºC and C_2/O_2/He: 5/5/90 molar ratio; [b] reaction rate as 10^3 molC_2 g_{cat}^{-1} h^{-1} at ethane conversions below 10%; [c] reaction rate as mmolC_2 m^{-2} h^{-1} at ethane conversions below 10%; [d] reaction rate per active site as 10^3 molC_2 g_V^{-1} h^{-1} at ethane conversions below 10%; [e] reaction rate per active site and area as 10^3 molC_2 (100 %V)$^{-1}$ m^{-2} h^{-1} at ethane conversions below 10%; [f] selectivity to ethylene for an ethane conversion of 50%.

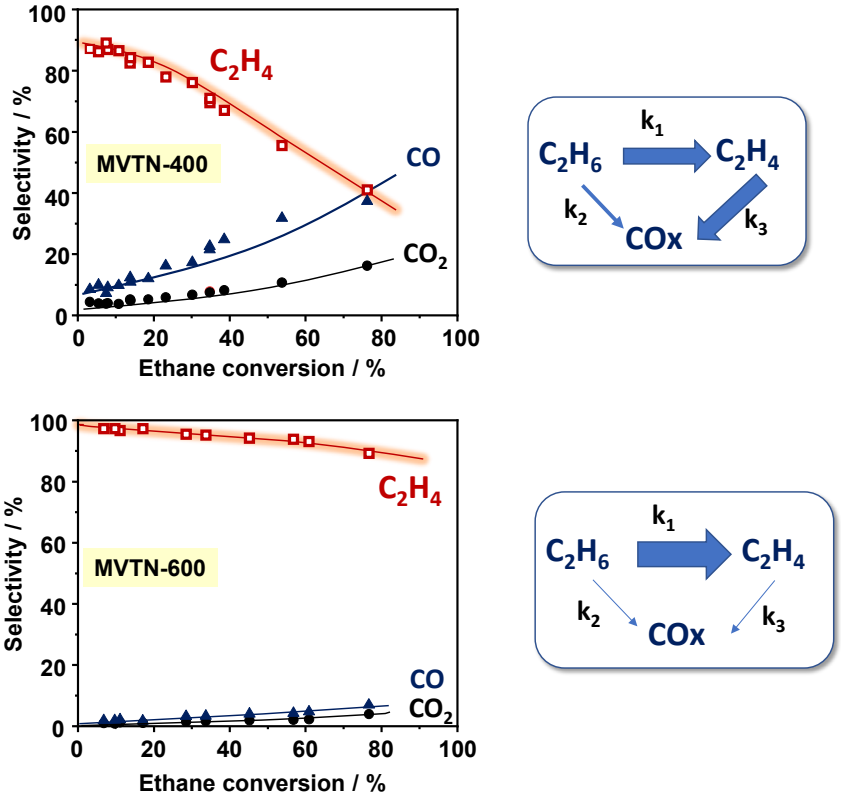

Figure. 5.4. Variation of the selectivity to the main reaction products (ethylene, CO, and CO_2) with the ethane conversion, at 390 ºC, for Mo-V-Te-Nb-O catalysts heat-treated at 400 ºC (up) and 600 ºC (bottom).

These results suggest a different influence of ethane conversion on selectivity to ethylene, favoring changes in both the reaction network and the kinetic constants, depending on the activation temperature of MoVTeNbO catalysts.

In this way, **Figures 5.5** shows the variation of the selectivity to ethylene as a function of ethane conversion for MoVO (MV-t series, **Fig. 5.5-A)**,

MoVTeO (MVT-t series, **Fig. 5.5-B)**, and MoVTeNbO (MVTN-t series, **Fig. 5.5-C**) catalysts heat-treated in N_2 at 400, 500 or 600 ºC.

In the case of MV-t series, the selectivity to ethylene decreases, when increasing the activation temperature, being **MV-400** catalyst the most selective one. However, in the case of MVT-t series, it can be observed an opposite trend, being **MVT-600** the catalyst that shows the highest selectivity to ethylene.

Nevertheless, strong differences are observed in the case of the **MVTN-t** samples (**Fig. 5.5-C**). As expected, catalysts that do not present the M1 phase (**MVTN-400** and **MVTN-500**) show remarkably poorer catalytic properties than **MVTN-600** as selectivity to ethylene is closely related to the formation of the M1 structure [36]. In addition, **MVTN-600** is the catalyst that presents the best selectivity to ethylene regardless of the chemical composition, where selectivity to ethylene exceeds 90% at ethane conversion up to 75%, in contrast to the high deactivation shown by **MVTN-500** and **MVTN-400** samples.

Considering the three catalytic systems and all the different activation temperatures, the selectivity to ethylene decreases as follows:

MVTN-600 > **MVT-17-600** > **MVT-17-500** > **MV-400** > **MVT-17-400** > **MV-500** = **MVTN-500** = **MVTN-400** > **MV-600**.

Furthermore, these catalytic results show that, in addition to clear differences in selectivity to ethylene, the catalytic activity is also influenced

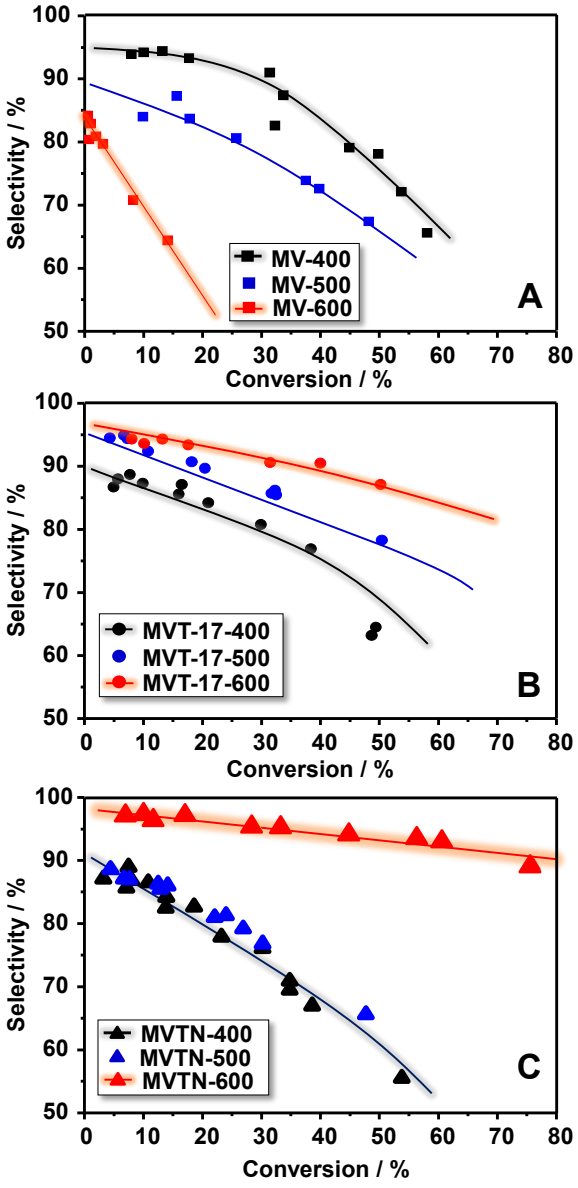

Figure 5.5. Ethylene selectivity as a function of ethane conversion, at 390 ºC and a feed mixture with C_2H_6/O_2/He molar ratio of 5/5/90, for mixed metal oxides catalysts: (**A**) **MV-t** series; (**B**) **MVT-17-t** series; and (**C**) **MVTN-t** series**.**

by the chemical composition and the thermal activation of the samples. Then, the results in **Figure 5.6-A** show that, considering the catalysts heat-treated at 400 ºC, bimetallic **MV-400** sample is the most active sample studied, followed by **MVT-17-400** and **MVTN-400**. However, when it comes to the catalysts heat-treated at 600 ºC, the inverse trend is observed, with **MVTN-600** catalyst being the most active one.

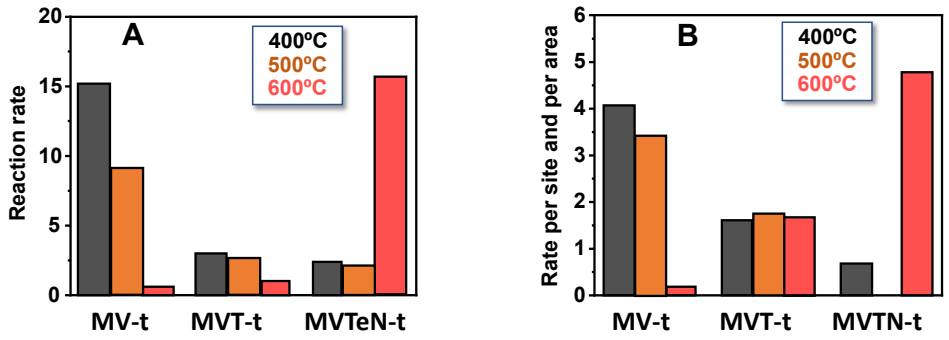

Figure 5.6. Reaction rate values of bi-, tri- and tetra-metallic catalysts (MV-t, MVT-t and MVTN-t series), heat-treated at 400 ºC (black), 500 ºC (orange) or 600 ºC (red), without normalization (**A**) and normalized by surface area and active site (**B**). Reaction rate as 10^3 mol_{C2H6} $g_{cat}^{-1}h^{-1}$ at ethane conversions below 10 %. Reaction rate per active site and area as 10^3 mol_{C2H6} $(100\ \%V)^{-1}$ m^{-2} h^{-1} at ethane conversions below 10 %.

Nevertheless, if the catalytic activity for ethane conversion is normalized by surface area and active center (V-atoms) interesting differences can be observed (**Fig. 5.6-B**). In this way, although both trends for catalysts heat-treated at 400 or 600 ºC are maintained, maximum values change. Therefore, in **Figure 5.6-B** it is shown that not only was the **MVTN-600** sample the most selective catalyst, but it is also the most active one

regardless the composition and the thermal activation, with the **MV-400** behind it.

In addition to this, apart from ethylene, CO and CO_2 were the by-products obtained during the reaction in all cases, with a minimal presence of acetic acid (lower than 2% selectivity) in the case of the binary catalysts (i.e., **MV-t** samples), and only traces for tri- and tetrametallic samples. Nevertheless, by decreasing the space velocity and consequently increasing the ethane conversion, selectivity to CO_x is unfortunately also increased in a greater or lesser extent. Furthermore, among the carbon oxides formed, CO is the predominant, suggesting that it is formed through deep ethylene oxidation.

In conclusion, the catalysts that presented the best performance in terms of activity and selectivity to ethylene among the series were: **MV-400**, **MVT-17-600** and **MVTN-600**. Then, it can be stated that the presence of Te^{4+} and (Te^{4+} plus Nb^{5+}) has a positive effect in the selectivity to ethylene but only at higher thermal activation temperatures.

5.4. Study of the surface composition of MoV(Te,Nb)O_x catalysts treated at different activation temperatures

As it has been demonstrated throughout the present thesis, the presence of an adequate crystalline phase, in our case the M1 phase, is crucial to obtain decent catalytic behaviors [44-46], nevertheless, it also has been manifested that the surface of the M1 structure is directly involved in the activation of alkanes and their subsequent selective activations. Therefore,

a comparative XPS study was performed, and the experimental results are shown in **Figure 5.7** and **Table 5.1**.

XPS results of Mo *3d* core level spectra for catalysts activated at 400 and 600 ºC are shown in **Figs. 5.7 (A-C)**. These results indicate some changes depending on the chemical composition of the catalysts. As seen in previous chapters, both bi- and trimetallic catalysts present a unique doublet at 235.7 and 232.5 eV, corresponding to the Mo $3d_{5/2}$ and Mo $3d_{3/2}$ components, respectively, that are associated to molybdenum in the +6 oxidation state [23, 47, 48]. However, by looking at the spectra of tetrametallic catalysts (**Fig. 5.7-C**), the presence of a second doublet (for both **MVTN-400** and **MVTN-600** catalysts) suggests the presence of a certain amount of Mo^{5+} species, probably due to the inclusion of Nb^{5+} cations in the center of the pentagonal units of the M1 structure. On the contrary, given the fact that these materials can be easily charged, the presence of said second doublet in the Mo *3d* spectra is more probably due to differential charge associated to the experimental measurement itself.

On the other hand, V $2p_{3/2}$ core level spectra are formed by two components at binding energies of 516.5 eV and 515.5 eV, which are attributed to V^{5+} and V^{4+} species, respectively [23, 47, 49, 50] and are shown in **Figures 5.7 (D** to **F)**. Interestingly, in previous chapters it was stablished a clear relationship between the concentration of V^{4+} species and the selectivity to ethylene, however, those species are the predominant ones in both **MVTN-400** and **MVTN-600** catalysts (**Fig. 5.7-F**), with notable differences in selectivity among them. Nevertheless, for the **MVTN-400** catalyst, XPS results must be taken carefully since the lack of presence of the M1 phase

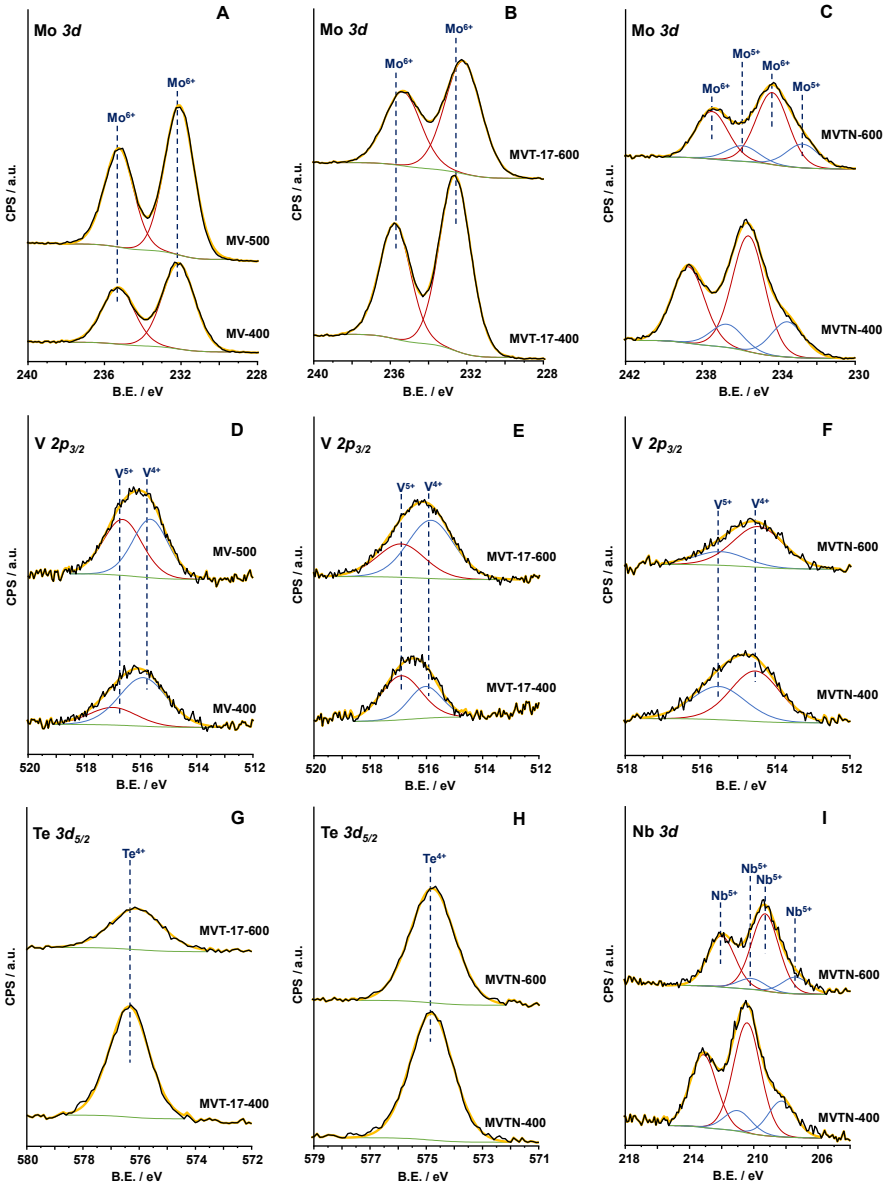

Figure 5.7. XPS analysis of Mo *3d* core level (**A**, **B** and **C**) for **MV-t** (**A**), **MVT-17-t** (**B**) and **MVTN-t** (**C**); V $2p_{3/2}$ core level (**D**, **E** and **F**) for **MV-t** (**D**), **MVT-17-t** (**E**) and **MVTN-t** (**F**); Te $3d_{5/2}$ core level (**G** and **H**) for **MVT-17-t** (**G**) and **MVTN-t** (**H**); and Nb *3d* core level for **MVTN-t** (**I**) catalysts.

supposes a clear drawback for making any assumption. Additionally, spectra of the Mo-V-Te-Nb catalysts seem to be shifted 1 eV to lower binding energies. This shift can be associated with the incorporation of Nb cations and a different chemical environment.

Figures 5.7 (G and **H)** show the spectra for the Te $3d_{5/2}$ core level, in this case for tri- and tetrametallic catalysts. In all of them, a unique tellurium signal at 576.3 eV is displayed, corresponding to Te^{4+} species into the structure [18, 47, 50], whereas **Figure 5.7-I** shows the Nb *3d* core level spectra for the tetrametallic catalysts.

In both cases, two doublets can be ascertained [18, 47, 50], however, the explanation for them is quite different. In one hand, the two doublets for the **MVTN-400** sample can be interpreted on the basis of the non-crystallization of the M1 phase, therefore existing Nb^{5+} species in different coordination. Additionally, and as suggested in the Mo *3d* spectra of these samples, the low intensity doublet that appears in the **MVTN-600** sample is clearly due to charge issues, since these types of oxides can be easily charged during the XPS analysis.

According to the XPS results, no clear relationship can be stablished with the selectivity to ethylene regarding Mo, Te and Nb atoms. However, a wider relationship that the one observed in **Chapter 4** (see **Figure 4.9-B**, page 199) can be proposed considering the selectivity to ethylene as a function of the V^{4+}/V_{total} relationship. Therefore, the results plotted in **Figure 5.8** clearly show that, the higher the V^{4+} concentration the higher the selectivity to ethylene regardless of the chemical composition and the activation temperature.

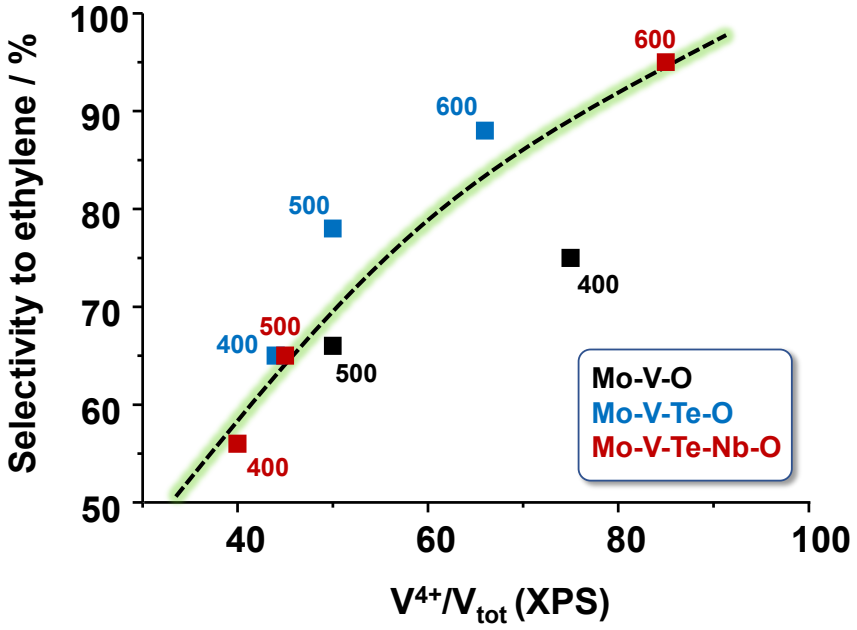

Figure 5.8. Selectivity to ethylene as a function of the V^{4+}/V_{total} relationship, determined by XPS, for Mo-V-O (black), Mo-V-Te-O (blue) and Mo-V-Te-Nb-O (red) catalysts, heat-treated at 400, 500 or 600 ºC.

For a more suitable comparison, data used in the figure is taken from 390 ºC of reaction temperature and 50% of ethane conversion. In this manner, it is suggested that a compact morphology as the one exhibited by the tetra-metallic catalysts should contain V^{4+} species, which are known to be the active sites [51], in a more favorable environment for the selective partial oxidation of ethane to ethylene.

5.5. Study of the electrochemical behavior of bi-, tri- and tetrametallic MoV(Te,Nb)O_x catalysts

Provided that the oxidation state of the active species (see above) and lattice-surface oxygen transfer with its corresponding electron transfer are involved in the selective oxidation of ethane to ethylene, this part of the chapter is devoted to study the semiconducting nature of the catalysts as well as the electrochemical properties of their interfaces.

Firstly, in order to study the resistance of the different catalysts to charge-transfer processes, Electrochemical Impedance Spectroscopy (EIS) analyses were undertaken. Accordingly, in **Figures 5.9 (A** and **B**) Nyquist and Bode-module plots are shown, respectively, for bi-, tri- and tetrametallic catalysts heat-treated at 400 and 600 ºC. Nyquist plot results (**Fig. 5.9-A**) showed, in all cases, two semicircles that are related to two regions with different slopes in the Bode-module plots (**Fig. 5.9-B**). The first semicircle, observed in the high-intermediate frequencies region, is associated with charge-transfer response of the oxide/electrolyte interface [52, 53], therefore providing information on the active sites of the catalyst. Additionally, the second semicircle that appears in the Nyquist plots is ascribed to catalysts' bulk [52, 53]. As a general trend, higher semicircle amplitudes mean an enhanced impedance of the electrochemical process related to it. In this way, experimental results indicate that the **MVTN-600** catalyst is the sample that presents the highest amplitude of semicircle, with binary and ternary oxides showing clearly lower impedance values.

Moreover, the morphology of both Nyquist and Bode-module plots suggests that to simulate the electrochemical results an electrical circuit

with two parallel Resistor-Capacitor time constants should be used, like the one showed in **Figure 5.9-C**. However, for this circuit, constant phase elements (CPEs) have been used to account for the non-ideality of the system instead of capacitors. In this manner, the resistance (R_1) values can be calculated as the charge-transfer resistance at the active parts of the catalysts/electrolyte interface (**Fig. 5.9-D**).

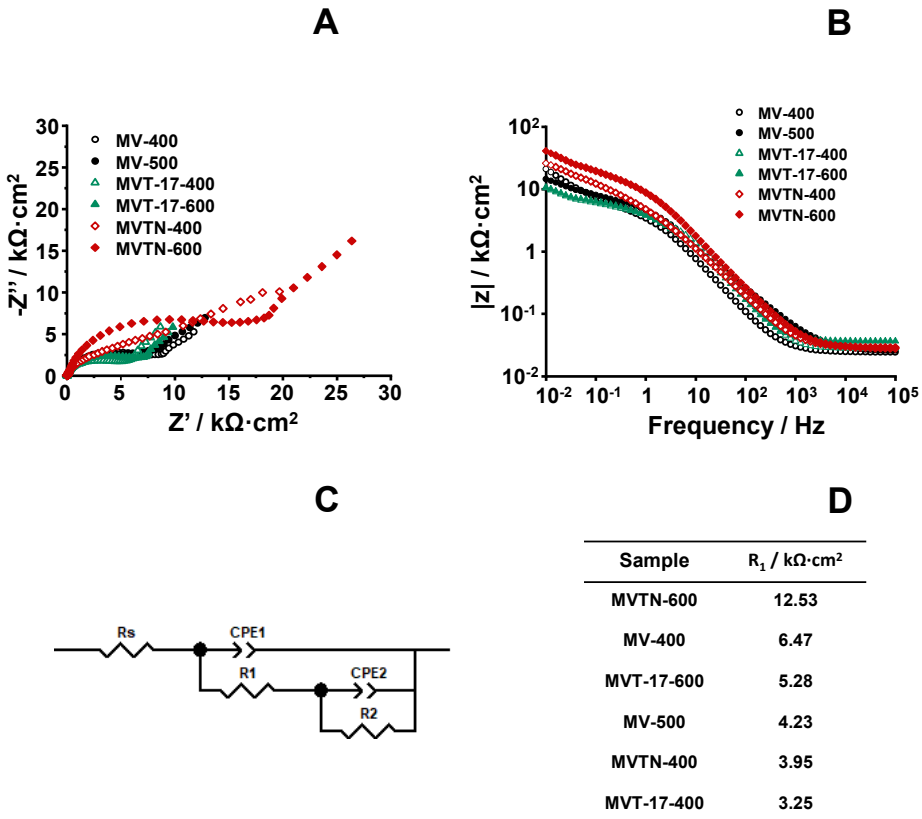

Sample	R_1 / kΩ·cm²
MVTN-600	12.53
MV-400	6.47
MVT-17-600	5.28
MV-500	4.23
MVTN-400	3.95
MVT-17-400	3.25

Figure 5.9. Nyquist (**A**) and Bode-module (**B**) plots for bi-, tri- and tetrametallic catalysts heat-treated at 400 ºC and 600 ºC with equivalent circuit used for the EIS data fit (**C**) and calculated resistance (R_1) values derived from it (**D**).

Interestingly, the highest resistance values (R_1) were obtained for the samples that presented the best catalytic performance in ethane ODH (i.e., **MVTN-600**, **MV-400** and **MVT-17-600**) highlighting the **MVTN-600** catalyst, whose calculated resistance value is remarkably higher than any other catalyst, the same as its performance in terms of selectivity to ethylene. In any case, it can be concluded that, in the aim of design catalysts that present optimal performance in the oxidative dehydrogenation of ethane to ethylene, said materials must present high charge-transfer resistance values at the interfacial active parts.

What is more, the semiconducting properties of these catalysts were also studied by Mott-Schottky analyses, trying to correlate them with their catalytic performance. Thus, Mott-Schottky plots of bi-, tri- and tetrametallic catalysts are shown in **Figure 5.10**. Also, analyses for pure MoO_3 and V_2O_5 are shown in said figure (see right part).

For bi-metallic MoV oxide samples heat-treated at 400 ºC and 500 ºC (i.e., **MV-400** and **MV-500** catalysts), the linear region observed with a positive slope in the -0.6 to 0.1 V range indicates an *n*-type semiconducting behavior, however, at higher potentials the negative slope is characteristic of *p*-type semiconductivity. Then, by looking at the plots for pure oxides, it can be stated that the *n*-type semiconductivity is related to the molybdenum content, provided that MoO_3 is clearly an *n*-type semiconductor, while *p*-type semiconductivity is ascribed to the vanadium content (negative slope in pure V_2O_5). Nevertheless, it has been previously reported that V_2O_5 behaves as a *p*-type semiconductor when the mean oxidation state of vanadium is lower than 4.6, this is, when V^{4+} species are the majority in the

surface of the oxide [33]. Therefore, and according to the XPS deconvolution results (see **Table 5.1**), **MV-400** and **MV-500** catalysts present a mean vanadium oxidation state of 4.25 and 4.50, respectively.

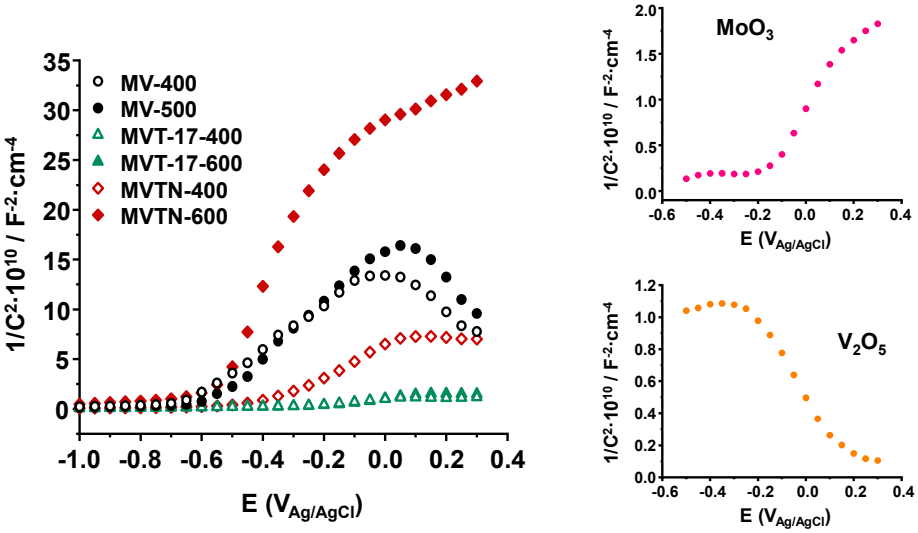

Figure 5.10. Mott-Schottky plots for **MV-400** (black, empty), **MV-500** (black, full), **MVT-17-400** (green, empty), **MVT-17-600** (green, full), **MVTN-400** (red, empty) and **MVTN-600** (red, full). Note that Mott-Schottky plots for MoO_3 (up) and V_2O_5 (bottom) are also shown on the right.

Hence, for these two catalysts, the main donor species that are responsible for the *n*-type semiconductivity are oxygen vacancies [33, 54, 55]. In addition to this, by using Kröger-Vink notation, this donning process can be written as V_O^X in the neutral form and as $V_O^{\bullet\bullet}$ in the double-ionized state. On the contrary, the main acceptor species (related to *p*-type semiconductivity) are cation vacancies, written as V_M^X or $V_M^{''}$ for neutral and ionized vacancy, respectively.

Furthermore, by incorporating Te^{4+} cations in the trimetallic **MVT-17-t** catalysts, it can be seen only values corresponding to an *n*-type semiconductivity, as reported before for this MoVTe-M1 oxides [33]. Lastly, the further incorporation of Nb^{5+} species for **MVTN-t** catalysts provokes a clear enhancement in the *n*-type semiconductivity since the linear region with negative slope in the Mott-Schottky plots completely disappears [33].

Values for positive slopes in Mott-Schottky plots have been inversely related to the density of donor species (i.e., oxygen vacancies), according to the Mott-Schottky equation. Thus, a greater positive slope means a lower number of oxygen vacancies in the oxide structure. Then, from the plots shown in **Figure 5.10** it can be concluded that the **MVTN-600** sample is the catalyst that presents the lowest density of oxygen defects, followed by bimetallic **MV-400** and **MV-500** and **MVTN-400** catalysts, with trimetallic **MVT-17-400** and **MVT-17-600** having the highest density of oxygen vacancies (i.e., smallest positive slope).

Besides that, it can be stablished a relationship between the resistance (R_1) values showed in **Fig. 5.9-D** and the different slopes in the Mott-Schottky plots, indicating that higher slopes are related to both lower density of oxygen vacancies but also to higher resistance to interfacial charge-transfer processes. In consequence, the best selectivity to ethylene should be obtained for catalysts that present pronounced slopes in the Mott-Schottky plots. This, in fact, is the case of the **MVTN-600** sample.

Also, the influence of the semiconducting behavior in the catalytic performance of the materials studied can be explained in terms of the

different structural defects (cationic vacancies) and oxygen species within the oxide lattice. It is a well-kwon fact that in partial oxidation reactions two types of oxygen species can be involved, namely: **i)** electrophilic oxygen species (O^-), also known as non-stoichiometric oxygen (NSO), which lead to deep oxidation reactions (formation of CO and CO_2) and **ii)** nucleophilic oxygen species (O^{2-}), which favor selective partial oxidation reactions [56-59]. Therefore, information about the semiconducting properties of a catalyst and the prevailing oxygen species within its structure can be directly related to their catalytic performance in ODH reactions.

Accordingly, for oxides showing a *p*-type semiconductivity, as in the case of bimetallic **MV-400** and **MV-500** catalysts, the taking of two surrounding electrons by a cationic vacancy led to the formation of two positive electron holes and a doubly ionized cationic vacancy ($V_M^{''}$) according to the reaction described below:

$$V_M^X \rightarrow V_M'' + 2h^\bullet$$

At the same time, these positive holes can subsequently interact with a nucleophilic oxygen anion (O^{2-}) located within the lattice (written as O_O^X in the Kröger-Vink notation), forming in this way a positively effective charged oxygen anion ($O_O^\bullet$), which should be equivalent to an electrophilic O^- anion [60, 61]:

$$O_O^X + h^\bullet \rightarrow O_O^\bullet$$

In conclusion, the presence of cationic vacancies can promote the formation of electrophilic oxygen species, resulting in a decrease in the

selectivity to partial oxidation products. All in all, this fact should explain the drop in selectivity observed in the **MV-400** sample at high ethane conversion values in contrast with the **MVTN-600** catalyst (**Fig. 5.5**), that does not present any *p*-type semiconductivity.

Conversely, in samples with very little to non *p*-type semiconductivity, but also very low positive slopes in the Mott-Schottky plots, as in the case of trimetallic **MVT-17-400** and **MVT-17-600** catalysts (**Fig. 5.10**), oxygen vacancies are the prevailing defects, being the highest out of the series. In this case, an oxygen vacancy is created from the transfer of a lattice oxygen (O^{2-} or O_O^X) to the gaseous state. Taking into account the double-ionized form of the vacancy ($V_O^{\bullet\bullet}$), the global reaction can be written as:

$$O_O^X \rightarrow V_O^{\bullet\bullet} + 2e' + \frac{1}{2}O_2(g)$$

Consequently, in systems like the trimetallic M1 oxides, it exists a competition between nucleophilic oxygen species (O^{2-}/O_O^X) and oxygen vacancies. In that sense, a high density of said vacancies may lead to lower selectivity to ethylene, especially if compared to **MVTN-600** (significantly lower oxygen vacancies) [35], however, the **MVTN-400** catalyst that presents a higher Mott-Schottky slope than **MVT-17-400**, shows clearly lower selectivity to ethylene (**Table 5.2**). This result, in fact, along with the V *2p3/2* results (**Table 5.3**) allow us to conclude that, regardless the composition and the thermal treatment, a good selectivity to ethylene during ethane ODH is subject to the formation of the M1 phase.

Furthermore, an inverse correlation can be stablished between the anodic current density values of the catalysts and their selectivity to ethylene, as it

can be seen in **Figure 5.11**, in which catalysts with the highest current densities exhibit the lowest selectivity to ethylene. The explanation for this fact may lie on the fact that higher current densities are associated to an enhanced electrochemical activity, favoring in this way total oxidation reactions.

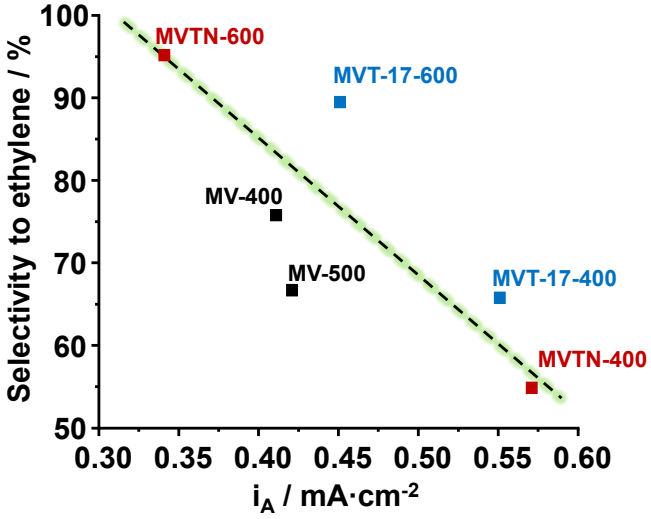

Figure 5.11. Selectivity to ethylene (values taken at an ethane conversion of 50%) as a function of the anodic current density for mixed oxide catalysts, heat-treated at 400 ºC, 500 ºC or 600 ºC: **MV-t** (black), **MVT-17-t** (blue) and **MVTN-t** (red).

Therefore, according to **Figure 5.11**, the synthesis of catalysts with low current density values is preferred to improve the catalytic performance in ethane ODH, avoiding this way the formation of deep oxidation products such as CO and CO_2. Moreover, there is also an opposite trend between the anodic current density (**Fig. 5.11**) and the resistance to interfacial charge-transfer processes, R_1, depicted in **Fig. 5.9-D** when it comes to their relationship with the selectivity to ethylene. In addition to resistance,

anodic current density follows the same opposite trend as for the V^{4+} relative concentration (**Fig. 5.8**). This fact may be associated with a lower number of electrophilic oxygen species in catalysts with a higher proportion of surface V^{4+} species, which are known to perform partial oxidation reactions.

5.6. Conclusions

In the present chapter, it has been comparatively studied the catalytic performance in the ethane ODH of the three families of catalysts that present the M1 phase (i.e., MoVO, MoVTeO and MoVTeNbO), thermally activated at 400, 500 or 600 ºC. Then, it has been demonstrated that the presence of well-defined M1 phase crystals, regardless of the chemical composition, is key to obtain optimal catalytic performances in terms of selectivity to ethylene.

Additionally, it has also been shown that the ideal activation temperature for each family of catalysts depends on their chemical composition. In this sense, as reported in **Chapter 3**, for bimetallic MoVO catalysts, the best selectivity values to ethylene were the ones obtained for the sample heat-treated at 400 ºC (i.e., **MV-400**), and the catalytic performance starts to decrease as the activation temperature raises (**MV-400** > **MV-500** > **MV-600**), due in this case to the partial (**MV-500**) or nearly total (**MV-600**) decomposition of the M1 phase into non-catalytic phases at temperatures over 400 ºC [26-29].

Furthermore, discussed in **Chapter 4**, trimetallic MoVTeO catalysts maintain the M1 phase structure throughout the three different calcination temperatures, however, the catalytic performance increased concomitantly with the activation temperature. This fact was attributed to the different relative presence of V^{4+} species on the surface of the catalyst heat-treated at the highest temperature (i.e., **MVT-17-600**), in where those species are directly involved (known to perform partial oxidation reactions).

Interestingly, tetrametallic MoVTeNbO catalysts followed a completely different trend. Thus, samples heat-treated at 400 ºC and 500 ºC did not show an XRD corresponding to the fully formation of the M1 phase (**Fig. 5.1-C**), and that crystallization only happens at temperatures above 550 ºC [62] like in sample **MVTN-600**. Consequently, catalytic activity strongly depended on the crystalline phase, and more specifically, on the presence of the M1 phase.

Nonetheless, among the catalysts that presented the M1 phase, differences in terms of selectivity should be explained supported on different characterization techniques. For instance, taking the data shown in previous chapters, a correlation between the relative presence of V^{4+} species and the selectivity of each catalyst to ethylene was established. Then, in **Figure 5.8**, it was demonstrated that the catalysts that performed the better in the ethane ODH (i.e., **MV-400**, **MVT-17-600** and **MVTN-600**) were also the ones that, after XPS analyses, presented the highest proportion of V^{4+} species.

Needless to say, textural properties of the synthesized oxides also play an important role in the catalytic activity of the samples studied (**Figure 5.6-A**). Therefore, catalytic activity for the catalysts heat-treated at 400 ºC

decreased as follows: **MV-400** > **MVT-17-400** > **MVTN-400**, however, catalysts heat-treated at 600 ºC followed the inverse trend: **MVTN-600** > **MVT-17-600** > **MV-600**. All in all, cases such as the **MV-600** and **MVTN-400** could be explained in terms of the non-formation of the M1 phase. Noteworthy, since vanadium atoms are the ones responsible for the catalytic activity, the normalization of the data plotted in **Figure 5.6-A** led to a drastic change observed in **Figure 5.6-B**, in where not only was the **MVTN-600** sample the most selective catalyst, but also the most active one if normalized by active site and surface area.

M1-type oxides, as a consequence of their chemical formulation, can be also considered as semiconductors. Then, the different oxidation states and the oxygen transfer phenomena that occur within the oxides was electrochemically studied by several techniques such as Electrochemical Impedance Spectroscopy and Mott-Schottky plots. It was found by EIS that, for every catalyst, a relationship between the resistance of the material and the catalytic performance exists. In **Figure 5.12** it is shown that, the higher the resistance value (which is the charge-transfer resistance at the interfacial active parts) the higher the selectivity to ethylene. Then, optimal catalysts should present high resistance (R_1) values.

Moreover, Mott-Schottky plots shown in **Fig. 5.9** revealed that binary **MV-t** samples present a majority of *p*-type semiconductivity behavior at higher potentials (mostly because of the vanadium content), with the *n*-type semiconductivity due to the presence of oxygen vacancies [33, 54, 55]. On the contrary, tri- and tetrametallic catalysts (i.e., **MVT-17-t** and **MVTN-t** samples) are consistent with a *n*-type semiconductivity as there was no

negative slope showed in the Mott-Schottky plots at higher potentials, being this *n*-type semiconductivity behavior mostly related to the presence, in a greater or lesser extent, of oxygen vacancies.

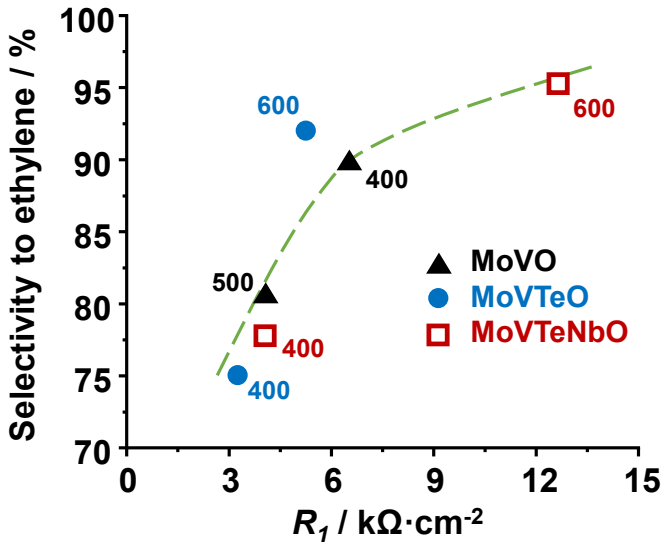

Figure 5.12. Relationship between the selectivity to ethylene and the R_1 data for **MV-t**, **MVT-17-t** and **MVTN-t** samples. Note that selectivity to ethylene is taken at 10% of ethane conversion and 390 ºC of reaction temperature.

In conclusion, regarding the extensive characterization results shown throughout the present chapter, in order to obtain optimal catalytic properties of Mo-based mixed metal oxides for the oxidative dehydrogenation of ethane, it is mandatory that these catalysts present the M1 crystalline phase. Furthermore, within the oxides that do present said phase, the presence of oxygen vacancies that, in turn, may lead to the formation of electrophilic oxygen species has been proved to be associated with deep oxidation reactions, on the contrary to nucleophilic lattice

oxygen species, that are ascribed to perform partial oxidation reactions, therefore increasing the selectivity to ethylene during ethane ODH.

Then, best catalysts synthesized should present the M1 phase and their surface should be in majority composed by V^{4+} species, in detriment to V^{5+} species. Furthermore, taken into account their electrochemical properties, those catalysts showing an *n*-type semiconductivity, would present a low density of oxygen vacancies and a low current density (unenhanced electrochemical activity), that lead to the optimal partial oxidation performances in the oxidative dehydrogenation of ethane to ethylene.

An important aspect is to be able to understand how, being the V^{5+} species (V^{5+}=O ↔ $^{4+}V^{\bullet}$–$O^{\bullet}$) the active species for ethane activation [6, 9, 46, 60, 63], the best selectivity is found for catalysts presenting high V^{4+}/V^{5+} ratios on the catalyst surface (**Fig. 5.7**). However, it is well known the importance of nucleophilic bridging oxygen atoms between reduced and oxidized metal centers during the partial oxidation of C_2-C_4 alkanes [46, 63], specifically the bridging oxygen atoms in V^{n+}-O-Me units (Me= V or Mo) in which the nucleophilicity of the oxygen bounded to V^{4+} should be higher than that bounded to V^{5+} [65-67].

However, an excess of active lattice oxygen, related to V^{5+}=O on the catalyst surface, could also favor the deep oxidation of the olefins. This could agree to the site isolation hypothesis proposed by Grasselli [60]. Thus, the importance of the presence of V^{4+} species on the catalyst surface could be due to a decrease in the concentration of V^{5+} species (that is, of active oxygen species, V^{5+}=O, which would facilitate a greater combustion of ethylene).

A similar effect has been proposed by Callahan & Grasselli to explain the selectivity to acrolein in the oxidation of propylene on copper oxide catalysts [68]. There, these authors proposed that, two essential postulates in oxidation reactions should be considered: **i)** the oxygen atoms must be distributed on the surface of a selective oxidation catalyst in an arrangement which provides for limitation of the number of active oxygen atoms in various isolated groups; and **ii)** the metal-oxygen bond energy of the active oxygen atoms, at the reaction conditions, must be in a range where rapid removal (hydrocarbon oxidation) and addition (regeneration by oxygen) is assured.

For this reason, and in addition to the isolation of active sites in the ab plane of M1 phase [6, 9, 26, 46, 60, 63], an optimization of V^{4+}/V^{5+} ratio on the surface of catalyst, could prevent the undesirable deep oxidation of ethylene at high ethane conversion, favoring the higher selectivity to ethylene as observed in MoVTeNbO catalysts activated in the 550-650 ºC range [62].

5.7. References

1) P. Botella, E. García-González, A. Dejoz, J. López Nieto, M. Vázquez, J. González-Calbet, J. Catal. 225 (2004) 428-438.

2) J.M. López Nieto, P. Botella, P. Concepción, A. Dejoz, M.I. Vázquez, Oxidative dehydrogenation of ethane on Te-containing MoVNbO catalysts, Catal. Today 91-92 (2004) 241-245.

3) H. Tsuji, Y. Koyasu, Synthesis of MoVNbTe(Sb)Ox Composite Oxide Catalysts via Reduction of Polyoxometalates in an Aqueous Medium, J. Am. Chem. Soc. 124 (2002) 5608-5609.

4) J.M.M. Millet, H. Roussel, A. Pigamo, J.L. Dubois, J.C. Jumas, Characterization of tellurium in MoVTeNbO catalysts for propane oxidation or ammoxidation, Appl. Catal. A- Gen. 232 (2002) 77-92.

5) S. Ishikawa, W. Ueda, Microporous crystalline Mo-V mixed oxides for selective oxidations, Catal. Sci. Technol. 6 (2016) 617-629.

6) J.M. López Nieto, B. Solsona, P. Concepción, F. Ivar, A. Dejoz, M.I. Vázquez, Reaction products and pathways in the selective oxidation of C2–C4 alkanes on MoVTeNb mixed oxide catalysts, Catal. Today 157 (2010) 291–296.

7) Z. Han, X. Yi, Q. Xie, R. Li, H. Lin, Y. He, L. Chen, W. Weng, H. Wan, Oxidative dehydrogenation of ethane over MoVTeNbO catalyst prepared by a slurry method, Chinese J. Catal. 26 (2005) 441-442.

8) J. S. Valente, H. Armendáriz-Herrera, R. Quintana-Solórzano, P. Del Ángel, A. Massó, J. M. López Nieto, Chemical, structural, and morphological changes of a MoVTeNb catalyst during oxidative dehydrogenation of ethane, ACS Catal. 4 (2014) 1292-1301.

9) T.T. Nguyen, B. Deniau, P. Delichere, J.M.M. Millet, Influence of the content and distribution of vanadium in the M1 phase of the MoVTe(Sb)NbO catalysts on their catalytic properties in light alkanes oxidation, Top. Catal. 57 (2014) 1152–1162.

10) P. Kube, B. Frank, S. Wrabetz, J. Kröhnert, M. Hävecker, J. Velasco-Vélez, J. Noack, R. Schölgl, A. Trunschke, Functional Analysis of Catalysts for Lower Alkane Oxidation, ChemCatChem 9 (2017) 573-585.

11) T. Blasco, A. Galli, J. M. López Nieto, F. Trifirò, Oxidative dehydrogenation of ethane and n-butane on VO_x/Al_2O_3 catalysts, J. Catal 169 (1997) 203-211.

12) G. Grubert, E. Kondratenko, S. Kolf, M. Baerns, P. van Geem, R. Parton, Fundamental insights into the oxidative dehydrogenation of ethane to ethylene over catalytic materials discovered by an evolutionary approach, Catal. Today 81 (2003) 337–345.

b) A.M. Gaffney, N. V. Duprez, K. J. Louthan, B. Borders, J. Gasque, A Siegfried, Th. G. Stanford, K. L. Roberts, Y. Alcheikhhamdona, M. Hoorfar, B. Chen, S. Majumdar, H. Murnen, Ethylene production using oxidative dehydrogenation: effects of membrane-based separation technology on process safety & economics, Catal. Today 371 (2021) 11–28.

13) Y. Zhu, P. V. Sushko, D. Melzer, E. Jensen, L. Kovarik, C. Ophus, M. Sánchez-Sánchez, J.A. Lercher, N.D. Browning, Formation of Oxygen Radical Sites on MoVNbTeOx by Cooperative Electron Redistribution, J. Am. Chem. Soc. 139 (2017) 12342.

14) D. Melzer, G. Mestl, K. Wanninger, Y. Zhu, N. D. Browning, M. Sánchez-Sánchez, J. A. Lercher, Design and synthesis of highly active MoVTeNb-oxides for ethane oxidative dehydrogenation, Nat. Commun. 10 (2019) 4012.

15) A.M. Gaffney, Q. An, W.A. Goddard III, W. Diao, M.V. Glazoff, Toward Concurrent Engineering of the M1-Based Catalytic Systems for Oxidative Dehydrogenation (ODH) of Alkanes, Top. Catal. 63 (2020) 1667-1681.

16) L. Annamalai, Y. Liu, S. Ezenwa, Y. Dang, S.L Suib, P. Deshlahra, Influence of Tight Confinement on Selective Oxidative Dehydrogenation of Ethane on MoVTeNb Mixed Oxides, ACS Catal. 8 (2018) 7051-7067.

17) A.M. Gaffney, O.M. Mason, Ethylene production via Oxidative Dehydrogenation of Ethane using M1 catalyst, Catal. Today. 285 (2017) 159–165.

18) T. Y. Kardash, E. V. Lazareva, D. A. Svintsitskiy, A. V. Ishchenko, V.M. Bondareva, R. B. Neder, The evolution of the M1 local structure during preparation of VMoNbTeO catalysts for ethane oxidative dehydrogenation to ethylene, RSC Adv. 8 (2018) 35903-35916.

19) B. Chu, H. An, X. Chen, Y. Cheng, Phase-pure M1 MoVNbTeOx catalysts with tunable particle size for oxidative dehydrogenation of ethane, Appl. Catal. A- Gen. 524 (2016) 56–65.

20) Y. S. Yun, M. Lee, J. Sung, D. Yun, T. Y. Kim, H. Park, K. R. Lee, C. K. Song, Y. Kim, J. Lee, Y.-J. Seo, I. K. Song, J. Yi, Promoting effect of cerium on MoVTeNb mixed oxide catalyts for oxidative dehydrogenation of ethane to ethylene, Appl. Catal. B Environm. 37 (2018) 554-562.

21) E.V. Lazareva, V.M. Bondareva, D.A. Svintsitskiy, A.V. Ishchenko, A.S. Marchuk, E.P. Kovalev, T.Yu. Kardash, Oxidative dehydrogenation of ethane over M1 MoVNbTeO catalysts modified by the addition of Nd, Mn, Ga or Ge, Catal. Today 361 (2021) 50–56.

22) G. A. Zenkovets, A.A. Shutilov, V.M. Bondareva, V. I. Sobolev, A. S. Marchuk, S.V. Tsybulya, I.P. Prosvirin, A.V. Ishchenko, V.Yu. Gavrilov, New Multicomponent $MoVSbNbCeO_x/SiO_2$ Catalyst with Enhanced Catalytic Activity for Oxidative Dehydrogenation of Ethane to Ethylene, ChemCatChem 12 (2020) 4149–4159.

23) D.A. Svintsitskiy, T.Y. Kardash, E.V. Lazareva, A.A. Saraev, E.A. Derevyannikova, M.Vorokhta, B. Šmídc, V. M. Bondareva, NAP-XPS and in situ XRD study of the stability of Bi-modified MoVNbTeO catalysts for oxidative dehydrogenation of ethane, Appl. Catal. A-Gen. 579 (2019) 141–150.

24) X. Tu, M. Niwa, A. Arano, Y. Kimata, E. Okazaki, S. Nomura, Controlled silylation of MoVTeNb mixed oxide catalyst for the selective oxidation of propane to acrylic acid, Appl. Catal. A-Gen. 549 (2018) 152–160.

25) B. Chu, L. Truter, T.A. Nijhuis, Y. Cheng, Performance of phase-pure M1 MoVNbTeOx catalysts by hydrothermal synthesis with different post-treatments for the oxidative dehydrogenation of ethane, Appl. Catal. A-Gen. 498 (2015) 99–106.

26) T. Konya, T. Katou, T. Murayama, S. Ishikawa, M. Sadakane, D. Buttrey, W. Ueda, An orthorhombic Mo_3VOx catalyst most active for oxidative dehydrogenation of ethane among related complex metal oxides, Catal. Sci. Technol. 3 (2013) 380-387.

27) S. Ishikawa, X. Yi, T. Murayama, W. Ueda, Heptagonal channel micropore of orthorhombic Mo_3VOx as catalysis field for the selective oxidation of ethane, Appl. Catal. A-Gen. 474 (2014) 10–17.

28) Sadakane, K. Kodato, N. Yasuda, S. Ishikawa, W. Ueda, Thermal behavior, crystal structure, and solid-state transformation of orthorhombic Mo–V oxide under nitrogen flow or in air, ACS Omega 4 (2019) 13165−13171.

29) R. Obunai, K. Tamura, I. Ogino, Sh.R. Mukai, Wataru Ueda, Mo-V-O nanocrystals synthesized in the confined space of a mesoporous carbon, Appl. Catal. A-Gen. 624 (2021) 118294.

30) P. Botella, A. Dejoz, M. C. Abelló, M. I. Vázquez, L. Arrúa, J. M. López Nieto, Selective oxidation of ethane: Developing an orthorhombic phase in Mo–V–X (X= Nb, Sb, Te) mixed oxides, Catal. Today 142 (2009) 272-277.

31) M. Aouine, T. Epicier, J.-M. M. Millet, In Situ Environmental STEM Study of the MoVTe Oxide M1 Phase Catalysts for Ethane Oxidative Dehydrogenation, ACS Catal. 6 (2016) 4775−4781.

32) D. Melzer, G. Mestl, K. Wanninger, A. Jentys, M. Sanchez-Sanchez, J.A. Lercher, On the Promoting Effects of Te and Nb in the Activity and Selectivity of M1 MoV-Oxides for Ethane Oxidative Dehydrogenation, Top. Catal. 63 (2020) 1754–1764.

33) A.M. Wernbacher, P. Kube, M. Hävecker, R. Schlögl, A. Trunschke, Electronic and Dielectric Propreties of MoV-Oxide (M1 Phase) under Alkane Oxidation Conditions, J. Phys. Chem. C. 123 (2019) 13269–13282.

34) C. Heine, M. Hävecker, A. Trunschke, R. Schlögl, M. Eichelbaum, The impact of steam on the electronic structure of the selective propane oxidation catalyst MoVTeNb oxide (orthorhombic M1 phase), Phys. Chem. Chem. Phys. 17 (2015) 8983-8993.

35) M. Caldararu, M. Scurtu, C. Hornoiu, C. Munteanu, T. Blasco, J.M. López Nieto, Electrical conductivity of a MoVTeNbO catalyst in propene oxidation measured in operando conditions, Catal. Today. 155 (2010) 311–318.

36) P. Concepción, S. Hernández, J. M. López Nieto, On the nature of active sites in MoVTeO and MoVTeNbO catalysts: The influence of catalyst activation temperature, Appl. Catal. A-Gen. 391 (2011) 92-101.

37) P. Botella, J.M. López Nieto, B. Solsona, A. Mifsud, F. Márquez, The preparation, characterization, and catalytic behavior of MoVTeNbO catalysts prepared by hydrothermal synthesis, J. Catal. 209 (2002) 445–455.

38) J.M. López Nieto, P. Botella, B. Solsona, J.M. Oliver, The selective oxidation of propane on Mo-V-Te-Nb-O catalysts: The influence of Te-precursor, Catal. Today 81 (2003) 87–94.

39) I.E. Wachs, J.-M. Jehng, W. Ueda, Determination of the chemical nature of active surface sites present on bulk mixed metal oxide, Catal., J. Phys. Chem. B 109 (2005) 2275–2284.

40) G. Mestl, In situ Raman spectroscopy for the characterization of MoVW mixed oxide catalysts, J. Raman Spectrosc. 33 (2002) 333–347.

41) B. Solsona, M.I. Vázquez, F. Ivars, A. Dejoz, P. Concepción, J.M. López Nieto, Selective oxidation of propane and ethane on diluted Mo–V–Nb–Te mixed-oxide catalysts, J. Catal. 252 (2007) 271–280.

42) H. Knözinger, H. Jezlorowski, Raman Spectra of Molybdenum Oxide Supported on the Surface of Aluminas, J. Phys. Chem. 82 (1978) 2002–2005.

43) L. Koudelka, J. Pospísil, P. Mosner, L. Montagne, L. Delevoye, Structure and properties of potassium niobato-borophosphate glasses, J. Non-Cryst. Solids 354 (2008) 129–133.

44) A. Celaya Sanfiz, T.W. Hansen, A. Sakthivel, A. Trunschke, R. Schlögl, A.Knoester, H.H. Brongersma, M.H. Looi, S.B.A. Hamid, J. Catal. 258 (2008) 35–43.

45) Y.V. Kolen'Ko, W. Zhang, R.N. D'Alnoncourt, F. Girgsdies, T.W. Hansen, T.Wolfram, R. Schlögl, A. Trunschke, ChemCatChem 3 (2011) 1597–1606.

46) R. Schlögl, Active sites for propane oxidation: some generic considerations, Top. Catal. 54 (2011) 627–638.

47) P. Botella, J.M. López Nieto, B. Solsona, A. Mifsud, F. Márquez, The Preparation, Characterization, and Catalytic Behavior of MoVTeNbO Catalysts Prepared by Hydrothermal Synthesis, J. Catal. 209 (2002) 445-455.

48) A. Trunschke, J. Noack, S. Trojanov, F. Girgsdies, T. Lunkenbein, V. Pfeifer, M. Hävecker, P. Kube, C. Sprung, F. Rosowski, R. Schlögl, The impact of the bulk structure on surface dynamics of complex Mo–V-based oxide catalysts, ACS Catal. 7 (2017) 3061-3071.

49) A. Celaya Sanfiz, T. W. Hansen, F. Girgsdies, O. Timpe, E. Rodel, T. Ressler, A. Trunschke, R. Schlögl, Preparation of Phase-Pure M1 MoVTeNb Oxide Catalysts by Hydrothermal Synthesis-Influence of Reaction Parameters on Structure and Morphology, Top. Catal. 50 (2008) 19-32.

50) D.A. Svintsitskiy, T.Yu Kardash, E.V. Lazareva, V.M. Bondareva, X-ray-induced transformations on the surface of MoVNbTe mixed oxide catalyst: An XPS study, Applied Surface Science 535 (2021) 147676.

51) N. Watanabe, W. Ueda, Comparative study on the catalytic performance of single-phase Mo−V−O-based metal oxide catalysts in propane ammoxidation to acrylonitrile, Ind. Eng. Chem. Res. 45 (2006) 607-614.

52) R.M. Fernández-Domene, R. Sánchez-Tovar, B. Lucas-granados, M.J. Muñoz-Portero, J. García-Antón, Elimination of pesticide atrazine by photoelectrocatalysis using a photoanode based on WO_3 nanosheets, Chem. Eng. J. 350 (2018) 1114–1124.

53) R.M. Fernández-Domene, G. Roselló-Márquez, R. Sánchez-Tovar, B. Lucas-Granados, J. García-Antón, Photoelectrochemical removal of chlorfenvinphos by using WO_3 nanorods: Influence of annealing temperature and operation pH, Sep. Purif. Technol. 212 (2019) 458–464.

54) I.A. de Castro, R.S. Datta, J.Z. Ou, A. Castellanos-Gomez, S. Sriram, T. Daeneke, K. Kalantar-zadeh, Molybdenum Oxides – From Fundamentals to Functionality, Adv. Mater. 29 (2017) 1–31.

55) Y. Zhu, Y. Yao, Z. Luo, C. Pan, J. Yang, Y. Fang, H. Deng, C. Liu, Q. Tan, F. Liu, Y. Guo, Nanostructured MoO_3 for efficient energy and environmental catalysis, Molecules. 25 (2020) 1–26.

56) S. Najari, S. Saeidi, P. Concepcion, D.D. Dionysiou, S.K. Bhargava, A.F. Lee, K. Wilson, Oxidative dehydrogenation of ethane: Catalytic and mechanistic aspects and future trends, Chem. Soc. Rev. 50 (2021) 4564–4605.

57) E. Heracleous, A.A. Lemonidou, Ni-Nb-O mixed oxides as highly active and selective catalysts for ethene production via ethane oxidative dehydrogenation. Part I: Characterization and catalytic performance, J. Catal. 237 (2006) 162–174.

58) X. Zhao, M.D. Susman, J.D. Rimer, P. Bollini, Tuning selectivity in nickel oxide-catalyzed oxidative dehydrogenation of ethane through control over non-stoichiometric oxygen density, Catal. Sci. Technol. 11 (2021) 531–541.

59) D.M. Gómez, V. V. Galvita, J.M. Gatica, H. Vidal, G.B. Marin, TAP study of toluene total oxidation over a Co_3O_4/La-CeO_2 catalyst with an application as a washcoat of cordierite honeycomb monoliths, Phys. Chem. Chem. Phys. 16 (2014) 11447–11455.

60) J.M.M. Millet, Mechanism of first hydrogen abstraction from light alkanes on oxide catalysts, Top. Catal. 38 (2006) 83–92.

61) I. Popescu, Z. Skoufa, E. Heracleous, A. Lemonidou, I.C. Marcu, A study by electrical conductivity measurements of the semiconductive and redox properties of Nb-doped NiO catalysts in correlation with the oxidative dehydrogenation of ethane, Phys. Chem. Chem. Phys. 17 (2015) 8138–8147.

62) J. M. López Nieto, P. Botella, M. I. Vázquez, A. Dejoz, The selective oxidative dehydrogenation of ethane over hydrothermally synthesised MoVTeNb catalysts, Chem. Commun. 17 (2002) 1906-1907.

63) R.K. Grasselli, Site isolation and phase cooperation: Two important concepts in selective oxidation catalysis: a retrospective, Catal. Today 238 (2014) 10–27.

64) P. DeSanto Jr., D.J. Buttrey, R.K. Grasselli, C.G. Lugmair, A.F. Volpe, B.H. Toby, Th. Vogt, Structural characterization of the orthorhombic phase M1 in MoVNbTeO propane ammoxidation catalyst, Top. Catal. 23 (2003) 23–38.

65) B. Grzybowska-Swierkosz, Active centres on vanadia-based catalysts for selective oxidation of hydrocarbons, Appl. Catal. A-Gen. 157 (1997) 409–422.

66) A. Corma, J.M. López Nieto, N. Paredes, Influence of the preparation procedure methods of V-Mg-O catalysts in their catalytic properties for the Oxidative dehydrogenation of propane, J. Catal. 144 (1993) 425-438.

67) J.M. López Nieto, The selective oxidative activation of light alkanes. From supported vanadia to multicomponent bulk V-containing catalysts, Top. Catal. 41 (2006) 3–15.

68) J.L. Callahan and R.K. Grasselli, A selectivity factor in vapor-phase hydrocarbon oxidation catalysis, AIChE J. 9 (1963) 755-760.

Chapter 6

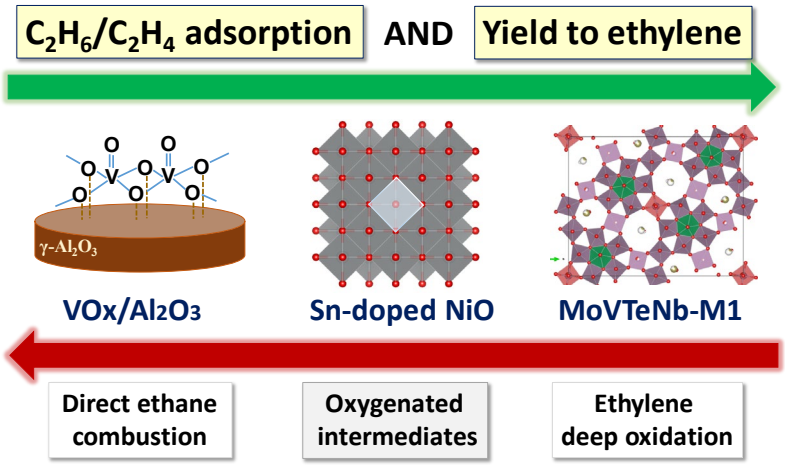

Evolution of the optimal catalytic systems for ethane ODH: the role of adsorption in catalytic performance

6.1. Previous considerations

Preceding chapters throughout the present thesis have been devoted to study the best performing catalytic systems for the oxidative dehydrogenation of ethane (ODHE) presenting the M1 phase, culminating in **Chapter 5**, in which a comparison between the best bi-, tri- and tetrametallic M1 catalysts, i.e., Mo-V-(Te,Nb)-O_x, was stablished.

Nevertheless, and as discussed in the Introduction section (**Chapter 1**), multicomponent MoV(Te,Nb)O materials were not the only catalytic systems employed for this reaction along the years. Therefore, this chapter is dedicated to compare some the best type of catalysts that have presented optimal catalytic properties in the ODHE all over the last 30 years. In our case, the three catalytic systems that are compared in this chapter are: **i)** alumina-supported vanadium oxide, **ii)** tin-promoted nickel oxide; and **iii)** multicomponent tetrametallic Mo-V-Te-Nb-O mixed metal oxide.

Alumina supported vanadium oxide catalysts were initially proposed in the nineties of the last century [1-5]. The reason of using this support is based on the acidic properties that it presents, and the strong interaction between this oxide and the dispersed vanadium oxide species onto its surface. In its best formulations, relatively low vanadium loadings are required [1-10], in order to achieve isolated vanadium oxide species (ca. 1.4-4.2 Vanadium atoms nm^{-2}) [8], preventing the formation of bulk nanoparticles of vanadium pentoxide [1-10], and mitigating partially the overoxidation of the olefin formed [6, 8, 9].

In the case of promoted nickel oxide catalysts [11-19], initially with Nb-promoted NiO catalysts proposed by Lemonidou group [11-13], several promotors have been proposed in the last years [14-19]. It is known that NiO present a very low selectivity to ethylene during the ODHE [11-19], although recently [20], it has been demonstrated that, by tuning the preparation method and the activation temperature, a selectivity to ethylene near to 70% at ethane conversion lower than 20% can be achieved by undoped NiO. However, the addition of promoters [11-19] or incorporating NiO over metal oxide supports [12, 21] dramatically decrease the direct transformation of ethane into CO_2, especially at ethane conversions lower than 30%. This is the case of promoters such as Sn^{4+}, Ti^{4+} or Nb^{5+} (in general with a promoter/Ni ratio of ca. 0.03-0.20 [11-19] or supporting NiO on specific metal oxide supports/dilute such as γ-Al_2O_3 [12, 21] , TiO_2 [22, 23], mixed Ti-Si-O materials [24] or Nb-containing siliceous porous clay heterostructure [25], those are particularly interesting for optimizing this type of catalysts.

The catalytic performance of NiO-based catalysts has been discussed in terms of the reducibility of Ni-O-sites, but also considering the specific chemical nature of Ni species on each catalyst. However, the influence of the particle size and the presence of Ni and O vacancies, as well as the elimination of unselective electrophilic O^- species, have a positive effect on the catalytic performance in the ODH of ethane [22], and in the case of supported NiO, maximizing the Ni-O-support interaction [23]. However, a low selectivity to ethylene achieved by NiO-based catalysts has been

related to a low interaction between NiO and dilute/support, which hinders the elimination of unselective electrophilic O^- species [14, 17, 23].

Indeed, the explanation for this enhanced catalytic performance of promoted/supported NiO catalyts lies on the apparent elimination of electrophilic oxygen species by the addition of these promoters, whether in the form of an isomorphical substitution of the Ni^{2+} cations for the promoter of the formation of nanocrystal oxides on the surface of the NiO [11, 13, 17, 26].

Lastly, the third group of catalysts compared in this chapter is multicomponent Mo-V-Te-Nb-O oxide [27, 28], studied along the present thesis, whose goodness have been widely reported in the previous chapters. Nevertheless, even lots of efforts are being put in the improvement of the catalytic properties of the three systems, the nature of both active and selective sites is not completely understood.

Therefore, this chapter presents a comparative study of the catalytic performance in ethane ODH of VO_x/Al_2O_3 (**5V/AL**, with 5 wt% of V atoms), Sn-doped NiO (**(Sn)NiO**, with a Sn/Ni ratio of 0.10) and a multicomponent Mo-V-Te-Nb-O mixed metal oxides (**MVTN-600**, with a Mo/V/Te/Nb atomic ratio of 1.00/0.25/0.17/0.17) catalysts, and their physicochemical characteristics, by means of the effect of surface Lewis acid sites and adsorption enthalpy, correlating in situ ethylene and oxygen coadsorption IR experiments with microcalorimetric studies, where the role of surface oxygen species in the overoxidation of ethylene will be also discussed.

6.2. Physicochemical characterization of catalysts

The main characteristics of the three catalysts synthesized are summarized in **Table 6.1**, considering the vanadium (i.e., **MVTN-600** and **5V/AL** catalysts) and nickel (i.e., **(Sn)NiO** catalyst) atoms the active centers for each catalyst, respectively, and using reported data for each type of catalyst [5, 15, 27, 29-32]. Moreover, **Figure 6.1** shows the most representative basic characterization of the samples.

Table 6.1. Characteristics of catalysts.

Catalyst	**5V/AL**	**(Sn)NiO**	**MVTN-600**
Composition (at. ratio)	V:Al = 5.5:94.5	Ni:Sn = 92:8	Mo:V:Te:Nb = 63:15:11:11
V or Ni (wt.%)	5.0	66.9	3.8
S_{BET} (m^2 g^{-1})	144	84	10
V- or Ni- surface content (10^{18} atoms m^{-2})	4.0 [a]	8.7 [b]	1.8
Heat-treatment (2h)	Air 550 ºC	Air 500 ºC	N_2 600 ºC
XRD crystalline phases	γ-Al_2O_3	NiO	M1
Other species present (Raman)	(VO_4) + (VO_4)$_n$ species	SnO_2 nanoparticles	none

a) Cross-sectional area of a molecule of supported V_2O_5 is 0.201 nm^2 using [42], thus, 4.98 x 10^{14} molec. V_2O_5 cm^{-2} would form a monolayer that covers the support completely.
b) Using [45], a monolayer of nickel oxide completely covering the surface of a support should need 9.7 x 10^{14} molec. NiO cm^{-2} (considering a Ni/Sn atomic ratio of 92/8).

In this way, **Fig. 6.1-A** shows the XRD pattern of the **MVTN-600** catalyst already seen in the previous chapter (see **Chapter 5**, **Figure 5.1-C**). This pattern shown is characterized by the single presence of the diffraction peaks corresponding to the M1 phase [27, 29, 32-37].

Furthermore, **Fig. 6.1-B** plots both the Raman (with laser of 514 nm) and the UV-Raman (with laser of 325 nm) for this sample. Both spectra showed, in a higher or lesser extent, the presence of an intense peak centered at ca. 872 cm^{-1}, with a broad shoulder at lower frequencies (770-840 cm^{-1}) and a signal at 477 cm^{-1}, all of them related to symmetric and antisymmetric stretching vibrations of Me-O-Me bonds. Additionally, a shoulder appearing at 980 cm^{-1} and further bands at 664 and 820 cm^{-1} are assigned to stretching vibrations of terminal Mo=O and V=O bonds [38], the former, and Nb-O-Nb bonds [39], the latter. Lastly, in **Fig. 6.1-C** it is shown the XPS spectrum of the V $2p_{3/2}$ core level for the **MVTN-600**. This signal can be deconvoluted into a unique contribution centered at 515.2 eV of Binding Energy (B.E.), confirming the single presence of V^{4+} species [27].

In the same manner, **Figs. 6.1-D**, **6.1-E** and **6.1-F** show the XRD, Raman and XPS analysis for the **(Sn)NiO**, respectively. As seen for its XRD pattern (**Fig. 6.1-D**), the **(Sn)NiO** catalyst presents the classical diffraction peaks at 2θ= 37.2º, 43.2º, 62.8º and 79.3º, that correspond to the (111), (200), (220), (311) and (222) planes in the face-centered cubical structure of the NiO (JCPDS: 78-0643), but also the minority presence of SnO_2 crystallites (JCPDS: 41-1445) [15]. Moreover, UV-Raman spectrum displayed in **Fig. 6.1-E** consist of bands at 516 and 580 cm^{-1}, corresponding to one-phonon LO modes, as well as bands at 707 cm^{-1} (two-phonon 2TO

mode), 906 cm^{-1} (TO+LO mode) and 1109 cm^{-1} (2LO mode). In addition to this, the presence of a broad signal at ca. 516 cm^{-1} in the Raman spectrum, seen in other doped NiO materials [23], confirms the presence of NiO nanoparticles [40]. Furthermore, **Fig. 6.1-F** shows the XPS spectrum of the Ni *2p3/2* core level, that can be deconvoluted into the three typical signals of NiO: **i)** a main peak at ca. 853.7 eV that corresponds to structural Ni^{2+} species; **ii)** followed by a second signal (named Sat I) at 2eV higher energy (855.7 eV), assigned to the presence of defects such as Ni^{3+} species, cationic vacancies or Ni^{2+}-OH species [15, 17]; **iii)** and a second broad satellite (Sat II), centered at 860.9 eV, that is attributed to ligand-metal charge transfers [15, 33, 41, 42].

Finally, the characterization results for the vanadium oxide supported on γ-alumina catalyst (**5V/AL**) are presented in **Figs. 6.1-G**, **H** and **I**. The XRD pattern shown in **Fig. 6.1-G** exhibits the diffraction peaks of Al_2O_3 (2θ = 38º, 46º and 67º, corresponding to the (311), (400) and (440) planes [43]), with no visible presence of peaks associated to bulk V_2O_5, suggesting that vanadium oxides species are properly dispersed all over the support [5]. This was further confirmed by Raman and UV-Raman spectra shown in **Fig. 6.1-H**, with the single presence of a band at ca. 927 cm^{-1} (this is, 920-940 cm^{-1} region in UV-Raman spectrum) that was reported to be characteristic of polymeric vanadium species well dispersed onto the γ-Al_2O_3 surface [44]. Also, in contrast with the **MVTN-600** sample, the V *2p3/2* core level XPS spectrum for the **5V/AL** catalyst (**Fig. 6.1-I**) shows the presence of two components, one minority at 515.2 eV (associated to V^{4+})

and a main signal at 516.8 eV, which confirms the majority presence of V^{5+} in the case of the **5V/AL** sample [45].

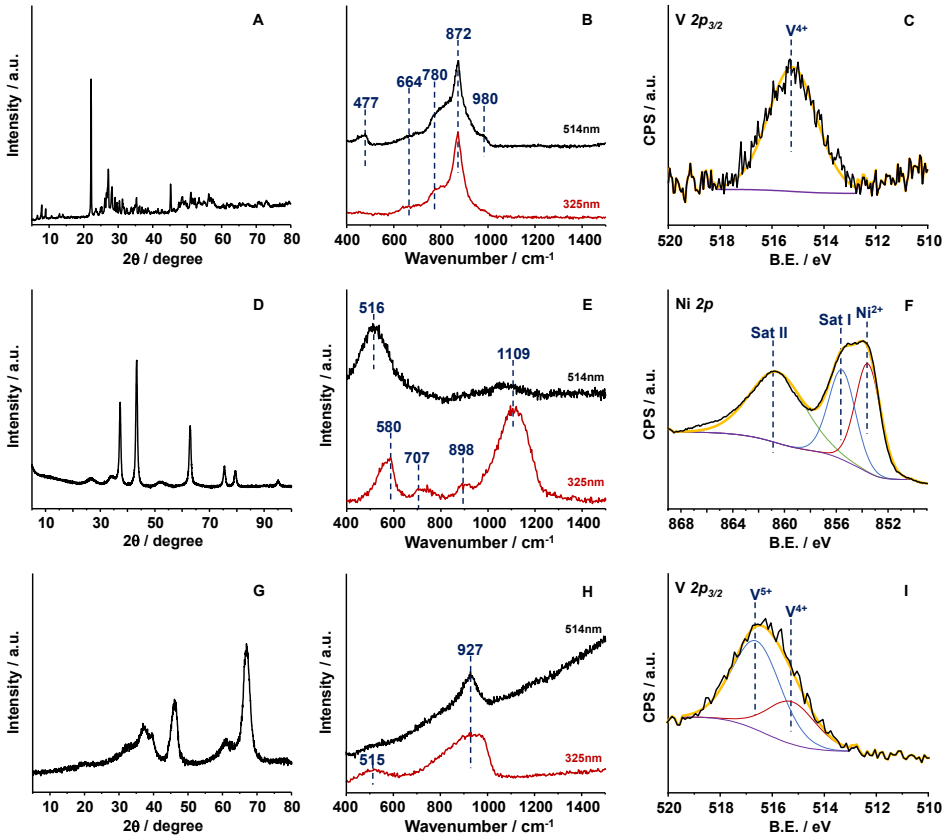

Figure 6.1. XRD (**A, D, G**); UV-Raman (325nm, red) + Raman (514nm, black) (**B, E, H**); and V $2p_{3/2}$ (**C, I**) and Ni $2p_{3/2}$ (**F**) core level XPS spectra of catalysts: **MVTN-600** (**A, B, C**), **(Sn)NiO** (**D, E, F**) and **5V/AL** (**G, H, I**) catalysts.

Reducibility of the catalysts was subsequently studied by H_2-TPR experiments and results are comparatively plotted in **Figure 6.2**. The

MVTN-600 catalyst shows two reduction maxima at 500 ºC and 520 ºC, being the first one related to the reduction of surface V-O-Mo bonds, while the second one is ascribed to the bulk reduction [32, 46]. Nevertheless, for **(Sn)-NiO** and **5V/AL** samples, a unique reduction peak is observed in both cases at 320 ºC and 475 ºC, respectively, that has been associated to the consecutive reduction process of each catalytic system: **i) (Sn)NiO** goes under NiO → $Ni^{\delta+}$ → Ni^{0} [15, 47] and **ii) 5V/AL** goes under V^{5+} → V^{4+} → V^{3+} [15, 48]. Moreover, the explanation of the little reduction observed in the **5V/AL** sample is that this catalyst only suffers a reduction of the vanadium species of the surface, whereas both **MVTN-600** and **(Sn)-NiO** catalysts also suffer a bulk reduction.

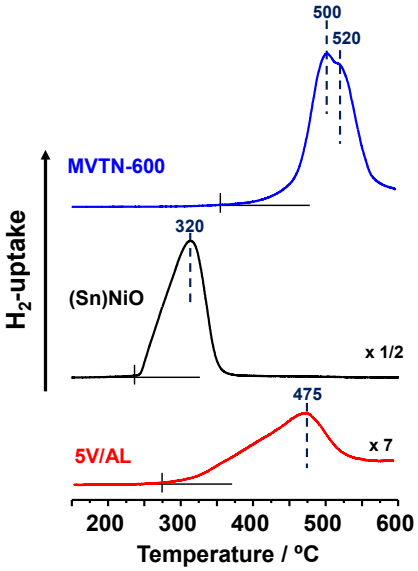

Figure 6.2. H_2-TPR analysis of **MVTN-600** (blue), **(Sn)NiO** (black) and **5V/AL** (red) catalysts.

Furthermore, microcalorimetry studies took place in order to calculate the heat of adsorption of both ethane and ethylene for each catalytic system, with experimental results displayed in **Table 6.2**. By looking at the calorimetric results, it is suggested that a high surface coverage occurs, in which strong and weak adsorption sites are presumably covered. In this sense, the **MVTN-600** sample is the catalyst that presents the highest values of hydrocarbon heat of adsorption, interacting slightly stronger with the olefin compared to the paraffin (39 kJ mol^{-1} for ethylene vs 32 kJ mol^{-1} for ethane), agreeing with previously reported results [29]. However, heat of adsorption for **(Sn)NiO** and **5V/AL** samples is notably lower (ca. 10-13 kJ mol^{-1}), values close to the condensation of the adsorbed molecules [29], so it indicates that no strong interaction exits between the hydrocarbons and the surfaces of said catalysts.

Moreover, it can be also observed that the amount of ethane/ethylene adsorbed over the **MVTN-600** catalyst is, more or less, the half than that calculated for **(Sn)NiO** and **5V/AL** (**Table 6.2**). Therefore, to carry out a more precise comparison between the three different catalytic systems, results can be normalized by surface area. Thus, values obtained where the ones as follows, **i)** for ethane: **MVTN-600** (4.9 μmol_{C2H6} m^{-2}) > **(Sn)NiO** (1.8 μmol_{C2H6} m^{-2}) > **5V/AL** (0.8 μmol_{C2H6} m^{-2}); whereas **ii)** for ethylene: **MVTN-600** (5.3 μmol_{C2H4} m^{-2}) > **(Sn)-NiO** (1.5 μmol_{C2H4} m^{-2}) > **5V/AL** (0.8 μmol_{C2H4} m^{-2}). Interestingly, these values calculated kept a similar range regardless of the molecule studied.

Table 6.2. Comparative results of hydrocarbon microcalorimetic measurements.

Catalyst	Hydrocarbon	Heat ($J\ g_{cat}^{-1}$)	Adsorbed HC ($\mu mol\ g_{cat}^{-1}$)	Heat of adsorption ($kJ\ mol_{HC}^{-1}$)
MVTN-600	Ethane	1.546	48.6	32
MVTN-600	Ethylene	2.072	53.3	39
(Sn)NiO	Ethane	2.004	154.1	13
(Sn)NiO	Ethylene	1.299	124.8	10
5V/AL	Ethane	1.334	110.7	12
5V/AL	Ethylene	1.184	122.9	10

In addition, acidic properties of the three different catalysts were investigated by IR studies of CO and NH_3 adsorption (**Figs. 6.3-A**, **B** and **C**, respectively), correlating these values and the ones obtained from the calorimetric experiments by means of IR of adsorbed ethylene (**Fig. 6.3-D**).

In the case of the IR spectra of CO adsorption, carbon monoxide has been used as a probe molecule for surface Lewis acid titration (experiments taken place at -165 ºC). In our case, for **MVTN-600**, it is observed the single presence of a low intense band at ca. 2131 cm^{-1} (presumably related to a CO bonded to a reduced specie of Mo and/or V), which is characterized by π back-donation, and shifting the ν(CO) to lower values [49]. However,

physisorbed CO molecules into the hexagonal channels of the M1 structure could also be considered.

The spectrum for **(Sn)NiO** sample showed, however, the presence of multiple bands. For this catalyst, it is ascertained a predominant peak at 2151 cm^{-1} associated to CO coordinated to hydroxyl groups, in addition to a peak at 2174 cm^{-1} ascribed to a red-shifted carbonyl frequency of Ni^{2+} [41] and/or Sn^{4+} [50] related to lower acid strength. In any case, CO-IR spectrum of **(Sn)NiO** suggests a marked density of Lewis acid sites.

In the case of **5V/AL** spectrum of adsorbed CO showed two bands at 2185 cm^{-1} (very weak) and 2157 cm^{-1} (strong). The first signal has been related to V^{4+} cations, while the latter is due to coordinated CO molecules to the hydroxyl groups of the γ-Al_2O_3 support, as reported in [51].

Furthermore, NH_3-IR spectra of the catalysts after ammonia adsorption at RT are shown in **Fig. 6.3-B** (desorption at 25 ºC) and **Fig. 6.3-C** (desorption at 100 ºC). For the **MVTN-600** catalyst, bands at 1650, 1601, 1420, 1265 and 1197 cm^{-1} are observed (**Fig. 6.3-B**). In detail, and according to previous studies [49, 52], bands at 1601($\delta_{as}NH_3$), 1265 and 1197 cm^{-1} (splitting of the symmetric deformation mode, $\delta_{sym}NH_3$) are related to ammonia coordinated to Lewis acid sites, while bands at 1650 and 1420 cm^{-1} are ascribed to ammonium cations formed as a consequence of the interaction between NH_3 and Brønsted acid sites. Thus, NH_3-IR studies did show that the **MVNT-600** sample presents both Lewis and Brønsted acid site, although the latter in a fair in a lesser extent. In addition, the **5V/AL** catalyst shows a similar spectrum in the case of the NH_3-IR analysis,

however, the intensity of the bands is notably lower than that in **MVTN-600**, suggesting a marked lower density of acid sites.

Finally, experimental results for **(Sn)NiO** catalyst show the presence of bands at 1629, 1560, 1363, 1259 and 1185 cm^{-1}, assigned all of them to the formation of hydrazine on the surface of the sample, probably formed from the oxidation of ammonia due to the highly oxidizing behavior of NiO-based materials.

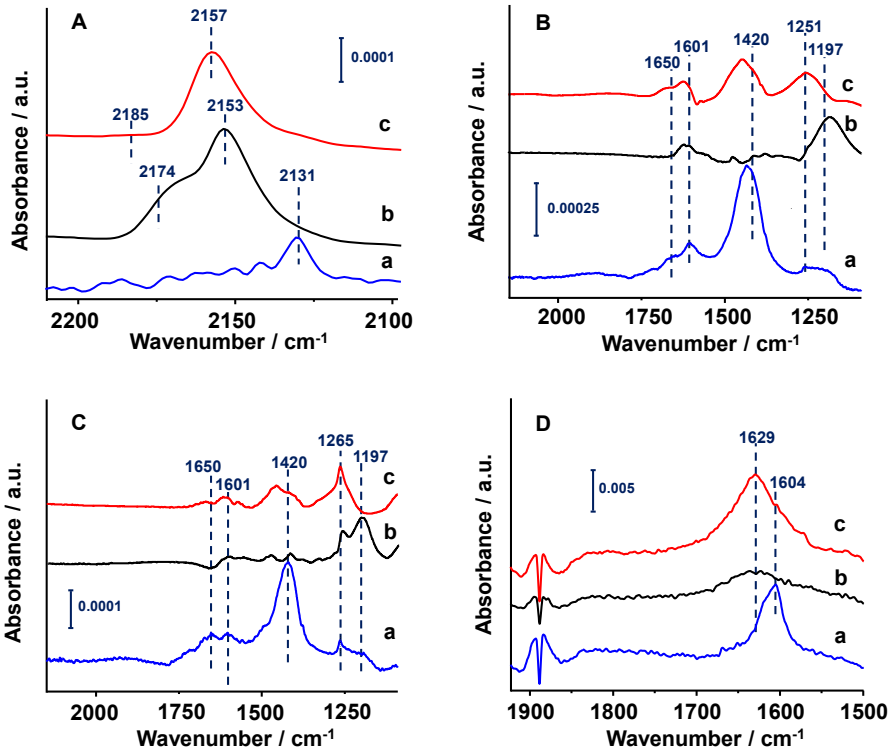

Figure 6.3. IR spectra of: **A**) CO adsorption at saturation coverage at -165ºC; (**B, C**) NH_3 adsorption after evacuation at 25 ºC (B) or 100 ºC (C); **D)** and ethylene adsorbed (43 mbar) after evacuation at 25 ºC. Catalysts: **MVTN-600** (a), **(Sn)NiO** (b) and **5V/AL** (c) catalysts.

Accordingly, in **Fig. 6.3-C** it is presented the spectra of ammonia desorption at 100 ºC instead of 25 ºC. In all of them, a clear decrease in the intensity of the signals is observed. Nevertheless, the appearance of a new band at 1265 cm^{-1} in the **(Sn)NiO** sample indicates that it is also working as a redox catalyst, however, the drastic decrease in the intensity of the bands for all the catalysts suggests a fairly low strength of their acid sites, as reported before [37, 52].

Therefore, to correlate data from calorimetry and CO/NH_3-IR studies, ethylene adsorption IR experiments were undertaken, and experimental results are plotted in **Figure 6.3-D**. Accordingly, all the catalysts presented a band in the range of 1600-1630 cm^{-1}, ascribed to the presence of ν(C=C) of adsorbed ethylene on the surface of every catalyst. Nonetheless, this absorbance maximum is shifted to lower wavenumber values in the case of the **MVTN-600** catalyst (1604 cm^{-1}) compared to both **(Sn)NiO** and **5V/AL** that present their absorbance maximum at 1629 cm^{-1}. Thus, this shift to lower wavenumber in the case of the M1 phase presenting catalyst indicate that there is a stronger interaction between the olefinic double bond in ethylene and its Lewis acid sites, as observed in the microcalorimetric experiments.

6.3. Catalytic properties of three different catalytic systems in ethane oxidative dehydrogenation

These three types of catalysts have been tested in the oxidative dehydrogenation of ethane (ODHE) with the following conditions: reaction

temperature of 400 and 450 ºC, reactant feed (C_2H_6/O_2/He) of 5/5/90 molar ratio and different contact times (modifying whether the catalyst weight and/or the total flow) in order to achieve higher hydrocarbon conversions. Moreover, in **Table 6.3**, several catalytic results are shown including: ethane reaction rates, turnover frequency (TOF), reaction order and ethylene reaction rates. Noteworthy, all these values have been expressed considering the different catalysts but also per active site (i.e., V atoms in the case of **MVTN-600** [27, 29, 32-37, 53-56] and **5V/AL** [5, 48] catalysts, and Ni atoms for **(Sn)NiO** [11-17]).

Therefore, by looking at the ethane transformation reaction rate values (**Table 6.3**), for the **MVTN-600** sample, the value obtained for r_{C2H6} was 2.29 $mmol_{C2H6}\ g_{cat}^{-1}h^{-1}$, while the rate considering the active sites (only vanadium atoms) is 38.8 $mmol_{C2H6}\ g_V^{-1}h^{-1}$, since it is well known that molybdenum oxide-derived catalysts are only active at reaction temperatures beyond 500 ºC [6] and Te- and Nb-oxides are inactive under the conditions used in this chapter.

In addition to this, reactivity values for the **(Sn)NiO** sample shown in **Table 6.3** reported values of r_{C2H6} of 17.6 $mmol_{C2H6}\ g_{cat}^{-1}\ h^{-1}$ and 26.3 $mmol_{C2H6}\ g_{Ni}^{-1}\ h^{-1}$, respectively. For this catalyst, the Ni sites are the actives ones since Sn atoms are inactive under our reaction conditions [15].

On the other hand, for the **5V/AL** catalyst, considering completely inactive the γ-Al_2O_3 support, reaction rate value (r_{C2H6}) obtained in this case was 0.424 $mmol_{C2H6}\ g_{cat}^{-1}\ h^{-1}$ while considering the active centers (vanadium) was 13.7 $mmol_{C2H6}\ g_V^{-1}\ h^{-1}$.

Table 6.3. Catalytic data in the ethane and ethylene oxidation of representative catalysts.

Catalyst	5V/AL	(Sn)-NiO	MVTN-600
Ethane ODH			
Reaction rate of ethane consumption ($mmol_{C2H6}\ g_{cat}^{-1}\ h^{-1}$)	0.68	17.6	2.29
Reaction rate of ethane consumption per active site ($mmol_{C2H6}\ g_{active\ site}^{-1}\ h^{-1}$)	13.7	26.3	60.3
Reaction rate of ethane consumption per surface area ($mmol_{C2H6}\ m^{-2}\ h^{-1}$)	0.09	0.31	6.0
Reaction rate of ethylene formation ($mmol_{C2H4}\ g_{cat}^{-1}\ h^{-1}$)	0.42	14.9	2.27
$n(C_2H_6)$ in ethylene formation[b]	0.80	0.52	0.88
$n(O_2)$ in ethylene formation[b]	0.15	0.26	0.22
Ethylene oxidation			
Reaction rate of ethylene consumption, ($mmol_{C2H4}\ g_{cat}^{-1}\ h^{-1}$)	1.76	3.71	0.17
Reaction rate of ethylene conversion per active site ($mmol_{C2H4}\ g_{active\ site}^{-1}\ h^{-1}$)	35.2	5.55	4.37
Rate per surface area ($mmol_{C2H4}\ m^{-2}\ h^{-1}$)	0.24	0.07	0.44
Relative reactivity ethylene/ethane	2.58	0.21	0.072

Note: reaction temperature = 400ºC, Hydrocarbon/O_2/He = 5/5/90 (molar ratio); reaction rates were determined for conversions lower than 5%; [b] reaction order in the ethylene formation during the ethane oxidation $r = k\ P_{C2H6}^{n(C2H6)}\ P_{O2}^{n(O2)}$.

Thus, by using the mass of catalyst as reference, the reactivity of the catalysts varies according to the following trend: **(Sn)NiO** (17.6 $mmol_{C2H6}\ g_{cat}^{-1}\ h^{-1}$) > **MVTN-600** (2.29 $mmol_{C2H6}\ g_{cat}^{-1}\ h^{-1}$) > **5V/AL** (0.424 $mmol_{C2H6}\ g_{cat}^{-1}\ h^{-1}$); however, a completely different disposition is obtained taking

into account the active centers: **MVTN-600** (38.8 $mmol_{C2H6}$ g_V^{-1} h^{-1}) > **(Sn)NiO** (26.3 $mmol_{C2H6}$ g_{Ni}^{-1} h^{-1}) > **5V/AL** (13.7 $mmol_{C2H6}$ g_V^{-1} h^{-1}).

Furthermore, in **Figure 6.4** it is plotted the selectivity to ethylene for the three different catalysts studied (**Fig. 6.4-A**, **B** and **C**), as well as the selectivity to carbon oxides (CO_x) observed as minor by-products during the reaction (**Fig. 6.4-D**, **E** and **F**), respectively.

For the **MVTN-600** sample (**Fig. 6.4-A**), as reported in **Chapter 5**, ethylene is practically the only product obtained (99% selectivity at 2% of ethane conversion), being consistently stable throughout the different ethane conversion (96% at 40% ethane conversion). Moreover, both CO and CO_2 were observed as traces (**Fig. 6.4-D**), whereas no noticeable differences were ascertained between the two reaction temperatures employed (400 and 450 ºC). These reactivity and selectivity values gave rise to a 70% yield to ethylene.

In the case of the **(Sn)NiO** catalyst (**Fig. 6.4-B**), quite high selectivity values (ca. 86%) were obtained at low ethane conversion (2%), nevertheless, the drop in selectivity is higher than for **MVTN-600**, showing a 76% of selectivity at 40% of ethane conversion. Additionally, when looking at by-products (**Fig. 6.4-E**), CO_2 was the only carbon oxide observed, no CO was detected. Moreover, no differences between 400 ºC and 450 ºC were observed. The calculated yield to ethylene for this catalyst was ca. 30%.

On the other hand, the catalytic performance for the **5V/AL** catalyst (**Fig. 6.4-C**) showed some differences when compared to the **MVTN-600** and

(Sn)NiO catalysts. In this sense, the selectivity to ethylene dramatically decreases upon ethane conversion, however, it increases with the reaction temperature. Thus, an initial selectivity to ethylene of 90% is observed at 450 ºC, whereas 80% is the value obtained at 400 ºC. Nevertheless, these values are clearly lower than those reported elsewhere for this type of materials [7, 48] since reaction temperatures should be set around 500-550 ºC to favor the reduction-reoxidation of the catalyst [48]. Nonetheless, for a proper comparison between catalysts, 400 and 450 ºC were the temperatures set for this study. Accordingly, in the best scenario, an ethylene yield of 9% is obtained. As evidenced, a higher formation of carbon oxides is observed for this catalyst (**Fig. 6.4-F**), in where at initial ethylene conversion the CO selectivity ranged from 6 to 16%, while 4% selectivity to CO_2 was obtained regardless of the reaction temperature.

Moreover, these catalysts were also tested in the ODH of ethylene, and results are displayed in **Figs. 6.5-A** and **6.5-B** for the selectivity to CO_2 and CO, respectively.

In the case of the **MVTN-600** and **5V/AL** catalysts, both deep oxidation products were detected (in a higher or lower extent depending on the catalyst), being majority the formation of CO_2 for **MVTN-600**, whereas CO was the main product observed for **5V/AL** (although acetic acid was also detected as traces for this catalyst). In addition, the selectivity to both CO and CO_2 kept constant during the reaction, suggesting that there is not a further oxidation of CO to CO_2 over these catalysts. However, CO_2 was only observed over **(Sn)NiO** catalyst.

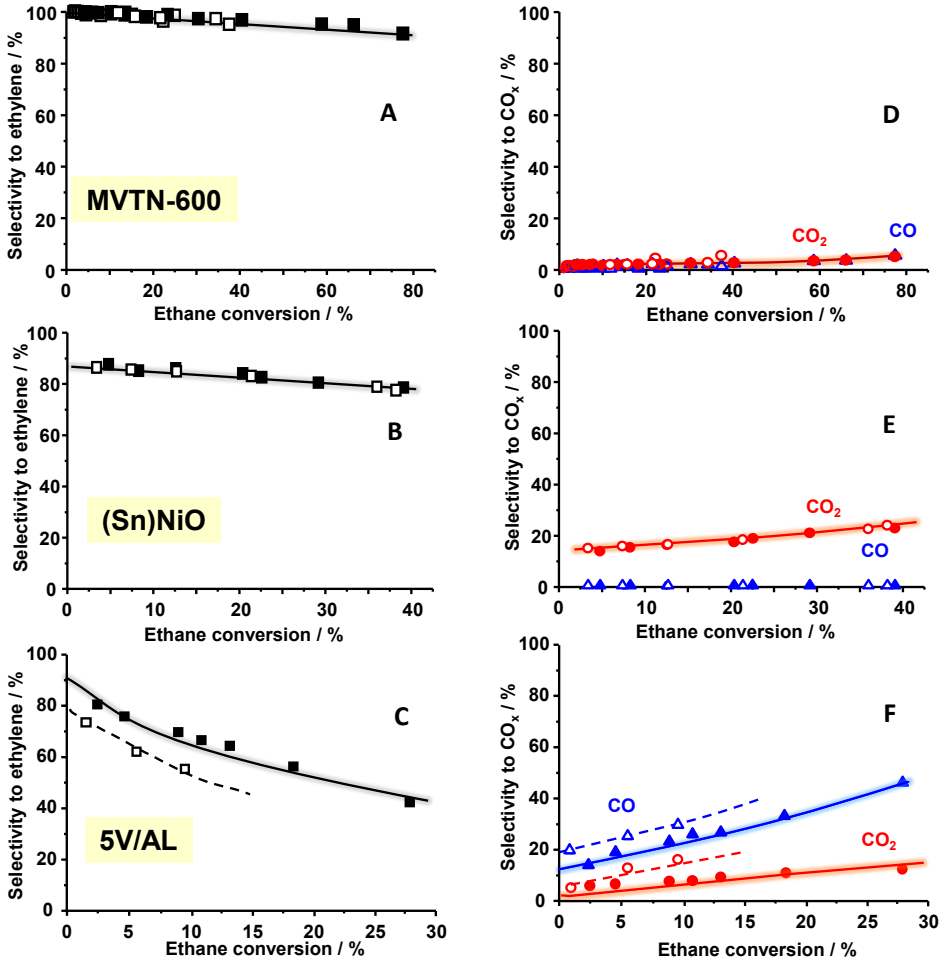

Figure 6.4. Variation of the selectivity to ethylene (**A, B, C**) and CO_x (**D, E, F**) with the ethane conversion at 400 ºC (full dots) and 450 ºC (empty dots) for **MVTN-600** (**A**, **D**), **(Sn)-NiO** (**B**, **E**) and **5V/AL** (**C**, **F**) catalysts. Ethylene (black); CO (blue) and CO_2 (red).

In order to understand the capacity of catalysts for CO oxidation, additional CO oxidation experiments took place (**Fig. 6.5-C**). It can be seen that the **(Sn)NiO** catalyst fully oxidizes CO to CO_2, reaching complete conversion

at temperatures below 300 ºC, which far lower than those used in this study of the ODH of both ethane and ethylene. However, **MVTN-600** and **5V/AL** were shown as inactive in the CO oxidation in the temperatures range used. This catalytic performance explains why CO is not observed during the ethane ODH over the **(Sn)NiO** catalyst.

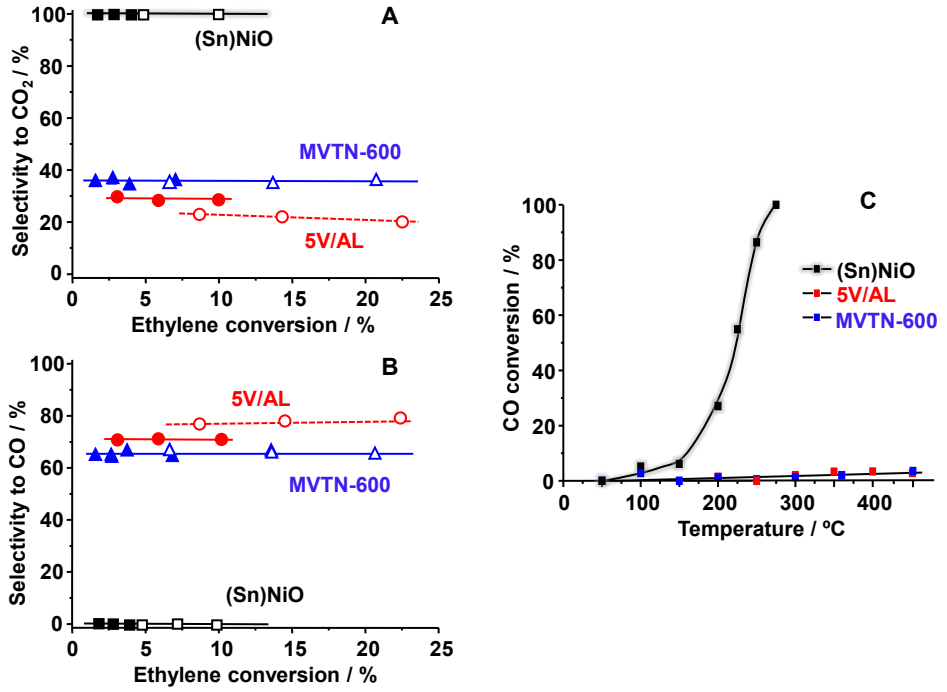

Figure 6.5. Variation of the selectivity to CO_2 (**A**) and CO (**B**) with during the ODH of ethylene, and CO conversion as a function of the temperature (**C**) for **MVTN-600** (blue), **(Sn)NiO** (black) and **5V/AL** (red) catalysts.

These results perfectly agree with works previously published in where the catalytic activity for CO oxidation is explained based on the extent of homomolecular exchange of oxygen atoms, that depends on the number of

Me=O bonds and their strength [57]. Accordingly, undoped and doped NiO catalysts reported higher rates of homomolecular oxygen exchange [15] than V-based catalysts (i.e., **MVTN-600** [38] and **5V/AL** [58]). Nevertheless, a correlation between CO oxidation (or the homomolecular oxygen exchange) and the selectivity to ethylene during the ethane ODH is not observed.

Figure 6.6 shows the variation of both ethane and ethylene conversion with different contact times (W/F) for **MVTN-600** (**Fig. 6.6-A**), **(Sn)NiO** (**Fig. 6.6-B**) and **5V/AL** (**Fig 6.6-C**) catalysts. It must be noted that values are extracted from experiments at 400 ºC and reaction rates (r_{C2H4} / r_{C2H6}) were calculated at hydrocarbon conversions lower than 5%.

For the **MVTN-600** sample (**Fig. 6.6-A**), it can be seen that ethylene practically does not react over this catalyst, whereas ethane does, in fact, reaction rate for ethane is nearly 14 times the one of its corresponding olefin, which agrees with the only subtle drop in selectivity observed in **Fig. 6.5-A**. Same trend was observed with the **(Sn)NiO** catalyst (**Fig. 6.6-B**), less marked though, with ethylene reacting slower than ethane (5 times). Conversely, the **5V/AL** sample presents an olefin reaction rate almost 3 times higher than the paraffin (**Fig. 6.6-C**).

Moreover, it must be noted that, for undoped and (Zr/Nb)-doped NiO catalysts, minimal differences have been previously reported in terms of r_{C2H4} / r_{C2H6} ratio (ranging from 0.41 to 0.53 [59]), nevertheless, in the case of supported vanadium oxide catalysts, those r_{C2H4} / r_{C2H6} ratios heavily

vary from 2 to 10 depending on the support employed and also the hydrocarbon fed [60].

Hence, in here it is shown that the reactivity is not only related to the active center itself, but also to its environment and the reaction rates of both ethane and ethylene. These results correlate to the selectivity to ethylene shown in the ODH of ethane by these catalysts in **Fig. 6.5**.

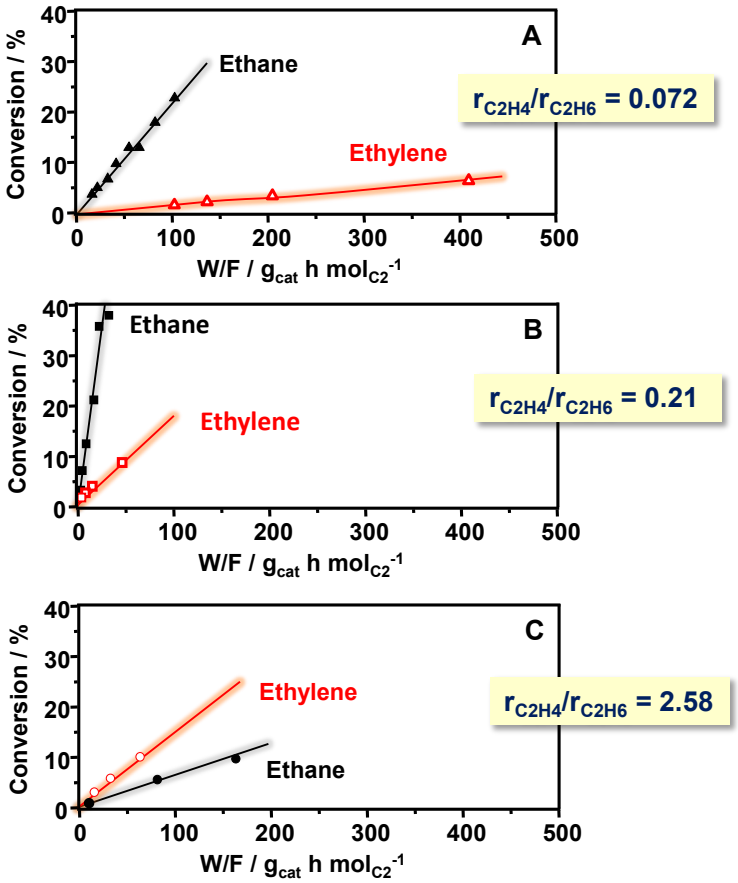

Figure 6.6. Variation of ethane (open symbols) and ethylene (full symbols) conversion with contact time (W/F) for **MVTN-600** (**A**), **(Sn)NiO** (**B**) and **5V/AL** (**C**) catalysts. Reaction conditions: 5 C_2H_6/5 O_2/ 90 He molar ratio and a reaction temperature of 400 ºC.

Accordingly, two different reaction pathways for the oxidative dehydrogenation of ethane can be suggested depending on the active center of the catalyst. Nevertheless, the values of the kinetic constant do dramatically depend on the crystalline phase of the catalyst. In one side, for V-containing catalysts (**Figure 6.7-A**), it can be observed that ethane is initially transformed into ethylene (almost exclusively), carbon monoxide and carbon dioxide (in different proportion). However, the ethylene formed can also be transformed into CO (mainly) and CO_2, in a lesser (**MVTN-600**) or greater (**5V/AL**) extent.

Conversely, the different mechanism for Ni-based catalysts (**Figure 6.7-B**), **(Sn)NiO** sample for instance, comprehends a route where, like in the case of the V-containing catalysts, ethane is preferentially transformed into ethylene, but also CO_2 is formed. Nonetheless, even not being detected, the formation of CO and its further oxidation to CO_2 is very likely.

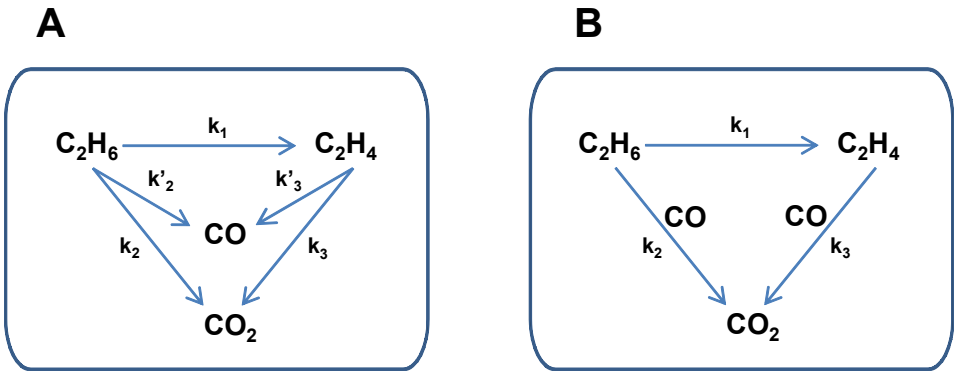

Figure 6.7. Reaction mechanism for the oxidative dehydrogenation of ethane over: **A**) V-containing catalysts, **MVTN-600** and **5V/AL**; and **B**) Ni-containing catalysts, **(Sn)NiO.**.

6.4. In-situ IR studies of coadsorbed ethylene and O_2

Although olefin in-situ IR experiments have taken place throughout the present chapter (**Fig. 6.3-D**), real catalytic conditions must consider the presence of molecular oxygen in the reaction media. Therefore, in order to explain the catalytic behavior of the different systems studied, the last part of this chapter is devoted to in situ IR experiments of coadsorbed ethylene and O_2, with spectra obtained in the 25-250 ºC temperature range, and results are shown in **Figure 6.8**. It must be noted that, for every catalyst, a RT experiment after thermal desorption has been collected and it is plotted in highlighted orange within the figure.

In this sense, **Fig. 6.8-A** shows the evolution of the ethylene desorption with temperature for the **MVTN-600** sample. In this figure, it can only be seen an IR band at 1605 cm^{-1}, that corresponds to the ethylene adsorbed (also seen in **Fig. 6.3-D**), further disappearing at temperatures higher than 100 ºC. Moreover, it hardly appears extremely low intense broad bands at 1516 and 1350 cm^{-1}, which correspond to ν_{asym} and ν_{sym} modes of carboxylate species, respectively. This result indicates a fast desorption of ethylene on this catalyst. Furthermore, no ethylene readsorption was observed for this catalyst.

Fig. 6.8-B shows the spectra for **(Sn)NiO** catalyst, which look quite different from those obtained in the case of **MVTN-600** (**Fig. 6.8-A**). Thereby, in this catalyst, ethylene is also desorbed at 100 ºC (red spectrum in **Fig. 6.8-B**), nevertheless, new IR bands at 1576, 1511, 1345 and 1304 cm^{-1} appear. All these bands have been linked to carbonate/carboxylate species, probably due to the formation of oxygenated compounds that lead

to the production of carbon oxides that, what is more, grow in intensity with the temperature.

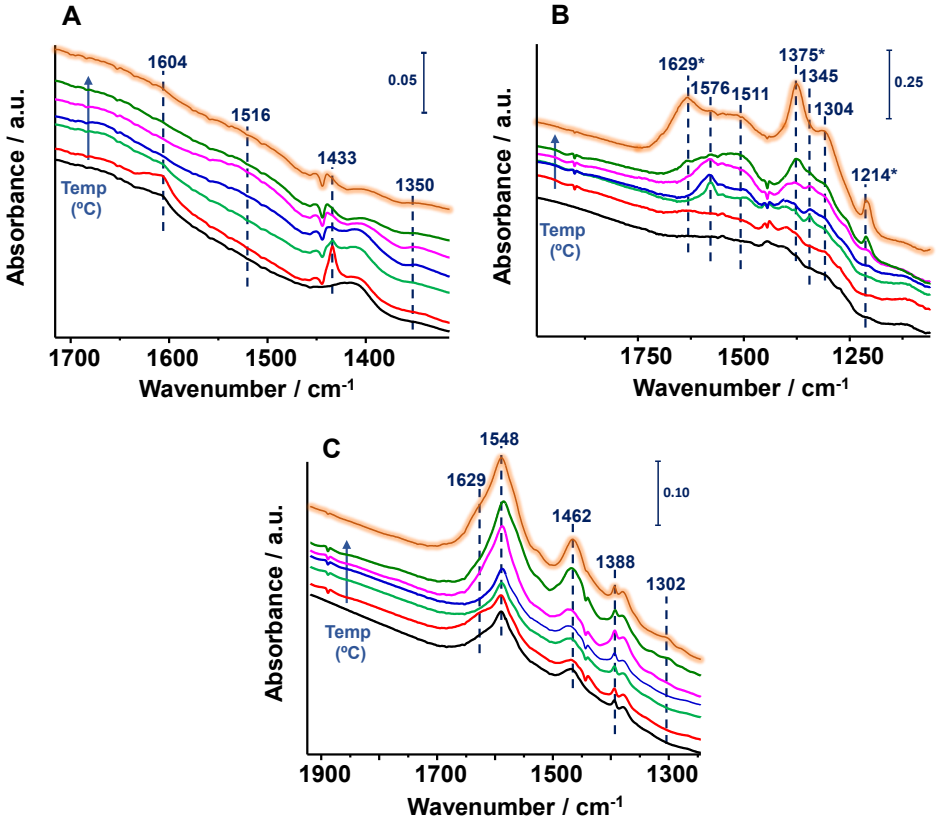

Figure 6.8. In situ IR spectra of coadsorbed ethylene and O_2 at constant reaction pressure (128 mbar, 43 mbar of C_2H_4 and 84 mbar of O_2) and increasing temperatures with reference spectrum prior to adsorption (black): 25 ºC (red), 100 ºC (green), 150 ºC (blue), 200 ºC (magenta) and 250 ºC (dark green). Samples studied: **MVTN-600** (**A**); **(Sn)NiO** (**B**); and **5V/AL** (**C**). Additionally, spectrum from each catalyst at 25 ºC after heating is presented in highlighted orange.

Moreover, spectrum after cooling at 25 ºC (highlighted orange, **Fig 6.8-B**) displays the presence of bands at 1629, 1375 and 1214 cm^{-1}, characteristics of ethylene [61], which suggests that readsorption of ethylene occurs in this catalyst and, therefore, free Lewis acid sites not involved in the overoxidation of ethylene must be present.

Finally, IR spectra of coadsorbed ethylene and O_2 for the **5V/AL** catalyst are shown in **Fig. 6.8-C**. Ethylene is desorbed at 100 ºC, and no additional bands are observed at 150 ºC (blue spectrum). In return, bands at 1548 and 1388 cm^{-1}, along with bands at 1462 and 1302 cm^{-1} that appear at 200 (magenta spectrum) and 250 ºC (dark green spectrum), respectively, are associated to carbonate species. Additionally, ethylene readsorption does occur in **5V/AL**, although notoriously less marked than in the **(Sn)NiO** sample analysis (small shoulder at 1629 cm^{-1}). Thus, in **5V/AL**, almost all the active sites are involved in the oxidation reaction.

In fact, this information may explain its strong decrease in the selectivity to ethylene in the oxidative dehydrogenation of ethane, since the presence of free Lewis acid sites in **(Sn)NiO** is suggested to favor the dehydrogenative pathway instead to the total oxidation of the olefin/paraffin.

Noteworthy, a good correlation can be established between data obtained from above IR experiments, concerning the reactivity of surface oxygen species (**Figure 6.8**), and reducibility studies by TPR-H_2 shown in **Figure 6.2**, in where reducibility decreases as follows: **(Sn)NiO** (350 ºC) > **5V/AL** (480 ºC) > **MVTN-600** (520 ºC). However, despite presenting a higher reducibility, IR experiments determined that **(Sn)NiO** catalyst presents free

active centers that allow to continue the dehydrogenation route. In this sense, partial oxidation reactions like ethane ODH are known to follow the Mars-van Krevelen mechanism, and this means that lattice oxygen species on the surface of the catalyst that participate in the oxidation process must be replaced with molecular oxygen present in the reaction mixture. Consequently, based on the catalytic and characterization results shown in this chapter, the selectivity to ethylene during ethane ODH is directly related to the extent of the reactivity of the surface oxygen species of each catalyst studied.

6.5. Conclusions

In this chapter, the three catalytic systems that have presented the best performance in the oxidative dehydrogenation of ethane, in terms of activity and selectivity to ethylene, have been studied: vanadium oxide supported on alumina (**5V/AL**), modified nickel oxide (**(Sn)NiO**), and multicomponent Mo-V-Te-Nb oxide presenting the so-called M1 phase (**MVTN-600**).

As it has been demonstrated, the catalytic behavior cannot be explained only by the different crystalline phases, nor the nature of the active sites. In this sense, several factors such as the environment of said active sites, their reducibility, oxygen surface species and adsorption/desorption of products and reactants must be considered [62-70].

Moreover, the selectivity to ethylene is also affected by the different kinetic behavior showed by the catalysts. Thus, depending on the active site,

different deep oxidation products were observed. For the **(Sn)NiO** sample, CO_2 was the only oxidation product detected, however, V-containing catalysts (i.e., **5V/AL** and **MVTN-600**) produce both CO and CO_2 as by-products. This performance can be explained by the CO oxidation ability showed in **Figure 6.5-C**, nevertheless, it has also been exhibited that this catalytic activity is not especially influent in developing optimized catalysts for ethane ODH, as doped and undoped NiO materials present same properties in CO oxidation [11-17], but large differences in the selectivity to ethylene in the ODHE. On the contrary, for V-containing catalysts, the nature of the vanadium species, as well as the support, preparation method and vanadium loading leads to different proportion of CO/CO_2 formation [5-8, 27, 32-37]. Therefore, no clear relationship can be stablished with ethylene selectivity.

Nonetheless, these three catalytic systems do present big differences in the rate of ethane/ethylene transformation, as seen in **Figure 6.7** and **Table 6.3**. In this way, ethylene reacts ca. 2.5 times faster than ethane in the **5V/AL** catalyst, while the opposite trend is observed in the case of **(Sn)NiO** and, mainly, **MVTN-600** samples, in where ethane reacts almost 15 times faster than ethylene. These dissimilar reaction rates can explain the different selectivity to ethylene observed among the catalysts, principally at high ethane conversion. However, characteristic physicochemical properties of each system should strongly influence the selectivity to ethylene.

Thus, supported vanadium oxide (**5V/AL**) or promoted NiO (**(Sn)NiO**) catalysts suffer notable modifications due to their inherent nature. In the **5V/AL** catalyst, the use of an appropriate support and V-loading changes

the proportion of VO_4/V_2O_5 molecules, being the former less reactive [1-8]. Nevertheless, the majority presence of V^{5+} species in this catalyst (**Fig. 6.1-I**) leads to the overoxidation of both ethane and ethylene. In addition, for **(Sn)NiO**, the use of a dopant/promoter, or even modifications in the synthesis parameters [20], modifies the amount of nucleophilic oxygen species that drastically affect the catalytic performance of this type of materials.

Regarding the **MVTN-600** sample, compared to the other two catalysts studied in this chapter, it can be considered as a host structure/support in where the vanadium species (V^{4+}/V^{5+}) are properly dispersed on the surface of a layer consisting of Mo^{6+}/Mo^{5+} species close to {-O-Te^{4+}-O-} and pentagonal Nb^{5+}-containing units [71]. This sample, as deeply studied during **Chapter 5**, presents a unique property that neither **5V/AL** and **(Sn)NiO** have, this M1 structure possess empty heptagonal (seven-membered rings) channels with a micropore diameter of ca. 0.4nm (very similar to ethane size [33]), in whose entrance the reaction is believed to take place, that turns into a higher ethylene and CO adsorption by the **MVTN-600** sample (**Figs. 6.3-A** and **D**).

Furthermore, microcalorimetry experiments (**Table 6.2**) highlighted the importance of suitable active sites on the surface of the catalyst. Then, heat of adsorption calculations for the **MVTN-600** sample reported a value of 32 kJ mol^{-1}, which is not too low to guarantee a good ethane-surface interaction but not too high to suppose a drastic drop in catalytic activity. On the other hand, the marked low heat of adsorption offered by both **(Sn)NiO** and **5V/AL** (10 and 13 kJ mol^{-1}, respectively) catalysts, close to

the ethane heat of condensation [29], lead to an extremely poor ethane-surface interaction. What is more, if we calculate activity per active site, the **MVTN-600** catalyst is the most active one, despite presenting low specific surface area (**Table 6.3**).

Consequently, the addition of a promotor and/or a support implies a modification in the reducibility of the active sites, as seen in H_2-TPR experiments shown in **Fig. 6.2**, but also to a different reactivity of surface oxygen species.

In this regard, the selectivity to ethylene by the different catalytic systems can be explained in terms of the ethylene and O_2 coadsorption IR experiments results displayed in **Fig. 6.8**. For the **MVTN-600** catalyst, ethylene desorbs at relatively a low temperature (100 ºC) and the absence of additional IR bands shows that there is no interaction between ethylene and molecular oxygen. Conversely, both **(Sn)NiO** and **5V/AL** catalysts present additional IR bands that are associated to O-containing molecules, even at low-moderate temperatures (below 200-250 ºC), that are further transformed into CO_x at higher temperatures.

Therefore, in this chapter, it has been demonstrated that the higher selectivity to ethylene exhibited by multicomponent M1-presenting Mo-V-Te-Nb oxide catalysts above other catalytic systems traditionally used in the oxidative dehydrogenation of ethane (doped NiO and supported vanadium oxide) is based on a combination of facts, such as the majority existence of non-overoxidizing V^{4+} species along with the presence of suitable heptagonal channels with a kinetic diameter very similar to ethane and ethylene molecules (4.0 Å) that, in whose entrance, favor the H-

abstraction of the ethane molecule [27, 29, 32-37, 53, 71-73], avoiding at the same time a further O-insertion that ends up in the formation of carbon oxides.

6.6. References

1) A. Galli, J.M. López Nieto, A. Dejoz, M.I. Vazquez, The effect of potassium on the selective oxidation of n-butane and ethane over Al_2O_3-supported vanadia catalysts, Catal. Lett. 34 (1995) 51 – 58.

2) J. Le Bars, A. Auroux, M. Forissier, J.C. Vedrine, Active sites of V_2O_5/γ-Al_2O_3 catalysts in the oxidative dehydrogenation of ethane, J. Catal. 162 (1996) 250 – 259.

3) T. Blasco, J.M. López Nieto, Oxidative dehydrogenation of short chain alkanes on supported vanadium oxide catalysts, Appl. Catal. A Gen 157 (1997) 117 – 142.

4) M.A. Bañares, X. Gao, J.L.G. Fierro, I.E. Wachs, Partial oxidation of ethane over monolayers of vanadium oxide. Effect of the support and surface coverage, Stud. Surf. Sci. Catal. 110 (1997) 295 – 304.

5) T. Blasco, A. Galli, J.M. López Nieto, F. Trifiró, Oxidative Dehydrogenation of Ethane and n-Butane on VOx/Al_2O_3 Catalysts, J. Catal. 169 (1) (1997) 203–211.

6) K. Chen, A.T. Bell, E. Iglesia, The Relationship between the Electronic and Redox Properties of Dispersed Metal Oxides and Their Turnover Rates in Oxidative Dehydrogenation Reactions, J. Catal. 209 (2002) 35–42.

7) M. D. Argyle, K. Chen, A. T. Bell, E. Iglesia, Effect of Catalyst Structure on Oxidative Dehydrogenation of Ethane and Propane on Alumina-Supported Vanadia, J. Catal. 208 (2002) 139–149.

8) A. Dinse, R. Schomäcker, A. T. Bell, The role of lattice oxygen in the oxidative dehydrogenation of ethane on alumina-supported vanadium oxide, Phys. Chem. Chem. Phys. 11 (2009) 6119-6124.

9) B. Frank, R. Fortrie, Ch. Hess, R. Schlögl, R. Schomäcker, Reoxidation dynamics of highly dispersed VOx species supported on c-alumina, Appl. Catal. A Gen 353 (2009) 288–295.

10) H. Kim, G. A. Ferguson, L.Cheng, S.A. Zygmunt, P. C. Stair, L. A. Curtiss, Structure-Specific Reactivity of Alumina-Supported Monomeric Vanadium Oxide Species, J. Phys. Chem. C 116 (4) (2012) 2927–2932.

11) **a)** E. Heracleous, A.A. Lemonidou, Ni–Nb–O mixed oxides as highly active and selective catalysts for ethene production via ethane oxidative dehydrogenation. Part I: Characterization and catalytic performance, J. Catal.237 (2006) 162–174; **b)** E. Heracleous, A.A. Lemonidou, Ni–Nb–O mixed oxides as highly active and selective catalysts for ethene production via ethane oxidative dehydrogenation. Part II: Mechanistics aspects and kineting modeling, J. Catal. 237 (2006) 175–189.

12) E. Heracleous, A.F. Lee, K. Wilson, A.A. Lemonidou, Investigation of Ni-based alumina-supported catalysts for the oxidative dehydrogenation of ethane to ethylene: structural characterization and reactivity studies, J. Catal. 231 (2005) 159–171.

13) E. Heracleous, A.A. Lemonidou, Ni–Me–O mixed metal oxides for the effective oxidative dehydrogenation of ethane to ethylene- Effect of promoting metal Me, J. Catal. 270 (2010) 67–75.

14) **(a)** Liu, US Patent 6, 891,075, 2005; **(b)** Y. Liu, U.S. Patent 7,227,049 A2, 2007 (Assigned to Symyx Solutions Inc).

15) **a)** B. Solsona, P. Concepción, B. Demicol, S. Hernández, J.J. Delgado, J.J. Calvino, J.M. López Nieto, Selective oxidative dehydrogenation of ethane over SnO_2-promoted NiO catalysts, J. Catal. 295 (2012) 104–114; **b)** B. Solsona, Patricia Concepción, Selene Hernández, Benjamin Demicol, José M. López Nieto, Oxidative dehydrogenation of ethane over NiO–CeO_2 mixed oxides catalysts, Catal. Today 180 (2012) 51– 58.

16) H. Zhu, D.C. Rosenfeld, M. Harb, D.H. Anjum, M.N. Hedhili, S. Ould-Chikh, J.M. Basset, Ni-M-O (M = Sn, Ti, W) Catalysts Prepared by a Dry Mixing Method for Oxidative Dehydrogenation of Ethane, ACS Catal. 6 (2016) 2852–2866.

17) J.M. López Nieto, B. Solsona, R.K. Grasselli, P. Concepcion, Promoted NiO Catalysts for the Oxidative Dehydrogenation of Ethane, Top. Catal. 57 (2014) 1248–1255.

18) J.L. Park, S.K. Balijepalli, M.D. Argyle, K.J. Stowers, Low temperature Oxidative dehydrogenation of ethane by Ce-modified NiNbO, Ind. Eng. Chem. Res. 57 (2018) 5234–5240.

19) D. Delgado, B. Solsona, A. Ykrelef, A. Rodríguez-Gómez, A. Caballero, E. Rodríguez-Aguado, E. Rodríguez-Castellón, J. M. López Nieto, Redox and Catalytic Properties of Promoted NiO Catalysts for the Oxidative Dehydrogenation of Ethane, J. Phys. Chem. C 121 (2017) 25132-25142.

20) Y. Abdelbaki, A. De Arriba, R. Issaadi, R. Sánchez-Tovar, B. Solsona, J. M. López Nieto, Optimization of the performance of bulk NiO catalyst in the oxidative dehydrogenation of ethane by tuning the synthesis parameters, Fuel Process. Technol. 229 (2022) 107182.

21) Y. Abdelbaki, A. De Arriba, B. Solsona, D. Delgado, E. García-González, R. Issaadi, J. M. López Nieto, The nickel-support interaction as determining factor of the selectivity to ethylene in the oxidative dehydrogenation of ethane over nickel oxide/alumina catalysts, Appl. Catal. A Gen 623 (2021) 118242.

22) D. Delgado, R. Sanchís, J.A. Cecilia, E. Rodríguez-Castellón, A. Caballero, B. Solsona, J.M. López Nieto, Support effects on NiO-based catalysts for the oxidative dehydrogenation (ODH) of ethane, Catal. Today 333 (2019) 10–16.

23) D. Delgado, B. Solsona, R. Sanchis, E. Rodríguez-Castellón, J.M. López Nieto, Oxidative dehydrogenation of ethane on diluted or promoted nickel

oxide catalysts: Influence of the promoter/diluter, Catal. Today 363 (2021) 27–35

24) A. Ykrelef, L. Nadji, R. Issaadi, S. Agouram, E. Rodríguez-Castellón, B. Solsona, J.M. López Nieto, Mixed oxide Ti-Si-O prepared by non-hydrolytic Xerogel method as a diluter of nickel oxide for the oxidative dehydrogenation of ethane, Catal. Today 299 (2018) 93–101

25) E. Rodríguez-Castellón, D. Delgado, A. Dejoz, I. Vázquez, S. Agouram,] J. A. Cecilia, B. Solsona, J.M. López Nieto, Enhanced NiO Dspersion on a High Surface Area Pillared Heterostructure Covered by Niobium Leads to Optimal Behaviour in the Oxidative Dehydrogenation of Ethane, Chem. Eur. J. 26 (2020) 9371 – 9381

26) J.J. Varghese, S.H. Mushrif, Insights into the C-H Bond Activation on NiO Surfaces: The Role of Nickel and Oxygen Vacancies and of Low Valent Dopants on the Reactivity and Energetics, J. Phys. Chem. C 121 (2017) 17969–17981.

27) P. Botella, E. García-González, A. Dejoz, J.M. López Nieto, M.I. Vázquez, J. González-Calbet, Selective oxidative dehydrogenation of ethane on MoVTeNbO mixed metal oxide catalysts, J. Catal. 225 (2004) 428–438

28) J.M. López Nieto, P. Botella, M.I. Vázquez, A. Dejoz, U.S. Patent 7,319,179 B2, 2008 (Assigned to CSIC and UPV).

29) P. Kube, B. Frank, S. Wrabetz, J. Kröhnert, M. Hävecker, J. Velasco-Vélez, J.Noack, R. Schlögl, A. Trunschke, Functional Analysis of Catalysts for Lower Alkane Oxidation, ChemCatChem 9 (2017) 573–585.

30) G.C. Bond, K. Bruckman, Selective oxidation of o-xylene by monolayer V_2O_5-TiO_2 catalysts, Faraday Discuss. Chem. Soc. 72 (1981) 235–246.

31) X. Wang, B. Zhao, D. Jiang, Y. Xie, Monolayer dispersion of MoO3, NiO and their precursors on γ-Al_2O_3, Appl. Catal. A Gen. 188 (1999) 201–209.

32) P. Botella, A. Dejoz, M.C. Abelló, M.I. Vázquez, L. Arrúa, J.M. López Nieto, Selective oxidation of ethane. Developing an orthorhombic phase in Mo-V-X (X=Nb, Sb, Te) mixed oxides, Catal. Today 142 (2009) 272–277.

33) **a)** T. Konya, T. Katou, T. Murayama, S. Ishikawa, M. Sadakane, D. Buttrey, W.Ueda, An orthorhombic Mo_3VOx catalyst most active for oxidative dehydrogenation of ethane among related complex metal oxides, Catal. Sci. Technol. 3 (2013) 380–387; **b)** S. Ishikawa, D. Kobayashi, T. Konya, S. Ohmura, T. Murayama, N. Yasuda, M. Sadakane, W. Ueda, Redox Treatment of Orthorhombic $Mo_{29}V_{11}O_{112}$ and Relationships between Crystal Structure, Microporosity and Catalytic Performance for Selective Oxidation of Ethane, J. Phys. Chem. C 119 (2015) 7195–7206.

34) P.J. Donaubauer, D.M. Melzer, K. Wanninger, G. Mestl, M. Sanchez-Sanchez, J.A. Lercher, O. Hinrichsen, Intrinsic kinetic model for oxidative dehydrogenation of ethane over MoVTeNb mixed metal oxides: A mechanistic approach, Chem. Eng. J. 383 (2020) 123195.

35) L. Annamalai, Y. Liu, S. Ezenwa, Y. Dang, S.L. Suib, P. Deshlahra, Influence of Tight Confinement on Selective Oxidative Dehydrogenation of Ethane on MoVTeNb Mixed Oxides, ACS Catal. 8 (2018) 7051–7067.

36) **a)** D. Melzer, G. Mestl, K. Wanninger, Y. Zhu, N.D. Browning, M. Sanchez-Sanchez, J.A. Lercher, Design and synthesis of highly active MoVTeNb oxides for ethane oxidative dehydrogenation, Nat. Commun. 10 (2019) 4012; **b)** D. Melzer, P. Xu, D. Hartmann, Y. Zhu, N.D. Browning, M. Sanchez-Sanchez, J.A. Lercher, Atomic-Scale Determination of Active Facets on the MoVTeNb Oxide M1 Phase and Their Intrinsic Catalytic Activity for Ethane Oxidative Dehydrogenation, Angew. Chem. Int. Ed. 55 (2016) 8873–8877.

37) M. Baca, A. Pigamo, J.L. Dubois, J.M.M. Millet, Catal. Commun. 6 (2005) 215–220.

38) P. Concepción, S. Hernández, J.M. López Nieto, On the nature of active sites in MoVTeO and MoVTeNbO catalysts: The influence of catalyst activation temperature, Appl. Catal. A Gen. 391 (2011) 92–101.

39) L. Koudelka, J. Pospísil, P. Mosner, L. Montagne, L. Delevoye, Structure and properties of potassium niobato-borophosphate glasses, J. Non-Cryst. Solids 354 (2008) 129–133.

40) E. Aytan, B. Debnath, F. Kargar, Y. Barlas, M.M. Lacerda, J.X. Li, R.K. Lake, J. Shi, A.A. Balandin, Spin-phonon coupling in antiferromagnetic nickel oxide, Appl. Phys. Lett. 111 (2017) 252402.

41) G. Busca, V. Lorenzelli, V. Sánchez-Escribano, Preparation, solid-state characterization, and surface chemistry of high-surface-area nickel aluminum ($N_ixAl_{2-2x}O_{3-2x}$) mixed oxides, Chem. Mater. 4 (1992) 595–605.

42) V. Biju, Ni 2p X-ray photoelectron spectroscopy study of nanostructured nickel oxide, Mater. Res. Bull. 42 (2007) 791–796.

43) A. B. Sifontes, B. Gutiérrez, A. Mónaco, A. Yanez, Y. Díaz, F. J. Méndez, L. Llovera, E. Cañizales, J. L. Brito, Preparation of functionalized porous nano-γ-Al_2O_3 powders employing colophony extract, Biotechnol. Rep. 4 (2014) 21-29.

44) **a)** M.A. Vuurmant, I.E. Wachs, In Situ Raman Spectroscopy of Alumina-Supported Metal Oxide Catalysts, J. Phys. Chem. 96 (1992) 5008–5016; **b)** Z. Wu, H.-S. Kim, P.C. Stair, S. Rugmini, S.D. Jackson, On the Structure of Vanadium Oxide Supported on Aluminas: UV and Visible Raman Spectroscopy, UV-Visible Diffuse Reflectance Spectroscopy, and Temperature-Programmed Reduction Studies, J. Phys. Chem. B 109 (2005) 2793–2800.

45) L.E. Briand, O.P. Tkachenko, M. Guraya, X. Gao, I.E. Wachs, W. Grünert, Surface- Analytical Studies of Supported Vanadium Oxide Monolayer Catalysts, J. Phys. Chem. B 108 (2004) 4823–4830.

46) A. Massó Ramirez, F. Ivars-Barceló, J.M. López Nieto, Optimizing Reflux Synthesis Method of Mo-V-Te-Nb mixed oxide Catalysts for Light Alkane Selective Oxidation, Catal. Today 356 (2020) 322–329.

47) D. Delgado, B. Solsona, A. Ykrelef, A. Rodríguez-Gómez, A. Caballero, E. Rodríguez-Aguado, E. Rodríguez-Castellón, J.M. López Nieto, Redox and Catalytic Properties of Promoted NiO Catalysts for the Oxidative Dehydrogenation of Ethane, J. Phys. Chem. C 121 (2017) 25132–25142.

48) J.M. López Nieto, J. Soler, P. Concepcion, J. Herguido, M. Menendez, J. Santamaria, Oxidative Dehydrogenation of Alkanes over V-based Catalysts: Influence of Redox Properties on Catalytic Performance, J. Catal. 185 (1999) 324–332.

49) J.M. Gallardo Amores, V. Sanchez Escribano, G. Ramis, G. Busca, An FT-IR study of ammonia adsorption and oxidation over anatase-supported metal oxides, Appl. Catal. B Environ. 13 (1997) 45–58.

50) N. Sergent, P. Gelin, L. Perier-Camby, H. Praliaud, G. Thomas, FTIR study of low-temperature CO adsorption on high surface area tin(IV) oxide: Probing Lewis and Brønsted acidity, Phys. Chem. Chem. Phys. 4 (2002) 4802–4808.

51) a) P. Concepción, K. Hajiivanov, H. Knözinger, Low-Temperature CO Adsorption on V-Containing Aluminophosphates: An FTIR Study, J. Catal. 184 (1999) 172–179; b) K.I. Hadjiivanov, G.N. Vayssilov, Characterization of oxides surfaces and zeolites by carbon monoxide as IR probe molecule, Adv. Catal. 47 (2002) 307–511.

52) P. Concepción, P. Botella, J.M. López Nieto, Catalytic and FT-IR study on the reaction pathway for oxidation of propane and propylene on V- or Mo–V-based catalysts, Appl. Catal. A Gen. 278 (2004) 45–56.

53) J.M. López Nieto, P. Botella, M.I. Vázquez, A. Dejoz, U.S. Patent 7,319,179 B2, 2008 (Assigned to CSIC and UPV).

54) S. Lwin, W. Diao, Ch. Baroi, A.M. Gaffney, R.R. Fushimi, Characterization of MoVTeNbOx Catalysts during Oxidation Reactions Using In Situ/Operando Techniques: A Review, Catalysts 7 (2017) 109.

55) A.M. Gaffney, Q. An, W.A. Goddard III, W. Diao, M.V. Glazoff, Toward Concurrent Engineering of the M1-Based Catalytic Systems for Oxidative Dehydrogenation (ODH) of Alkanes, Top. Catal. 63 (2020) 1667–1681.

56) J.M. López Nieto, P. Botella, P. Concepción, A. Dejoz, M.I. Vázquez, Oxidative dehydrogenation of ethane on Te-containing MoVNbO catalysts, Catal. Today 91–92 (2004) 241–245.

57) F. Trifiró, I. Pasquon, Classification of oxidation catalysts according to the type of metal-oxygen bond, J. Catal. 12 (1968) 412–416.

58) C. Doornkamp, M. Clement, X. Gao, G. Deo, I.E. Wachs, V. Ponec, The Oxygen Isotopic Exchange Reaction on Vanadium Oxide Catalysts, J. Catal. 185 (1999) 415–422.

59) D. Delgado, R. Sanchis, B. Solsona, P. Concepción, J.M. López Nieto, Influence of the Nature of the Promoter in NiO Catalysts on the Selectivity to Olefin During the Oxidative Dehydrogenation of Propane and Ethane, Top. Catal. 63 (2020) 1731–2174.

60) J. M. López Nieto, The Selective Oxidative Activation of light Alkanes. From Supported Vanadia to Multicomponent Bulk V-Containing Catalysts, Top. Catal. 41 (2006) 3–15.

61) K.R. William, G.E. Ewing, Infrared spectra and structure of ethane on NaCl (100), J. Phys. Chem. 99 (1995) 2186–2193.

62) J. Haber, Oxidation of hydrocarbons, in: G. Ertl, H. Knoezinger, J. Weitkamp (Eds.), Handbook of Heterogeneous Catalysis, vol. 4.6.2., Wiley-VCH, 1997, pp. 2253–2274.

63) R.K. Grasselli, Ammoxidation, in: G. Ertl, H. Knoezinger, J. Weitkamp (Eds.), Handbook of Heterogeneous Catalysis, vol. 4.6.6, Wiley-VCH, 1997, pp. 302 (and references therein).

64) J. Haber, The concept of structure-sensitivity in catalysis by oxides, Stud. Surf. Sci. Catal. 48 (1989) 447–466.

65) J. Haber, Catalytic oxidation- State of the art and prospects, Stud. Surf. Sci. Catal. 72 (1992) 279–304.

66) J. Haber, Selectivity in Heterogeneous Catalytic Oxidation of Hydrocarbons, in Heterogeneous Hydrocarbon Oxidation, ACS Symp. Series 638 (1996) 20–34.

67) R.K. Grasselli, Site isolation and phase cooperation: Two important concepts in selective oxidation catalysis: A retrospective, Catal. Today 238 (2014) 10–27.

68) R.K. Grasselli, J.D. Burrington, D.J. Buttrey, P. DeSanto Jr., Cl.G. Lugmair, A.F. Volpe Jr., T. Weingand, Multifunctionality of active centers in (amm)oxidation catalysts: from Bi–Mo–Ox to Mo–V–Nb–(Te;Sb)–Ox, Top. Catal. 23 (2003) 5–22.

69) R.K. Grasselli, Fundamental principles of selective heterogeneous oxidation catalysis, Top. Catal. 21 (2002) 79–88.

70) R. K. Grasselli, Advances and future trends in selective oxidation and ammoxidation catalysis, Catal. Today 49 (1999) 141–153.

71) M. Hävecker, S. Wrabetz, J. Kröhnert, L.-I. Csepei, R.N. d'Alnoncourt, Y.V. Kolen'ko, F. Girgsdies, R. Schlögl, A. Trunschke, Surface chemistry of phase pure M1 MoVTeNb oxide during operation in selective oxidation of propane to acrylic acid, J. Catal. 285 (2012) 48–60.

72) **a)** S. Ishikawa, X. Yi, T. Murayama, W. Ueda, Heptagonal channel micropore of orthorhombic Mo_3VO_x as catalysis field for the selective oxidation of ethane, Appl. Catal. A Gen 474 (2014) 10–17; **b)** S. Ishikawa, W. Ueda,

Microporous crystalline Mo–V mixed oxides for selective oxidations, Catal. Sci. Technol. 6 (2016) 617–629.

73) **a)** M. Sadakane, K. Kodato, T. Kuranishi, Y. Nodasaka, K. Sugawara, N. Sakaguchi, T. Nagai, Y. Matsui, W. Ueda, Molybdenum-vanadium-based molecular sieves with microchannels of seven-membered rings of corner-sharing metal oxide octahedra, Angew. Chem. Int. Ed. 47 (2008) 2493–2496; **b**) M. Sadakane, K. Kodato, N. Yasuda, S. Ishikawa, W. Ueda, Thermal Behavior, Crystal Structure, and Solid-State Transformation of Orthorhombic Mo-V Oxide under Nitrogen Flow or in Air, ACS Omega 4 (2019) 13165–13171.

Chapter 7

Overall conclusions

In order to fulfill the Paris Agreement on climate change and the UN's Agenda 2030, a transition in the way the humanity obtains energy and chemical goods must be implemented, from non-renewable sources to sustainable less-polluting green solutions. In this sense, it is clear that catalysis will be a pivotal agent in the forthcoming transformation, needing a new approach and design of solid-based materials that can contribute to meet the consumption demands while lowering these uncontrolled emissions of carbon oxides to the atmosphere.

The present doctoral thesis provides some insights into how the design of mixed metal oxide solid catalysts (specifically Mo-V-based oxides that present the orthorhombic crystalline structure known as M1), as well as the study and understanding of them and their properties can potentially lead to the implementation of new industrial processes, as the oxidative dehydrogenation (ODH) of ethane, based on largely available natural gas feedstocks for the production of ethylene, the most demanded light olefin worldwide, that may substitute current extremely energy demandant industrial steam cracking, either from oil or natural gas, a non-catalyzed highly polluting process. Therefore, by tunning the synthesis parameters, the chemical composition and the activation temperature, the catalytic performance of the M1 phase catalysts can be optimized.

For the bimetallic Mo-V-O catalysts, it was demonstrated that only specific synthetic conditions lead to the formation of the M1 phase, crucial to obtain appropriate selectivity values to ethylene. Then, a hydrothermal method should be applied to an aqueous solution of the metallic precursors, in a fixed synthesis time and atmosphere ambient (72 hours and inert

atmosphere, N_2). Nevertheless, although these conditions lead to the formation of the M1 phase, the catalytic performance can be further optimized by several post synthesis treatments. An important factor to be taken into account in the activation temperature, thus, decomposition of the M1 phase into non-active Mo_5O_{14}-like structures occurs at temperatures above 400 ºC, with the subsequent lose in the selectivity to ethylene. Moreover, purification steps, and the order in which they are performed also were studied. In this sense, the optimal Mo-V-O (M1) catalyst must be activated at 400 ºC with a later H_2O_2 purification, to dissolve inactive crystalline phases. Finally, a set of distinctly synthesized bimetallic Mo-V-O (M1) catalysts were tested in the ethane ODH observing large differences among them. Interestingly, these despair selectivies reported were associated with differences in the surface composition in the active centers of the catalysts (i.e., vanadium species). Accordingly, it was found that the higher the relative amount of V^{4+} species on the surface of the material, the higher the selectivity to ethylene.

Once the optimal bimetallic M1 catalyst conditions were set, the study was forwarded to the incorporation of tellurium cations into the structure, to form a trimetallic Mo-V-Te-O system with increasing Te-loadings ($0.00 <$ Te/Mo ratio < 0.17), and two different activation temperatures, either 400 or 600 ºC. We observed that the inclusion of said tellurium atoms affected dramatically the thermal stability of the materials, even from the lowest concentration (Te/Mo= 0.01), obtaining trimetallic Mo-V-Te-O catalysts that maintain the M1 structure at temperatures up to 600 ºC. In addition to this, the different tellurium loading also had a deep influence on the

morphology and the textural properties of the solids. In this way, by FESEM micrographs studies it was observed that in the absence of tellurium, M1 crystals are composed by a rather elongated needle-like forms, however, when Te is incorporated into the structure, those needles tend to assemble in the form of a coalescence of needles, much thicker, looking like rods. Consequently, said changes in the morphology of the crystals depending on the chemical composition also led to important changes in the textural properties of the catalysts, however, they were notable only for samples activated at 400 ºC. Especially interesting were the values of micropore volume observed samples with Te/Mo ratios of 0.05 and 0.10 where, despite showing practically identical surface area values, micropore volume of the former was ca. 3 times of the latter, thus translating this into huge differences in the catalytic activity. Explanation for this lies on the fact that it is suggested that the ethane ODH reaction takes places inside and/or at the entrance of the heptagonal channels of the M1 structure, therefore a less amount of Te^{4+} cations that are allocated in the hexagonal, but also maybe in the heptagonal channels, would lead to an enhanced catalytic activity.

Accordingly, the catalytic study of these two sets of materials (i.e., Mo-V-(Te)-O solids activated at 400 or 600 ºC) led to two inverse trends. On one hand, for the catalysts activated at 400 ºC, results showed that the higher the tellurium loading, the lower the selectivity to ethylene, being bimetallic Mo-V-O catalyst the one that presented the highest ethylene selectivity values. On the other hand, in the 600 ºC activated catalysts, the best performing material was the one with the highest tellurium content

(Te/Mo= 0.17). Interestingly, although these two sets of catalysts seem to display inverse trends depending on the thermal activation, by investigating the selectivity to ethylene as a function of the V^{4+} species, a direct correlation is also observed, regardless of the composition and the thermal activation.

Finally, a comprehensive comparative study was conducted including best bi- and trimetallic catalysts (Mo-V-O and Mo-V-Te0.17-O catalysts) and tetrametallic Mo-V-Te-Nb-O catalysts. In this sense, it was investigated the effect of the chemical composition and the activation temperature (400, 500 or 600 ºC) on the selectivity to ethylene. Surprisingly, by performing XPS analyses, the same trends in the selectivity to ethylene as a function of the V^{4+} species relative amount on the surface of the catalyst were observed, suggesting that optimal catalysts in the ethane ODH should present a partially reduced surface, this way perfectly isolating the active centers (V^{5+} species) preventing the overoxidation of the ethylene formed. Moreover, a brand-new electrochemical study was performed over these catalysts, provided that all these mixed metal oxides can be also considered as semiconductors. Then, several techniques as Nyquist, Bode-Module or Mott-Schottky plots were applied, and electrical resistance values were calculated. A direct correlation was observed between the selectivity to ethylene of the different catalyst and the calculated resistance values that, given the fact that they are related to electrochemical processes occurring on the surface of the catalysts, it explains the catalytic behavior as ethane ODH is known to be driven by a redox Mars-van Krevelen mechanism. Then, by comparing the electrochemical and the XPS calculations (in terms

of relative abundance of V^{4+} species) in the influence on the selectivity to ethylene, exactly the same results can be ascertained.

Apart from the M1 phase, other catalytic systems reported in the literature with interesting results in the ethane ODH are alumina supported vanadium oxide and tin doped NiO. Nevertheless, although these three catalytic systems are able to produce ethylene, enormous differences are observed by increasing the ethane conversion. In this manner, in the last part of the present thesis we carried out a comparative characterization study to explain those marked differences. Microcalorimetry and in situ IR studies of coadsorbed ethylene and O_2 (trying to imitate ODH reaction conditions), as well as reaction rate calculations of ethane/ethene oxidation explained that the extraordinary selectivity to ethylene over Mo-V-Te-Nb oxide catalyst is due to the lack of ability to activate the ethylene molecule, which readily desorbs from the its surface, therefore avoiding reacting and the subsequent formation of CO_x observed in both VO_x/Al_2O_3 and Sn-doped NiO catalysts.

Appendix I

Index of Figures

Chapter 1. Introduction

activation; and a multicomponent mixed metal molybdate, e.g., $Cs_aK_bNi_cMg_dM_eBi_fSb_gMo_hO_x$ for olefin ammoxidation catalyst [148].

Figure 1.12. Representation of orthorhombic M1 (**A**) and hexagonal M2 (**B**) crystalline structures, derived from Mo_5O_{14} (**C**).

Figure 1.13. Influence of the activation procedure on the stability of M1 phase for Mo-V-O catalysts. Adapted from ref. [220].

Fig. 1.14. Catalytically active center of Mo-V-Te-Nb-O (M1) in [001] projection. Adapted from ref. [152, 177, 178, 200, 215, 216].

Figure 1.15. General scheme for ethane ODH by considering a Mars-van Krevelen mechanism.

Figure 1.16. Selectivity to ethylene as a function of ethane conversion for alumina supported vanadium oxide (VO_x/Al_2O_3, in black), tin doped NiO (Sn-NiO, in blue), and multicomponent MoVTeNb-M1 oxide, in red.

Figure 1.17. XRD patters of Mo-V-Te-Nb-O catalysts, heat-treated in the 500-750 ºC temperature interval. On the right, comparative catalytic results are shown for catalysts activated in the same temperature interval. Adapted from ref. [167b].

Figure 1.18. Mars-van Krevelen mechanisms for ethane ODH considering: **A)** single oxygen site model with two close lattice oxygens involved in hydrogen abstraction, **B)** single oxygen site model without hydrogen abstraction by close oxygen, **C)** single oxygen site model accounting inner and outer sphere reoxidation routes and **D)** dual oxygen site model considering irreversible dissociative adsorption steps and adsorbed oxygen species in quasi-equilibrium with gas phase O_2. Reproduced from [246].

Chapter 2. Experimental section

Chapter 3. Bimetallic MoVOx mixed metal oxides: optimization of the synthesis parameters and catalytic performance

Figure 3.2. XRD patterns of bimetallic MoV oxide catalysts synthesized at pH values of: 2.0 (**A-2.0**, black), 2.5 (**A-2.5**, red), 3.0 (**A-3.0**, blue) and 3.5 (**A-3.5**, green).

Figure 3.3. XRD patterns of solid synthesized: **A)** under N_2 atmosphere with 2 (**B-N2-t2**, black), 3 (**B-N2-t3**, red), 4 (**B-N2-t4**, blue) and 7 (**B-N2-t7**, green) days of synthesis time; and **B)** under air atmosphere with 2 (**B-Air-t2**, black), 3 (**B-Air-t3**, red) and 6 (**B-Air-t6**, blue) days of synthesis time.

Figure 3.4. XRD patterns of oxides purified with 15%wt H_2O_2 (**B-H_2O_2**, green), or with oxalic acid solution of 0.2M (**B-Oxa/0.2**, black), 0.4M (**B-Oxa/0.4**, red) and 0.6M (**B-Oxa/0.6**, blue).

Figure 3.5. XRD pattern of 400 ºC heat-treated solids with 15%wt H_2O_2 (**B-H_2O_2-400**, green), or with oxalic acid solutions of: 0.2M (**B-Oxa/0.2-400**, black), 0.4M (**B-Oxa/0.4-400**, red) and 0.6M (**B-Oxa/0.6-400**, blue). Note that an unpurified sample, **B-UNP-400** (purple), is also displayed in the figure.

Figure 3.6. XRD pattern of: **A)** an unpurified MoV oxide solid (**B-UNP-400**, purple) washed after the heat treatment (**MV-400**, green); and **B)** MoV oxide purified with a 0.2M oxalic acid solution (**B-Oxa/0.2-400**, black) or washed with 0.4M oxalic acid solution after the heat-treatment (**MV-Oxa-400-Oxa**, orange).

Figure 3.7. XRD of MoV-M1 oxides: (**A**) Samples washed with 0.2M oxalic acid solutions before heat-treatment at 400 (**B-Oxa/0.2-400**, black), 500 (**B-Oxa/0.2-500**, light blue) and 600 ºC (**B-Oxa/0.2-600**, red); or (**B**) Samples washed with 15% wt. hydrogen peroxide solution, after heat-treatment at 400 (**MV-400**, green), 500 (**MV-500**, dark blue) or 600ºC (**MV-600**, garnet) under N_2 stream.

Figure 3.8. Raman spectra of MoV-M1 oxides: (**A**) Samples washed with 0.2M oxalic acid solutions before a heat-treatment at 400 (**B-Oxa/0.2-400**, black), 500 (**B-Oxa/0.2-500**, light blue) and 600 ºC (**B-Oxa/0.2-600**, red); or (**B**) Samples

washed with 15% wt. hydrogen peroxide solution after a heat-treatment at 400 (**MV-400**, green), 500 (**MV-500**, dark blue) or 600 ºC (**MV-600**, garnet) under N_2 stream.

Figure 3.9. Variation of the ethylene selectivity as a function of the ethane conversion for selected M1-MoVO catalysts.

Figure 3.10. Variation of the selectivity to ethylene as a function of ethane conversion of MoV-M1 oxides: (**A**) Samples washed with 0.2M oxalic acid solutions and then activated at 400 (**B-Oxa/0.2-400**, black), 500 (**B-Oxa/0.2-500**, light blue) and 600 ºC (**B-Oxa/0.2-600**, red). (**B**) Samples washed with 15% wt. hydrogen peroxide solution and then activated at 400 (**MV-400**, green), 500 (**MV-500**, dark blue) or 600 ºC (**MV-600**, garnet) under N_2 stream.

Figure 3.11. XPS spectra of V $2p_{3/2}$ core level of: A) **MV-400**, **MV-500** and **MV-600**; B) **B-Oxa/0.2-400**, **B-Oxa/0.2-500** and **B-UNP-400**; and C) **B-Oxa/0.4-400, B-Oxa/0.6-400** and **MV-Oxa-400-Oxa**, catalysts.

Figure 3.12. Selectivity to ethylene as a function of the V^{4+}/V_{total} ration on the surface of selected catalysts subjected to different post-synthesis treatments. Characteristics of catalysts in **Table 3.2**.

Chapter 4. Te-doped M1-MoVOx catalysts: the role of tellurium on textural properties, thermal stability and catalytic behavior

Figure 4.1. Physicochemical characterization of $MoVTe_x$ catalysts: XRD patterns (**A**, **B**), FTIR spectra (**C**, **D**) and Raman spectra (**E**, **F**) of samples heat-treated at 400 ºC (**A, C, E**) and 600 ºC (**B, D, F**): a) **MVT-1-400**; b) **MVT-5-400**; c) **MVT-10-400**; d) **MVT-17-400**; e) **MVT-1-600** ; f) **MVT-5-600**; g) **MVT-10-600**; h) **MVT-17-600**.

Figure 4.2. FESEM (left) and HRTEM (right) micrographs of **MVT-1-400** (**A**), **MVT-5-400** (**B**), **MVT-10-400** (**C**) and **MVT-17-400** (**D**) catalysts.

Figure 4.3. Low magnification (5K and 3.9K, respectively) of selected catalysts: **MVT-5-as** (**A**), **MVT-5-600** (**B**), **MVT-17-as** (**C**) and **MVT-17-600** (**D**).

Figure 4.4. N_2-adsorption isotherms (**A**, **B**); t-Plot in N_2 adsorption, highlighting the points used for the linear fit (**C, D**) and CO_2-adsorption isotherms (**E**, **F**) of Te-doped MoVOx catalysts heat-treated at 400 ºC (**A**, **C, E**) or 600 ºC (**B**, **D**, **F**).

Figure 4.5. H_2-TPR profiles of **MVT** catalysts calcined at 400 ºC (**A**) and 600 ºC (**B**); NH_3-TPD profiles of representative **MVT** samples: normalized by BET surface area calcined at 400 ºC (**C**) and 600 ºC (**D**); or normalized by mass of catalyst and calcined at 400 ºC (**E**) and 600 ºC (**F**).

Figure 4.6. Variation of the selectivity to ethylene as a function of the ethane conversion of Te-doped $MoVO_x$ catalysts activated at 400 ºC, MVT-x-400 series (**A**) or 600 ºC, MVT-x-600 series (**B**). Experimental conditions described in page 123. Variation of the specific activity and the rate of ethylene formation (STY_{C2H4}) with the Te/Mo ratio in the synthesis gel for preparation of Te-doped MoVOx catalysts heat-treated at 400 ºC (**C**) and 600 ºC (**D**). In all cases, **MV-400** or **MV-600** catalysts (from **Chapter 3**) have been used as references.

Figure 4.7. XPS spectra of V $2p_{3/2}$ (**A, B**), Te $3d_{5/2}$ (**C, D**) and Mo *3d* (**E, F**) core level of catalysts heat-treated at 400 ºC (**A, C, E**) or 600 ºC (**B, D, F**).

Figure 4.8. Variation of the Te/Mo and V/Mo atomic ratios, determined by EDX, with the Te/Mo ratio in the synthesis gel for catalysts heat-treated at 400 ºC (**A**) or 600 ºC (**B**). Variation of the Te/Mo and V/Mo atomic ratios, determined by XPS, with the Te/Mo atomic ratio determined by EDX for catalysts calcined at 400 ºC (**C**) and 600 ºC (**D**).

Figure 4.9. Variation of the selectivity to ethylene as a function of Te/Mo ratio in the synthesis gel (**A**) or as a function of the V^{4+}/V_{total} relationship (calculated by XPS) on the surface of the catalysts (**B**), for catalysts heat-treated at 400 ºC (**MVT-x-400** series) or 600 ºC (**MVT-x-600**, series). Data obtained for an ethane conversion of 40% and 390 ºC of reaction temperature (**Table 4.2**). V^{4+}/V_{total} ratio of catalysts, calculated by XPS (see **Table 4.3**).

Chapter 5. Influence of composition and thermal treatment on M1-containing catalysts: catalytic and electrochemical approach

Figure 5.1. XRD patterns (**A**, **B** and **C**), FT-IR (**D**, **E** and **F**) and Raman (**G**, **H** and **I**) spectra of Mo-V-O (**A**, **D** and **G**), Mo-V-Te-O (**B**, **E** and **H**) and Mo-V-Te-Nb-O (**C**, **F** and **I**) mixed oxides heat-treated at 400, 500 or 600 ºC. Note that XRD patterns of as-synthesized materials are also shown.

Figure 5.2. FESEM micrographs of **MV-400** (**A**), **MV-500** (**B**), **MVT-17-400** (**C**), **MVT-17-600** (**D**), **MVTN-400** (**E** and **G**) and **MVTN-600** (**F** and **H**). Note that **G** and **H** micrographs are magnifications of **E** and **F**, respectively.

Figure 5.3. N_2 adsorption isotherms for catalysts heat-treated at 400 ºC (**A**) and 600 ºC (**B**), and t-Plot calculations derived from adsorption isotherms for catalysts heat-treated at 400 ºC (**C**) and 600 ºC (**D**), highlighting the points used for the linear fit. Note that data from bimetallic Mo-V-O catalyst (**MV-500** sample) is also shown together with the results from catalysts heat-treated at 600 ºC.

Figure. 5.4. Variation of the selectivity to the main reaction products (ethylene, CO, and CO_2) with the ethane conversion, at 390 ºC, for Mo-V-Te-Nb-O catalysts heat-treated at 400 ºC (left) and 600 ºC (right).

Figure 5.5. Ethylene selectivity as a function of ethane conversion, at 390 ºC and a feed mixture with C_2H_6/O_2/He molar ratio of 5/5/90, for mixed metal oxides catalysts: (**A**) **MV-t** series; (**B**) **MVT-17-t** series; and (**C**) **MVTN-t** series**.**

Figure 5.6. Reaction rate values of bi-, tri- and tetra-metallic catalysts (MV-t, MVT-t and MVTN-t series), heat-treated at 400 ºC (black), 500 ºC (orange) or 600 ºC (red), without normalization (**A**) and normalized by surface area and active site (**B**). Reaction rate as 10^3 mol_{C2H6} $g_{cat}^{-1}h^{-1}$ at ethane conversions below 10 %. Reaction rate per active site and area as 10^3 mol_{C2H6} $(100\ \%V)^{-1}$ m^{-2} h^{-1} at ethane conversions below 10 %.

Figure 5.7. XPS analysis of Mo *3d* core level (**A**, **B** and **C**) for **MV-t** (**A**), **MVT-17-t** (**B**) and **MVTN-t** (**C**); V $2p_{3/2}$ core level (**D**, **E** and **F**) for **MV-t** (**D**), **MVT-17-t** (**E**) and **MVTN-t** (**F**); Te $3d_{5/2}$ core level (**G** and **H**) for **MVT-17-t** (**G**) and **MVTN-t** (**H**); and Nb *3d* core level for **MVTN-t** (**I**) catalysts.

Figure 5.8. Selectivity to ethylene as a function of the V^{4+}/V_{total} relationship, determined by XPS, for Mo-V-O (black), Mo-V-Te-O (blue) and Mo-V-Te-Nb-O (red) catalysts, heat-treated at 400, 500 or 600 ºC.

Figure 5.9. Nyquist (**A**) and Bode-module (**B**) plots for bi-, tri- and tetrametallic catalysts heat-treated at 400 ºC and 600 ºC with equivalent circuit used for the EIS data fit (**C**) and calculated resistance (R_1) values derived from it (**D**).

Figure 5.10. Mott-Schottky plots for **MV-400** (black, empty), **MV-500** (black, full), **MVT-17-400** (green, empty), **MVT-17-600** (green, full), **MVTN-400** (red, empty) and **MVTN-600** (red, full). Note that Mott-Schottky plots for MoO_3 (up) and V_2O_5 (bottom) are also shown on the right.

Figure 5.11. Selectivity to ethylene (values taken at an ethane conversion of 50%) as a function of the anodic current density for mixed oxide catalysts, heat-treated at 400 ºC, 500 ºC or 600 ºC: **MV-t** (black), **MVT-17-t** (blue) and **MVTN-t** (red).

Figure 5.12. Relationship between the selectivity to ethylene and the R_1 data for **MV-t**, **MVT-17-t** and **MVTN-t** samples. Note that selectivity to ethylene is taken at 10% of ethane conversion and 390 ºC of reaction temperature.

Chapter 6. Evolution of the optimal catalytic systems for ethane ODH: the role of adsorption in catalytic performance

Figure 6.1. XRD (**A, D, G**); UV-Raman (325nm, red) + Raman (514nm, black) (**B, E, H**); and V $2p_{3/2}$ (**C, I**) and Ni $2p_{3/2}$ (**F**) core level XPS spectra of catalysts: **MVTN-600** (**A, B, C**), **(Sn)NiO** (**D, E, F**) and **5V/AL** (**G, H, I**) catalysts.

Figure 6.2. H_2-TPR analysis of **MVTN-600** (blue), **(Sn)NiO** (black) and **5V/AL** (red) catalysts.

Figure 6.3. IR spectra of: **A)** CO adsorption at saturation coverage at -165ºC; (**B, C**) NH_3 adsorption after evacuation at 25 ºC (B) or 100 ºC (C); **D)** and ethylene adsorbed (43 mbar) after evacuation at 25 ºC. Catalysts: **MVTN-600** (a), **(Sn)NiO** (b) and **5V/AL** (c) catalysts.

Figure 6.4. Variation of the selectivity to ethylene (**A, B, C**) and CO_x (**D, E, F**) with the ethane conversion at 400 ºC (full dots) and 450 ºC (empty dots) for **MVTN-600** (**A**, **D**), **(Sn)-NiO** (**B**, **E**) and **5V/AL** (**C**, **F**) catalysts. Ethylene (black); CO (blue) and CO_2 (red).

Figure 6.5. Variation of the selectivity to CO_2 (**A**) and CO (**B**) with during the ODH of ethylene, and CO conversion as a function of the temperature (**C**) for **MVTN-600** (blue), **(Sn)NiO** (black) and **5V/AL** (red) catalysts.

Figure 6.6. Variation of ethane (open symbols) and ethylene (full symbols) conversion with contact time (W/F) for **MVTN-600** (**A**), **(Sn)NiO** (**B**) and **5V/AL** (**C**) catalysts. Reaction conditions: 5 C_2H_6/5 O_2/ 90 He molar ratio and a reaction temperature of 400 ºC.

Figure 6.7. Reaction mechanism for the oxidative dehydrogenation of ethane over: **A**) V-containing catalysts, **MVTN-600** and **5V/AL**; and **B**) Ni-containing catalysts, **(Sn)NiO**.

Figure 6.8. In situ IR spectra of coadsorbed ethylene and O_2 at constant reaction pressure (128 mbar, 43 mbar of C_2H_4 and 84 mbar of O_2) and increasing temperatures with reference spectrum prior to adsorption (black): 25 ºC (red), 100 ºC (green), 150 ºC (blue), 200 ºC (magenta) and 250 ºC (dark green). Samples studied: **MVTN-600** (**A**); **(Sn)NiO** (**B**); and **5V/AL** (**C**). Additionally, spectrum from each catalyst at 25 ºC after heating is presented in highlighted orange.

Appendix II

Index of Tables

Chapter 1. Introduction

Chapter 2. Experimental section

No tables.

Chapter 3. Bimetallic MoVOx mixed metal oxides: optimization of the synthesis parameters and catalytic performance

Chapter 4. Te-doped M1-MoVOx catalysts: the role of tellurium on textural properties, thermal stability and catalytic behavior

Chapter 5. Influence of composition and thermal treatment on M1-containing catalysts: catalytic and electrochemical approach

Chapter 6. Evolution of the optimal catalytic systems for ethane ODH: the role of adsorption in catalytic performance

Appendix III

List of publications and selected conferences

Publications directly related to the present doctoral thesis:

- A. De Arriba, B. Solsona, A. Dejoz, P. Concepción, N. Homs, P. Ramírez de la Piscina, J. M. López Nieto; **Evolution of the optimal catalytic systems for the oxidative dehydrogenation of ethane: The role of adsorption in the catalytic performance,** Journal of Catalysis, 408 (2022) 388-400.

- A. De Arriba, B. Solsona, E. García-González, P. Concepción, J. M. López Nieto; **Te-doped MoV-Oxide (M1 phase) for ethane ODH. The role of tellurium on morphology, thermal stability and catalytic behaviour,** Applied Catalysis A: General, 643 (2022) 118780.

- A. De Arriba, G. Sánchez, R. Sánchez-Tovar, P. Concepción, R. Fernández-Domene, B. Solsona, J. M. López Nieto; **On the selectivity to ethylene during ethane ODH over M1-based catalysts. A surface and electrochemical study,** Catalysis Today, 418 (2023) 114112.

Other related publications:

- Y. Abdelbaki, A. De Arriba, B. Solsona, D. Delgado, E. García-González, R. Issaadi, J. M. López Nieto; **The nickel-support interaction as determining factor of the selectivity to ethylene in the oxidative dehydrogenation of ethane over nickel oxide/alumina catalysts**, Applied Catalysis A: General 623 (2021) 118242.

- L. Ruiz-Rodríguez, A. De Arriba, A. Vidal-Moya, T. Blasco, E. Rodríguez-Castellón, J. M. López Nieto; **The role of promoters on the catalytic**

performance of $M_xV_2O_5$ bronzes for the selective partial oxidation of H_2S, Applied Catalysis A: General 647 (2022) 118900.

- Y. Abdelbaki, A. De Arriba, R. Issaadi, R. Sánchez-Tovar, B. Solsona, J. M. López Nieto; **Optimization of the performance of bulk NiO catalyst in the oxidative dehydrogenation of ethane by tuning the synthesis parameters**, Fuel Processing Technology 229 (2022) 107182.

- Y. Abdelbaki, R. Sánchez-Tovar, A. De Arriba, E. García-González, R. Fernández-Domene, B. Solsona, J. M. López Nieto; **Predicting the catalytic perfomance of Nb-doped nickel oxide catalysts for the oxidative dehydrogenation of ethane by knowing their electrochemical properties**, Journal of Catalysis 420 (2023) 9-22.

- A. Massó, A. De Arriba, F. Ivars-Barceló, A. Ykrelef, B. Solsona, J. M. López Nieto; **Upgrading the reflux method as novel route for competitive catalysts in alkane selective oxidation**, Catalysis Science & Technology 13 (2023) 4802.

Selected conferences:

Oral: A. De Arriba, R. Sanchis, D. Delgado, B. Solsona, J.M López Nieto; "ODH of ethane on Orthorhombic MoV-based catalysts: the key aspect is the control of the olefinoveroxidation" 7th ENMIX WORKSHOP, Rome (Italy), 3^{th}-5^{th} May 2019.

Oral: A. De Arriba, D. Delgado, B. Solsona, J.M López Nieto; "Efecto de promotores en la síntesis y propiedades catalíticas para deshidrogenación

oxidativa de etano de catalizadores Mo-V-Me-O" SECAT'19, Córdoba (Spain), 24th-29th June 2019.

Poster: A. De Arriba, D. Delgado, B. Solsona, J.M López Nieto; "ODH of ethane on Orthorhombic MoV-based catalysts: the key aspect is the control of the olefin overoxidation" 14th European Congress on Catalysis (EuropaCat 2019), Aachen (Germany), 18th-23th August 2019.

Oral: A. De Arriba, B. Solsona, J.M López Nieto, "Influencia del estado de oxidación de los metales en óxidos tipo Mo-V-Te-O para la ODH de etano" IV Encuentro de Jóvenes Investigadores de la Secat (IV JJII SECAT 2020), Bilbao (Spain), 21th-23th September 2020.

Oral: A. De Arriba, B. Solsona, E. García-González, J.M López Nieto; "Efecto de la composición y morfología en las propiedades catalíticas de óxidos tipo Mo-V-Te-O para la deshidrogenación oxidativa de etano" SECAT'21, Valencia (Spain), 18th-20th October 2021.

Oral: A. De Arriba, D. Delgado, P. Concepción, J.M López Nieto; "One-pot valorization of glycerol into acrylic acid using bronze-based mixed oxides: differences between acid and acid-redox catalysts" 9th Tokyo Conference on Advanced Catalytic Science and Technology (TOCAT9), Fukuoka (Japan) – online, 24th-29th July 2022.

Oral: A. De Arriba, B. Solsona, E. García-González, P. Concepción, J.M López Nieto; "Ethane ODH over M1-MoVTeNbO catalysts: the role of Te and Nb" 9th World Congress on Oxidation Catalysis (9WCOC), Cardiff (Wales), 4th-8th September 2022.

Oral: A. De Arriba, B. Solsona, J.M López Nieto; "Mo-V-(Te)-O mixed oxides (M1 phase): correlations between adsorption and catalytic properties in the oxidative hydrogenation of ethane" 42 Reunión Ibérica de Adsorción (42RIA), Valencia (Spain), 13th-19th September 2022.

Flash oral + poster: A. De Arriba, B. Solsona, A. Dejoz, P. Concepción, N. Homs, P. Ramírez de la Piscina, J. M. López Nieto "Evolution of the optimal catalytic systems for the oxidative dehydrogenation of ethane: the role of adsorption in the catalytic performance" SECAT'23, Málaga (Spain), 20th-23th June 2023.

Oral: A. De Arriba, D. Delgado, P. Concepción, J. M. López Nieto; "Valorization of glycerol into acrylic acid using bronze-based mixed oxides catalysts: single or double catalytic beds approaches" 10th International Symposium on Group Five Elements, Montreal (Canada), 25th-28th June 2023.

Poster: A. De Arriba, D. Delgado, P. Concepción, J. M. López Nieto "One pot valorization of glycerol into acrylic acid: a catalytic and spectroscopic study" 15th European Congress on Catalysis (EuropaCat 2023), Prague (Czech Republic), 27th August- 1st September 2023.

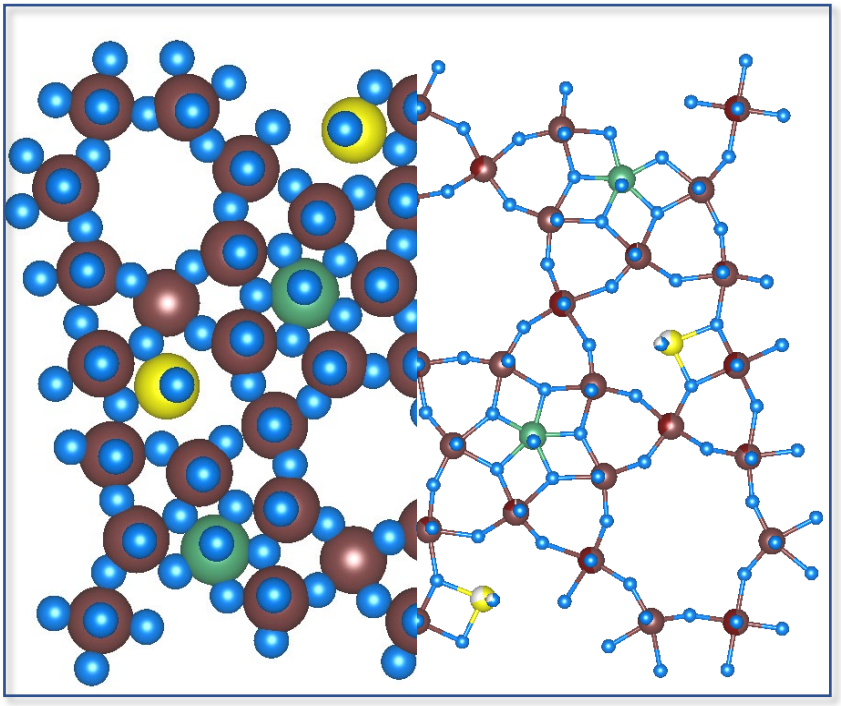

Orthorhombic M1 structure: ball in space-filling (left) and ball-and-stick (right). Mo or V (●); Nb (●); Te (●) and O (●).